

A precision measurement of ν_μ disappearance in the T2K experiment

Thomas J. Dealtry

Magdalen College, Oxford



Thesis submitted in partial fulfilment of the requirements for the
degree of Doctor of Philosophy at the University of Oxford

Trinity Term, 2014

A precision measurement of ν_μ disappearance in the T2K experiment

Thomas J. Dealtry
Magdalen College, Oxford

Thesis submitted in partial fulfilment of the requirements for the degree of
Doctor of Philosophy at the University of Oxford
Trinity Term, 2014

Abstract

T2K is long-baseline accelerator neutrino oscillation experiment using the high-intensity ν_μ beam produced at J-PARC. Sitting 295 km away, the giant Super-Kamiokande detector, a 50 kt water tank instrumented with 11,129 photo-sensitive detectors, sees a narrow band beam peaked at 600 MeV. The baseline to energy ratio is finely tuned for studying neutrino oscillations at the *atmospheric* neutrino squared-mass splitting. The beam is also sampled 280 m downstream of the neutrino production target by a series of finely segmented solid scintillator and time projection chamber detectors. Observing changes in the neutrino beam between the two detectors allows oscillation parameters to be accurately extracted.

A ν_μ -disappearance analysis was performed on the combined T2K Run 1+2+3+4 dataset, corresponding to integrated J-PARC neutrino beam exposure of 6.57×10^{20} POT, in a framework of three active neutrino flavour oscillations including matter effects in constant-density matter. The observed reconstructed energy spectrum of 1 μ -like ring events was fitted, and separate fits were made for the normal and the inverted mass hierarchies. In these fits, $\sin^2 \theta_{23}$ and either $|\Delta m_{32}^2|$ (normal mass hierarchy) or $|\Delta m_{31}^2|$ (inverted mass hierarchy) were allowed to float. The oscillation parameters $\sin^2 \theta_{13}$, $\sin^2 \theta_{12}$, Δm_{21}^2 , δ_{CP} , and all 41 systematic parameters considered in this analysis were also allowed to float in the fit.

This analysis predicts 445.98 ± 23.46 (syst) 1 μ -like ring events in SK in the absence of any oscillation, but only 120 were observed. The observed deficit has a strong energy dependence; the ratio of observed to expected, under the no-oscillation hypothesis, is $\sim 26\% < 0.5$ GeV, $\sim 10\%$ between 0.5 and 1 GeV and $\sim 72\% > 1$ GeV.

The 68% confidence intervals on the oscillation parameters can be summarised as $\sin^2 \theta_{23} = 0.514_{-0.050}^{+0.049}$ $|\Delta m_{32}^2| = 2.51 \pm 0.10$ eV $^2/c^4$ for the normal mass hierarchy, and $\sin^2 \theta_{23} = 0.511_{-0.049}^{+0.050}$ $|\Delta m_{31}^2| = 2.48 \pm 0.10$ eV $^2/c^4$ for the inverted mass hierarchy. This is the most precise measurement of $\sin^2 \theta_{23}$ to date.

Declaration

I declare that this thesis and the work presented in it are my own and were produced by me as the result of my own original research. The work was done while a candidate for a degree at the University of Oxford, and has not been submitted for any other qualification. Results and figures from published works have been clearly attributed.

The work presented in Chapters 2 and 3 was performed by others. The analysis in Chapter 4 was performed by myself, Costas Andreopoulos, Steve Dennis, Lorena Escudero, and Nick Grant and has been published in Ref. [1]. The analysis in that chapter is a continuation of work performed by myself, Costas Andreopoulos, Lorena Escudero, and Nick Grant that has been published in Ref. [2], which again built on work performed by Costas Andreopoulos, Nick Grant, and Jelana Illic that has been published in Ref. [3].

Contents

List of Figures	viii
List of Tables	xiii
List of acronyms	xvi
1 Introduction	1
1.1 A brief history of neutrinos	1
1.1.1 Postulation and discovery of neutrinos	1
1.1.2 Neutrino properties	3
1.2 Standard Model of particle physics	5
1.2.1 Dirac mass	9
1.2.2 Majorana mass	10
1.3 Neutrino interactions in matter	12
1.4 Neutrino oscillations	15
1.4.1 Theory of three active neutrino oscillations	15
1.4.2 Three active flavour neutrino oscillation experiments . . .	20
1.4.3 Current knowledge	28
1.4.4 Anomalies	32
1.4.5 Future prospects	34

2 The T2K Experiment	37
2.1 The neutrino beam	38
2.1.1 J-PARC accelerator complex	38
2.1.2 Neutrino beamline	39
2.1.3 Global alignment and time synchronisation	41
2.1.4 Neutrino spectrum at off-axis locations	42
2.2 On-axis beam monitors	43
2.2.1 Proton beam monitors	44
2.2.2 Muon monitors	45
2.2.3 INGRID	46
2.3 ND280	48
2.3.1 Time projection chambers (TPCs)	50
2.3.2 Fine grained detectors (FGDs)	52
2.3.3 TRIP-t subdetectors (PØD, ECal, and SMRD)	57
2.3.4 Reconstruction and Monte Carlo simulation	58
2.4 Super-Kamiokande	61
2.4.1 The Super-Kamiokande detector	61
2.4.2 Calibration and detector stability	64
2.4.3 Reconstruction and Monte Carlo simulation	66
2.5 T2K status and physics goals	69
3 Inputs to the ν_μ disappearance analysis	71
3.1 Neutrino beam flux prediction & uncertainties	72
3.1.1 Neutrino flux simulation	72
3.1.2 Neutrino flux prediction uncertainties	76
3.2 Neutrino interaction modelling and systematics	78
3.2.1 NEUT neutrino Monte Carlo event generator	79
3.2.2 Comprehensive model tuning	83

3.2.3	Cross-section model systematics	87
3.2.4	Final state interaction systematics	90
3.3	ND280 flux and cross-section constraint	91
3.3.1	ν_μ charged current inclusive event selection	92
3.3.2	ν_μ CC semi-inclusive event selections	95
3.3.3	Event selection systematics	98
3.3.4	Flux and cross-section constraint	100
3.4	Super-Kamiokande measurements of 1 μ -like ring events	108
3.4.1	Fully-contained and fully-contained fiducial-volume selections	109
3.4.2	1 μ -like ring event selection cuts	111
3.4.3	Event selection systematics	113
3.4.4	Combined SK detector and pion interaction modelling systematics	118
4	ν_μ disappearance analysis	120
4.1	SK 1 μ -like ring spectrum prediction	121
4.1.1	Methodology	121
4.1.2	Construction of nominal SK Monte Carlo templates	122
4.1.3	Flux tuning based on NA61/SHINE data	126
4.1.4	Flux and cross-section tuning based on ND280 data	126
4.1.5	Effect of three active neutrino flavour oscillations in constant-density matter	127
4.1.6	Predictions of MC 1 μ -like ring spectra	128
4.2	Effect of systematics	136
4.2.1	Input systematic parameters	136
4.2.2	Evaluation of effects of systematic parameters on the predicted 1 μ -like ring reconstructed energy spectrum	138

4.3	Procedure for the joint determination of ν_μ disappearance oscillation parameters	145
4.3.1	Choice of ν_μ disappearance oscillation parameters	145
4.3.2	Construction of likelihood	147
4.3.3	Numerical implementation	149
4.3.4	Goodness-of-fit tests	151
4.3.5	Fitter validation	152
4.3.6	Evaluation of the effects of systematic parameters on the determination of ν_μ disappearance oscillation parameters	161
4.3.7	Construction of confidence regions	166
4.3.8	Sensitivity for the joint determination of ν_μ disappearance oscillation parameters	172
4.4	Results	175
4.4.1	Best-fit 1 μ -like ring reconstructed energy spectra	180
4.4.2	Confidence regions for the joint determination of the atmospheric mass squared splitting and 23-mixing angle	184
4.4.3	Confidence regions for the individual determination of the atmospheric mass squared splitting and 23-mixing angle	191
4.5	Discussion	195
5	Summary and Outlook	197
	Appendices	200
A	ND280 ν_μ CC selection systematics	201
A.1	FGD detector systematics	201
A.2	TPC detector systematics	203
A.3	Other systematics	206

Bibliography	210
---------------------	------------

List of Figures

1.1	Total, QE, RES, and DIS CC ν_μ -nucleon and $\bar{\nu}_\mu$ -nucleon cross sections	14
1.2	Schematic of neutrino oscillations	16
1.3	Predicted solar neutrino energy spectrum from the pp chain	22
1.4	Three-flavour oscillation parameter 1-dimensional $\Delta\chi^2$ projections from a global fit to world neutrino data	29
1.5	Three-flavour oscillation parameter 2-dimensional regions from a global fit to world neutrino data	30
2.1	Plan view of the T2K beamline	39
2.2	Side view of the T2K secondary beamline	39
2.3	T2K flux for different off-axis angles and ν_μ survival probability at 295 km	43
2.4	INGRID on-axis neutrino detector	47
2.5	A typical neutrino event in the Proton Module	49
2.6	Exploded view of the ND280 off-axis neutrino detector	50
2.7	Energy loss as a function of momentum for charged particles in the TPC	59
2.8	Deposited energy as a function of range for charged particles stopping in FGD1	60

2.9	A typical neutrino event in FGD1	60
2.10	Layout of the SK neutrino detector	62
2.11	Typical 1 μ -like ring and 1 e-like ring events in SK	68
2.12	Accumulated POT delivered by the J-PARC beam to T2K	69
3.1	Phase space of π^+ , π^- , and K^+ contributing to the predicted neutrino flux at SK	74
3.2	Differential cross section for π^+ production in p ^{12}C interactions at $p_p = 31$ GeV/ c	75
3.3	Ratio of the reweighted flux over the nominal flux at SK	76
3.4	Reweighted SK flux predictions	77
3.5	Fractional SK flux error including all sources of uncertainties	79
3.6	Differential CCQE cross-section distributions from MiniBooNE data and MC predictions	85
3.7	Differential pion production cross-section distributions from Mini-BooNE data and MC predictions	86
3.8	Low energy π^+ ^{12}C scattering data, and the FSI model spread	92
3.9	High energy π^\pm ^{12}C scattering data, and the FSI model spread	93
3.10	Comparison between data and MC for the ND280 ν_μ CC samples	101
3.11	Correlations of parameters used in the ND280 fit	103
3.12	ν_μ CC samples as a function of $\cos \theta_\mu$ after the ND280 fit	105
3.13	ν_μ CC-0- π sample as a function of p_μ , in slices of $\cos \theta_\mu$, after the ND280 fit	105
3.14	ν_μ CC-1- π^+ and CC-other samples as a function of p_μ , in slices of $\cos \theta_\mu$, after the ND280 fit	106
3.15	Correlations of ND280-constrained flux and cross-section parameters used in the ν_μ disappearance oscillation fit	108
3.16	Time distribution of FC events at SK	110

3.17	Cumulative number of observed FCFV events in T2K as a function of POT	110
3.18	Distributions of 1 μ -like ring event selection variables at each selection stage for T2K data	112
3.19	Correlations of the combined SK detector, FSI and SI parameters used in the ν_μ disappearance oscillation fit	119
4.1	Predicted number of 1 μ -like ring events, as a function of $\sin^2 \theta_{23}$ and $ \Delta m_{32}^2 $	129
4.2	Predicted E_{reco} spectrum of 1 μ -like ring events, and contributions from various true neutrino reaction modes	132
4.3	Fractional difference in the predicted number of 1 μ -like ring events as a result of applying the NA61 flux tuning to the nominal MC templates, and ND280 flux and cross-section tuning to the NA61-tuned MC templates	132
4.4	Reconstructed-energy spectra of 1 μ -like ring events for nominal, NA61-tuned, and ND280-tuned MC predictions. Also shown are the ratios between spectra for each successive tuning step	135
4.5	Total error envelope of the 1 μ -like ring event reconstructed energy spectrum	143
4.6	Comparative size of systematic and statistical error effects on the 1 μ -like ring spectra	144
4.7	Comparative size of the uncertainty due to all systematic parameters, and individual systematic categories on the 1 μ -like ring spectra	144
4.8	Distributions of fitter residuals for $\sin^2 \theta_{23}$ and $ \Delta m_{32}^2 $ generated at $\sin^2 \theta_{23} = 0.370$	153

4.9	Distributions of fitter residuals for $\sin^2 \theta_{23}$ and $ \Delta m_{32}^2 $ generated at $\sin^2 \theta_{23} = 0.513$	154
4.10	Ratio of number of events in a single bin at the lowest part of the oscillation dip for toy datasets created with different input values of $\sin^2 \theta_{23}$ to number without oscillations against the input value of $\sin^2 \theta_{23}$	155
4.11	Systematic pull distributions for all systematic parameters	157
4.12	Summary of systematic pull distributions for all systematic parameters	158
4.13	Pull distributions for δ_{CP} , $f_{SF;t,r}$, $f_{\pi-less\Delta;t,r}$, $f_{E;r}^{SK}$, and $f_{5;r}^{SK+FSI}$. .	159
4.14	Effect of $\pm 3\sigma$ and $\pm 1\sigma$ tweaks of $f_{E;r}^{SK}$ on the SK 1 μ -like ring reconstructed energy spectrum	161
4.15	Effect of $\pm 3\sigma$ and $\pm 1\sigma$ tweaks of $f_{5;r}^{SK+FSI}$ on the SK 1 μ -like ring reconstructed energy spectrum	161
4.16	Difference between the $\Delta\chi^2_{\text{critical}}$ values obtained from the constant- $\Delta\chi^2$ method and those from the Feldman-Cousins method at confidence levels of 68% and 90%, as a function of $\sin^2 \theta_{23}$ and $ \Delta m_{32}^2 $	169
4.17	One-dimensional slices through the 68% and 90% 2-dimensional surfaces of Feldman-Cousins $\Delta\chi^2_{\text{critical}}$ values as a function of $\sin^2 \theta_{23}$ for 3 different values of $ \Delta m_{32}^2 $	170
4.18	One-dimensional slices through the 68% and 90% 2-dimensional surfaces of Feldman-Cousins $\Delta\chi^2_{\text{critical}}$ values as a function of $\sin^2 \theta_{23}$ for 3 different values of $\sin^2 \theta_{23}$	171
4.19	True input values of $ \Delta m_{32}^2 $ to the toy MC experiments used to find the 1-dimensional critical value of $\Delta\chi^2$ for $\sin^2 \theta_{23} = 0.55$. . .	172

4.20 True input values of $\sin^2 \theta_{23}$ to the toy MC experiments used to find the 1-dimensional critical value of $\Delta\chi^2$ for $ \Delta m_{32}^2 = 2.90 \times 10^{-3} \text{ eV}^2/\text{c}^4$	172
4.21 Comparison between the MINOS 90% C.L. allowed region and the results of a sensitivity study at the MINOS best-fit point	174
4.22 Comparison between the SK 90% C.L. allowed region and the results of a sensitivity study at the SK best-fit point	174
4.23 Results of a sensitivity study at maximal mixing	174
4.24 Systematic parameter pulls from the fit of the Run 1+2+3+4 dataset	178
4.25 Ratio of σ_{bf} to σ_{input} from the fit of the Run 1+2+3+4 dataset	179
4.26 Distribution of χ^2_{gof} from 1k toy MC experiments whose true input values were the Run 1+2+3+4 best-fit oscillation parameters	179
4.27 Best-fit reconstructed energy spectrum and ratio to the no-oscillation hypothesis	181
4.28 Best-fit reconstructed energy spectrum and its components	182
4.29 Comparison between best-fit reconstructed energy spectra obtained from the normal and inverted mass hierarchy fits of the Run 1+2+3+4 dataset	183
4.30 $\Delta\chi^2$ surface from the fit of the Run 1+2+3+4 dataset	184
4.31 Fractional difference between the $\Delta\chi^2$ surfaces obtained from the fits to the Run 1+2+3+4 dataset assuming the normal and inverted mass hierarchies	185
4.32 68% C.L. and 90% C.L. allowed regions obtained with the Feldman-Cousins method from the fit of the Run 1+2+3+4 dataset. Also shown are the 1σ effect of systematic and statistical errors at the best-fit point	186

4.33 Comparison between the 68% C.L. and 90% C.L. allowed regions obtained using the constant- $\Delta\chi^2$ and Feldman-Cousins methods	188
4.34 Comparison between the 68% C.L. and 90% C.L. allowed regions for the normal and inverted mass hierarchies obtained using the Feldman-Cousins method	188
4.35 Comparison between the 90% C.L. allowed region obtained using the Feldman-Cousins method from the fit to the T2K Run 1+2+3+4 dataset, and the allowed regions from MINOS, SK, and T2K Run 1+2+3	189
4.36 Comparison between the 68% C.L. and 90% C.L. allowed regions using the constant- $\Delta\chi^2$ method from the fit of the Run 1+2+3+4 dataset and the results of a sensitivity study at the best-fit point for Run 1+2+3+4	190
4.37 Comparison between the 68% C.L. and 90% C.L. allowed regions obtained from separate analyses to the Run 1+2+3+4, Run 1+2+3 and Run 4 datasets	191
4.38 Comparison between the 1-dimensional $\Delta\chi^2$ from the fit of the Run 1+2+3+4 data and the MC estimation of the 1-dimensional 68% and 90% critical values of $\Delta\chi^2$ as a function of $\sin^2\theta_{23}$ and $ \Delta m_{32}^2 $	192
4.39 Profile likelihood, as a function of $\sin^2\theta_{23}$ and $ \Delta m_{32}^2 $, from the fits of the Run 1+2+3+4, Run 1+2+3 and Run 4 datasets	193
5.1 The precision of $\sin^2\theta_{23}$ and $ \Delta m_{32}^2 $ as a function of T2K POT	198
5.2 T2K ultimate sensitivity for the joint determination of $\sin^2\theta_{23}$ and $ \Delta m_{32}^2 $	199

List of Tables

1.1	Particles of the Standard model	6
1.2	Quantum numbers of fermion doublets and singlets associated with the electroweak interaction	7
1.3	Three-flavour oscillation parameters from a global fit to world neutrino data	28
3.1	Summary of the cross-section errors used in the ND280 fit and ν_μ disappearance oscillation fit	87
3.2	Error on the number of events in the ND280 ν_μ CC samples from individual systematic parameters	100
3.3	Number of events in the ND280 ν_μ CC samples	104
3.4	Error on the number of events in the ND280 ν_μ CC samples from groups of systematic parameters	104
3.5	Summary of the ND280-constrained errors used in the ν_μ disappearance oscillation fit	107
3.6	Efficiencies and purities of the SK 1 μ -like ring event selection .	113
3.7	Summary of the systematic errors for the 1 μ -like ring event selection	114
3.8	Summary of the combined SK detector, FSI and SI errors used in the ν_μ disappearance oscillation fit	119
4.1	Statistics and normalisation of input SK MC samples	124

4.2	Best-fit values and 1σ range for the measured <i>non-23-sector</i> oscillation parameters	128
4.3	Calculated numbers of 1μ -like ring events without oscillations using the nominal MC templates, the NA61-tuned MC templates and the ND280-tuned MC templates without oscillations	133
4.4	Calculated numbers of 1μ -like ring events without oscillations using the nominal MC templates, the NA61-tuned MC templates and the ND280-tuned MC templates with oscillations	134
4.5	Table showing which of the 32 MC templates are effected by each of the 45 systematic parameters	137
4.6	Effect of 1σ systematic parameter variation, for groups of systematics, on the number of 1μ -like ring events	138
4.7	Effect of 1σ systematic parameter variation, for individual systematics, on the number of 1μ -like ring events	141
4.8	Numbers of events in a single bin at the lowest part of the oscillation dip with oscillations and ratio to number without oscillations for a true input value $\sin^2\theta_{23} = 0.513$	156
4.9	Maximum deviation as a fraction of statistical error, for fits to toy MC generated with $\pm 1\sigma$ shifts of individual systematic parameters, at a range of <i>23-sector</i> oscillation points. The values are sorted by the size of the deviation in $\sin^2\theta_{23}$	164
4.10	As in Tab. 4.9, but sorted by the size of the deviation in $ \Delta m_{32}^2 $. . .	166
4.11	Summary of best-fit parameters from fits to T2K data	176
4.12	Summary of 1-dimensional limits on $\sin^2\theta_{23}$ and $ \Delta m_{32}^2 $ or $ \Delta m_{31}^2 $ derived from T2K data	194
4.13	Exclusion of MINOS and SK best-fit points using T2K data	196

List of acronyms

$0\nu\beta\beta$ neutrino-less double beta decay

BLM beam loss monitor

C.L. confidence level

CC charged current

CCD charge-coupled device

CCQE charged current quasi-elastic

CNO carbon-nitrogen-oxygen

CPU central processing unit

CT current transformer

DAQ data acquisition

DIS deep inelastic scattering

dof degree of freedom

DS-ECal downstream electromagnetic calorimeter

ECal electromagnetic calorimeter

ES elastic scattering

ESM electrostatic monitor

FC fully-contained

FCFV fully-contained fiducial-volume

FEB front-end board

FEC front-end card

FEM front-end mezzanine

FGD fine grained detector

FSI final state interactions

FV fiducial volume

GPS Global Positioning System

ID inner detector

IH inverted mass hierarchy

INGRID Interactive Neutrino GRID

J-PARC Japan Proton Accelerator Research Complex

LINAC linear accelerator

MC Monte Carlo

MCMC Markov chain Monte Carlo

MPPC multi-pixel photon counter

MR main ring synchrotron

NC neutral current

ND280 Near Detector at 280 m

NH normal mass hierarchy

OD outer detector

OOFV out-of-fiducial-volume**OTR** optical transition radiation monitor**p.d.f.** probability density function**PID** particle identification**PMNS** Pontecorvo, Maki, Nagagawa, and Sakata**PMT** photomultiplier tube**PØD** π^0 detector**PØD-ECal** PØD electromagnetic calorimeter**POT** protons on target**QE** quasi-elastic**RC** ring-counting**RCS** rapid-cycling synchrotron**RES** resonance production**RFG** relativistic Fermi gas**SF** spectral function**SI** secondary interactions**SK** Super-Kamiokande**SMRD** side muon range detector**SSEM** segmented secondary emission monitor**T2K** Tokai to Kamioka**TFB** TRIP-t front-end board**TOF** time-of-flight

TPC time projection chamber

WLS wavelength shifting

Chapter 1

Introduction

1.1 A brief history of neutrinos

1.1.1 Postulation and discovery of neutrinos

- **Postulation.** The neutrino was first postulated by Pauli in 1930¹ to explain the continuous electron spectrum and the spin-statistics problem observed in β -decay experiments.
- **Discovery of the electron neutrino.** The neutrino ($\bar{\nu}_e$) was first directly detected by experiments performed by Reines and Cowan in 1956 [5], with a liquid scintillator detector positioned near a nuclear reactor detecting the inverse β -decay reaction

$$\bar{\nu}_e + p \rightarrow e^+ + n. \quad (1.1)$$

The event signature was a prompt e^+ signal in coincidence with a delayed signal from n capture on cadmium.

- **Discovery of the muon neutrino.** The muon neutrino ($\nu_\mu + \bar{\nu}_\mu$) was dis-

¹The original German-language letter is translated into English in Ref. [4].

covered in 1962 [6] by observing the interactions of neutrinos produced by pions decaying in flight,

$$\pi^\pm \rightarrow \mu^\pm + \overset{(-)}{\nu_\mu}, \quad (1.2)$$

in a spark chamber. The $\overset{(-)}{\nu_\mu}$ produced μ^\pm , not e^\pm , indicating that the $\overset{(-)}{\nu_\mu}$ is a distinct particle to the $\overset{(-)}{\nu_e}$.

- **Discovery of weak neutral currents.** Weak neutral current (NC) interactions were discovered by the Gargamelle experiment in 1973 [7]. The reaction

$$\overset{(-)}{\nu_\mu} + N \rightarrow \overset{(-)}{\nu_\mu} + \text{hadrons} \quad (1.3)$$

was distinguished from the weak charged current (CC) reaction

$$\overset{(-)}{\nu_\mu} + N \rightarrow \mu^\pm + \text{hadrons}, \quad (1.4)$$

that had been observed by previous experiments, by rejecting events with a muon track.

- **Discovery of the tau neutrino.** The tau neutrino (ν_τ) was discovered in 2000 by the DONuT experiment [8] by observing the interactions of neutrinos, produced by a proton beam incident on a beam dump. The decay of D_s ,

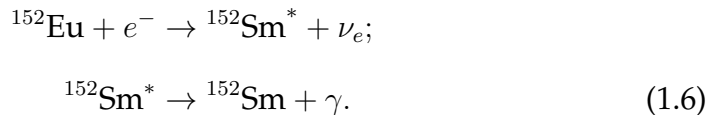
$$\begin{aligned} D_s^+ &\rightarrow \nu_\tau \tau^+, \\ D_s^- &\rightarrow \bar{\nu}_\tau \tau^-, \end{aligned} \quad (1.5)$$

and subsequent decay of the τ , produce a ν_τ and $\bar{\nu}_\tau$ within a few millimetres. The tau neutrinos were observed in an emulsion detector by searching

for the characteristic track kink from τ^- decay.

1.1.2 Neutrino properties

- **Helicity.** The helicity of the neutrino (ν_e) was found to be left handed in the Goldhaber experiment [9] via electron capture:



For resonant-scattered photons, the helicity of the photon is the same as the neutrino.

- **Number of light active neutrinos.** The number of light neutrinos which couple to the Z boson, N_ν , is measured by subtracting the partial Z widths for decays to charged leptons and quarks from the total Z width. This invisible width is then N_ν times the partial Z width from neutrinos. A combination of data from the LEP and SLC e^+e^- colliders finds $N_\nu = 2.9840 \pm 0.0082$ [10], consistent with the observations of three generations of particles in the Standard Model. Cosmological observations are consistent with this; the number of relativistic degrees of freedom is found to be 3.02 ± 0.27 , in agreement with theoretical value of 3.046 [11].
- **Mass.** Neutrino mass eigenstates ν_i and neutrino weak eigenstates ν_α are not the same (see Sec. 1.4.1), therefore a measurement of the neutrino mass weak eigenstate mass is a measurement of the superposition of the mass eigenstates. Observations of neutrino oscillations (see Sec. 1.4.3) tell us that neutrino masses are non-zero², but they are small and have not been measured. [Current observations give no strong indication of whether \$\nu_3\$](#)

²The lightest neutrino mass eigenstate could be zero.

is heavier or lighter than ν_1 and ν_2 . These possibilities are known as the **normal and inverted neutrino mass hierarchies**, respectively.

Observations of the beta decay of tritium (${}^3\text{H}$) set limits on the effective ν_e mass, $m_{\nu_e}^{\text{eff}} = \sqrt{\sum_i |U_{ei}|^2 m_{\nu_i}^2}$, by observing the end-point of the electron spectrum; the tightest limit is $m_{\nu_e}^{\text{eff}} < 2.05 \text{ eV}/c^2$ [12] (95% C.L.). Limits on $m_{\nu_\mu}^{\text{eff}}$ and $m_{\nu_\tau}^{\text{eff}}$, defined in an analogous way, are found by reconstructing charged pion and hadronic tau decays respectively, to be $m_{\nu_\mu}^{\text{eff}} < 0.17 \text{ MeV}/c^2$ (90% C.L.) [13] and $m_{\nu_\tau}^{\text{eff}} < 18.2 \text{ MeV}/c^2$ (95% C.L.) [14].

The neutrino-less double beta decay ($0\nu\beta\beta$) process,

$${}^A_Z N \rightarrow {}^A_{Z+2} N' + 2e^-, \quad (1.7)$$

can proceed only if a Majorana neutrino mass exists (see Sec. 1.2.2). The process can be studied only in nuclear isotopes where $2\nu\beta\beta$ is allowed and $1\nu\beta$ is energetically forbidden, leading to a long half-life. The signature of $0\nu\beta\beta$ is a peak in the sum of e masses, and the e^+ and e^- being emitted with equal and opposite momenta. The $0\nu\beta\beta$ half-life, $T_{1/2}^{0\nu\beta\beta}$, is related to the effective Majorana neutrino mass as

$$1/T_{1/2}^{0\nu\beta\beta} = G^{0\nu\beta\beta} |M^{0\nu\beta\beta}|^2 |\langle m_{\beta\beta} \rangle|^2, \quad (1.8)$$

where $G^{0\nu\beta\beta}$ and $M^{0\nu\beta\beta}$ are the phase space factor and matrix element of the $0\nu\beta\beta$ process respectively, and $\langle m_{\beta\beta} \rangle = |\sum_i U_{ei}^2 m_{\nu_i}|$ is the effective neutrino mass. The best limit on $\langle m_{\beta\beta} \rangle$ lies in the range $140\text{--}380 \text{ meV}/c^2$ (90% C.L.), is dependent on the matrix element calculation and uses ${}^{136}\text{Xe}$ [15].

Cosmological observations give an upper limit on the sum of neutrino masses of $\sum_i m_{\nu_i} < 0.66 \text{ eV}/c^2$ (95% C.L.) [11].

Plotting $\langle m_{\beta\beta} \rangle$ against the lightest neutrino mass, m_l ³, may allow the neutrino mass hierarchy to be determined. For large values of $m_l \gtrsim 10^{-2} \text{ eV}/c^2$, $m_1 \approx m_2 \approx m_3$ and the mass hierarchies are degenerate. For small values of m_l , in the inverted mass hierarchy (IH), $\langle m_{\beta\beta} \rangle$ is constrained to a band $10^{-2} \text{ eV}/c^2 \lesssim \langle m_{\beta\beta} \rangle \lesssim 5 \times 10^{-1} \text{ eV}/c^2$, and in the normal mass hierarchy (NH) $\langle m_{\beta\beta} \rangle \lesssim 5 \times 10^{-3} \text{ eV}/c^2$ [16].

- **Charge.** The neutrino is thought to have zero charge. The tightest constraint on this property is $q_\nu < 2 \times 10^{-15} e$ from observations of neutrinos from supernova 1987a [17].
- **Magnetic moment.** The best limit on the neutrino magnetic moment is from the GEMMA experiment, studying $\bar{\nu}_e$ cross sections at a nuclear reactor, and is $\mu_\nu < 3.2 \times 10^{-11} \mu_b$ at 90% C.L. [18].
- **Charge radius.** The best limit on the neutrino charge radius is from an experiment studying $\bar{\nu}_e$ cross sections at a nuclear reactor, and is $-2.1 \times 10^{-32} \text{ cm}^2 < r_\nu^2 < 3.3 \times 10^{-32} \text{ cm}^2$ at 90% C.L. [19].
- **Lifetime.** The best limit on the neutrino mean lifetime divided by mass is from an experiment searching for photons from the decay of $\bar{\nu}_e \rightarrow \nu' + \gamma$ at a nuclear reactor, where ν' is an undetectable neutral particle [20]. The limit is $\tau_\nu/m_\nu > 3 \times 10^2 \text{ sc}^2/\text{eV}$ [21].

1.2 Standard Model of particle physics

The Standard Model of particle physics is a quantum field theory describing the strong, weak, and electromagnetic interactions of all known elementary particles, as shown in Tab. 1.1. It is a gauge theory based on the local symmetry group $SU(3)_C \times SU(2)_L \times U(1)_Y$, where C is colour, L is left-handed chirality, and Y is

³ $m_l = m_1$ and $m_l = m_3$ for the normal and inverted mass hierarchies respectively.

weak hypercharge. There are eight coloured bosons, gluons, g , which mediate the strong force, arising from $SU(3)_C$. There are four electroweak bosons arising from $SU(2)_L \times U(1)_Y$; after electroweak symmetry breaking (in which the Higgs, H , acquires a non-zero vacuum expectation value) these are the massive W^\pm and Z^0 , and the massless photon, γ .

	Vector bosons			Higgs boson	
Quarks	$+\frac{2}{3}u$ $\frac{1}{2}$	$+\frac{2}{3}c$ $\frac{1}{2}$	$+\frac{2}{3}t$ $\frac{1}{2}$	${}^0_1 g$	${}^0_0 H$
Leptons	$-\frac{1}{3}d$ $\frac{1}{2}$	$-\frac{1}{3}s$ $\frac{1}{2}$	$-\frac{1}{3}b$ $\frac{1}{2}$	${}^0_1 \gamma$	
	$-\frac{1}{2}e$	$-\frac{1}{2}\mu$	$-\frac{1}{2}\tau$	${}^0_1 Z$	
	$\frac{0}{2}\nu_e$	$\frac{0}{2}\nu_\mu$	$\frac{0}{2}\nu_\tau$	${}^{\pm 1}_1 W$	

Table 1.1: The particles of the Standard model. The preceding superscript and subscript are the electric charge and spin respectively.

Fermions can be split into two groups depending on whether they are coloured: the quarks are coloured and therefore take part in the strong interaction to form hadrons, while the leptons do not. All fermions take part in electroweak interactions. There are three generations of fermions, each having identical quantum numbers, but different mass⁴.

Since leptons are colourless, the symmetry group $SU(2)_L \times U(1)_Y$ determines the interactions of neutrinos. The three generators of the weak isospin $SU(2)_L$ symmetry group are $I_a = \sigma_a/2$, where σ_a are the Pauli matrices. The generator of the hypercharge $U(1)_Y$ symmetry group is $Y = 2(Q - I_3)$, where Q is the charge. The vector gauge boson fields are then A_a^μ and B^μ for $SU(2)_L$ and $U(1)_Y$ respectively. Operating with the generators on the lepton fields (arranging

⁴For example, the e^- , μ^- , τ^- have masses $0.511 \text{ MeV}/c^2$, $105.66 \text{ MeV}/c^2$, $1776.82 \text{ MeV}/c^2$ respectively [21].

the left-handed fermion fields in doublets, L_L and Q_L , and the right-handed fermion fields in singlets, f_R) fixes the quantum numbers of the particles shown in Tab. 1.2. Neutrinos therefore only undergo weak interactions. Since the weak interaction is chiral, right-handed neutrinos (and left-handed antineutrinos) do not interact by the weak interaction, and so may not exist.

		I	I_3	Y	Q
lepton doublet	$L_l \equiv \begin{pmatrix} \nu_{eL} \\ e_L \end{pmatrix}$	1/2	1/2 -1/2	-1	0 -1
lepton singlet	e_R	0	0	-2	-1
quark doublet	$Q_l \equiv \begin{pmatrix} u_L \\ d_L \end{pmatrix}$	1/2	1/2 -1/2	1/3	2/3 -1/3
quark singlets	u_R d_R	0	0	4/3 -2/3	2/3 -1/3

Table 1.2: Quantum numbers of fermion doublets and singlets associated with the electroweak interaction.

The electroweak Lagrangian is then defined as the most general renormalisable Lagrangian, invariant under a local $SU(2)_L \times U(1)_Y$ symmetry:

$$\begin{aligned}
 \mathcal{L} = & i\overline{L_L} \not{D} L_L + i\overline{Q_L} \not{D} Q_L + \sum_{f=e,u,d} i\overline{f_R} \not{D} f_R & (1.9) \\
 & - \frac{1}{4} A_{\mu\nu}^a A^{a\mu\nu} - \frac{1}{4} B_{\mu\nu} B^{\mu\nu} \\
 & + (D_\mu \Phi)^\dagger (D^\mu \Phi) - \mu^2 \Phi \Phi^\dagger - \lambda (\Phi \Phi^\dagger)^2 \\
 & - y^e (\overline{L_L} \Phi e_R + \overline{e_R} \Phi^\dagger L_L) - y^d (\overline{Q_L} \Phi d_R + \overline{d_R} \Phi^\dagger Q_L) - y^u (\overline{Q_L} \Phi u_R + \overline{u_R} \Phi^\dagger Q_L),
 \end{aligned}$$

where $\not{D} = \gamma^\mu D_\mu$, γ^μ are the gamma matrices, the covariant derivative is defined as $D_\mu = \partial_\mu + ig A_\mu^a I^a + ig' B_\mu \frac{Y}{2}$, and Φ is the Higgs field. The first line describes the kinetic energy of fermion fields and interactions of fermions and gauge bosons, the second line describes the kinetic energy and self-interactions of the gauge bosons, the third line describes the Higgs field, and, the fourth line describes Higgs-fermion Yukawa couplings, through which generate fermion masses. It is

through the Higgs mechanism that the W and Z bosons, and fermions acquire mass.

The interactions of fermions with the physical gauge bosons can be derived by considering the first line in Eq. 1.9. Defining the physical boson fields

$$W^{\pm\mu} \equiv \frac{A_1^\mu \pm iA_2^\mu}{\sqrt{2}}, \quad (1.10)$$

$$A^\mu \equiv \sin \theta_W A_3^\mu + \cos \theta_W B^\mu, \quad (1.11)$$

$$Z^\mu \equiv \cos \theta_W A_3^\mu - \sin \theta_W B^\mu, \quad (1.12)$$

the interaction terms for ν_e and e in the Lagrangian are then⁵

$$\mathcal{L}_I^{CC} = -\frac{g}{\sqrt{2}} \overline{\nu_{eL}} \gamma^\mu e_L W_\mu + h.c., \quad (1.13)$$

$$\mathcal{L}_I^{NC} = -\frac{g}{\cos \theta_W} (g_L^\nu \overline{\nu_{eL}} \gamma^\mu \nu_{eL} + g_L^l \overline{e_L} \gamma^\mu e_L + g_R^l \overline{e_R} \gamma^\mu e_R) Z_\mu, \quad (1.14)$$

$$\mathcal{L}_I^\gamma = g \sin \theta_W \overline{e} \gamma^\mu e A_\mu. \quad (1.15)$$

This shows that neutrinos interact with charged leptons via the W bosons, neutrinos interact with the Z boson with no flavour change, and neutrinos don't interact with the γ .

After the Higgs mechanism, fermion mass terms are found in the form

$$\mathcal{L}_{\text{fermion mass}} = - \sum_{\alpha=e,\mu,\tau,u,d,s,c,b,t} \frac{y_\alpha v}{\sqrt{2}} \overline{f_\alpha} f_\alpha, \quad (1.16)$$

$$= - \sum_{\alpha=e,\mu,\tau,u,d,s,c,b,t} m_\alpha \overline{f_{\alpha L}} f_{\alpha R} + m_\alpha \overline{f_{\alpha R}} f_{\alpha L}, \quad (1.17)$$

where y_α is the Yukawa coupling from the diagonalised matrices, v is the Higgs

⁵When extending the model to three lepton generations, the terms are similar, with the addition of mixing (see Sec. 1.4). Terms describing electroweak interactions of quarks are similar and were omitted for simplicity.

vacuum expectation value, $f_\alpha = f_{\alpha L} + f_{\alpha R}$ are fermion fields of definite mass, and $m_\alpha = y_\alpha/v\sqrt{2}$ is the fermion mass. It should be noted that, in the Standard Model, neutrinos are massless due to the lack of right handed neutrino fields, ν_R .

The observation of neutrino oscillations presented in Sec. 1.4.3 is clear evidence of physics beyond the Standard Model, as neutrinos are required to have mass. There are two proposed mechanisms for providing neutrinos with mass, Dirac and Majorana [16].

1.2.1 Dirac mass

Extending the Standard model by including right-handed neutrino fields allowing, in analogy with other fermions. These fields are singlets of $SU(2)_L$ and have hypercharge $Y = 0$, therefore they are invariant under Standard Model fields, and so are sterile (interact only via gravity). In analogy with Eq. 1.17, the neutrino Dirac mass term is

$$\mathcal{L}^{\text{Dirac mass}} = \sum_{i=1,2,3} -m_i \bar{\nu}_i \nu_i. \quad (1.18)$$

where $m_i = y_i v / \sqrt{2}$, y_i is the Yukawa coupling from the diagonalised matrix, v is the Higgs vacuum expectation value, and $\nu_i = \nu_{iL} + \nu_{iR}$ are neutrino fields of definite mass. Trilinear interactions of fermions with the Higgs, H , of the form

$$\mathcal{L}^{\nu H} = \sum_{i=1,2,3} -\frac{m_i}{v} \bar{f}_i f_i H, \quad (1.19)$$

are also possible, in analogy with other fermions. It is unknown why the Yukawa couplings of the neutrinos (y_{ν_e} , y_{ν_μ} , y_{ν_τ}) are much smaller than the couplings of the other fermions. It should be noted that the process of diagonalising the

mass matrix uses the neutrino mixing matrix (Eq. 1.34), therefore the form of the neutrino mass matrix determines the neutrino mixing parameters.

It is not possible to find a global $U(1)$ gauge transformation of the right-handed fields of the form

$$\nu_{iR} \rightarrow e^{i\phi_\alpha} \nu_{iR}, \quad (i = 1, 2, 3), \quad (1.20)$$

that leaves both the Higgs-neutrino coupling (Eq. 1.19) and the neutrino kinetic term invariant. Therefore lepton flavour violation is allowed, and this has been observed in neutrino oscillations (see Sec. 1.4.3). The Lagrangian is invariant under the global transformations

$$\nu_{iL} \rightarrow e^{i\phi} \nu_{iL}, \quad \nu_{iR} \rightarrow e^{i\phi} \nu_{iR}, \quad (i = 1, 2, 3), \quad (1.21)$$

$$l_{\alpha L} \rightarrow e^{i\phi} l_{\alpha L}, \quad l_{\alpha R} \rightarrow e^{i\phi} l_{\alpha R}, \quad (\alpha = e, \mu, \tau), \quad (1.22)$$

which leads to the conservation of the *total* lepton number.

1.2.2 Majorana mass

A Majorana fermion is a fermion that is its own antiparticle⁶

$$\nu = \nu_L + \nu_L^C = \nu^C, \quad (1.23)$$

which is only possible for a particle whose (additive) quantum numbers are zero. This leads to a Majorana mass term

$$\mathcal{L}^{\text{Majorana mass}} = -\frac{1}{2} m \overline{\nu}_L^C \nu_L + -\frac{1}{2} m \overline{\nu}_L \nu_L^C. \quad (1.24)$$

⁶It is common to use the terminology neutrino and antineutrino to denote a Majorana neutrino with negative helicity and a Majorana neutrino with positive helicity respectively.

It is not possible to find a global $U(1)$ gauge transformation, under which $\mathcal{L}^{\text{Majorana mass}}$ is invariant. Total lepton number can therefore be considered as only an approximate symmetry, holding in all processes that are insensitive to the Majorana masses. The Majorana mass term can be included as a perturbation, with

$$\Delta L = \pm 2. \quad (1.25)$$

This can be seen experimentally in $0\nu\beta\beta$.

It should be noted that, although $\mathcal{L}^{\text{Majorana mass}}$ involves only ν_L , which is present in the Standard Model, Majorana mass terms are not allowed in the Standard Model. This is because $\mathcal{L}^{\text{Majorana mass}}$ breaks the $SU(2)$ gauge symmetry, unless a dimension 5 (or greater) operator is introduced in order to generate it. The simplest possible operator corresponds to 4-point $\nu_L - \nu_L - H - H$ Feynman diagrams, and is not renormalisable. A new exchange particle⁷ is therefore required to restore the renormalisability to the theory. For type I see-saw models both Dirac and Majorana mass terms are created. Many different assumptions about the relative sizes of Dirac and Majorana mass scales (m and \mathcal{M}) can be made, one of which ($m \ll \mathcal{M}$ with $\mathcal{M} \sim 10^{14}$ GeV) gives rise to the known neutrino states masses of $m_\nu \sim m^2/\mathcal{M}$, and heavy new right handed neutrinos $m_R \sim \mathcal{M}$. Mixing between the known and heavy states will occur, but is typically small ($\tan 2\theta = 2m/\mathcal{M}$). This process is therefore a possible explanation of the naturally very small neutrino masses.

The visible Universe contains an asymmetry between matter and antimatter. In order to generate the small observed baryon asymmetry⁸, the Sakharov conditions [23] must be satisfied: baryon number violation; C and CP violation;

⁷The new particle could be a fermion singlet, a scalar triplet, or a fermion triplet, corresponding to classes of see-saw models labelled type I, II, and III respectively.

⁸Measurements of the cosmic micro background suggests $\eta \equiv (n_B - n_{\bar{B}})/n_\gamma = (6.11 \pm 0.19) \times 10^{-10}$ [22].

and a departure from thermal equilibrium must occur. A possible mechanism for this is leptogenesis [24], in which the heavy Majorana neutrinos from a type I see-saw model have decays which violate lepton number due to C and CP violation. The lepton number asymmetry can then be converted into a baryon number asymmetry via sphaleron processes.

1.3 Neutrino interactions in matter

A review of neutrino interactions can be found in Ref. [25], and Sec. 3.2.1 summarises the models used in the present work. Here the types of neutrino CC interactions with nuclei that are important at neutrino energies of ~ 1 GeV, as at the T2K experiment, are introduced.

The neutrino-nucleon scattering dynamics are described by the invariant amplitude \mathcal{M} . The neutrino-nucleon cross-section depends on the squared amplitude which can be factorised into the hadronic tensor $W_{\mu\nu}$ and the leptonic tensor $L_{\mu\nu}$

$$\overline{|\mathcal{M}|^2} = 4G_F^2 L_{\mu\nu} W^{\mu\nu}, \quad (1.26)$$

where G_F is the Fermi constant. $L_{\mu\nu}$ describes the leptonic vertex, and is known exactly in the Standard Model. $W_{\mu\nu}$ describes the hadronic vertex. Although the quark currents are known exactly in the Standard Model, the nucleon is a complicated composite structure of valence quarks, sea quarks, and gluons and so $W_{\mu\nu}$ is not known. The most general form is given by:

$$\begin{aligned} W_{\mu\nu} = & -W_1 g_{\mu\nu} + W_2 \frac{p_\mu p_\nu}{M^2} + W_3 i \epsilon_{\mu\nu\alpha\beta} \frac{p^\alpha p^\beta}{2M^2} + W_4 \frac{q_\mu q_\nu}{M^2} \\ & + W_5 \frac{p_\mu q_\nu + p_\nu q_\mu}{M^2} + W_6 \frac{p_\mu q_\nu - p_\nu q_\mu}{M^2} \end{aligned} \quad (1.27)$$

where the six structure functions, $W_i = W_i(q\cdot, q^2)$, need to be determined by

experiment. For interactions on nuclear targets, the nucleon itself is bound within the nucleus and effects arising from the nuclear binding, Fermi motion and nucleon-nucleon correlations need to be taken into account. In addition, the so-called final state interactions (FSI), re-interactions in the nuclear medium of the hadrons emerging from the primary neutrino interactions, have a significant effect in the phenomenology of neutrino interactions in the few-GeV energy range and also need to be taken into account.

In quasi-elastic (QE) scattering the neutrino interacts with a nucleon, leaving it in the ground state:

$$\begin{aligned} \nu_\ell + n &\rightarrow \ell^- + p, \\ \bar{\nu}_\ell + p &\rightarrow \ell^+ + n, \end{aligned} \tag{1.28}$$

where $\ell = e, \mu, \tau$. In resonance production (RES) the neutrino interacts with a nucleon, exciting it into a resonance state:

$$\stackrel{(-)}{\bar{\nu}_\ell} + N \rightarrow \ell^\pm + N^*, \tag{1.29}$$

where N is a nucleon and N^* is a resonant state that will decay. The resonance most frequently decays to a nucleon and pion (e.g. $N^* = \Delta^{++} \rightarrow p + \pi^+$), but a variety of mesonic and photonic final states are possible. In coherent pion production the neutrino interacts with an entire nucleus, transferring negligible energy to the nucleus, A :

$$\stackrel{(-)}{\bar{\nu}_\ell} + A \rightarrow \ell^\mp + A + \pi^\pm. \tag{1.30}$$

The nucleus is left in the ground state, and the experimental signature of this process is a forward-scattered pion. In deep inelastic scattering (DIS) the neutrino

interacts with a single quark resulting in a hadronic shower:

$$\overset{(-)}{\nu_\ell} + q \rightarrow \ell^\pm + q', \quad (1.31)$$

where q and q' are initial and final state quarks. The final state quark will hadronise, producing most frequently pion(s). NC analogues of the processes above exist, for example the NC-elastic process is

$$\overset{(-)}{\nu_\ell} + N \rightarrow \overset{(-)}{\nu_\ell} + N. \quad (1.32)$$

Cross sections for ν_μ and $\bar{\nu}_\mu$ CC interactions, comparing data with a Monte Carlo (MC) prediction, are shown in Fig. 1.1.

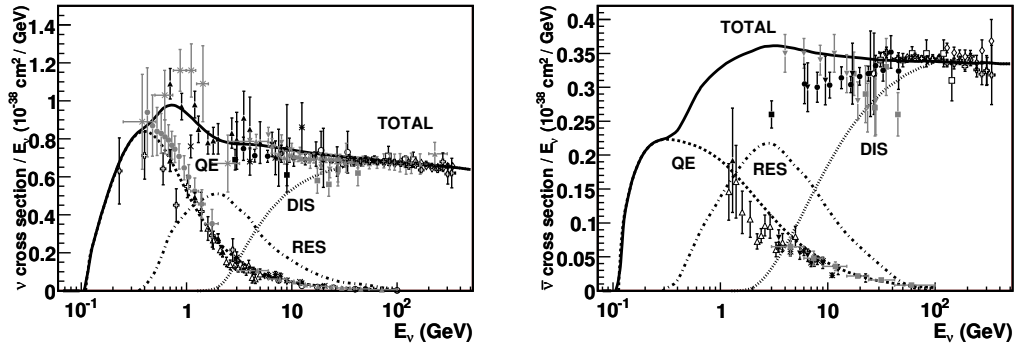


Figure 1.1: Total ν_μ (left) and $\bar{\nu}_\mu$ (right) per nucleon CC cross sections divided by neutrino energy as a function of energy. Also shown are the various contributing processes QE (dashed), RES (dot-dashed), and DIS (dotted). Example predictions for each are provided by the NUANCE neutrino MC event generator [26]. Note that the QE scattering data and predictions have been averaged over neutron and proton targets and hence have been divided by a factor of 2 for the purposes of this plot. Figure taken from [25].

1.4 Neutrino oscillations

1.4.1 Theory of three active neutrino oscillations

In the PMNS⁹ model for neutrino mixing, neutrino mass eigenstates, ν_i , and neutrino weak (flavour) eigenstates, ν_α , are not the same, but are related by a unitary matrix U ¹⁰, called the PMNS matrix:

$$|\nu_\alpha\rangle = \sum_i U_{\alpha i}^* |\nu_i\rangle. \quad (1.33)$$

In general, U can be parameterised by $N(N - 1)/2$ mixing angles and $(N - 1)(N - 2)/2$ physical phases¹¹. For the three-flavour case, the matrix is commonly expressed as three rotation matrices parameterised by angles θ_{ij} , with an additional phase, δ_{CP} :

$$U = \begin{pmatrix} 1 & 0 & 0 \\ 0 & c_{23} & s_{23} \\ 0 & -s_{23} & c_{23} \end{pmatrix} \begin{pmatrix} c_{13} & 0 & s_{13}e^{-i\delta_{CP}} \\ 0 & 1 & 0 \\ -s_{13}e^{i\delta_{CP}} & 0 & c_{13} \end{pmatrix} \begin{pmatrix} c_{12} & s_{12} & 0 \\ -s_{12} & c_{12} & 0 \\ 0 & 0 & 1 \end{pmatrix} \\ = \begin{pmatrix} c_{12}c_{13} & s_{12}c_{13} & s_{13}e^{-i\delta_{CP}} \\ -s_{12}c_{23} - c_{12}s_{23}s_{13}e^{i\delta_{CP}} & c_{12}c_{23} - s_{12}s_{23}s_{13}e^{i\delta_{CP}} & s_{23}c_{13} \\ s_{12}s_{23} - c_{12}c_{23}s_{13}e^{i\delta_{CP}} & -c_{12}s_{23} - s_{12}c_{23}s_{13}e^{i\delta_{CP}} & c_{23}c_{13} \end{pmatrix} \quad (1.34)$$

where $s_{ij} = \sin \theta_{ij}$ and $c_{ij} = \cos \theta_{ij}$.

If the masses of the neutrinos are not the same, neutrino oscillations, as shown schematically in Fig. 1.2, are possible. The massive neutrino states are eigenstates

⁹Named after the scientists who proposed neutrino oscillations: Pontecorvo [27, 28], and Maki, Nagagawa, and Sakata [29].

¹⁰This is the lepton equivalent of the CKM mixing matrix in the quark sector.

¹¹For Dirac neutrinos, this is the case. For Majorana neutrinos, extra phases exist (there are $N(N - 1)/2$ total phases), but are not observable in neutrino oscillations and so are not discussed further.

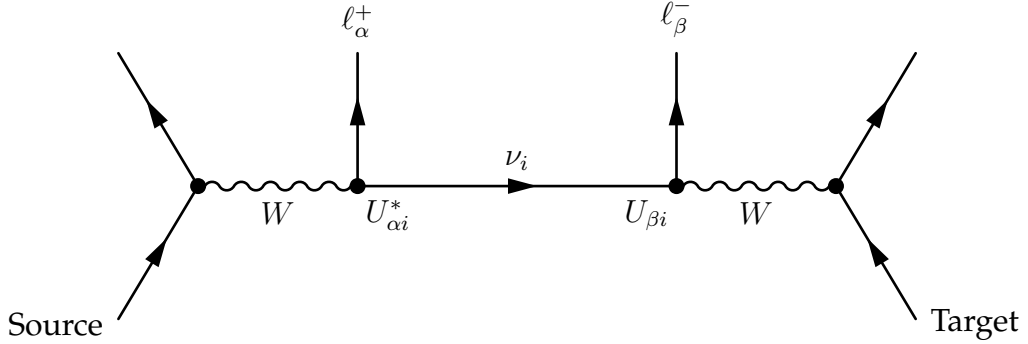


Figure 1.2: Schematic of neutrino oscillations. A neutrino mass eigenstate ν_i is created in coincidence with a lepton of flavour α , with probability $U_{\alpha i}^*$. The neutrino mass eigenstate is then detected at a later time, creating a lepton of flavour β , with probability $U_{\beta i}$.

of the Hamiltonian, and so have a solution to the Schrödinger equation

$$|\nu_i(t)\rangle = e^{-iE_i t} |\nu_i\rangle. \quad (1.35)$$

Substituting this into Eq. 1.33 gives

$$|\nu_\alpha(t)\rangle = \sum_i U_{\alpha i}^* e^{-iE_i t} |\nu_i\rangle, \quad (1.36)$$

the time evolution of a neutrino flavour eigenstate created at $t = 0$. Using the unitarity property of U ($\sum_i U_{\alpha i} U_{\beta i}^* = \delta_{\alpha\beta}$), Eq. 1.33 can be inverted and substituted into Eq. 1.36 to give

$$|\nu_\alpha(t)\rangle = \sum_\beta \left(\sum_i U_{\alpha i}^* e^{-iE_i t} U_{\beta i} \right) |\nu_\beta\rangle. \quad (1.37)$$

Using the orthonormal property of flavour eigenstates, the amplitude of transition from ν_α to ν_β as a function of time is

$$A_{\nu_\alpha \rightarrow \nu_\beta}(t) \equiv \langle \nu_\beta | \nu_\alpha(t) \rangle = \sum_i U_{\alpha i}^* e^{-iE_i t} U_{\beta i}. \quad (1.38)$$

If the momentum of the neutrino has a definite value, \vec{p} , and if the neutrino is ultrarelativistic ($|\vec{p}| \gg m_i$ for all i), the energy of each mass eigenstate is $E_i = \sqrt{|\vec{p}|^2 + m_i^2} \simeq |\vec{p}| + \frac{m_i^2}{2|\vec{p}|}$. The probability of oscillation $\nu_\alpha \rightarrow \nu_\beta$ is then

$$P(\nu_\alpha \rightarrow \nu_\beta) = |A_{\nu_\alpha \rightarrow \nu_\beta}(L, E)|^2 = \sum_{i,j} U_{\alpha i}^* U_{\beta i} U_{\alpha j} U_{\beta j}^* e^{-i \frac{\Delta m_{ij}^2 L}{2E}}, \quad (1.39)$$

where $\Delta m_{ij}^2 = m_i^2 - m_j^2$, and the ultrarelativistic approximations $L = t$ and $E = |\vec{p}|$ have been made. This is a formula with amplitude quartic in U , and phase $2\Phi_{ij} = \frac{\Delta m_{ij}^2 L}{2E}$. Squaring the unitarity relation gives

$$\delta_{\alpha\beta} = \sum_i U_{\alpha i} U_{\beta i}^* \sum_j U_{\alpha j} U_{\beta j}^* \quad (1.40)$$

$$= \sum_i |U_{\alpha i}^2| |U_{\beta i}^2| - 2 \sum_{i>j} \Re [U_{\alpha i}^* U_{\beta i} U_{\alpha j} U_{\beta j}^*]. \quad (1.41)$$

Substituting this into Eq. 1.39, after separating the parts $i = j$ and $i \neq j$ and using trigonometric identities, gives

$$\begin{aligned} P(\nu_\alpha \rightarrow \nu_\beta) &= \delta_{\alpha\beta} - 4 \sum_{i>j} \Re [U_{\alpha i}^* U_{\beta i} U_{\alpha j} U_{\beta j}^*] \sin^2 \left(\frac{\Delta m_{ij}^2 L}{4E} \right) \\ &\quad + 2 \sum_{i>j} \Im [U_{\alpha i}^* U_{\beta i} U_{\alpha j} U_{\beta j}^*] \sin \left(\frac{\Delta m_{ij}^2 L}{2E} \right). \end{aligned} \quad (1.42)$$

It has been shown in Ref. [30] that the standard derivation [16] given above gives an equivalent result to a treatment using wavepackets and no assumption of a common mass eigenstate momentum.

In order for oscillations to occur (i.e. $P(\nu_\alpha \rightarrow \nu_\beta) \neq \delta_{\alpha\beta}$), Eq. 1.42 requires that there is a non-zero difference between neutrino masses, implying that at least one neutrino is massive (oscillations are insensitive to the absolute mass scale, only to the mass difference). It also requires U not be a diagonal matrix (i.e. $U_{\alpha i} U_{\beta \neq \alpha, i} \neq 0$). The probabilities obey unitarity, i.e. $\sum_\beta P_{\nu_\alpha \rightarrow \nu_\beta} = \sum_\alpha P_{\nu_\alpha \rightarrow \nu_\beta} = 1$.

The probability of disappearance reduces to

$$P(\nu_\alpha \rightarrow \nu_\alpha) = 1 - 4 \sum_{k>j} |U_{\alpha i}|^2 |U_{\alpha k}|^2 \sin^2 \left(\frac{\Delta m_{ij}^2 L}{4E} \right). \quad (1.43)$$

Using the PMNS matrix in Eq. 1.34, the survival probability of muon neutrinos is

$$\begin{aligned} P(\nu_\mu \rightarrow \nu_\mu) = & 1 - (c_{13}^4 \sin^2(2\theta_{23}) + s_{23}^2 \sin^2(2\theta_{13})) \sin^2 \Phi_{31} \\ & + [c_{13}^2 (c_{12}^2 - s_{13}^2 s_{12}^2) \sin^2(2\theta_{23}) + s_{12}^2 s_{23}^2 \sin^2(2\theta_{13}) \\ & - s_{23}^2 c_{13}^2 \sin(2\theta_{13}) \sin(2\theta_{23}) \sin(2\theta_{12}) c_\delta] \\ & \times \left[\frac{1}{2} \sin 2\Phi_{21} \sin 2\Phi_{31} + 2 \sin^2 \Phi_{21} \sin^2 \Phi_{31} \right] \\ & - [\sin^2(2\theta_{12}) (c_{23}^2 - s_{13}^2 s_{23}^2)^2 + s_{13}^2 \sin^2(2\theta_{23}) (1 - c_\delta^2 \sin^2(2\theta_{12})) \\ & + 2s_{13}^2 \sin(2\theta_{12}) \cos(2\theta_{12}) \sin(2\theta_{23}) \cos(2\theta_{23}) c_\delta \\ & - 2s_{23}^2 s_{12}^2 c_{13}^2 \sin(2\theta_{13}) \sin(2\theta_{23}) \sin(2\theta_{12}) c_\delta \\ & + \sin^2(2\theta_{23}) c_{13}^2 (c_{12}^2 - s_{13}^2 s_{12}^2) + s_{12}^2 s_{23}^2 \sin^2(2\theta_{13})] \sin^2 \Phi_{21}. \end{aligned} \quad (1.44)$$

where $c_\delta = \cos \delta_{CP}$.

Experimentally L and E are chosen to maximise either $\sin^2 \Phi_{31}$ or $\sin^2 \Phi_{21}$ in order to maximise the oscillation effect at the point of detection. Experiments have measured $\Delta m_{31}^2 / \Delta m_{21}^2 \sim 30$ (see Sec. 1.4.3), therefore the limit $\Delta m_{31}^2 \gg \Delta m_{21}^2$ can be taken to give the dominant terms:

$$\begin{aligned} P(\nu_\mu \rightarrow \nu_\mu) \simeq & 1 - [\cos^4 \theta_{13} \sin^2(2\theta_{23}) + \sin^2 \theta_{23} \sin^2(2\theta_{13})] \sin^2 \Phi_{31} \\ = & 1 - 4 \cos^2 \theta_{13} \sin^2 \theta_{23} (1 - \cos^2 \theta_{13} \sin^2 \theta_{23}) \sin^2 \Phi_{31}. \end{aligned} \quad (1.45)$$

From this equation, $P(\nu_\mu \rightarrow \nu_\mu)$ is maximised at $\sin^2 \theta_{23} \simeq 1/(2 - 2 \sin^2 \theta_{13})$. Using recent measurements of $\sin^2(2\theta_{13}) = 0.098$ [31], this maximal disappearance

occurs at $\sin^2 \theta_{23} \approx 0.513$. The oscillation probability is also symmetric about this maximal point, therefore more information is required to determine the octant of θ_{23} . The leading order term for electron appearance is

$$P(\nu_\mu \rightarrow \nu_e) \simeq \sin^2 \theta_{23} \sin^2(2\theta_{13}) \sin^2 \Phi_{31}, \quad (1.46)$$

therefore a joint analysis of $\nu_\mu \rightarrow \nu_\mu$ and $\nu_\mu \rightarrow \nu_e$ is required in order to lift the octant degeneracy.

The above discussion corresponds to neutrinos travelling in a vacuum. As neutrinos travel through matter, different species can experience different potentials due to coherent scattering¹². All species of neutrino propagating through matter (e^- , p , n) undergo virtual interactions via the Z boson, but ν_e has an extra tree-level virtual interaction with e^- via the W boson. This causes the Hamiltonian to be altered with respect to the vacuum Hamiltonian, with the addition of a potential given by

$$V_\alpha = \sqrt{2}G_F \left(N_e \delta_{\alpha e} - \frac{1}{2} N_n \right), \quad (1.47)$$

where G_F is the Fermi constant, and N_e and N_n are the number densities of electrons and neutrons respectively. The oscillation probability in matter can be derived [16] yielding a probability of oscillation that is again dependent only on neutrino mass squared differences and independent of Majorana phases. For

¹²Incoherent scattering does occur, but can be neglected in most instances; the electron number density must be high (supernova cores, neutron stars, ...), or at Earth densities the neutrino energy be high (>10 TeV).

in the two flavour case, the oscillation parameters are modified as

$$\begin{aligned}\Delta m_M^2 &= \sqrt{(\Delta m^2 \cos 2\theta - A_{CC})^2 + (\Delta m^2 \sin 2\theta)^2}, \\ \tan 2\theta_M &= \frac{\tan 2\theta}{1 - \frac{A_{CC}}{\Delta m^2 \cos 2\theta}},\end{aligned}\quad (1.48)$$

where $A_{CC} = 2\sqrt{2}EG_F N_e$. This causes the oscillation probability to be modified. Oscillations in matter do not occur if vacuum mixing does not occur, or in very dense matter ($A_{CC} \rightarrow \infty$). The probability is also dependent on the sign of Δm^2 , therefore matter effects are required to allow the mass hierarchy to be determined. A resonance occurs if $A_{CC} = \Delta m^2 \cos 2\theta$, in which the effective mixing angle becomes $\pi/4$ and a complete transition between two flavours is possible. All these features persist in the three flavour case.

1.4.2 Three active flavour neutrino oscillation experiments

A wide array of experiments are used to determine neutrino oscillation parameters. Due to the large experimentally-measured difference between Δm_{21}^2 and Δm_{32}^2 , a single experiment cannot measure all six oscillation parameters.

- θ_{12} and Δm_{21}^2 are measured using solar, and $L \sim 100$ km reactor neutrino experiments. They find that $\theta_{12} \sim 33^\circ$, and, using matter effects, Δm_{21}^2 is positive.
- θ_{23} is measured using atmospheric, and long-baseline accelerator neutrino experiments with $E_\nu \sim 1$ GeV and $L \sim 100$ km. θ_{23} is found to be nearly maximal, $\sim 45^\circ$.
- θ_{13} is measured using $L \sim 1$ km reactor, and long-baseline accelerator neutrino experiments. θ_{13} is found to be $\sim 8.5^\circ$.
- $|\Delta m_{32}^2|$ is measured using atmospheric, long-baseline accelerator, and $L \sim$

1 km reactor neutrino experiments. Experiments which study neutrinos subjected to large matter effects are required to determine the sign (mass hierarchy).

- δ_{CP} will be measured using long-baseline accelerator neutrino experiments.

The major experiments driving the world knowledge of three active flavour neutrino oscillations are described below. The results of a global fit [32] to these datasets are shown in Sec. 1.4.3.

Solar neutrino experiments

A standard solar model can be constructed to describe the Sun, using inputs such as the observed photon flux at Earth, to predict observables including acoustic pressure waves in the Sun and the solar neutrino flux. Helioseismology, the study of these pressure waves, is a good test of the models, and sub-percent level agreement is seen between data and predictions [33]. The Sun burns hydrogen in thermonuclear fusion, generating ${}^4\text{He}$ from the pp chain (${}^4\text{He}$ production from protons) and the carbon-nitrogen-oxygen (CNO) cycle (${}^4\text{He}$ production using ${}^{12}\text{C}$ as a catalyst); electron neutrinos are a product of these processes, and thus the Sun is a source of ν_e . A prediction of the neutrino fluxes from the pp chain is shown in Fig. 1.3, along with approximate thresholds of different solar neutrino experiments.

The Homestake experiment detected solar neutrinos through the inverse β -decay reaction

$$\nu_e + {}^{37}\text{Cl} \rightarrow {}^{37}\text{Ar} + e^-, \quad (1.49)$$

with a neutrino energy threshold of 0.814 MeV in a tank containing 615 t of tetrachloroethylene (C_2Cl_4), 2.16×10^{30} atoms of ${}^{37}\text{Cl}$. It was a counting experiment in which the tetrachloroethylene was processed every two months in order to

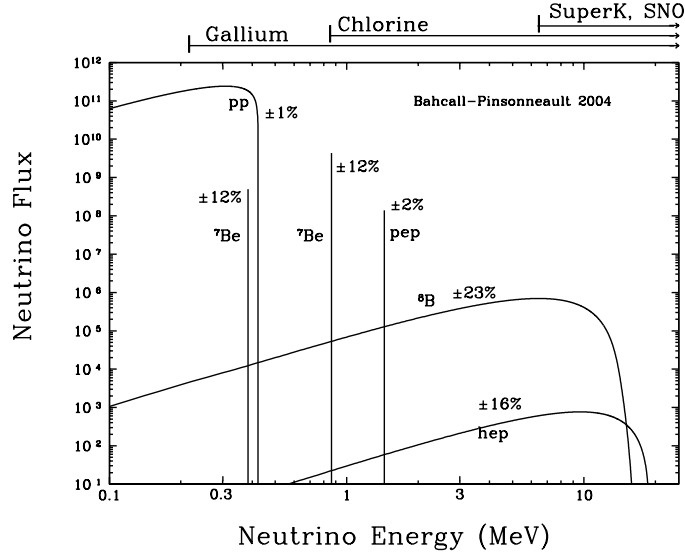


Figure 1.3: Predicted solar neutrino energy spectrum from the pp chain. For continuous sources, the flux is $\text{cm}^{-2}\text{s}^{-1}\text{MeV}^{-1}$; for line sources, the flux is $\text{cm}^{-2}\text{s}^{-1}$. The percentages indicate the uncertainties in the predictions. The energy thresholds of solar neutrino experiments are shown at the top of the figure. Figure taken from [34].

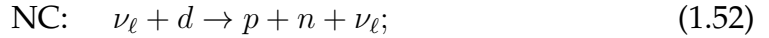
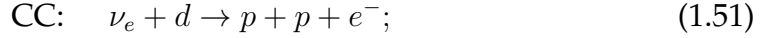
extract the ^{37}Ar atoms. The data used corresponds to 25 years of exposure [35].

Gallium experiments (GALLEX/GNO, SAGE) detect solar neutrinos, also using inverse β -decay

$$\nu_e + {}^{71}\text{Ga} \rightarrow {}^{71}\text{Ge} + e^-, \quad (1.50)$$

with a neutrino energy threshold of 0.233 MeV, from gallium targets of 30.3 t and 50 t respectively. Both experiments are counting experiments in which ${}^{71}\text{Ge}$ are extracted and counted monthly. The data used corresponds to around 12 years of exposure for GALLEX/GNO [36], and around 18 years of exposure for SAGE [37].

The SNO experiment detected solar neutrinos through three reactions:



with neutrino energy thresholds of 6.9 MeV, 2.2 MeV, and 5.7 MeV respectively. The CC reaction is only sensitive to the ν_e flux, the elastic scattering (ES) reaction is sensitive to a mix of the ν_e , ν_μ , and ν_τ fluxes, and the NC reaction is sensitive to all three flavours equally. SNO was a spherical Cherenkov detector with 1 kt of 99.92%-pure heavy water (D_2O), shielded by 7 kt of water (H_2O). Electrons were detected directly via their Cherenkov light by photomultiplier tubes (PMTs); neutrons were detected via their capture on a nucleus. In phase I, neutrons were detected via neutron capture on deuteron, with a single 6.25 MeV γ -ray product detected via the Cherenkov light from an electromagnetic shower. In phase II, the D_2O was doped with 2 t of NaCl. Cl has a higher neutron capture cross section, and produces multiple γ -rays totalling 8.6 MeV, therefore the neutron detection efficiency was higher. In phase III, an array of proportional counters filled with 3He were deployed in the D_2O , and neutrons were detected via the reaction



whose products have a total kinetic energy of 0.76 MeV. The proton was detected in the proportional counter via the production of ionisation electrons. The data used corresponds to 119.9(157.4) days, 176.5(214.9) days, and 176.6(208.6) days of day(night) exposure for phase I, II, and III respectively [38].

Super-Kamiokande (SK) is a 22.5 kt fiducial volume water Cherenkov detector, which detects neutrinos via the Cherenkov light from electrons from the ES

reaction (Eq. 1.53) using PMTs. The data used corresponds to 1496 days in SK-I (5 MeV recoil electron threshold) [39], 791 days in SK-II (7.5 MeV threshold) [40], 547.9 days and 298.2 days in SK-III (6.5–20.0 MeV and 5.0–6.5 MeV respectively) [41], and 1069 days in SK-IV (\sim 4 MeV threshold) [42].

Borexino is a 100 t fiducial volume liquid scintillator detector, which detects neutrinos via the scintillation light from electrons from the ES reaction (Eq. 1.53) using PMTs. The data used corresponds to 345.3 days (3 MeV threshold) for a measurement of the ${}^8\text{B}$ flux [43], and 740.7 days for a measurement of the ${}^7\text{Be}$ flux (862 keV line source) [44].

Atmospheric neutrino experiments

The SK detector is also used to study neutrinos produced by cosmic rays interacting with the atmosphere. Muon and electron neutrinos are produced in approximately the ratio 2:1, due to pion decay, and the subsequent decay of the muon. The complete calculation is more complicated; neutrinos are also produced from kaons and other exotic mesons, and high-energy muons can be stopped in the Earth before decaying into high-energy neutrinos. Events are selected at different mean neutrino energies: fully contained events at \sim 1 GeV start and stop within the inner detector; partially contained events at \sim 10 GeV start within the inner detector, but escape; upwards-going muon events at \sim 100 GeV start below the detector, and can pass straight through or stop inside. For fully contained and partially contained events, particle identification is performed in order to separate ν_e events from ν_μ events. The data used corresponds to 1489.2 days, 798.6 days, 518.1 days, and 1097.0 days for SK I, II, III, and IV respectively [45].

Reactor neutrino experiments

Many experiments have been performed using nuclear reactors as an isotropic and pure source of electron antineutrinos, which come from nuclear fission, with an energy of a few MeV. The distance to the reactor therefore determines which oscillation parameters can be studied; distances of $\mathcal{O}(1 \text{ km})$ probe θ_{13} and Δm_{32}^2 , while distances of $\mathcal{O}(100 \text{ km})$ probe θ_{12} and Δm_{21}^2 . The $\bar{\nu}_e$ are detected via the inverse β -decay reaction (Eq. 1.1); events are selected by requiring the coincidence between a prompt positron signal, and a delayed signal from γ -ray(s) from the capture of the neutron on a nucleus.

KamLAND is a 1.0 kt liquid scintillator detector, shielded by 3.2 kt of water. The e^+ and γ -ray are detected using PMTs. The $\bar{\nu}_e$ flux is dominated by 56 Japanese nuclear power reactors, with an average baseline of $\sim 180 \text{ km}$. The data used corresponds to 2135 days of exposure [46].

CHOOZ was a 5 t liquid scintillator detector, 0.09% loaded with gadolinium (Gd), surrounded by 17 t of undoped scintillator in order to contain the γ -ray and protect against PMT radioactivity. The detector was shielded by a further 90 t of undoped scintillator, which also acts as a muon veto. The Gd was used due to its large thermal neutron cross section and total γ -ray energy ($\sim 8 \text{ MeV}$) in order to maximise the neutron capture efficiency. The $\bar{\nu}_e$ flux comes from two reactors, 1115 m and 998 m from the detector. The data used corresponds to 342.1 days of exposure [47].

Palo Verde was a 11.34 t liquid scintillator experiment, 0.1% loaded with Gd, shielded by 105 t of water. The detector was segmented; 66 9 m-long acrylic cells are filled with scintillator, at each end there was 0.8 m of oil to protect from PMT radioactivity, and a PMT. The $\bar{\nu}_e$ flux comes from three reactors, 890 m, 890 m, and 750 m from the detector. The data used corresponds to 350 days of exposure [48].

Double Chooz is a 10.3 m^3 liquid scintillator detector, 0.123% loaded with Gd, surrounded by a 55 cm layer of undoped scintillator to contain the γ -rays, and a 105 cm layer of mineral oil, to protect from radioactivity. Outside of this is a 15 cm layer of scintillator, which acts as a muon veto. The $\bar{\nu}_e$ flux comes from two reactors, 1050 m from the detector. The data used corresponds to 227.93 days of exposure [49].

Daya Bay is an experiment utilising liquid scintillator detectors, 0.1% loaded with Gd. The detector design is modular; eight versions of the detector are planned. Each module consists of 20 t of Gd-loaded liquid scintillator, surrounded by 20 t of undoped scintillator, surrounded by 37 t of mineral oil. Each module is shielded by water, which is instrumented with PMTs to provide a Cherenkov muon veto. The $\bar{\nu}_e$ flux comes from six reactors, located in pairs with 88 m core separation. Currently two detector modules are situated at experimental hall 1 ($\sim 365\text{ m}$, $\sim 860\text{ m}$, and $\sim 1310\text{ m}$ from the reactor pairs), one detector module is situated at experimental hall 2 ($\sim 1345\text{ m}$, $\sim 480\text{ m}$, and $\sim 530\text{ m}$ from the reactor pairs), and three detector modules are situated at experimental hall 3 ($\sim 1910\text{ m}$, $\sim 1535\text{ m}$, and $\sim 1540\text{ m}$ from the reactor pairs). The data used corresponds to 217 days of exposure [50].

RENO is an experiment utilising liquid scintillator detectors, 0.1% loaded with Gd. Two identical detectors are used; a near and far detector. Each detector consists of 16 t of Gd-loaded liquid scintillator, surrounded by 60 cm of undoped scintillator, surrounded by 65 t of mineral oil. Each detector is shielded by 1.5 m of water, which is instrumented with PMTs to provide a Cherenkov muon veto. The $\bar{\nu}_e$ flux comes from six reactors, located in roughly equally spaced, 1280 m-long line. The flux-weighted baseline for the near and far detector are 408.56 m and 1443.99 m respectively. The data used corresponds to 402 days of exposure [51].

Long-baseline accelerator neutrino experiments

Accelerators are used to produce beams of neutrinos, which are predominately ν_μ (or $\bar{\nu}_\mu$). A proton beam is incident with a target, producing secondary hadrons. Pions are focussed using magnetic horns, in order to produce a more intense beam, and to select charge and so a ν_μ - or $\bar{\nu}_\mu$ -dominated beam. Kaons, and other mesons, produce a background of electron neutrinos. Long-baseline refers to experiments which have $E_\nu \sim 1$ GeV and $L \sim 100$ km, and are therefore sensitive to Δm_{32}^2 , θ_{23} , θ_{13} , and δ_{CP} .

MINOS is an on-axis long-baseline accelerator experiment. It uses near and far detectors at 1.04 km and 795 km from the beam target, with fiducial masses of 29 t and 3.8 kt respectively. Both detectors use the same detector technology, specifically layers of steel and plastic scintillator, forming a tracking calorimeter, with a toroidal magnetic field in order to measure particle momentum. ν_μ CC events are selected based on the presence of a muon, and the neutrino energy is reconstructed based on the calorimetric energy deposited and shower topology. ν_e CC events are selected based on the presence of an electromagnetic shower, with extra cuts to reject NC and ν_μ CC events with short muon tracks. The data used for ν_μ disappearance (ν_e appearance) is $10.71(10.6) \times 10^{20}$ POT (protons on target) in the ν_μ -dominated beam and $3.36(3.3) \times 10^{20}$ POT in the $\bar{\nu}_\mu$ -dominated beam [52, 53].

T2K is an off-axis long-baseline accelerator experiment, with a neutrino flux peaking at ~ 600 MeV. It uses the SK detector as the far detector, and a multi-purpose detector, ND280, as the near detector. The data used for ν_μ disappearance is 3.01×10^{20} POT [2], and for ν_e appearance is 6.39×10^{20} POT [54], both with a ν_μ -dominated beam.

1.4.3 Current knowledge

A number of global fits [32, 55, 56] of the neutrino oscillation data described in Sec. 1.4.2 are performed in order to determine the six oscillation parameters. The results from Ref. [32] are summarised in Tab. 1.3, the 1-dimensional confidence regions are shown in Fig. 1.4, and the 2-dimensional confidence regions are shown in Fig. 1.5. The fits use the experiments and datasets summarised in Sec. 1.4.2.

	Best fit $\pm 1\sigma$	3σ range
$\sin^2 \theta_{23}$	$0.444^{+0.037}_{-0.031} \oplus 0.592^{+0.028}_{-0.042}$	$0.361 \rightarrow 0.665$
$\sin^2 \theta_{12}$	$0.313^{+0.013}_{-0.012}$	$0.277 \rightarrow 0.355$
$\sin^2 \theta_{13}$	$0.0244^{+0.0019}_{-0.0019}$	$0.0187 \rightarrow 0.0303$
$\delta_{CP}/^\circ$	270^{+77}_{-67}	$0 \rightarrow 360$
$\Delta m_{21}^2/10^{-5} \text{ eV}^2/\text{c}^4$	$7.50^{+0.18}_{-0.17}$	$7.03 \rightarrow 8.08$
$\Delta m_{31}^2/10^{-3} \text{ eV}^2/\text{c}^4$ (NH)	$+2.429^{+0.055}_{-0.054}$	$+2.249 \rightarrow 2.639$
$\Delta m_{32}^2/10^{-3} \text{ eV}^2/\text{c}^4$ (IH)	$-2.422^{+0.063}_{-0.061}$	$-2.614 \rightarrow 2.235$

Table 1.3: Three-flavour oscillation parameters from Ref. [32]. The flux prediction from Ref. [57] is adopted. Note that 1σ and 3σ ranges are given with respect to the global minimum.

The determination of $\sin^2 \theta_{13}$ is dominated by the recent reactor experiments (Daya Bay, RENO, Double Chooz), but the choice of reactor flux (leaving it free and using short-baseline reactor experiments ($L < 100$ m), or fixing it to the new prediction [57]) causes a $\sim 0.7\sigma$ shift in best-fit point.

Non-maximal θ_{23} is favoured at $\sim 1.5\sigma$ and $\sim 2.2\sigma$ for NH and IH respectively. In the NH(IH), the first(second) octant is favoured at $\sim 1.0\sigma$ (1.4σ). The determination of θ_{23} comes from a variety of sources:

- $\nu_\mu \rightarrow \nu_\mu$ disappearance at long-baseline accelerator experiments is dependent on $\sin^2 \theta_{23} \cos^2 \theta_{13} (1 - \sin^2 \theta_{23} \cos^2 \theta_{13})$ to leading order (see Eq. 1.45). This is degenerate for points either side of maximal disappearance ($\sin^2 \theta_{23} \cos^2 \theta_{13} = 1$);

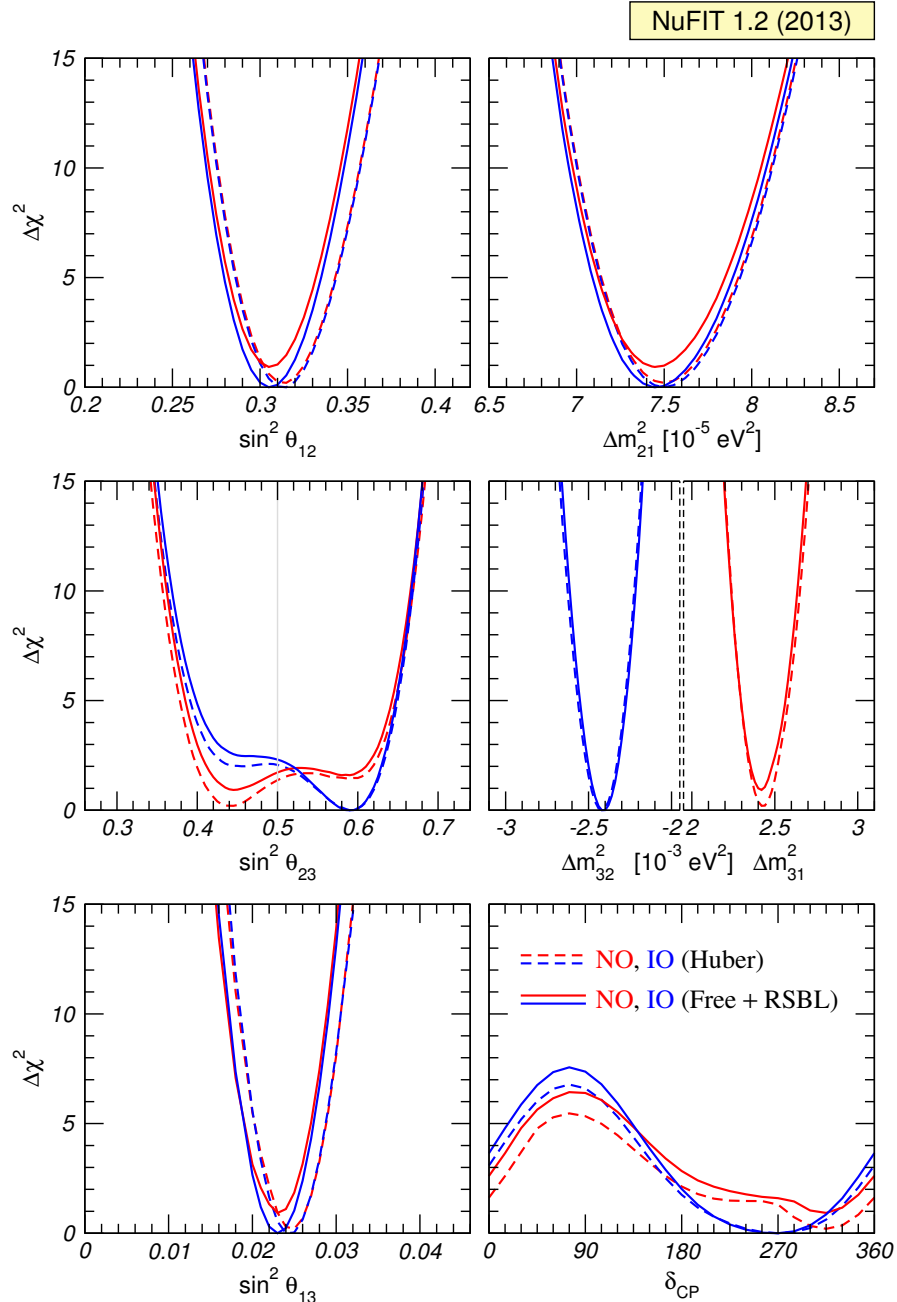


Figure 1.4: Three-flavour oscillation parameter 1-dimensional $\Delta\chi^2$ projections from Ref. [32]. The red(blue) curves are for NH(IH). For solid curves, the reactor flux normalisation is a free parameter and data from short-baseline reactor experiments ($L < 100$ m) is included. For dashed curves, the flux prediction from Ref. [57] is adopted, and the short-baseline reactor data is not used. Figure taken from [32].

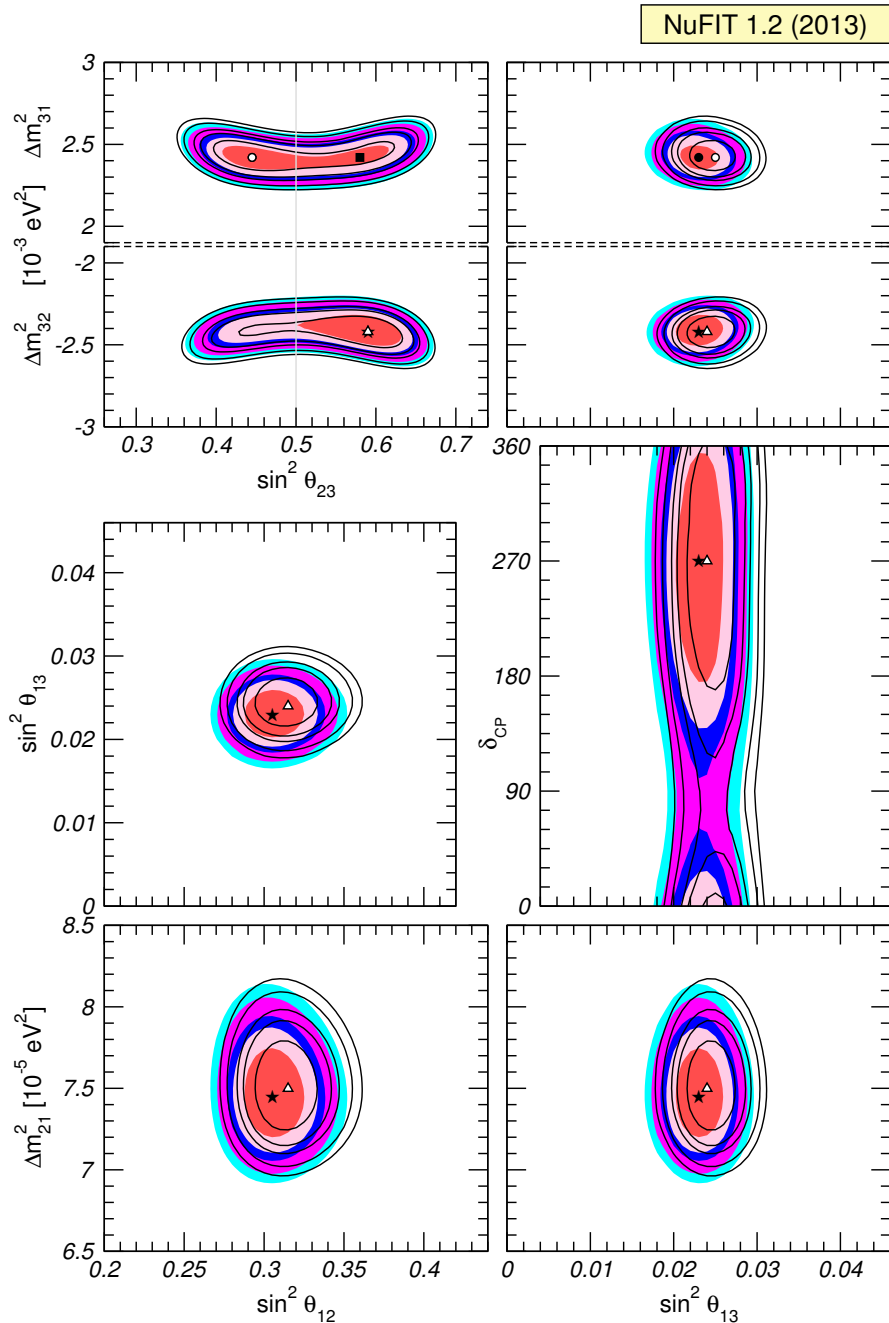


Figure 1.5: Three-flavour oscillation parameter 2-dimensional regions from Ref. [32], for 1σ , 90%, 2σ , 99%, and 3σ C.L. For filled regions, the reactor flux normalisation is a free parameter and data from short-baseline reactor experiments ($L < 100$ m) is included. For unfilled regions, the flux prediction from Ref. [57] is adopted, and the short-baseline reactor data is not used. Figure taken from [32].

- $\nu_\mu \rightarrow \nu_e$ appearance at long-baseline accelerator experiments is dependent on $\sin^2 \theta_{23} \sin^2(2\theta_{13})$ to leading order (see Eq. 1.46). Therefore using the accurate measurement of θ_{13} from reactor experiments allows $\sin^2 \theta_{23}$ to be measured in an octant-dependent way;
- The ν_e *e*-like excess in atmospheric neutrino events is suppressed (enhanced) in multi-GeV (sub-GeV) events for $\theta_{23} < 45^\circ$. A resonance also exists for neutrinos(antineutrinos) for the NH(IH).

There is no significant preference for either mass hierarchy.

The small hint for the octant is dependent on the details of the analysis. For the NH, the second octant is preferred until atmospheric neutrino data from SK is included. The analysis presented in [55] prefers the first octant for both NH and IH. This preference appears when adding SK atmospheric neutrino data in which the atmospheric best-fit moves from the second to the first octant for the IH. The NH first octant preference is enhanced by the same addition.

A number of simple lepton mixing patterns have been discussed in recent years, in order to describe the observed mixing patterns. For example, the tribimaximal mixing pattern [58] assumes $\sin^2 \theta_{13} = 0$, $\sin^2 \theta_{23} = \cos^2 \theta_{23} = 1/\sqrt{2}$, $\sin^2 \theta_{12} = 1/\sqrt{3}$, and $\cos^2 \theta_{12} = 1/\sqrt{2/3}$, leading to the PMNS matrix having values

$$U_{\text{PMNS}}^{\text{TB}} = \begin{pmatrix} \sqrt{\frac{2}{3}} & \frac{1}{\sqrt{3}} & 0 \\ -\frac{1}{\sqrt{6}} & \frac{1}{\sqrt{3}} & \frac{1}{\sqrt{2}} \\ \frac{1}{\sqrt{6}} & -\frac{1}{\sqrt{3}} & \frac{1}{\sqrt{2}} \end{pmatrix} \approx \begin{pmatrix} 0.816 & 0.577 & 0 \\ -0.408 & 0.577 & 0.707 \\ 0.408 & -0.577 & 0.707 \end{pmatrix}. \quad (1.55)$$

This pattern was consistent with experimental data, however the recent results showing that θ_{13} is non-zero, and hints of θ_{23} being non-maximal, require devia-

tions from this simple pattern; the 3σ ranges from Ref. [32] are:

$$U_{\text{PMNS}}^{\text{data}} = \begin{pmatrix} 0.799 - 0.844 & 0.515 - 0.581 & 0.132 - 0.170 \\ 0.214 - 0.526 & 0.427 - 0.706 & 0.598 - 0.805 \\ 0.234 - 0.537 & 0.451 - 0.721 & 0.573 - 0.787 \end{pmatrix}. \quad (1.56)$$

Perturbations around tri-bimaximal mixing provide a good approximation. In theoretical models these simple patterns can result from discrete symmetries such as A_4 or S_4 at leading order, and the deviations seen can be brought about via higher order terms. For a recent review of these models, see for example Ref. [59]).

1.4.4 Anomalies

A range of experimental results do not fit in the three active neutrino framework described above. One possibility to describe the anomalies is to add a number of neutrinos to the model. Experimentally, the new mass squared splitting is $\mathcal{O}(1 \text{ eV}^2/\text{c}^4)$. In order to be consistent with results which favour three active neutrinos (see Sec. 1.4.3) which has mass squared splittings of $\mathcal{O}(10^{-3} \text{ eV}^2/\text{c}^4)$ and $\mathcal{O}(10^{-5} \text{ eV}^2/\text{c}^4)$, and the measurement of the number of neutrinos from the Z boson decay width of $N_\nu = 2.9840 \pm 0.0082$, these neutrinos, n_{ν_s} , must be *sterile* (do not interact with the Z boson). A brief summary of the anomalies is presented here; for more details see Ref. [60] and references therein.

The LSND experiment provided the first piece of experimental evidence for physics beyond the three active flavour model. It was a 167 t liquid scintillator experiment, with a low concentration of scintillator allowing for Cherenkov light to also be visible. The neutrinos were created via a 798 MeV proton beam incident on a target; most of the π^- and μ^- are mostly absorbed by a beam

dump 30 m from the detector, while most of the π^+ and μ^- decay at rest ($>95\%$), with a small fraction decaying in flight ($<5\%$). Electron antineutrinos are selected by detecting inverse β -decay (Eq. 1.1), and observing $\bar{\nu}_\mu \rightarrow \bar{\nu}_e$. A total excess of 87.9 ± 23.2 events is seen, consistent with an oscillation probability of $0.264 \pm 0.081\%$ [61].

MiniBooNE is a spherical detector filled with 806 t of pure mineral oil (CH_2), reading out scintillation and Cherenkov radiation using PMTs. The neutrinos are created via horn-focussed pion decay in a 50 m-long decay volume. The detector is located 541 m from the target. In neutrino mode, the ν_μ flux peaks at 600 MeV, while in antineutrino mode, the $\bar{\nu}_\mu$ flux peaks at 400 MeV. 6.5×10^{20} POT and 11.27×10^{20} POT of data have been collected in neutrino mode and antineutrino mode respectively. Using CCQE events, a total excess of 240.3 ± 62.9 events are seen, consistent with $\overset{\leftarrow}{\nu}_\mu \rightarrow \overset{\leftarrow}{\nu}_e$ oscillations and the LSND result [62].

The GALLEX and SAGE experiments used intense ^{51}Cr and ^{37}Ar radioactive sources, placed inside the detectors, for calibration. The neutrinos produced are in the energy range 420–820 MeV, and have a path length of $\mathcal{O}(1 \text{ m})$ before escaping the detector. The average ratio of measured to predicted rate is 0.86 ± 0.05 or $0.76_{-0.08}^{+0.09}$, depending on cross-section model, a deviation from unity of $\sim 2.7\sigma$. The result is consistent with $\nu_e \rightarrow \bar{\nu}_e$ oscillations.

A range of short-baseline reactor experiments, with baselines of 9–95 m, have been performed over the past 50 years, seeing an average ratio of measured to expected event rates of $R = 0.976 \pm 0.024$. Recent re-evaluations of the $\bar{\nu}_e$ flux prediction have resulted in a net $\simeq +3\%$ shift [57], resulting in an increase of the mean cross section per fission of $\simeq 6\%$, which is directly proportional to the expected event rate. This gives a new value of $R = 0.943 \pm 0.023$, a deviation from unity at 98.6% C.L. [63]. The result is consistent with $\bar{\nu}_e \rightarrow \bar{\nu}_e$ oscillations.

Various studies of $\overset{\leftarrow}{\nu}_\mu \rightarrow \overset{\leftarrow}{\nu}_\mu$ oscillations have been performed, including

at MiniBooNE with a near detector (SciBooNE), at accelerators with higher neutrino energies (CDHSW, CCFR), and SK atmospheric data. Studies of $\overset{(-)}{\nu_\mu} \rightarrow \overset{(-)}{\nu_s}$ oscillations have also been performed using NC event rates at both SK and MINOS. No positive signals have been observed.

Using the above data, and constraints from other experiments, fits [60] can be performed using models in which there are one or more sterile neutrinos added to the three active neutrino flavour models. The “3+1” model includes one eV-scale sterile neutrino, and the “3+2” model includes two eV-scale sterile neutrinos. While there are three anomalies each of around 3σ (LSND, reactor, gallium) indicating physics beyond three active neutrinos, when performing sterile neutrino fits to all data, tensions arise. The “3+1” model fails due to differences in MiniBooNE $\nu_\mu \rightarrow \nu_e$ and $\bar{\nu}_\mu \rightarrow \bar{\nu}_e$ data, requiring the addition of CP violation, therefore multiple sterile neutrinos. The LSND signal predicts $\nu_\mu \rightarrow \nu_s$, but this has not been observed, causing tensions in the fit; if LSND is discarded, hints of $\overset{(-)}{\nu_e} \rightarrow \overset{(-)}{\nu_e}$ oscillations remain without the need for $\nu_\mu \rightarrow \nu_s$. The best-fit Δm^2 values require a sum of neutrino masses which is in tension with limits from cosmological data. More experimental data is required in order to reconcile the tensions.

1.4.5 Future prospects

Currently there are three major questions in the theory of three active neutrino oscillations:

- The mass hierarchy: $\Delta m_{32}^2 > 0$ (NH) or $\Delta m_{32}^2 < 0$ (IH);
- The octant of θ_{23} : $\theta_{23} < 45^\circ$ or $\theta_{23} > 45^\circ$;
- The amount of CP violation: the value of δ_{CP} ,

all requiring the study of neutrino oscillations driven by Δm_{32}^2 . The current generation of experiments (T2K, NO ν A, SK atmospheric analyses, IceCube, ...) will not be able to answer these questions conclusively¹³, therefore new experiments are required.

JUNO is a proposed \sim 60 km-baseline reactor neutrino experiment, using a spherical detector with 20 kt of liquid scintillator. It will achieve $\sim 3\sigma$ determination of the mass hierarchy with 6 years of data taking [64]. RENO-50 is a \sim 50 km-baseline using an 18 kt liquid scintillator detector, with similar mass hierarchy prospects.

IceCube is a \sim 1 km³ water-ice Cherenkov experiment, read out using PMTs on long strings drilled into the Antarctic ice, studying atmospheric neutrinos with a neutrino energy threshold of \sim 20 GeV. PINGU is a proposed extension, adding new strings to the detector, with smaller spacing, to bring the energy threshold down to \sim 5 GeV. This allows it to study resonance due to matter effects in the Earth, allowing 3σ (5σ) determination of the mass hierarchy within 2(6) years of data taking [65].

INO is a proposed magnetised calorimeter, with a mass of 50 kt, to study atmospheric neutrinos. It will achieve 4σ determination of the mass hierarchy, for true $\Delta m_{32}^2 = 2.0 \times 10^{-3}$ eV²/c⁴ and $\sin^2(2\theta_{13}) = 0.1$ for 1000 kt – years of atmospheric neutrino exposure [66].

LBNE is a proposed long-baseline accelerator neutrino experiment, using a 34 kt fiducial mass liquid argon TPC as a far detector, on-axis and \sim 1300 km away from a high-power conventional neutrino beam at Fermilab, with neutrino energy spectrum peak at \sim 3.5 GeV. The long baseline allows the true mass hierarchy to be determined at 3σ for all values of true δ_{CP} , and it will achieve 3σ determination of $\sin \delta_{CP} \neq 0$ for 40% of true δ_{CP} values. Atmospheric neutrino

¹³The sensitivity of these experiments is up to \sim 90% C.L. for each question, and is dependent on the true oscillation parameters.

data can provide complementary information [67].

Hyper-Kamiokande is a proposed long-baseline accelerator neutrino experiment, using a 1 mt water Cherenkov detector as a far detector, $\sim 2.5^\circ$ off-axis from and ~ 295 km away from a high-power upgrade of the conventional neutrino beam at J-PARC, with neutrino energy spectrum peak at ~ 0.6 GeV. The relatively short accelerator-baseline means it is not so sensitive to the mass hierarchy (3σ determination of mass hierarchy possible for 46% of true δ_{CP} values). If the mass hierarchy is known, it will achieve 3σ determination of $\sin \delta_{CP} \neq 0$ for 74% of true δ_{CP} values. Atmospheric neutrino data can provide complementary information [68].

Chapter 2

The T2K Experiment

Tokai to Kamioka (T2K) is a long-baseline neutrino oscillation experiment. It consists of four main components:

1. A muon neutrino beam, generated at the Japan Proton Accelerator Research Complex (J-PARC) located in Tokai on the east coast of Japan.
2. A number of monitors to measure the beam stability, including proton beam monitors, muon monitors, and the Interactive Neutrino GRID (IN-GRID), an on-axis neutrino detector located 280 m from the beam target.
3. A near neutrino detector, Near Detector at 280 m (ND280), located at 280 m from the beam target and 2.5° off-axis, to measure the neutrino flux and cross-section characteristics and to constrain the event rate prediction at the far detector.
4. A far neutrino detector, SK located at 295 km from the beam target and 2.5° off-axis, situated near Kamioka, in the west of Japan.

These components of the T2K experiment are summarised in Secs. 2.1, 2.2, 2.3 and 2.4 respectively. More detailed descriptions can be found in [69] and references therein.

The primary physics goals of T2K are to measure neutrino oscillation parameters through measurements of $\overline{\nu}_\mu \rightarrow \overline{\nu}_\mu$ and $\overline{\nu}_\mu \rightarrow \overline{\nu}_e$ oscillations. These are discussed more in Sec. 2.5.

2.1 The neutrino beam

2.1.1 J-PARC accelerator complex

The J-PARC accelerator complex [70] consists of three accelerators: a linear accelerator (LINAC), a rapid-cycling synchrotron (RCS), and the main ring synchrotron (MR). The LINAC is designed to accelerate a 50 mA H^- beam up to 400 MeV kinetic energy¹, with a peak beam power of 20 MW (presently 30 mA up to 181 MeV at a peak of 5.43 MW). At injection into the RCS, the beam is converted to a proton beam (H^+) by charge-stripping foils. The RCS accelerates the proton beam to 3 GeV with a 25 Hz cycle and two bunches per cycle, with a beam power of 1 MW (presently \sim 300 kW). Protons are supplied by the RCS to the MR (\sim 5%) and to the Material and Life Science Facility at J-PARC (\sim 95%). The MR accelerates protons in eight (six prior to June 2010) bunches to 30 GeV, with a beam power of 750 kW (presently \sim 240 kW, see Fig. 2.12). When running in fast extraction mode for the neutrino beamline, the eight proton bunches are extracted by a set of five kicker magnets in a single turn. The spill width is \sim 5 μ s, and the bunch spacing is 581 ns. This time structure is important for background rejection of cosmic ray interactions.

¹Throughout this chapter, all accelerator beam energies are given in terms of kinetic energy.

2.1.2 Neutrino beamline

The neutrino beamline is composed of a primary and secondary beamline, as shown in Fig. 2.1. The primary beamline directs the proton beam towards Kamioka; the secondary beamline produces the neutrino beam through the decay of a focused pion beam generated by the interaction of the primary proton beam with a graphite target.

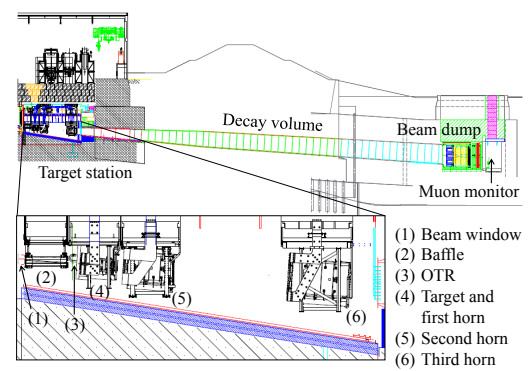
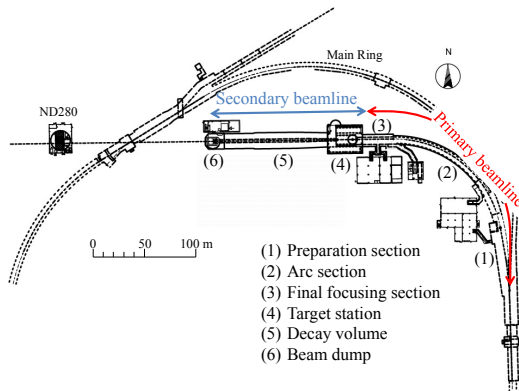


Figure 2.1: Plan view of the T2K beamline. Figure taken from [69].

Figure 2.2: Side view of the T2K secondary beamline. The length of the decay volume is ~ 96 m. Figure taken from [69].

Primary beamline

The primary beamline consists of preparation (54 m long), arc (147 m), and final focusing (37 m) sections. The preparation section takes the proton beam extracted from the MR, and tunes it so that the beam can be accepted by the arc section. The tuning is done using 11 normal conducting magnets (four steering, two dipole, five quadrupole). The arc section has a 104 m radius of curvature and bends the beam towards Kamioka. The bending is done using 14 doublets of superconducting combined function magnets [71], and there are also three pairs of horizontal and vertical superconducting steering magnets to correct the beam orbit. The final focusing section guides and focuses the beam onto the target,

and also directs the beam downward by 3.637° with respect to the horizontal, to achieve the desired 2.5° angle at SK². The focusing is done using 10 normal conducting magnets (four steering, two dipole, four quadrupole).

Secondary beamline

The secondary beamline consists of a target station, a decay volume, and a beam dump, as shown in Fig. 2.2. The target station and decay volume are contained within a single volume of $\sim 1500 \text{ m}^3$, filled with helium gas at 1 atm. Helium gas is used to reduce pion absorption and suppress beam-induced tritium and NO_X production. A titanium-alloy beam window separates the vacuum of the primary beamline with the helium gas volume of the secondary beamline. Protons from the primary beamline are directed to the target via the beam window.

The target station consists of:

- a baffle (a water-cooled graphite block with a beam hole of 30 mm diameter) to collimate the proton beam, to protect the magnetic horns;
- an optical transition radiation monitor (OTR) to monitor the proton beam profile upstream of to the target;
- a target to generate secondary pions. The target core is a 1.9 interaction lengths long (91.4 cm), 2.6 cm diameter graphite rod. Graphite is used because it is a low density material, and so is not melted by the pulsed beam heat load. The core is surrounded by a 2 mm thick graphite tube, and sealed inside a 0.3 mm titanium case. The target is cooled by helium gas flowing between the core and the tube, and between the tube and the case;
- three magnetic horns [72] to focus the pions, excited by a 250 kA (designed for up to 320 kA) current pulse. [The horns consist of two coaxial conductors](#),

²The beam centre is 2.377° below SK, and 0.795° to the south.

with a magnetic field of strength $1/r$ in the volume between the inner and outer surfaces, where r is the axis; no field is generated within the inner conductor. When wide-angled secondaries from proton interactions on the target pass through into the magnetic field, they are focussed, producing a narrower meson beam. This in turn produces a narrower neutrino beam. When run at 250 kA (maximum field 1.7 T), the horns increase the flux at SK by a factor of ~ 17 (compared to horn off) at the neutrino spectrum peak energy (~ 0.6 GeV).

The decay volume is a ~ 96 m long steel tunnel, in which pions and muons decay into neutrinos. The beam dump sits at the end of the decay volume. It has a 75 t graphite core, sandwiched by aluminium cooling modules containing water channels. Seventeen iron plates (two inside the helium vessel, fifteen outside) provide 2.40 m of further material. The beam dump stops all hadrons and muons below ~ 5 GeV/c. Neutrinos pass through the beam dump, and are used for physics.

2.1.3 Global alignment and time synchronisation

Global Positioning System (GPS) surveys have been performed at both Tokai and Kamioka, to allow accurate alignment and positioning to take place. The primary beamline, target, and horns were aligned to send the neutrino beam in the right direction, and to reduce irradiation in the high-intensity proton beamline. The muon monitors and neutrino near detectors were also aligned in order to monitor the neutrino beam direction. A long-baseline survey measured the distance from the target to the centre of SK to be 295.3352 ± 0.7 km, with an off-axis angle of $2.504 \pm 0.004^\circ$, well within the required directional accuracy of 0.057° .

T2K uses a GPS time synchronisation system which provides an $\mathcal{O}(50\text{ ns})$ scale synchronisation between SK event trigger timestamps and J-PARC beam spill timestamps. An independent optical fibre link sends J-PARC beam spill timestamps directly to the ND280 data acquisition system.

2.1.4 Neutrino spectrum at off-axis locations

T2K is the first long-baseline oscillation experiment to employ the off-axis method [73], to produce a narrow-band neutrino beam to study neutrino oscillations. The predominant production mechanism of neutrinos is via the two-body decay of pions and kaons (Eq. 1.2). At an angle away from the parent meson direction, the energy of the neutrino, E_ν , is only weakly dependent on the momentum of the parent, following

$$E_\nu = \frac{0.43E_\pi}{1 + \gamma^2\theta^2}, \quad (2.1)$$

where E_π is the parent pion energy, γ is the Lorentz factor of the pion, and θ is the neutrino angle relative to the parent pions' momentum. Parent π^+ (π^-) are focussed by the magnetic horns to produce the neutrino (antineutrino) beam. Therefore, if a neutrino detector is placed at an angle relative to this focussing axis, it will see neutrinos with a narrow energy spread, as illustrated in Fig. 2.3. T2K uses a 2.5° off-axis angle³ which provides a beam flux peak at $\sim 0.6\text{ GeV}$, near the first oscillation maximum. This method maximises the flux at the oscillation maximum thus enhancing the oscillation sensitivity and reduces the rate of high energy events which contribute mainly to the backgrounds, at the cost of a reduction in total neutrino flux.

Due to the off-axis angle dependence of the energy spectrum, the neutrino

³The off-axis angle can be changed in the range 2.0° to 2.5° to vary the position of the spectrum peak.

beam must be precisely monitored; a 0.025° change in off-axis angle results in a $\sim 1\%$ change in the flux prediction at SK [74]. At 295 km from the target, SK sees a point source from the specific 2.5° off-axis angle, while, at 280 m from the target, ND280 sees a range of off-axis angles⁴.

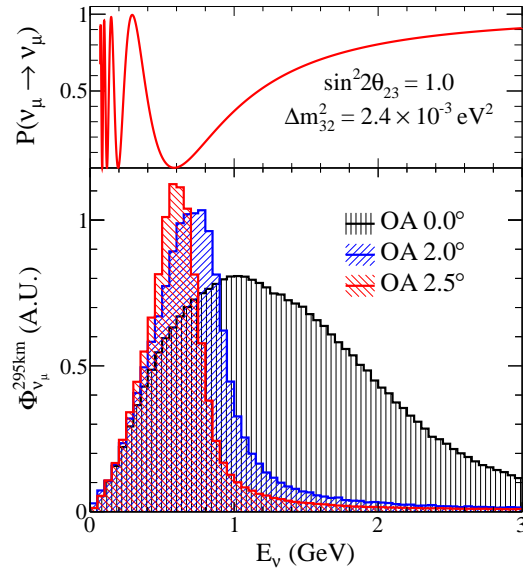


Figure 2.3: T2K fluxes for different off-axis angles (bottom) and muon neutrino survival probability at 295 km (top). Figure taken from [74].

2.2 On-axis beam monitors

The neutrino beam direction and event rate stability must be well monitored in order to predict neutrino event rates at SK. First, the proton beam monitors in the primary and secondary beamlines are described in Sec. 2.2.1. The muon monitors, located after the beam dump, are described in Sec. 2.2.2. Finally, the on-axis neutrino detector located at 280 m from the beam target, INGRID, is described in Sec. 2.2.3.

⁴ND280 covers a range of off-axis angles $\sim 0.802^\circ$, while SK covers a solid angle of $\sim 0.006^\circ$ [75].

2.2.1 Proton beam monitors

Proton beam monitors in the primary beamline

The proton beam is monitored within the primary beamline to ensure that the proton beam is well-tuned; a well-tuned proton beam is essential to minimise beam loss, and so achieve high-power beam operation, and also to give stable neutrino beam production. Five current transformers (CTs) track the beam intensity, 21 electrostatic monitors (ESMs) follow the beam position, 19 segmented secondary emission monitors (SSEMs) check the profile of the beam, and 50 beam loss monitors (BLMs) track beam loss.

Each CT consists of a cylindrical ferromagnetic core with a 50-turn toroidal coil. The proton beam runs through the centre of the cylinder axis, and induces a current in the coil which is proportional to the beam current. This is a non-destructive method of measuring the beam intensity. The CTs provide a 2% uncertainty on absolute proton beam intensity and a 0.5% uncertainty on the relative intensity. The CTs can also measure the beam timing, with a precision of better than 10 ns.

Each ESM consists of four segmented cylindrical electrodes surrounding the proton beam orbit (80° coverage per electrode). The beam centre is found non-destructively using by measuring the top-bottom and left-right asymmetries of the beam-induced current on the electrodes. The ESMs provide a position precision of $450\ \mu\text{m}$ ($500\ \mu\text{m}$ is required).

Each SSEM consists of two thin ($5\ \mu\text{m}$) titanium foils, segmented horizontally and vertically, with a HV anode foil between them. The strips produce secondary electrons, in proportion to the number of protons that pass through the strip, which drift along the electric field and induce currents on the strips. The SSEMs are only used during beam tuning due to the 0.005% beam loss they induce;

during continuous beam operation they are remotely extracted from the beam orbit. The SSEMs provide a beam width precision of $200\text{ }\mu\text{m}$ ($700\text{ }\mu\text{m}$ is required).

Each BLM is a wire proportional counter, filled with an Ar- CO_2 gas mixture. The signal is integrated during the spill and fires a beam abort interlock signal if a threshold is reached. The BLMs and beam loss sensitivity down to 16 mW .

Proton beam monitors in the secondary beamline

The proton beam is also measured in the secondary beamline by the OTR just upstream of the target. The OTR measures light produced in a narrow cone as the incident proton beam enters and exits a thin foil, placed at 45° to the proton beam. This light is directed out of the high-radiation environment, and a charge injection device camera is used to produce an image of the proton beam profile. The OTR has an eight-position carousel, controlled remotely, with four titanium foils (which produce visible light (transition radiation)), an aluminium foil (with higher reflectivity for a low intensity beam), a ceramic foil (produces high-intensity fluorescent light for a very low intensity beam), a calibration foil (for OTR alignment monitoring), and an empty slot (for mirror transport efficiency studies).

2.2.2 Muon monitors

Muons with $p_\mu \gtrsim 5\text{ GeV}/c$ are monitored behind the beam dump. Measuring muons is an indirect measurement of the neutrino beam, because muons are mainly produced with neutrinos from the two-body decay of pions (Eq. 1.2). Using the beam simulation (see Sec. 3.1.1), for 3.3×10^{14} protons/spill and 320 kA horn current, there is estimated to be 10^7 charged particles/ cm^2/bunch in the muon monitor at the beam centre. The flux is 87% muons, with the remainder being delta-rays, and the beam profile is Gaussian-like with width $\sim 1\text{ m}$.

There are two types of detector arrays, each covering an area of $150 \times 150 \text{ cm}^2$, each with 49 sensors. An array of ionisation chambers is located at 117.5 m from the target. It consists of seven chambers, each with seven sensors. The active volume of each sensor is made by two parallel plate electrodes, between which 200 V is applied. An array of silicon PIN photodiodes is located at 118.7 m from the target. 80 V is applied to fully deplete the silicon layer. The muon monitor can measure the muon profile with precision 2.95 cm (corresponding to a 0.0014° precision in neutrino beam direction), and the neutrino beam intensity with a precision better than 3%.

An emulsion tracker is located downstream of the detector arrays to measure the absolute flux and momentum distribution of the muons. The flux module is composed of eight emulsion films, and can measure the muon flux with a precision of 2%. Downstream of this, the momentum module is composed of 25 emulsion films interleaved with 1 mm lead plates. The muon momentum can be measured to a precision of 28% at a momentum of $2 \text{ GeV}/c$ via multiple Coulomb scattering.

2.2.3 INGRID

INGRID [76], an on-axis neutrino detector located at 280 m from the beam target, is made up of iron and plastic scintillator modules arranged in a cross. It was designed to monitor the neutrino beam directly, and has sufficient statistics to measure the neutrino beam intensity daily and the beam direction monthly, in order to assess the neutrino beam stability. At a beam intensity of $\sim 10^{18} \text{ POT/day}$, the neutrino event rate is monitored with 4% precision and the neutrino beam centre is measured monthly with accuracy better than 0.023° (0.057° required) [74].

INGRID utilises the same plastic-scintillator-based readout and electronics

as several ND280 subdetectors, which will be described in Secs. 2.3.2 and 2.3.3. INGRID is arranged in a cross, with seven modules laid horizontally and seven modules laid vertically (the two centre modules of each arm overlap, and correspond to the centre of the neutrino beam). A further two modules are located off-axis and are separate to the main cross, as shown in Fig. 2.4, to study the axial symmetry of the neutrino beam. The total area sampled is $10\text{ m} \times 10\text{ m}$, and the edge of the detector corresponds to an angle of $\sim 1.0^\circ$ from the beam centre.

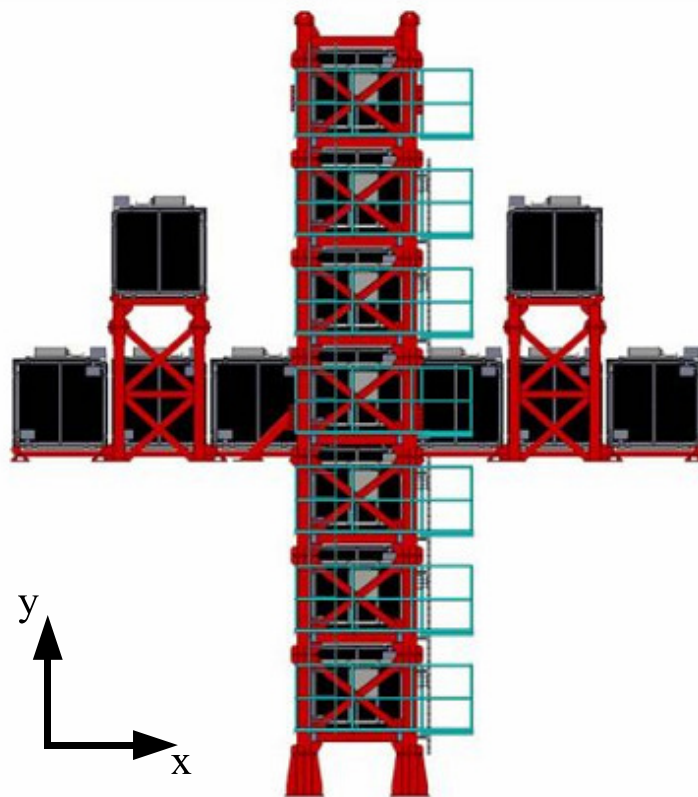


Figure 2.4: INGRID on-axis neutrino detector. Figure taken from [69].

Each INGRID module consists of a sandwich structure of nine $124 \times 124\text{ cm} \times 6.5\text{ cm}$ iron plates and eleven tracking scintillator planes⁵. Each scintillator plane consists of 24 horizontal and 24 vertical scintillator bars, each with dimensions of $1.0\text{ cm} \times 5.0\text{ cm} \times 120.3\text{ cm}$. The total iron mass is 7.1 t per module. Each

⁵There is no iron plate between the 10th and 11th tracking plate, due to weight restrictions; this does not effect the tracking performance.

module is surrounded by scintillator veto planes, to reject interactions occurring outside the module. A veto plane consists of 22 scintillator bars, segmented transverse to the beam direction, each with dimensions of $1.0\text{ cm} \times 5.0\text{ cm} \times 111.9\text{ cm}$ (bottom sides) or dimensions of $1.0\text{ cm} \times 5.0\text{ cm} \times 129.9\text{ cm}$ (top, right, and left sides). Each module is contained within a dark box, with the front-end electronics mounted outside the dark box.

The Proton Module is an additional module consisting of scintillator planes without iron plates, surrounded by veto planes, and is located between the horizontal and vertical central modules. The Proton Module is designed to see both the proton and muon track from neutrino-induced CCQE interactions, to compare with MC simulations of beamline and neutrino interactions.

Events are reconstructed by searching for hits within a 100 ns time window, where the first hit is within 100 ns of the expected neutrino beam bunch arrival time. There must be at least three scintillator planes that have hits in both x and y layers⁶. Tracks are reconstructed in x - z and y - z separately using a straight line fit, and then combined into 3-dimensional tracks. Veto and fiducial volume cuts are then applied. A typical neutrino interaction in the Proton Module is shown in Fig. 2.5.

2.3 ND280

ND280 is a near neutrino detector, located 280 m from the beam target and 2.5° off-axis. It is designed to measure the flux, energy spectrum, and electron neutrino contamination of the unoscillated 2.5° off-axis neutrino beam that will be seen by SK, in order to predict neutrino interaction rates at SK. It can be used to constrain the neutrino flux and cross-section systematics used in long-

⁶All detectors use the following coordinate convention: x is horizontal, y is vertical, and z is along the nominal beam axis.

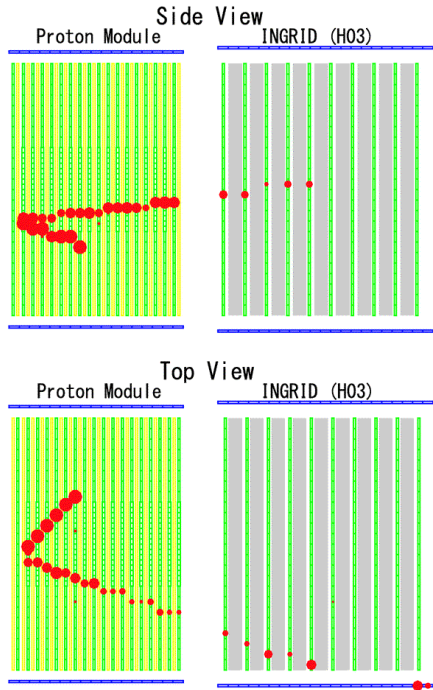


Figure 2.5: A typical neutrino event in the Proton Module. A neutrino enters from the left and interacts within the module, producing charged particles whose tracks are shown as the red circles. One of them exits the Proton Module and enters the central INGRID horizontal module. This event is probably a CCQE interaction; the heavily ionising track is a proton, and the other track is a muon. Each of the green cells in this figure is a scintillator, and the size of the red circles indicates the size of the observed signal in that cell. Blue cells indicate veto scintillators. Figure taken from [69].

baseline oscillation analyses, as described in Sec. 3.3.4, and can also produce measurements of cross sections for neutrino-induced interactions.

ND280 is magnetised, with all subdetectors contained within the recycled UA1 magnet [77], operating with a field of 0.2 T. The layout of the ND280 subdetectors are shown in Fig. 2.6. A π^0 detector (PØD) [78] is located at the most upstream end (closest to the beam production point). It is a plastic-scintillator-based detector containing water, lead, brass and carbon targets. The tracker is located downstream of the PØD, and is composed of three time projection chambers (TPCs) [79] interleaved with two fine grained detectors (FGDs) [80]. The most upstream FGD (FGD1) provides carbon targets, while FGD2 provides

both water and carbon targets. The downstream electromagnetic calorimeter (DS-ECal) [81] is located downstream of the tracker. The PØD, tracker and DS-ECal are contained with a metal “basket” frame, with dimensions $6.5\text{ m} \times 2.6\text{ m} \times 2.5\text{ m}$. The x and y faces of the PØD and tracker are surrounded by the PØD-ECal and barrel-ECal respectively. The yoke of the magnet, [having outer and inner dimensions of \$7.6\text{ m} \times 5.6\text{ m} \times 6.1\text{ m}\$ and \$7.0\text{ m} \times 3.5\text{ m} \times 3.6\text{ m}\$ respectively](#), is instrumented with plastic scintillator (SMRD) [82].

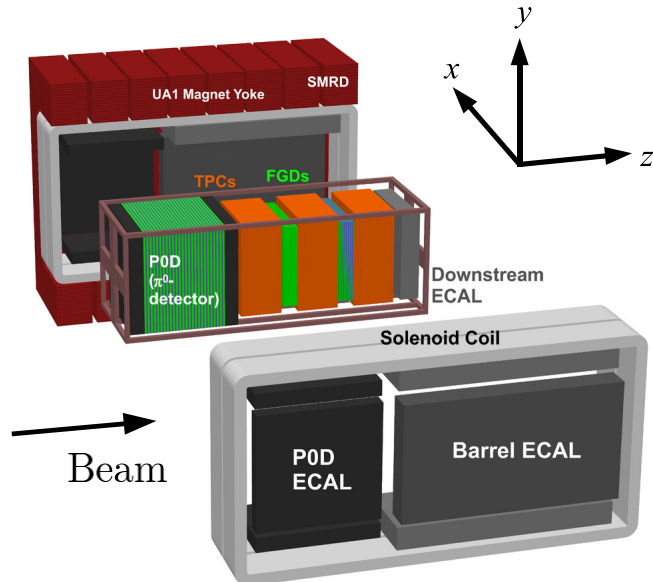


Figure 2.6: An exploded view of the ND280 off-axis neutrino detector. Figure taken from [69].

2.3.1 Time projection chambers (TPCs)

The TPCs were designed to perform three key functions. Firstly, their excellent three-dimensional imaging capabilities (e.g. spatial resolution of $\sim 1\text{ mm}$) allow the trajectories of charged particles traversing the detector to be determined. Secondly, since they are situated inside a magnetic field, track curvature can be used to determine the momenta of charged particles. Lastly, by examining the energy lost by particles due to ionisation as a function of momentum, and

comparing with the same quantity for known particles, the TPCs can be used to identify the particle species.

Each of the three TPCs consists of an inner box containing an argon-based drift gas, contained within an outer box ($2.3\text{ m} \times 2.4\text{ m} \times 1.0\text{ m}$) that holds CO_2 as an insulating gas. The drift gas, $\text{Ar:CF}_4:\text{iC}_4\text{H}_{10}$, in proportion 95:3:2, is used due to its low diffusion, high speed ($\sim 7.8\text{ cm}/\mu\text{s}$), and good performance with the micromegas detectors. The box is designed in such a way that, along with a central cathode, it provides a uniform electric field in the active drift volume of the TPC.

Ionisation electrons produced by charged particles passing through the TPCs drift in the gas away from the central cathode, towards readout planes. Each of the six (two per TPC) readout planes consists of twelve micromegas modules, arranged in two vertical columns, offset such that there is no alignment of the small inactive regions between modules. Each micromegas module consists of 1728 $7.0\text{ mm} \times 9.8\text{ mm}$ anode pads [behind a micromesh connected to a high voltage. A large electric field \$\mathcal{O}\(100\text{ V/cm}\)\$ is generated in the gap, creating a region in which charge is amplified with a gain \$\mathcal{O}\(1000\)\$, before being sampled by the anode pads.](#)

The 124,416 channels are readout using front-end cards (FECs) which read 288 channels into application specific integrated circuits (“AFTER”), which samples and digitises the signals, and stores the data in circular buffer containing 511 20 ns-width time bins. This process proceeds continuously until a trigger is received by the front-end mezzanine (FEM), at which point sampling is halted and the buffer is read out. Six FECs feed into a FEM which performs zero-suppression to reduce the data rate.

A photoelectron calibration system has been installed, in order to measure the transport properties of electrons in the TPCs. A series of 8 mm diameter

aluminium discs and 4 mm width strips are glued to the copper central cathode. A Nd:YAG laser shines 266 nm light at the cathode, producing localised photoelectrons ($2 \text{ photoelectrons/mm}^2$ on aluminium and $0.03 \text{ photoelectrons/mm}^2$ on copper), which drift towards the micromegas. The drift velocity can be precisely determined using the photoelectron arrival time relative to the laser trigger time. The transverse diffusion is found to be $15 \text{ mm}/\sqrt{\text{cm}}$ found by repeated measurements from the same strip target. During neutrino beam data taking, laser calibration triggers are taken during inter-spill periods. Laser calibration triggers can also be taken during magnet-off running, and compared with magnet-on data, to study distortions in the magnetic field.

2.3.2 Fine grained detectors (FGDs)

The FGDs provide 1.1 t of target mass for neutrino interactions, and also provide tracking of charged particles leaving the interaction vertex. They are composed of $9.61 \text{ mm} \times 9.61 \text{ mm} \times 1864.3 \text{ mm}$ plastic scintillator bars, arranged in alternating x and y layers. FGD1 contains a total of 15 XY modules, which are an x layer followed by a y layer. FGD2 contains a total of seven XY modules, alternating with six 2.5 cm thick layers of water target. The difference in composition between FGD1 and FGD2 allows for the neutrino interaction cross sections on water to be determined.

The FGD, along with several other ND280 subdetectors (PØD, ECal, SMRD) and INGRID utilise the same operation and readout principle: scintillation light is collected by and then carried along the scintillator bar along a wavelength shifting (WLS) fibre; the light is then transported to a photosensor, which converts the light into an electrical signal⁷.

⁷The DS-ECal, and the side modules of the barrel-ECal have a photosensor on each end of the fibre. Other detectors have a single photosensor per fibre, in order to minimise detector dead regions; The other end mirrored with a deposition of aluminium, to increase light-collection

Scintillator bars and planes are made of polystyrene doped with 1% PPO and 0.03% POPOP by weight [83]. A thin reflective coating of TiO_2 -infused polystyrene surrounds the whole of each scintillator bar, and improves light collection efficiency by reflecting back escaping light. A 3 mm diameter hole runs along the centre of each bar, allowing insertion of the WLS fibre, which is attached to the photosensor.

The WLS fibres used are 1 mm diameter Kuraray double-clad Y-11, which have an absorption spectrum centred at a wavelength of 430 nm (blue), which is well matched to the 420 nm (blue) emission peak of the scintillation light. The WLS fibre emission spectrum is centred at 476 nm (green) and has only a small overlap with the absorption spectrum, reducing self-absorption effects.

The photosensor used is a Hamamatsu S10362-13-050C multi-pixel photon counter (MPPC) [84], chosen with the restrictions of having to operate in a 0.2 T magnetic field, and fit into a limited space inside the magnet. The MPPC is a multi-pixel avalanche photodiode, consisting of $667 \text{ } 50 \times 50 \mu\text{m}^2$ independent sensitive pixels. The photodiodes are operated in Geiger mode (the reverse bias voltage is set greater than the breakdown voltage) therefore a photoelectron can induce an ionisation cascade (“avalanche”), which in turn generates a large reverse current. The MPPC gain is in the range $0.5\text{--}1.5 \times 10^6$. The active area of the MPPC is $1.3 \times 1.3 \text{ mm}^2$, providing good acceptance for light detection from the 1 mm WLS fibres. In total, around 64,000 MPPCs were produced for T2K.

The FGD uses the same AFTER chip described in Sec. 2.3.1 to readout the signal from the MPPCs. Two readout channels are linked to each MPPC: a high-gain channel which saturates at about 90 pixel avalanches, but has a good signal-to-noise ratio for single pixels; and a low-gain channel which extends the dynamic range. The low-gain channel is used when the high-gain channel mea-

sures a pulse corresponding to more than about 65 avalanches. This corresponds to a low-gain signal of about 7 avalanches. The ratio of high- to low-gain signals is linear and measured using cosmic rays.

The purpose of charge calibration is to convert a digitised signal to a normalised value representing the energy deposited in the scintillator bar. The charge calibration chain proceeds as follows:

- **Normalisation by temperature-dependent single-avalanche gain.** The number of pixels avalanching, N_{av} , is calculated by normalising the pulse height, PH, by the average pulse height corresponding to a single-pixel avalanche, $\langle PH_1 \rangle$, calculated by fitting a truncated Gaussian distribution to the first dark noise peak. The dark noise spectra are seen in beam triggers, and also in special runs taken with periodic triggers. $\langle PH_1 \rangle$ changes with MPPC gain, which itself is dependent on the temperature. During operation, temperature varies within $\pm 2^\circ$ C, which changes the breakdown voltage, in turn changing the gain by less than 10%. Temperature and operating voltage are measured every few minutes, allowing a time-dependent correction of $\langle PH_1 \rangle$ to be performed.
- **Effect of overvoltage on N_{av} .** Changes in the overvoltage can also change the photodetection efficiency, and the cross talk and after-pulsing probabilities, which change the value of N_{av} for a given number of photons hitting the MPPC. Using FGD through-going cosmic events, which have a narrow energy deposit per unit length, a linear temperature-dependent correction, the same for each MPPC, has been found to account for this effect.
- **MPPC pixel saturation.** Each MPPC has a finite number of pixels, therefore for larger signals the proportion of photons inducing a pixel avalanche will fall. A model to take this in account has been formulated assuming photons are uniformly distributed across the whole MPPC, and a pixel

cannot avalanche multiple times within the electronic pulse shaping time, and this model has been verified using test bench measurements. Using this model, the number of *detectable* photons, N_{DPE} , is calculated.

- **Bar-to-bar variations and light attenuation.** Difference between bars in the number of photons hitting the MPPC are expected from the variations in fibre-MPPC coupling, variations in scintillator material, variations in fibre mirroring, variations of the position of the fibre in the bar and the diameter of this hole, etc. Cosmic ray data is used, and N_{DPE} is calculated for each bar, normalised by the calculated track length through that bar. Variations from the mean of all bars, $C_{\text{bar}} = 1$, of $\sim 7\%$ are seen.

Attenuation along the bar is calculated by studying the variation of $N_{\text{DPE}}/C_{\text{bar}}$ as a function of hit distance from the MPPC, for cosmic ray events. The measured attenuation is consistent with test bench measurements, except within 5 cm of either end of the bar due to light leaking out before it is absorbed by the WLS fibre.

A combined correction is applied to N_{DPE} .

- **Conversion from scintillation photons to energy.** The corrected N_{DPE} is assumed to be proportional to the number of scintillation photons, N_{scint} . This is converted to the actual energy deposit in the detector using an empirical normalisation factor (about 21 $N_{\text{DPE}}/\text{MeV}$), a correction using Birks' formula [85], and an empirical correction in order to bring data and MC into agreement for the energy distributions of cosmic rays.

The charge calibration chain works well, as can be seen in Fig. 2.8 comparing data and MC energy loss as a function of momentum.

The AFTER chip has a spare channel for a timing marker, which is received with triggers. The timing calibration chain proceeds as follows:

- **Pulse fitting.** The leading edge of the waveform above 150 ADC (~ 4 avalanches) is fit from -240 ns before the peak time to the peak, using either the high- or low-gain channel using the ~ 65 avalanche cut as described above. Fitting only the leading edge gives better resolution, as the effect of after-pulsing and late photons (e.g. from reflections at the mirrored end of the fibre).
- **Timing markers.** Timing markers are not received by each AFTER chip simultaneously. A correction is made for each hit that is the time difference between the hit timing marker relative to the first FGD timing marker.
- **FEB-to-FEB (front-end board) corrections.** Differences are seen in cosmic muon data that show residual differences between front-end boards (FEBs). The correction is constant in time and is calculated using cosmic rays. For each cosmic ray track, the difference between the hit time and average track hit time is calculated. The correction used is the residual of this difference averaged over many tracks.
- **FGD hit time for a track.** FGD hits are corrected for the light propagation time down the fibre. The single-hit timing resolution is measured as the width of the time difference between a given hit and a reference hit in the first FGD layer as a function of N_{av} and the reference charge. From this, a measure of the single-avalanche timing resolution is found to be 12.5 ± 0.6 ns, which is related to the time constants of the scintillator and WLS fibre, smeared by reflection at the mirrored fibre ends.

The timing calibration performs well. For tracks that pass through both FGD1 and FGD2, two clear peaks of width 1.47 ns, with clear separation between them, are seen in the FGD1–FGD2 time difference. This allows track direction to be determined.

2.3.3 TRIP-t subdetectors (PØD, ECal, and SMRD)

The PØD, ECal, and side muon range detector (SMRD) all use the scintillator-bar and MPPC readout, as discussed in Sec. 2.3.2. These subdetectors, with INGRID, also use the same front-end electronics. A TRIP-t front-end board (TFB) [86], collects the signals from 64 MPPCs. The signal from each MPPC is split capacitively in the ratio 1:10, resulting in a high-gain (sensitive to low photoelectron signals) and low-gain (extends the dynamic range, takes over at ~ 50 photoelectrons) channels. Charge for each channel is collected in a 480 ns integration window, and a time stamp is recorded if the integrated charge goes above a threshold. The integration time is followed by a 100 ns reset period (dead time). Therefore the time structure closely matches the 581 ns beam bunch peak spacing.

The PØD was designed to measure NC1 π^0 interactions⁸ on a water target, with the same neutrino beam flux as reaches SK. It is composed of x and y plastic scintillator bar layers, interleaved with lead and brass sheets, and fillable water bags. The PØD can be operated with either all bags empty, or all bags full, enabling analyses to be done utilising a subtraction method to deduce water target cross sections.

The ECal surrounds the inner detectors (PØD, TPCs, FGDs) and provides complementary information through direction and energy measurements of photons, and additional particle identification capabilities (electron-muon-pion separation). The ECal is split into three sub-modules the DS-ECal is located in the basket after TPC3, the barrel-ECal surrounds the tracker region, and the PØD-ECal surrounds the PØD. The ECal is composed of layers of scintillator bars of cross section 4.0 cm \times 1.0 cm interleaved with 1.75 mm (DS-ECal and barrel-ECal) or 4.0 mm (PØD-ECal) lead layers. The DS-ECal (barrel-ECal) consists of 34(31)

⁸NC1 π^0 interactions are defined as NC resonant events with a single π^0 in the final state.

scintillator layers, arranged in two views. The PØD-ECal consists of 6 scintillator layers, orientated in a single view parallel to the beam axis.

The SMRD consists of 7 mm thick scintillation counters inserted into the 1.7 cm air gaps between 4.8 cm thick steel plates which make up the UA1 magnet flux return yokes. This allows the momentum of high angle muon tracks to be measured, as well as helping to identify neutrino interactions in the surrounding cavity walls, and iron of the magnet.

2.3.4 Reconstruction and Monte Carlo simulation

Neutrino fluxes are estimated from beam MC, as described in Sec. 3.1. These fluxes are passed to the NEUT [87], GENIE [88] or NUWRO [89] neutrino MC event generators, as described in Sec. 3.2.1, to simulate neutrino-induced interactions within ND280. Cosmic interactions are simulated using the Corsika flux [90]. Tracking of particles and their energy deposits within the detector are simulated using GEANT4 [91, 92]. The optical and electronics readout is simulated through custom-written code.

TPC reconstruction is performed in two stages. First, tracks of ionisation are formed in the TPC from signals in neighbouring pads that are consistent with originating from the same particle. Clusters are formed from neighbouring pads with hits above threshold in the same column (for horizontal tracks) or same row (for vertical tracks). A likelihood fit is performed on these clusters to determine the track momentum and direction [93]. The spatial resolution of tracks and clusters has a dependence on drift distance and angle, but is around 1 mm. This is sufficient to achieve the design momentum resolution of $0.1 p_{\perp} \text{ GeV}/c$. TPC particle identification (PID) is performed using a truncated mean of energy loss measurements of charged particles in the gas. Energy loss as a function of momentum from T2K Run 1 is shown in Fig. 2.7. The measured energy loss per

unit length is used to define a pull, $\delta_E(i)$, where

$$\delta_E(i) = \frac{dE/dx_{\text{measured}} - dE/dx_{\text{expected}}(i)}{\sigma_{dE/dx}}, \quad (2.2)$$

for particle hypothesis i . Using the pull, the probability of misidentifying a muon as an electron is 0.2% for tracks below $1 \text{ GeV}/c$ and $-1 < \delta_E(e) < 2$.

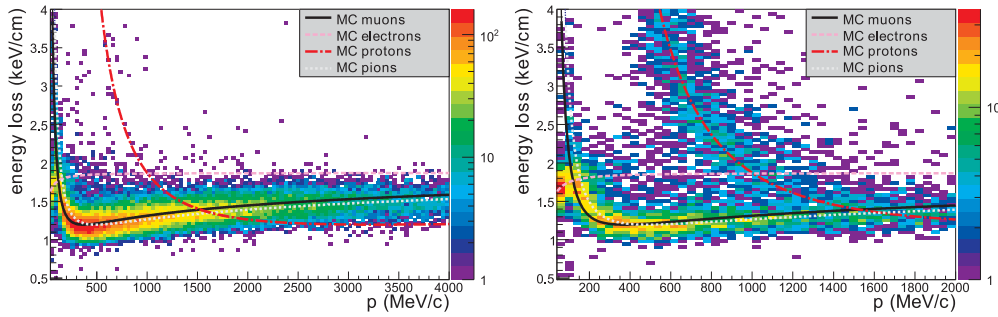


Figure 2.7: Energy loss as a function of momentum for negatively (left) and positively (right) charged particles in the TPC, from T2K Run 1 data. Also shown are the MC expectations for muons, electrons, protons and pions. Figures taken from [79].

The next reconstruction step is to associate TPC tracks with FGD hits. This both provides a seed to begin the FGD reconstruction, and a T_0 for the TPC track. Any remaining FGD hits are then reconstructed into tracks using straight line fitting algorithms (first 2-dimensional tracks are formed, which are combined into 3-dimensional tracks). The PID performance for FGD-only tracks is shown in Fig. 2.8.

Reconstruction in the other subdetectors proceeds in a similar way; tracks are found in 2-dimensional, then converted to 3-dimensional (if that information is available). Dedicated algorithms also exist in the PØD and ECal to find showers induced from electrons or photons.

The results of individual subdetector reconstruction are given to an ND280 global reconstruction package. This package refits all tracks and showers, utilising the RECPACK toolkit [94] which takes into account curvature due to magnetic

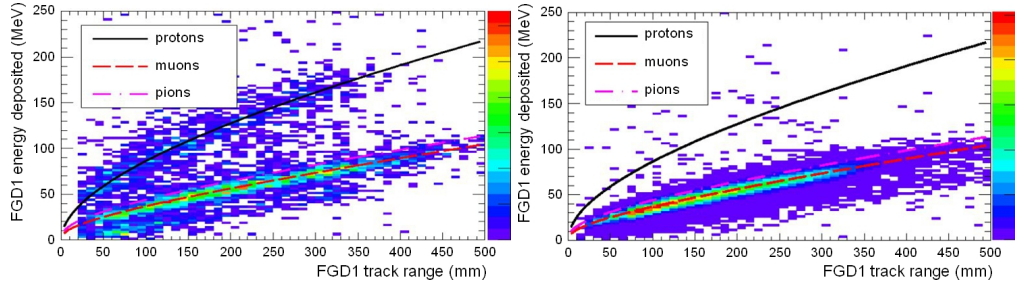


Figure 2.8: Deposited energy as a function of range for charged particles stopping in FGD1 in neutrino beam (left) and cosmic ray (right) data. Also shown are the MC expectations for muons, protons and pions. Figures taken from [80].

fields and energy loss along the track.

An example event, showing a neutrino-induced DIS event in FGD1 is shown in Fig. 2.9.

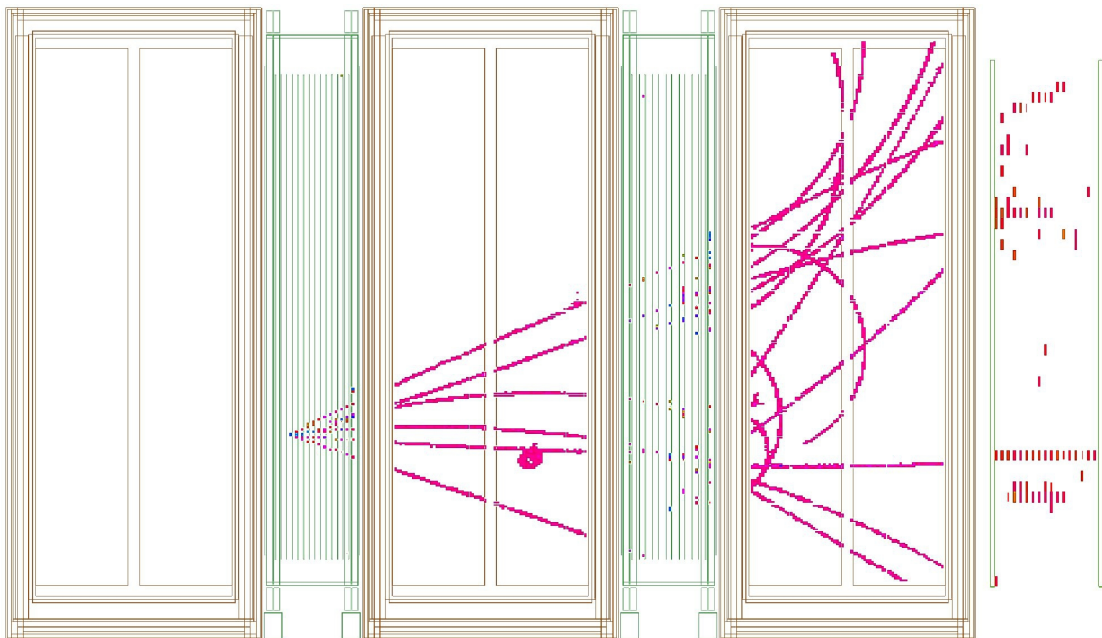


Figure 2.9: Event display showing the three TPCs, two FGDs, and DS-ECal. A DIS neutrino interaction occurs in FGD1, producing multiple tracks. Figure taken from [80].

2.4 Super-Kamiokande

At 50 kt (22.5 kt fiducial) Super-Kamiokande is currently the worlds' largest land-based water Cerenkov detector. It is built below Mt. Ikenoyama, located 295 km west of the neutrino beam target at J-PARC, with a mean rock overburden of 1 km (2.7 km water equivalent). SK has been running since 1996 in four run periods: SK-I (1996–2001) was halted by an accident in which 7877 PMTs imploded, SK-II (2002–2005) ran with the remaining PMTs redistributed and protected by an acrylic cover, SK-III (2006–2008) ran with a full complement of PMTs, and SK-IV (2008–present) uses new front-end electronics and data acquisition. T2K is taking place in SK-IV.

2.4.1 The Super-Kamiokande detector

SK consists of two volumes, a cylindrical inner detector (ID) separated by the outer detector (OD) by a \sim 50 cm steel scaffold as shown in Fig. 2.10, and with a diameter of 39 m and height of 42 m. The ID is 36.2 m high with a diameter of 33.8 m, and 11,129 inward-facing 50 cm-diameter PMTs are housed on its walls. The ID has a photocathode coverage of 40% and uses Hamamatsu R3600 hemispherical PMTs, with a combined quantum and collection efficiency of about 20%. The OD is about 2 m thick radially and at both ends, and 1,885 outward-facing 20 cm-diameter PMTs are housed on its inner walls. The OD uses 611 Hamamatsu R1408 PMTs and 1274 R5912 PMTs and is capable of almost 100% rejection of cosmic muon backgrounds. The structure separating the ID and OD is a steel scaffold covered by plastic sheets which optically separate the volumes, and is inactive. The wall facing the ID is covered in a black sheet of plastic to absorb light and minimise the number of photons reflected back into the ID or transmitted through into the OD. The walls facing the OD are lined

with Tyvek®, a highly reflective material, which give photons reflecting off the OD walls a higher chance of scattering into a OD PMT, to compensate for the sparse OD instrumentation.

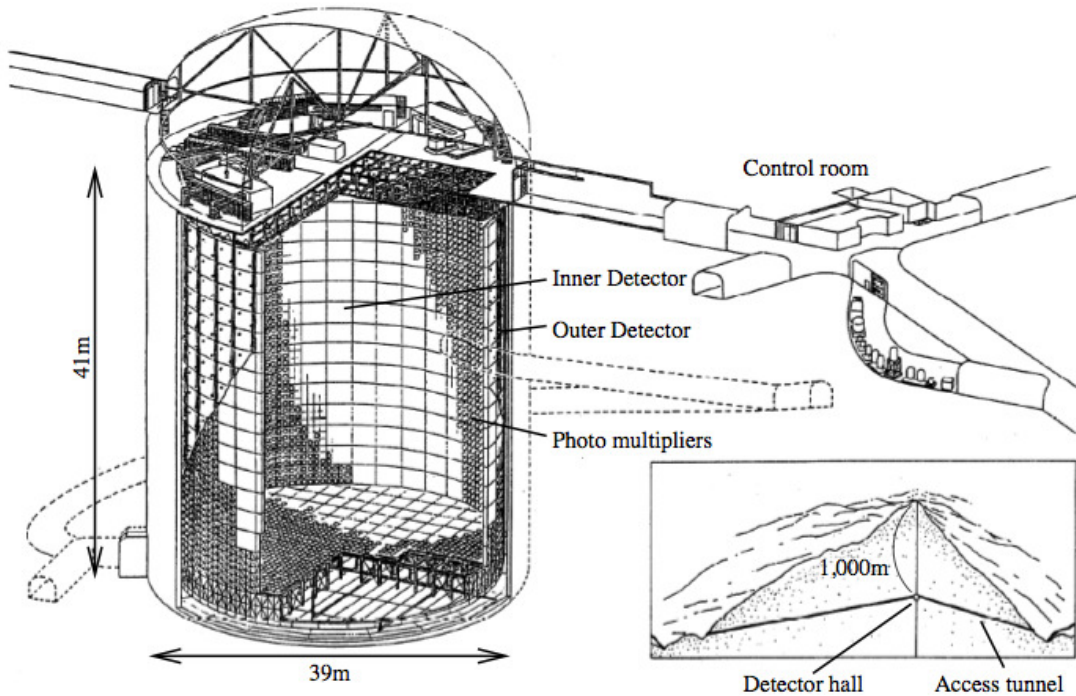


Figure 2.10: Layout of the SK neutrino detector. It is composed of a cylindrical inner detector volume, surrounded by the outer detector. Figure taken from [95].

Both volumes are filled with highly purified water to minimise background radiation, using a multi-step system including filtration, reverse osmosis, and degasification. Water is recirculated through the purification system to maintain purity. Fresh air from outside the mine, away from the site entrance, is pumped in to the tank area to reduce the effect of the high radon background in the mine.

Charged particles passing through the water emit Cherenkov radiation in a cone with angle

$$\cos \theta = \frac{1}{n\beta}, \quad (2.3)$$

where θ is the opening angle at which the photons are emitted, n is the refractive index of the medium (1.33 for water), and β is the speed of the charged

particle. It follows that there is a threshold at $\beta = 0.75$; only charged particles travelling faster than the local speed of light emit Cherenkov radiation. The threshold for detection is $p_\mu \geq 120 \text{ MeV}/c$, $p_\pi \geq 158 \text{ MeV}/c$, $p_p \geq 1064 \text{ MeV}/c$, and $p_e \geq 0.57 \text{ MeV}/c$ for muons, charged pions, protons, and electrons respectively, therefore, in interactions induced by the T2K neutrino beam, protons are rarely visible. There is also a non-negligible possibility of muons and pions being below Cherenkov threshold, although detection is possible with a $\sim 90\%$ Michel electron⁹ tagging efficiency. It should be noted that no charge separation occurs in SK.

The oscillation analysis described in Chap. 4 requires a high-purity selection of $\nu_\mu^{(\rightarrow)}$ CCQE events in order to reconstruct the neutrino energy accurately, by assuming quasi-elastic kinematics (Eq. 3.9). A selection has been developed for 1 μ -like ring events (see Sec. 3.4.2), in which the visible ring is hypothesised to be the muon and the proton is assumed to be below Cherenkov threshold (i.e. invisible). The major backgrounds occur due to charged pions from CC events being below Cherenkov threshold¹⁰ or absorbed within the nucleus, or charged pions from NC events mimicking a muon.

A water Cherenkov detector is a good choice for the T2K beam spectrum, in which the peak is at $\sim 0.6 \text{ GeV}$, meaning the majority of events are CCQE, as it gives excellent PID separation of electrons and muons and good neutrino energy reconstruction of these CCQE events. SK would not perform as well in a higher energy beam, in which the majority of events are not CCQE, where the hadronic system must be visible in order to reconstruct the neutrino energy, and for PID.

⁹ An electron from muon decay.

¹⁰ Alternatively, the muon can be below Cherenkov threshold, and the ring seen be due to a charged pion.

2.4.2 Calibration and detector stability

Various systems are used to calibrate the SK detector, and are described below. More details can be found in Ref. [96].

Water transparency

To measure water transparency, a diffuser ball which emits laser light at wavelengths between 350 nm and 500 nm is lowered into the SK tank, and imaged via a charge-coupled device (CCD) camera. The measurement is repeated at various depths and the laser stability is measured using a PMT. Since this measurement cannot be done during normal running, a sample of through-going cosmic muons is also used. Cosmic muons provide an almost constant ~ 2 MeV/cm of energy deposit, independent of particle energy, giving an in-situ measurement of transparency, at all wavelengths in the Cherenkov spectrum¹¹. The attenuation length was 105.4 ± 0.5 m in SK-I.

Attenuation length is dependent on the combined effects of scattering and absorption. Each effect is measured separately using a combination of lasers with wavelengths 337 nm, 371 nm, 400 nm, and 420 nm illuminating the detector from the top, flashing every 6 s during normal data taking. Photons that are not scattered cause PMT hits on the bottom of the tank, while other PMT hits are due to scattering and reflection from the bottom PMTs and black liner sheets. Scattered and reflected photons can be separated by the time distribution of photon arrival times; reflected photons are delayed. A Gaussian fit is performed on the bottom PMTs' charge distribution to adjust the laser beam shape and direction in the MC. The shape of the time distribution of photon arrival times at the PMTs is used to tune the MC absorption parameters, and the total number

¹¹The Cherenkov spectrum is continuous, running from 300 nm to 600 nm and peaking at 430 nm [97].

of scattered photons is used to tune Rayleigh scattering parameters.

PMT relative gain

Each PMT can be set with a different high voltage which changes the gain; the aim is that all PMTs have approximately equal gain. Light is injected into a scintillator ball lowered into the SK tank, which emits light at the sensitive region of the PMTs (at a peak of 440 nm). Each PMT detects a few tens of photoelectrons. The gain of each PMT is calculated using the pulse height, taking into account light attenuation, PMT acceptance, and scintillator ball uniformity. The measurement is repeated for various high voltage values and scintillator ball positions. After calibration at the start of SK-I (June 1996), the standard deviation of the gain was 7.0%, and this is corrected for by the offline software.

PMT relative timing

The relative timing of PMT hits is important for event reconstruction. It is affected by the cable length between PMT and electronics, and charge collected due to the discriminator slewing effect. An N_2 laser emits an intense pulse of light, with duration 3 ns. This is converted to 384 nm, passed through an optical filter (to adjust the pulse height), and emitted in the detector via a diffuser ball. The measurement is repeated for different pulse heights, and the timing resolution for each PMT is found to be better than 3 ns for one photoelectron, increasing to better than 1 ns above 30 photoelectrons.

Stability

SK has performed well and been stable throughout SK-IV. Using a sample of stopping cosmic muons, both the muon momentum to range ratio, and

decay-electron momentum are stable within 1%. The misidentification rate of the stopping cosmic muons and decay electrons have been below 1% and 2% respectively, both with an RMS of 2%. Finally for stopping cosmic muons, the decay-electron tagging efficiency is stable, with an RMS/mean of 0.81%.

Stability can also be analysed using atmospheric neutrino events. Using a sample of fully-contained fiducial-volume (FCFV) events (see Sec. 3.4.1), with a modified timing cut, the event rate is 8.14 ± 0.37 events/day, and is stable throughout SK-IV within statistical errors. Comparisons of FCFV sample distributions including the reconstructed vertex position, visible energy, number of rings, PID likelihood, momentum, number of Michel electrons, and reconstructed π^0 mass also show good agreement between T2K Run 1+2+3, T2K Run 4, and no T2K beam periods.

2.4.3 Reconstruction and Monte Carlo simulation

Neutrino events are simulated in SK using NEUT, as described in Sec. 3.2.1. Tracking of particles and their energy deposits within the detector are simulated using a GEANT3-based [98] simulation called SKDETSIM. For hadrons in water, a model based on the NEUT intranuclear rescattering cascade model (see Sec. 3.2.4) with additions from GCALOR [99] and custom code [100]. Absorption, Rayleigh scattering, and Mie scattering are simulated in SKDETSIMs' light propagation, and is tuned to data from laser calibration sources. The agreement between SKDETSIM and cosmic ray data for reconstructed momentum is within a few percent (see Fig. 31 of Ref. [69]).

Reconstruction is performed using a custom reconstruction package. First, PMT timing information is used to determine an initial vertex, and the initial direction and ring edge is determined using the PMT charge pattern. Next, extra Cherenkov ring candidates are found using a Hough transform [101] of the hit

PMT distribution. This step is iterative; once a ring is found, more rings are searched for and a likelihood method is used to determine if the data is more consistent with the presence of the extra ring. This step is repeated until up to a maximum of five rings are found. Next, PID is performed on all candidate rings using the expected PMT charge distributions, analytically calculated (based on muon energy loss and Cherenkov radiation models) for muons, and MC-generated for electrons. Finally, all rings are refit, taking into account the particle identification hypothesis, and the photoelectrons are distributed between the rings. The momentum of each ring is determined using the total number of photoelectrons for that ring, in a cone with 70° half-angle opening towards the reconstructed ring direction. This determination corrects for light attenuation, scattering, PMT gain, and PMT acceptance effects, as well as charge sharing between rings.

The vertex resolution is 33.5 cm, and 23.7 cm, for 1 e-like ring and 1 μ -like ring events respectively. The angular resolution is 1.2° , and 0.8° , for 1 e-like ring and 1 μ -like ring events respectively. The reconstructed momentum resolution is $1.7 + 0.7\sqrt{p/(GeV/c)}\%$, and $0.6 + 2.6\sqrt{p/(GeV/c)}\%$, for electrons and muons respectively. This leads to an expected resolution in reconstructed neutrino energy for 1 μ -like ring $\nu_\mu + \bar{\nu}_\mu$ CCQE events near the oscillation maximum is ~ 0.1 GeV.

Michel electrons are found by looking for time-delayed clusters occurring in the ID. The tagging efficiency is $\sim 90\%$, found by looking at stopping cosmic muons. This can be used to look for events with charged pions and muons that were not reconstructed.

Neutral pion events are a dominant background for 1 e-like ring events, therefore a dedicated maximum likelihood fit, FITQUN, which calculates charge and time probability density functions (p.d.f.s) for every PMT and for any initial

condition, is used. FITQUN is based on mathematical formalism developed by MiniBooNE [102], which was a Cherenkov detector using a ν_μ beam at a similar energy to T2K. A 2-dimensional cut is made between the ratio of best-fit likelihoods of the e and π^0 hypotheses, and the π^0 mass from the π^0 fit. An alternative established algorithm, POLFIT [103], is used to select control samples for the ν_μ systematic analysis, and also as a cross-check. POLFIT assumes there are two gamma rings in an event that is classified as 1-ring, and iteratively tests various patterns and energies until the likelihood is maximised. An invariant mass is calculated, and events with POLFIT mass of more than $105 \text{ MeV}/c^2$ are cut. The FITQUN cut rejects 69% of π^0 background from the T2K Run 1+2+3 ν_e appearance result (which used POLFIT) with only a 2% loss in efficiency [104].

Examples of 1 μ -like ring and 1 e-like ring events are shown in Fig. 2.11.

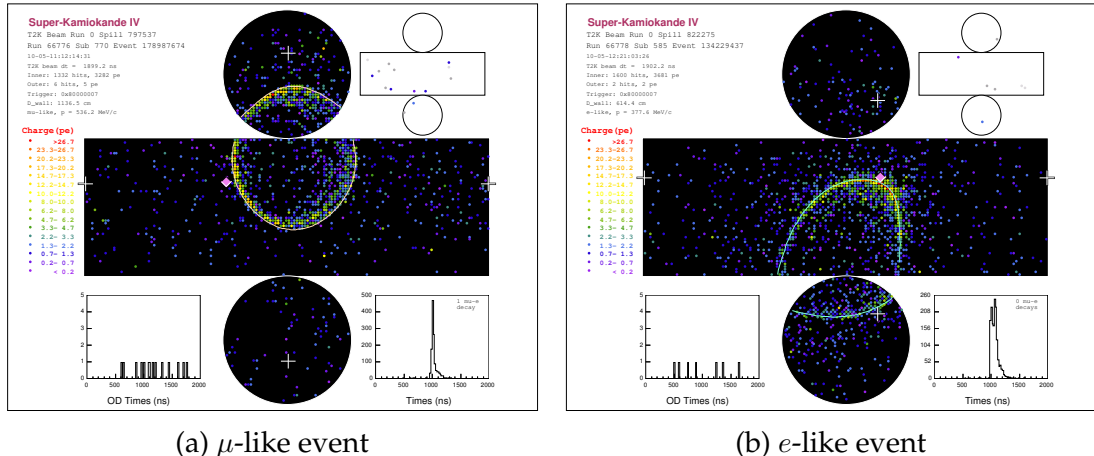


Figure 2.11: Example of reconstructed T2K events in SK for (a) a 1 μ -like ring and (b) an 1 e-like ring. The cylindrical ID is unrolled onto a plane, with coloured points representing hits of specific charge in a PMT. The white crosses indicate the reconstructed vertex, and the diamond marks the intersection of a ray between the vertex and the neutrino beam and the ID wall. The reconstructed cone is shown as a white line. The figure in the upper right corner shows the hit map for the OD. Time distributions are shown in the bottom left and bottom right for the OD and ID respectively. Figure taken from [69].

2.5 T2K status and physics goals

T2K has been running in four periods since 2010: Run 1¹² (January–June 2010), Run 2 (November 2010–March 2011), Run 3 (January–June 2012), and Run 4 (October 2012–May 2013), collecting a total of 6.57×10^{20} POT at SK while steadily increasing the beam power as shown in Fig. 2.12. The ultimate T2K POT goal is 7.80×10^{21} POT, therefore only 8% of the full T2K dataset has been recorded.

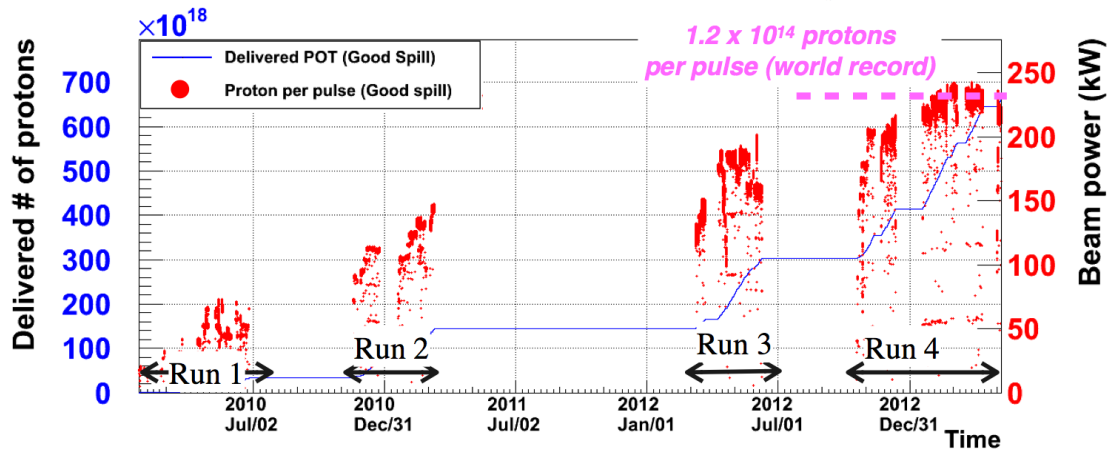


Figure 2.12: The accumulated POT delivered by the J-PARC beam to T2K in four run periods (blue). Also shown is the beam power (red).

T2K has recently published a discovery of $\nu_\mu \rightarrow \nu_e$ appearance with a measurement rejecting $\theta_{13} = 0$ at 7.3σ using the Run 1+2+3+4 dataset [104]. This achieves one of the primary physics goals as laid out in the T2K letter of intent [105]. Using the same measurement, δ_{CP} is excluded at 90% C.L. in the range 0.19π to 0.80π (-1.00π to -0.97π and -0.04π to 1.00π) for NH(IH). T2K has also recently published a precision measurement of $\nu_\mu \rightarrow \nu_\mu$ disappearance [1] with the design goal precision on $\delta(\Delta m_{32}^2) \sim 10^{-4} \text{ eV}^2/\text{c}^4$, and the world's strongest constraint on $\sin^2 \theta_{23}$. Therefore updated physics goals have been formulated [106]:

¹²The barrel-ECal and PØD-ECal were not installed during Run 1.

1. an initial measurement of CP violation in neutrinos up to a 2.5σ level of significance;
2. a precision measurement of ν_μ disappearance oscillation parameters at $\delta(\Delta m_{32}^2) \sim 10^{-4} \text{ eV}^2/\text{c}^4$ and $\delta(\sin^2(2\theta_{23})) \sim 0.01$ and determination of the θ_{23} octant at 90% C.L. if $|\theta_{23} - 45^\circ| > 4^\circ$; and
3. a contribution to the determination of the mass hierarchy.

These updated goals have been defined using realistic sensitivity studies [106–108]. The optimal combined sensitivity¹³ occurs for T2K with around 50% neutrino and 50% antineutrino running (despite equal neutrino and antineutrino statistics occurring at around 20%:80%) and is improved when combined with other experiments (e.g. NO ν A beam or SK atmospheric neutrino measurements). To achieve these goals, the systematic errors must be reduced to 5–8% and $\sim 10\%$ for the ν_e and $\bar{\nu}_e$ samples respectively (the error is currently 8.8% for the ν_e sample [104]).

T2K also has secondary physics goals, including cross-section measurements from neutrinos and antineutrinos on a variety of nuclear targets using the near detectors. A CC inclusive cross-section measurement has been published in [109], and many other analyses are in progress. The search for sterile neutrinos is also ongoing with multiple studies being performed, including ν_e appearance in a model with one sterile neutrino at both ND280 and SK [110]. Other topics (both potential or under study) include a test of non-standard interactions, a measurement of the neutrino time-of-flight, and [a test of Lorentz invariance based on the sidereal time and the concept of preferred directions](#).

¹³The combined sensitivity for excluding $\sin \delta_{CP} = 0$, excluding maximal θ_{23} mixing, the ability to reject a θ_{23} octant, and the ability to determine the mass hierarchy.

Chapter 3

Inputs to the ν_μ disappearance analysis

In order to perform the oscillation analysis described in Chap. 4, simulations must be developed in order to be able to predict the neutrino event rates as seen in the T2K detectors. The event rate is a combination of flux and cross section, therefore detailed simulations of both are required.

- The neutrino beam flux simulation models primary interactions of protons with the target, secondary interactions of particles with the surrounding material, and particle decays. The model is tuned to external data, mainly from NA61/SHINE. Systematics are evaluated from uncertainties in the model itself, and measurements of the geometry of the T2K beamline. This is presented in Sec. 3.1.
- The neutrino cross section simulation must describe interactions in the ~ 1 GeV region. The simulation is tuned to external data, mainly from Mini-BooNE, and systematics are evaluated using these fits and other external datasets. This is summarised in Sec. 3.2.

The model is tuned on data collected with the unoscillated 2.5° off-axis neutrino beam, using semi-inclusive selections of ν_μ CC events at ND280. This involves performing a fit to the ND280 datasets, including systematics related to the flux, the cross sections, and the event selection. Uncertainties which are correlated between the near and far detector (flux, and some nucleus-independent cross-section parameters) are propagated to the oscillation fits in order to tune the model further, and provide a large reduction in uncertainties. This is presented in Sec. 3.3.

A selection of $1\,\mu$ -like ring events at SK is performed in order to maximise the purity of charged current quasi-elastic (CCQE) events, which allows the neutrino energy to be reconstructed using the lepton kinematics. The selection, and associated systematics, are presented in Sec. 3.4.

The work presented in this chapter corresponds to the official T2K inputs, which are common to all T2K oscillation analyses.

3.1 Neutrino beam flux prediction & uncertainties

The neutrino beam flux simulation, including tuning to external datasets, is presented in Sec. 3.1.1. The systematics related to the simulation are presented in Sec. 3.1.2.

3.1.1 Neutrino flux simulation

The T2K flux prediction is based on a simulation, beginning with the primary proton beam upstream of the baffle, tracking the secondary hadrons through the target, horns, and decay volume, and ending with the decay of hadrons and muons that produce neutrinos. Measurements of the beam profile, intensity, and position, and the magnetic field of the horns, and external hadron production

data drive the simulation and its associated uncertainties.

Primary proton interactions in the target and baffle, where the proton beam first interacts and produces the majority of secondary pions, are modelled using FLUKA2008 [111, 112]. Kinematics of particles emitted from the target are passed to the JNUBEAM simulation, based on GEANT3 [98]. JNUBEAM simulates the baffle, target, horn magnets, helium vessel, decay volume, beam dump, and muon monitor (with a geometry based on final mechanical drawings of the beamline) and also the INGRID, ND280, and SK detectors (positioned in the simulation according to the latest survey results). The GCALOR model [99] is used to model hadronic interactions in JNUBEAM¹. In JNUBEAM, particles are propagated through the decay volume until they interact or decay.

Particle decays use branching ratios from Ref. [31]. In order to maximise central processing unit (CPU) efficiency, every neutrino that is generated is forced to point in the direction of SK, or at a random point in the near detector planes. This is achieved by forcing the decay kinematics of the parent particle² to produce the neutrino in that direction, and assigning a weight based on the probability of those kinematics. Decay kinematics are used to assign neutrino energy in the centre of mass frame. To move into the laboratory frame, the neutrino is boosted under the assumption that it points towards the desired detector, with an event weight stored for the probability of production in the selected direction.

Flux model tuning

The models are tuned to hadron production data, most notably from the NA61/SHINE [113] experiment at CERN. The components of the NA61/SHINE de-

¹Using both FLUKA and GCALOR to simulate hadronic interaction is not inconsistent; both are tuned to data.

²For particles which decay to two or more neutrinos, each neutrino is independently forced to point at a detector.

tector are: a group of detectors to measure the beam timing, position, and PID before interacting with the target; five TPCs (two within superconducting magnets) for charged particle tracking; and three scintillator detectors with a timing resolution better than 90 ps for time-of-flight (TOF) measurements. Track reconstruction proceeds by finding tracks in each TPC, matching tracks between TPCs, determining the interaction vertex, and matching TOF hits with the track. PID is performed using energy loss (dE/dx) and TOF, and track momenta and charge are determined via track curvature in a magnetic field. NA61/SHINE has published measurements of π^\pm [114] and K^+ [115] differential production cross sections using a thin (2 cm) graphite target, at the same proton beam energy as T2K. As shown in Fig. 3.1, this data covers more than 90% of the π^\pm phase space, and 60% of the K^+ phase space.

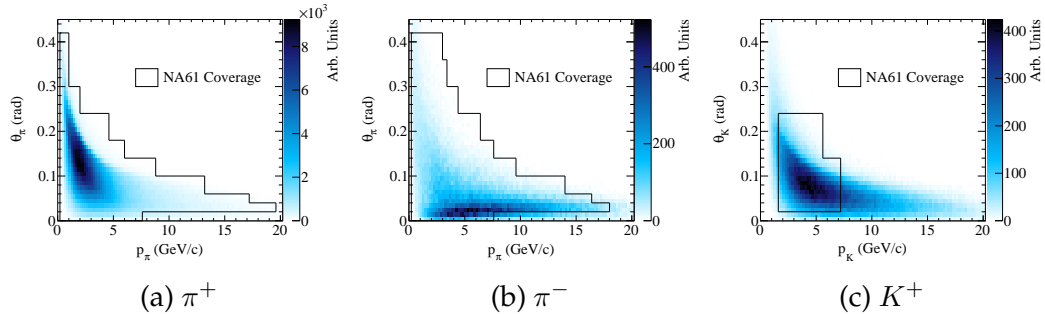


Figure 3.1: The phase space of π^+ , π^- , and K^+ contributing to the predicted neutrino flux at SK (shaded area), and the regions covered by NA61/SHINE measurements (unfilled box). Figure taken from [74].

In the π^\pm analysis, the dominant systematics are due to uncertainties in the secondary interaction and strange particle production models, particularly the highest momenta. In the K^+ analysis, the dominant systematic is due to uncertainties in the proportion of events with K^+ tracks not decaying before reaching the TOF detector, mostly due to uncertainties in the position of the kaon decay. Both analyses are dominated by statistical error in regions of the phase space, particularly at p_π . An example differential cross-section measurement is

shown in Fig. 3.2, for π^+ production.

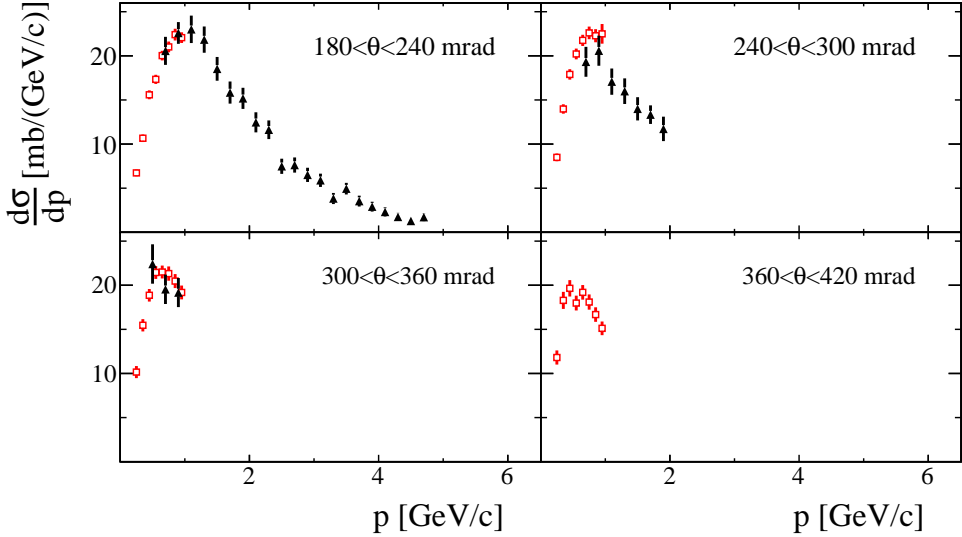


Figure 3.2: Differential cross section for π^+ production in $p-^{12}C$ interactions at $p_p = 31 \text{ GeV}/c$. Spectra are shown as a function of momentum in four polar angle bins. The red squares and black triangles are from analyses using dE/dx and $dE/dx + \text{TOF}$ information respectively. Error-bars are statistical only. Figure taken from [114].

Other datasets are used to expand the phase space coverage; Eichten *et al.* [116] and Allaby *et al.* [117] datasets cover the forward production of high energy kaons, and also include K^- measurements, while BNL-E910 [116–118] provides π^\pm data from a lower proton beam momentum that are used to evaluate tertiary pion production systematics. Inelastic cross-section measurements for proton, pion, and kaon beams on carbon and aluminium targets are used to tune particle interactions and absorption within the geometry. For details on the data used, see Tab. XII of Ref. [74]. T2K replica-target data has also been taken by NA61/SHINE, but the results are currently only available for a low-statistics portion of the full dataset [119].

Tuning is performed by reweighting the nominal MC models. Weights for the mean multiplicity of hadrons produced in nucleon nucleus interactions, are calculated in each meson $p-\theta$ bin using a ratio of data to nominal MC of this

quantity. This is calculated directly from data in the phase space and nuclei regions data covers, and is extrapolated to phase space and nuclei not covered by data. The rate at which hadrons interact is also reweighted, by accounting for both the change in the cross section, and the attenuation of the particle flux.

Each neutrino event is weighted by all relevant event weights in order to produce the tuned flux spectra. The ratio of reweighted flux to nominal flux for ν_μ and $\bar{\nu}_\mu$ are shown in Fig. 3.3. Pion tuning is the dominant effect at low neutrino energies ($\sim 8\%$ relative to a total of 10% for ν_μ), around the flux peak, while kaon tuning dominates the high energy region ($\sim 15\%$ at 3 GeV, increasing to a $\sim 40\%$ at 10 GeV for ν_μ). Differences are seen between ν_μ and $\bar{\nu}_\mu$ tunings due to the different parent particles; the ν_μ flux is dominated by π^+ and K^+ decays, while the $\bar{\nu}_\mu$ flux is dominated by π^- and K^- decays. The reweighted flux predictions at SK are shown in Fig. 3.4 for all neutrino species.

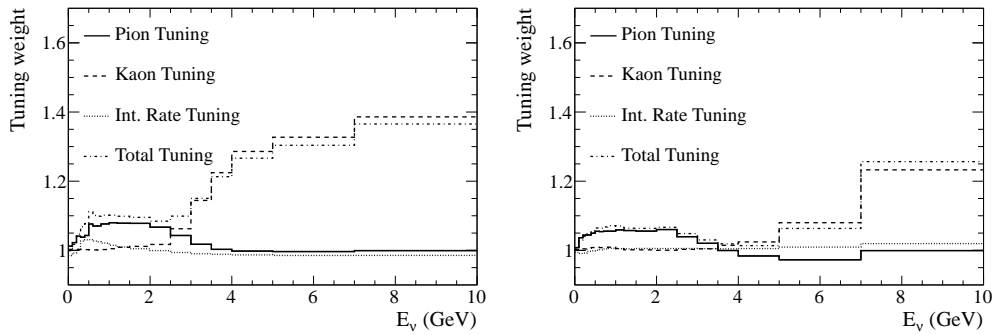


Figure 3.3: Ratio of the reweighted flux over the nominal flux for ν_μ (left) and $\bar{\nu}_\mu$ (right) at SK. Figure taken from [74].

3.1.2 Neutrino flux prediction uncertainties

Flux prediction uncertainties are studied by varying the inputs to the flux simulation (the hadron production model, the geometry, the horn currents, etc.) and evaluating the effect on the predicted flux. A covariance matrix is produced and

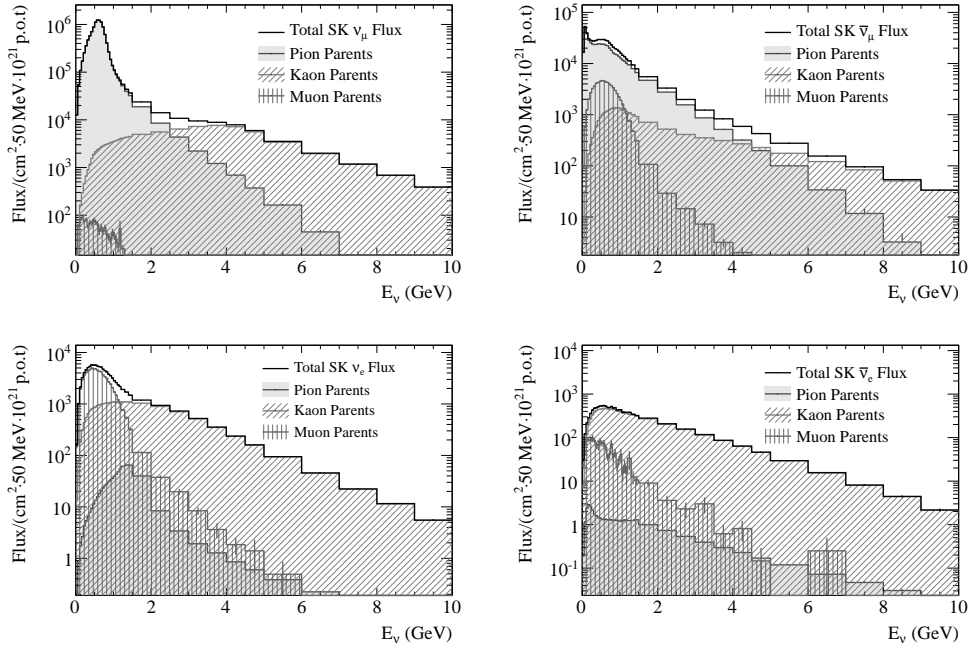


Figure 3.4: The reweighted SK flux predictions for ν_μ (upper left), $\bar{\nu}_\mu$ (upper right), ν_e (lower left), $\bar{\nu}_e$ (lower right) broken down by the neutrino parent particle type. Figure taken from [74].

used to evaluate the error due to flux prediction uncertainties in T2K analyses. The effect of each uncertainty is quantified by calculating a covariance matrix, with covariances between bins in neutrino energy, neutrino flavour, and neutrino detector. The total uncertainty is found by summing all covariance matrices.

The flux uncertainties are described in detail in Sec. V of Ref. [74], here is a summary. The uncertainties can be broken down into four categories:

1. **Hadron interaction uncertainties.** These arise from uncertainties in the experimental data from other experiments, uncertainties in scaling between targets (for example, from NA61/SHINE carbon data to aluminium for horn interactions), uncertainties in scaling data to lower incident nucleon momenta, uncertainties in extrapolating data to additional phase space not covered by its data points, uncertainties in the production of secondary nucleons, and the production cross section (total interaction rate) of parti-

cles in a given medium. The dominant errors are from secondary nucleon production and production cross sections at low neutrino energy including the beam peak, and experimental data on kaon production at high neutrino energy.

2. **Proton beam and off-axis angle uncertainties.** These arise from uncertainties on the position and angle of the primary proton beam on the baffle front surface (predominately the vertical position and angle, as the beam is predominately off-axis in the vertical direction), uncertainties on the primary proton beam intensity (from CT measurements), and uncertainties in the off-axis angle (from INGRID measurements).
3. **Target and horn alignment uncertainties.** These arise from uncertainties in the angles and positions of the target and three horns, as measured in surveys. The vertical position of the horns and the angular position of the target are the dominant effects.
4. **Horn current and magnetic field uncertainties.** These arise from uncertainties on the measurements of the horn current and the magnetic field strength, and measurements of deviations from the expected field shape.

The total flux uncertainty, as a function of neutrino energy, is shown in Fig. 3.5 for all neutrino species. The flux uncertainty in the beam peak region is $\sim 15\%$ (20% for $\bar{\nu}_e$). The uncertainty is dominated by hadron interaction uncertainties across most of the spectrum for all neutrino species. In the peak region, proton beam and off-axis angle uncertainties are also important for ν_μ , and the same is true at higher energies ~ 4 GeV for $\bar{\nu}_\mu$.

3.2 Neutrino interaction modelling and systematics

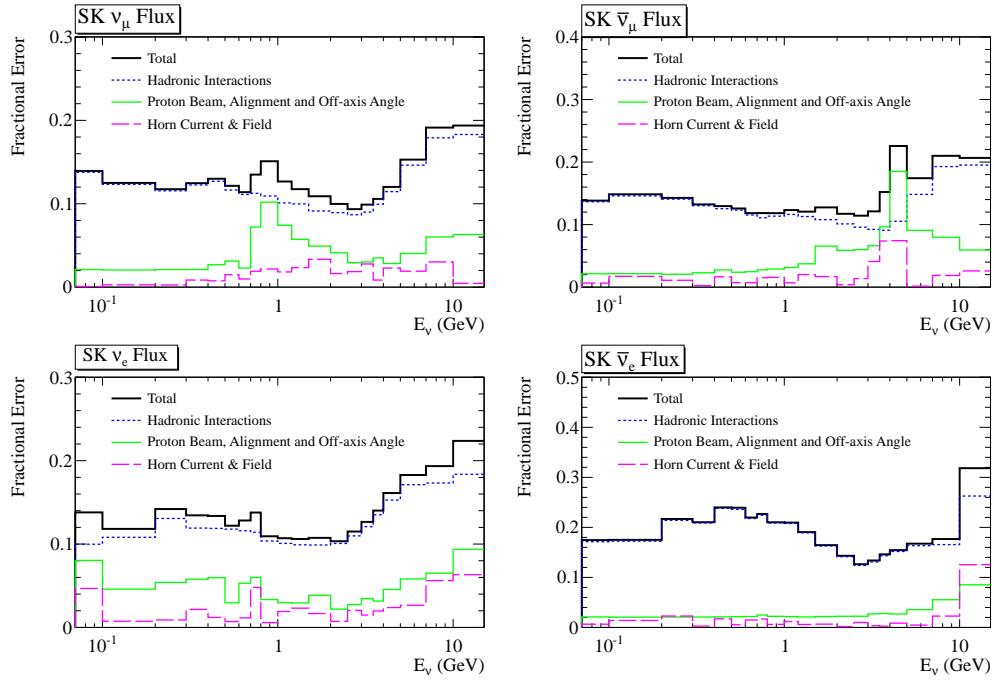


Figure 3.5: Fractional flux error including all sources of uncertainties for ν_μ (upper left), $\bar{\nu}_\mu$ (upper right), ν_e (lower left), $\bar{\nu}_e$ (lower right) at SK. Figure taken from [74].

The neutrino cross section model must be able to simulate the most likely neutrino interaction processes in the $E_\nu \sim 1$ GeV region. This includes CCQE, NC elastic scattering, resonant particle production, coherent pion production, and deep inelastic scattering. The initial simulation is described in Sec. 3.2.1. By fitting to external datasets from MiniBooNE, parts of the default model controlling CCQE and resonant pion production are tuned, as presented in Sec. 3.2.2. Using the results of these fits, and other external datasets, systematics are assigned to parameters controlling each interaction process, as discussed in Sec. 3.2.3. The related topic of FSI systematics is described in Sec. 3.2.4.

3.2.1 NEUT neutrino Monte Carlo event generator

Cross-section modelling is done using the NEUT neutrino MC event generator [87]. Events are generated using the flux model described in Sec. 3.1.1. The

processes modelled, which were introduced in Sec. 1.3, are described briefly.

Elastic and quasi-elastic scattering

Neutrino free-nucleon CCQE scattering cross section predictions are based on the Llewellyn-Smith model [120]. The relativistic Fermi gas (RFG) model by Smith and Moniz [121] is used to calculate the cross section off bound nucleons in the nucleus. Different RFG model parameters are used for each nucleus: the Fermi momentum (p_F) and nuclear binding energy (E_b). In $^{12}\text{C}(^{16}\text{O})$, p_F and E_b are 217(225) MeV/c and 25(27) MeV respectively. The models assume that the axial-vector form factor has a dipole form, such that

$$F_A(Q^2) = F_A(Q^2 = 0) / (1 + Q^2 / (M_A^{\text{QE}})^2)^2, \quad (3.1)$$

where M_A^{QE} is the quasi-elastic axial-vector mass parameter. Similar assumptions are made for the vector form factors. M_A^{QE} is set by default to 1.21 GeV/c² to give good agreement with results from MiniBooNE [122], and other experiments in the few-GeV neutrino energy region experiments on O [123], C [124], and Fe [125], but is inconsistent with older neutrino-deuterium scattering experiments [126] and the $E_\nu \sim 10$ GeV NOMAD experiment [127] that prefer values of M_A^{QE} closer to 1 GeV/c².

Neutrino nucleon neutral current elastic scattering cross sections are calculated using scaling relations of the charged current cross sections from Ref. [128].

Resonant single pion, kaon, eta, and photon production

Charged-current and neutral-current resonance neutrino-production cross sections are based on Rein and Sehgal's model [129, 130]. The interaction is handled

in two steps:

$$\nu + N \rightarrow l + N^*, \quad (3.2a)$$

$$N^* \rightarrow N' + X, \quad (3.2b)$$

where N and N' are the nucleons and N^* is an intermediate baryon resonance, and X is a pion, kaon, eta, or photon. Eighteen resonances below $2 \text{ GeV}/c^2$ are considered³. The model assumes that axial-vector form factor has a dipole form, and M_A^{RES} , defined in an analogous way to Eq. 3.1, is set to $1.21 \text{ GeV}/c^2$ by default. Cross sections are obtained by multiplying the resonance production amplitude (i.e. Eq. 3.2a) by the probability of decay to a single pion and single nucleon (i.e. Eq. 3.2b). Pauli blocking, [due to the exclusion principle](#), is included such that the nucleon from the resonance decay should have momentum greater than the Fermi surface momentum, suppressing the cross section by a few percent. In nuclei, pion-less delta decay occurs in 20% of resonance events; only the lepton and nucleon are generated (events are generated with no pion, kaon, eta, photon). Cross sections of single photon, K , and η production are also calculated in an analogous way.

Deep inelastic scattering and hadronisation

Charged current neutrino nucleus DIS cross sections are computed in the region of hadronic invariant mass (W) above $1.3 \text{ GeV}/c^2$. To prevent double counting with the single pion production model (described above) below $W = 2 \text{ GeV}/c^2$, in the range $1.3 \text{ GeV}/c^2 < W < 2.0 \text{ GeV}/c^2$ only the probability for multiple pion production is used to construct the cross section. Nucleon structure functions are taken from the GRV98 parton distribution functions [131], with corrections

³The $2 \text{ GeV}/c^2$ limit is imposed to prevent double counting between resonant particle production and deep inelastic scattering.

to improve agreement with data as proposed by Bodek and Yang [132].

Hadronisation is performed using two models. At $W > 2.0 \text{ GeV}/c^2$, PYTHIA [133] is used to determine the final state multiplicities and kinematics. For W below $2.0 \text{ GeV}/c^2$, custom code is used utilising KNO scaling [134] to determine the pion multiplicity. The mean multiplicity of pions is estimated from a $\bar{\nu} + p$ scattering experiment [135], and the forward-backward asymmetry of pion multiplicity uses measurements from the BEBC experiment [136]. The concept of a *formation length* (the idea that hadronisation is not an instantaneous process) is used to determine the position of hadrons generated in the nucleus; they are stepped a distance L away from the neutrino interaction point, where $L = p/\mu^2$, p is the hadron momentum, and $\mu^2 = 0.08 \text{ GeV}^2/\hbar c^2$ as measured in the SKAT experiment [137].

Neutrino nucleon neutral current DIS cross sections are calculated using scaling relations of the charged current cross sections using experimental data from Ref. [138, 139].

Coherent single pion production

Coherent neutrino nucleus single pion production can be thought of as the neutrino interacting with the entire nucleus, and, since the nucleus is much heavier than the neutrino, this gives an enhancement of pion production in the forward direction. The Rein and Sehgal model [140, 141] is used to calculate the neutral current cross section. For charged current coherent scattering, the correction for the lepton mass described in Ref. [142] is used, [which causes a drop off in the cross section at low \$Q^2\$; the effect is more pronounced for muons than electrons.](#)

Intranuclear rescattering cascade model

Hadrons created in neutrino interactions can interact with nucleons in the nucleus as they are ejected from the nucleus. Neutrino experiments can only observe the particles after they have exited the nucleus. Intranuclear rescattering, also known as final state interactions (FSI), has a significant impact on the observed event topologies (for example a CC1 π^+ event may appear to be CCQE due to a pion absorption), and degrades the hadron kinetic energy.

A cascade is used to model the FSI. The position of the neutrino interaction within the nucleus is calculated using a probability based on a Woods-Saxon type nucleon density distribution. All hadrons⁴ start at this interaction position. Each hadron takes an infinitesimal step, the probability of interaction is calculated using the local nuclear density and hadron-nucleon cross sections, and is used to determine whether an interaction takes place at that step. The particle is propagated until it interacts or exits from the nucleus. Pions and kaons can undergo inelastic scattering, charge exchange, absorption, and particle production, protons can undergo elastic scattering, single and double delta production, and etas can undergo absorption leading to pion production.

3.2.2 Comprehensive model tuning

External datasets are fitted in order to tune some NEUT model parameters, and to assign errors to these parameters. External data from the MiniBooNE experiment [143] is fitted in order to tune the NEUT CCQE and CC1 π^+ models [144]. This is a good choice because MiniBooNE is a 4π Cherenkov detector like SK and so has similar phase space acceptance, it uses similar target nuclei (CH_2) to T2K (mainly ^{12}C at ND280 and ^{16}O at SK), and a wide-band neutrino beam

⁴Hadrons produced in DIS events are offset due to the formation length.

covering the T2K energy range [144].

CCQE model tuning

The MiniBooNE CCQE-corrected measurement presented in Ref. [122] is used in the fit. The distribution fitted is the flux-integrated double-differential cross section in lepton kinematics (kinetic energy and angle) as this contains the most information, and uses the same kinematic variables as used in the ND280 fit (see Sec. 3.3.4).

The data is selected as events with one muon, zero pions, and no proton requirement, and so is mostly CCQE with a background of predominately CC1 π^+ events (the π^+ is absorbed in FSI or is too low energy for detection). The CC1 π^+ model in the NUANCE neutrino MC event generator [26] is tuned using a CC1 π^+ sample. After this tuning, a subtraction is applied to the CCQE-like sample to remove all non-CCQE events, to create the CCQE-corrected sample from which the cross section is determined.

The fit was performed by minimising a χ^2 function comparing the MiniBooNE data with the NEUT CCQE prediction. Two parameters controlling the MC are varied, the axial mass M_A^{QE} , and the CCQE normalisation (required due to an 11% MiniBooNE flux uncertainty). The best-fit predictions are shown in Fig. 3.6, as a function of Q^2 (the momentum exchange of the interaction squared reconstructed from final state kinematics) and E_ν^{QE} (the neutrino energy reconstructed from final state kinematics and corrected to true E_ν assuming the RFG model)⁵ and are compared with the MiniBooNE data and the NEUT nominal predictions. The result of the fit is a large value of $M_A^{QE} = 1.64 \pm 0.03$ GeV, significantly larger than the fit MiniBooNE performed themselves ($M_A^{QE} = 1.35 \pm 0.17$ GeV). This is mainly due to the fact that there is a

⁵The 1-dimensional Q^2 and E_ν^{QE} distributions shown here are not the distributions used in the fit; the 2-dimensional T_μ -cos θ_μ distribution is fit for.

large data-MC difference at low Q^2 , which MiniBooNE varies using an effective parameter to increase Pauli blocking at low Q^2 . The use of different neutrino MC event generators, and the fact that this T2K fit does not have access to correlated systematic errors, are other factors that contribute to the discrepancy. There are also large data-MC differences at low and high E_ν^{QE} , but the agreement is good in the flux peak region.

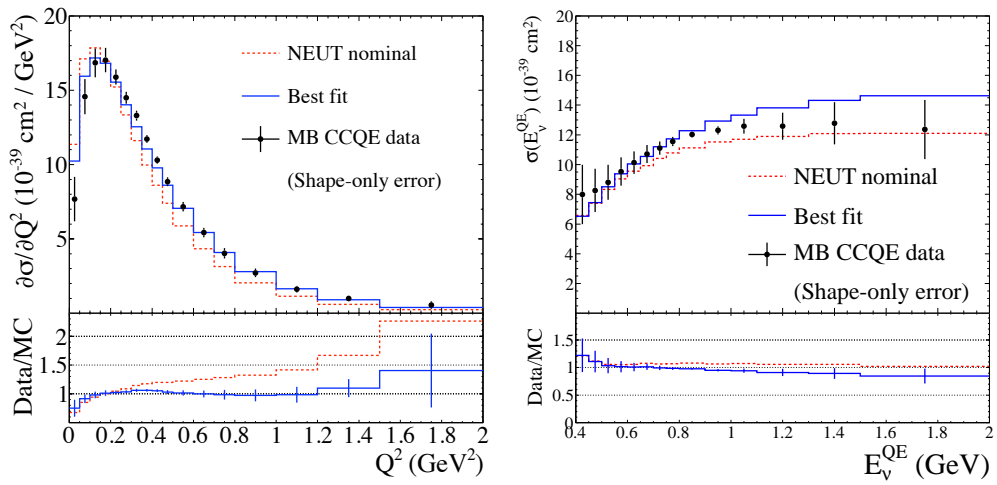


Figure 3.6: Differential CCQE cross-section distributions versus Q^2 (left) and E_ν^{QE} (right). MiniBooNE data, the nominal NEUT prediction and the best-fit NEUT prediction are all shown. Figures are taken from [145].

Single π production model tuning

NEUT has common parameters that control all resonant pion events, therefore a simultaneous fit of multiple MiniBooNE samples is performed. The distributions fitted are the CC1 π^0 Q^2 [146], the CC1 π^+ Q^2 [147], and the NC1 π^0 $|\mathbf{p}_{\pi^0}|$ [148] cross sections. Six cross-section normalisation parameters are varied in the fit (CC coherent, CC1 π , NC coherent, NC1 π^0 , NC1 π^\pm , NC other), along with M_A^{RES} (which varies the rate and Q^2 shape), an empirical parameter, “W shape”, which allows variation of the NC1 π^0 $|\mathbf{p}_{\pi^0}|$ shape to improve agreement with data, and “CC other shape” which modifies CC cross-section channels as a function of

E_ν . The best-fit point is found with the MIGRAD algorithm from MINUIT, and correlated fit errors are found using the HESSE algorithm. The best-fit predictions are shown in Fig. 3.7, as a function of the fitted variables, and are compared with the MiniBooNE data and the NEUT nominal prediction. FSI uncertainties effect the result of the fit, due to pion absorption, scattering, and charge exchange in the nucleus. Fits are therefore repeated a further sixteen times, for different sets of FSI model parameters (see Sec. 3.2.4). The fit is also repeated with the π -less Δ decay fraction set to zero.

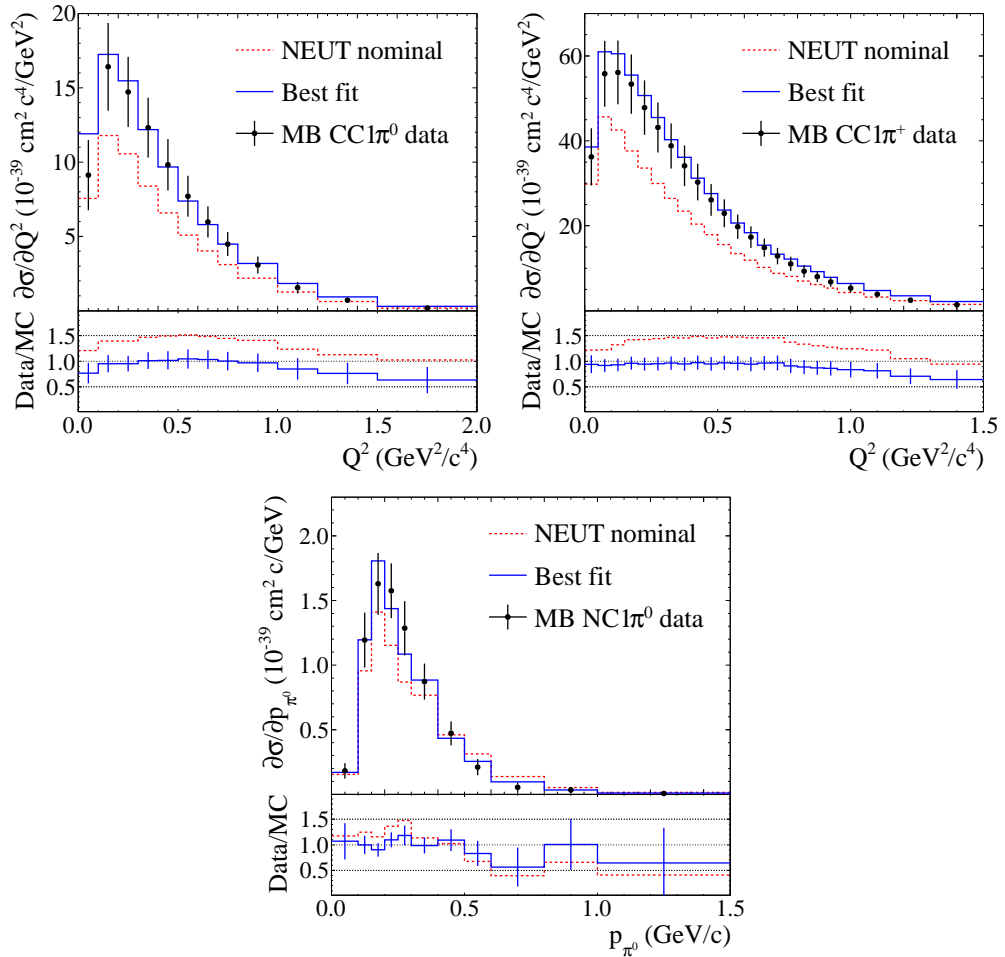


Figure 3.7: Differential pion production cross-section distributions for CC1 π^0 versus Q^2 (top left), CC1 π^+ versus Q^2 (top right) and NC1 π^0 versus p_{π^0} (bottom). MiniBooNE data, the nominal NEUT prediction and the best-fit NEUT prediction are all shown. Figures are taken from [145].

3.2.3 Cross-section model systematics

Errors are assigned to the cross-section model in order to cover the uncertainties in the current knowledge of neutrino scattering. This process is described in detail in Refs. [144, 149], and is summarised here. The results of the fits to MiniBooNE data in Sec. 3.2.2 are used. A summary best-fit values and errors of all cross-section parameters used in ND280 and SK fits are shown in Tab. 3.1.

Name	Description	Nominal value	Error	ND280	SK
CCQE model parameters					
$f_{16;t,r}^{ND280}$	M_A^{QE} (GeV/c ²)	1.21	0.45	✓	✓C
$f_{18;t}^{ND280}$	CCQE norm $E_\nu < 1.5$ GeV	1.00	0.11	✓	✓C
$f_{19;t}^{ND280}$	CCQE norm	1.00	0.30	✓	✓C
$f_{20;t}^{ND280}$	1.5 GeV < E_ν < 3.5 GeV				
	CCQE norm $E_\nu > 3.5$ GeV	1.00	0.30	✓	✓C
	p_F (¹² C) (MeV/c)	217	30	✓	✗
$f_{pF;t,r}$	p_F (¹⁶ O) (MeV/c)	225	30	✗	✓
	E_b (¹² C) (MeV)	25	9	✓	✗
$f_{bindE;t,r}$	E_b (¹⁶ O) (MeV)	27	9	✗	✓
	SF (¹² C)	0 (RFG)	1 (SF)	✓	✗
$f_{SF;t,r}$	SF (¹⁶ O)	0 (RFG)	1 (SF)	✗	✓
Single pion production model parameters					
$f_{17;t,r}^{ND280}$	M_A^{RES} (GeV/c ²)	1.16	0.11	✓	✓C
$f_{20;t}^{ND280}$	CC1 π norm $E_\nu < 2.5$ GeV	1.63	0.43	✓	✓C
$f_{20;t}^{ND280}$	CC1 π norm $E_\nu > 2.5$ GeV	1.00	0.40	✓	✓C
	NC1 π^0 norm	1.19	0.43	✓	✗
$f_{Wshape;t,r}$	W shape (MeV/c ²)	87.7	45.3	✓	✓
$f_{\pi-less\Delta;t,r}$	π -less Δ decay	0.00	0.20	✓	✓
Other model parameters					
$f_{CCcoh;t}$	CC coh norm	1.00	1.00	✓	✓
$f_{CCothShape;t,r}$	CC other shape (GeV)	0.00	0.40	✓	✓
$f_{NC1\pi^\pm;t}$	NC1 π^\pm norm	1.00	0.30	✗	✓
$f_{NCoth;t}$	NC other norm	1.00	0.30	✓	✓
$f_{CC\nu_e;t}$	ν_e to ν_μ ratio	1.00	0.03	✗	✓
$f_{CC\bar{\nu};t}$	ν to $\bar{\nu}$ ratio	1.00	0.20	✗	✓

Table 3.1: Summary of the cross-section errors used in the ND280 fit (see Sec. 3.3.4) and ν_μ disappearance oscillation fit (see Chap. 4). A ✓ symbol denotes that this systematic with this value and error is used in the fit, C denotes that this systematic is constrained by the ND280 fit before being used in the SK fit, and ✗ denotes that this systematic is not used. [The name of each parameter corresponds to the convention used in Chap. 4.](#)

CCQE constraints

MiniBooNE data constrains M_A^{QE} (the error is the sum of the fit error and the difference between the NEUT nominal and the fitted value) and the CCQE normalisation for $E_\nu < 1.5 \text{ GeV}$ (the error is the MiniBooNE flux uncertainty). Two higher energy CCQE cross-section normalisations parameters are included, with errors assigned from differences seen between MiniBooNE and NOMAD data [122, 127]. The RFG parameters p_F (Fermi momentum) and E_b (binding energy) are nucleon dependent, and are set to the NEUT nominal with an error determined by electron scattering data [150]. It should be noted that p_F provides cross-section variations at low Q^2 . An alternative to the RFG model is the spectral function (SF) model [151], and an uncertainty is included that is the difference between these models, as calculated using the NUWRO neutrino MC event generator [89].

Single π production constraints

The uncertainties on parameters that the MiniBooNE data can constrain (M_A^{RES} , the CC1 π normalisation for $E_\nu < 2.5 \text{ GeV}$, and the NC1 π^0 normalisation) are assigned using the fit to MiniBooNE data. The NEUT model is tuned using the best-fit values of these parameters (for the fit assuming the nominal parameterisation of FSI and the π -less Δ decay fraction). The covariance of the fitted parameters is built up of three parts:

- The covariance matrix calculated using the HESSE algorithm from the fit using the nominal parameterisation of FSI and the π -less Δ decay fraction.
- The covariance between the best-fit values of the fits with and without π -less Δ decay included.
- The covariance between the best-fit values of the fits using the sixteen

alternative FSI parameter sets (see Sec. 3.2.4) and the best-fit values of the fit using the nominal FSI model.

The W shape parameter is shifted by a large amount, suggesting that this empirical parameter is acting as a proxy for a more general model change (e.g. altering sizes of higher resonances, changing the relative fraction of resonant and DIS events, or the current NEUT cascade model does not alter scattered pion momenta), therefore the nominal value is used with an error determined as the difference between the nominal and the best fit.

The CC1 π $E_\nu > 2.5$ GeV normalisation parameter error is assigned as the difference between MiniBooNE data and the NEUT nominal prediction, extrapolated to higher energy. The CC coherent normalisation is set to 100% due to the process never being measured by experiments at energies $\mathcal{O}(1)$ GeV, and the best data [152, 153] setting 90% limits significantly below the default model prediction. The NC coherent normalisation is poorly constrained by the MiniBooNE data fit, due to a degeneracy with NC1 π^0 , therefore data is used [154] which shows a 15% discrepancy with NEUT with a 20% error. The NC1 π^\pm and NC other normalisations are not constrained by the fit, due to small fractions of these events in the samples.

Other cross-section model constraints

The CC multi- π model has an energy-dependent systematic, $f_{CCothShape}$, assigned as 40% / (E_ν / GeV). This comes from the data in Ref. [155] which has an uncertainty of $\mathcal{O}(10\%)$ at 4 GeV. The multi- π fraction below 1 GeV is small, with a threshold of ~ 0.6 GeV, therefore the convergence of the error towards infinity at low energy is not a concern.

The NC1 π^\pm and NC other normalisation errors are taken from comparing the NEUT prediction with external datasets at the T2K energies [156, 157].

Differences between ν_e and ν_μ cross sections arise in terms in theoretical calculations, due to the differences in final state lepton mass. The work presented in Ref. [158] uses external data to quantify the effect of such terms not included in NEUT calculations.

Differences between ν and $\bar{\nu}$ cross sections are expected due to angular momentum conservation. The interaction of a ν (left handed) with a left-handed quark (as in the valance quarks in nucleons) has a total angular momentum of 0, therefore decays proceed isotropically, and are flat in the inelasticity, y . Conversely, the interaction of a $\bar{\nu}$ (right handed) with a left-handed quark has a total angular momentum of -1 against the neutrino direction, therefore decays with the lepton emitted against the neutrino direction are forbidden, while other angles are suppressed, leading to $\frac{d\sigma}{dy}$ having a triangular dependence on y . The total cross section for $\bar{\nu}$ is therefore approximately half of that as for ν . High quality CCQE scattering data for both neutrinos and antineutrinos have been released by MINER ν A [159, 160] and MiniBooNE [122, 161] and is used to assign an error on the expected $\nu/\bar{\nu}$ cross-section ratio.

3.2.4 Final state interaction systematics

FSI results in modified observable final states, and so is an important systematic to take into account. External pion-carbon scattering data is used to assign errors on each of the possible FSI interactions (the data sets are described in Ref. [162]).

At low energy ($|\mathbf{p}_\pi| < 500 \text{ MeV}/c$), three parameters control the FSI model by varying the mean free path of absorption, QE scattering and low energy single charge exchange. Each of the three parameters is varied from 40% to 160% of its nominal value in 10% steps to generate 2197 (13^3) parameter sets. For each parameter set, a χ^2 is calculated comparing the MC for that parameter set with data. A 68% confidence interval is created in this three-parameter region, and

the eight (2^3) parameter sets at the extrema of the confidence interval are chosen in order to span the uncertainties on the data. The eight parameter sets are shown in Fig. 3.8 with $\pi^+ {}^{12}\text{C}$ scattering data.

At high energy ($|\mathbf{p}_\pi| > 500 \text{ MeV}/c$), three parameters control the FSI model by varying the mean free path of pion production, high energy QE scattering, and high energy single charge exchange. These parameters are not fit, but instead varied, in two parameter sets, to span the data as shown in Fig. 3.9.

There are therefore sixteen FSI-controlling parameter sets (in addition to the nominal set). These errors are propagated to the ND280 fit (Sec. 3.3.4) and oscillation fit (Chap. 4) by constructing a covariance matrix \mathbf{V} using the equation

$$V_{ij} = \frac{1}{16} \sum_{k=1}^{k=16} (p_i^{nom} - p_i^k)(p_j^{nom} - p_j^k), \quad (3.3)$$

where p_i is an observable quantity in bin i (e.g. p_μ, θ_μ or E_ν bin), nom denotes the nominal parameter set, and k denotes the k^{th} parameter set.

3.3 ND280 flux and cross-section constraint

A selection of CC ν_μ events are made using the ND280, as described in detail in Ref. [163] and supporting documents. First a CC inclusive selection is performed, as described in Sec. 3.3.1. The CC inclusive sample is split into CC-0- π , CC-1- π^+ , and CC-other samples, as described in Sec. 3.3.2. The systematics related to the event selections are described in Sec. 3.3.3. These samples are then fitted to constrain the flux and common cross-section parameters (the so-called ND280 fit), as described in Sec. 3.3.4 [164].

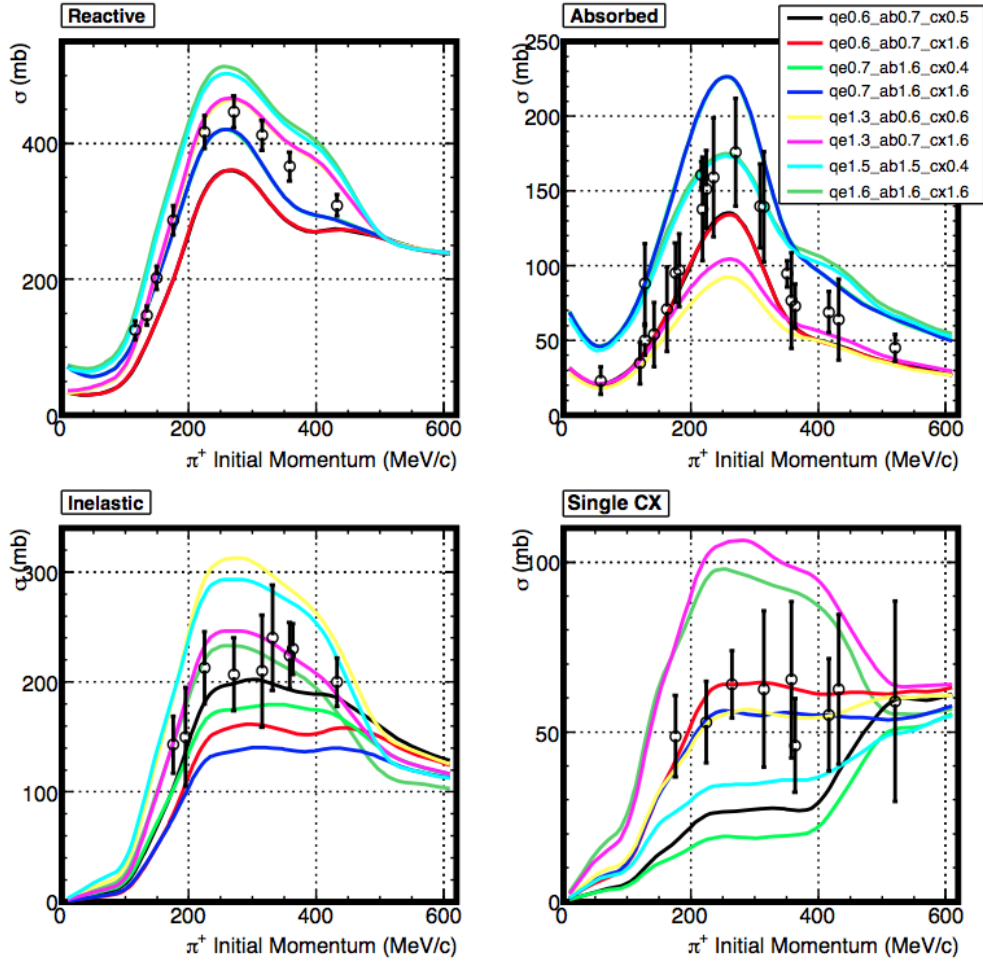


Figure 3.8: The eight low energy parameter variation 1σ curves from fits to $\pi^+{}^{12}\text{C}$ scattering data. Shown are cross sections for reactive (total – elastic, top left), absorption (top right), QE (bottom left), and single charge exchange (bottom right). The data sets are described in Ref. [162]. Figure taken from [144].

3.3.1 ν_μ charged current inclusive event selection

A ν_μ CC inclusive event selection is performed using the ND280 tracker region, by selecting for the highest momentum negative track, with an FGD1 fiducial volume and a *good* TPC track segment. The cuts are as follows:

1. **Data quality.** The beam spill must be defined as a good spill (e.g. the horn current is nominal to within ± 5 kA). The ND280 must have a good global data quality flag; all ND280 subdetectors must be functioning (e.g. the

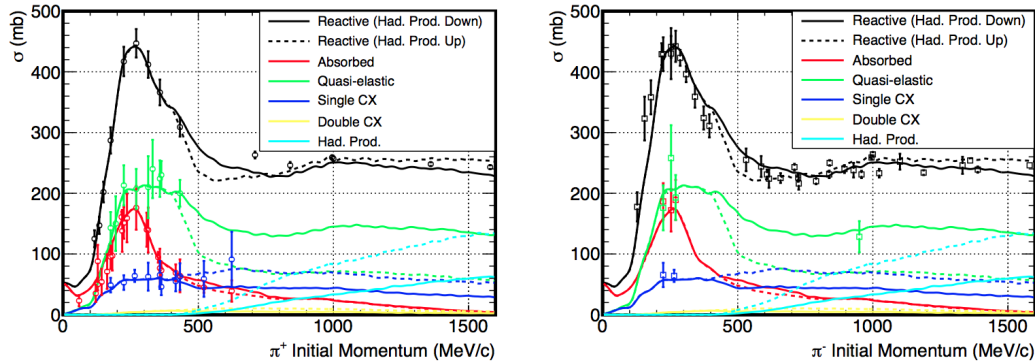


Figure 3.9: High energy parameter variation $\pm 1\sigma$ curves (solid and dashed lines) compared with $\pi^+ {}^{12}\text{C}$ (left) and $\pi^- {}^{12}\text{C}$ (right) scattering data. The low energy parameters are set to nominal in this figure. The data sets are described in Ref. [162]. Figure taken from [144].

TPC central cathode high voltage must be within the range $24950 \text{ V} < V < 25550 \text{ V}$). The amount of data used in this section is 5.900×10^{20} POT, corresponding to the full Run 1+2+3+4 dataset after these data quality cuts. The MC sample used 9.545×10^{21} POT of interactions simulated within the magnet, and 6.643×10^{21} POT of interactions simulated in the sand and concrete surrounding the detector pit.

2. **Bunching.** The beam spill (corresponding to 6 or 8 beam bunches) is divided by beam bunch using timing information; tracks within 60 ns (four times the bunch width) are grouped together. This allows spill pile-up to be handled correctly. Bunch pile-up may still be an issue, but the average number of expected FGD1 interactions per spill during Run 4⁶ is ~ 0.35 .
3. **Total multiplicity.** There must be at least one reconstructed track in the TPC.
4. **Negative track in FGD1 fiducial volume and with good TPC track quality.** There must be at least one negative track that starts in the fiducial

⁶From [165], there are 2.968 ± 0.005 events/ 10^{15} POT after applying low-level cuts, and from Fig. 2.12 there are a maximum of $\sim 1.2 \times 10^{14}$ protons per pulse.

volume of FGD1, that also has >18 vertical TPC clusters⁷. The vertex is taken as where the 3-dimensional reconstructed track intercepts the vertical plane of the most upstream matched FGD hit. The fiducial volume requirements are $|x| < 874.51$ mm, $|y - 55| < 874.51$ mm and $136.875 \text{ mm} < z < 446.955$ mm. In x and y , five bars on each end of the layer are excluded (the 55 mm y offset is due to the coordinate system definition). In z , the first XY module is excluded. The >18 vertical TPC clusters requirement is used to exclude short tracks with less reliable reconstruction. If multiple tracks pass this cut, the muon candidate track is taken to be the track of highest momentum.

5. **Backwards-going tracks and TPC1 veto.** If the muon candidate is backwards going (start position downstream of end position) the event is rejected. The majority of these tracks are misreconstructed forward-going positive tracks. The highest momentum track with a TPC segment (with no track quality requirement), that is not the muon candidate, should not start more than 150 mm upstream (i.e. in z) of the muon candidate. This rejects events that probably have tracks entering the tracker from the PØD or magnet regions.
6. **Broken track cut.** If the muon candidate start position is more than 425 mm from the upstream edge of FGD1, and there is at least one FGD-only track with start position outside the FGD fiducial volume, the event is rejected. This is to reject tracks from backgrounds which start outside of the FGD fiducial volume, and are misreconstructed such that the track is broken into two (the second track can start in the FGD1 fiducial volume, and so can be misidentified as the muon candidate).

⁷This requirement corresponds to a track length in the z direction of ~ 20 cm.

7. **Muon particle identification cut.** Likelihood cuts are applied to the dE/dx distribution⁸ of the muon candidate track

$$L_{\text{MIP}} = \frac{L_\mu + L_\pi}{1 - L_p} > 0.80 \quad \text{if } p < 500 \text{ MeV}/c, \\ L_\mu > 0.05, \quad (3.4)$$

where the first cut rejects electrons, and the second cut rejects protons and pions. L_{particle} is defined as

$$L_i = \frac{e^{-\text{pull}_i^2}}{\sum_l e^{-\text{pull}_l^2}}, \quad (3.5)$$

where l runs over proton, muon, pion and

$$\text{pull}_i = \frac{(dE/dx_{\text{measured}} - dE/dx_{\text{expected},i})}{\sigma_{\text{expected},i}}. \quad (3.6)$$

$dE/dx_{\text{expected},i}$ is the value of the truncated mean for particle hypothesis i and $\sigma_{\text{expected},i}$ is the deposited energy resolution.

The purity of the selection is 90.73%. In this selection 89.8% of negative muon candidates are true negative muons; the main background is negative pions (7.5%), due to the TPC PID being unable to distinguish between them.

3.3.2 ν_μ CC semi-inclusive event selections

The CC inclusive events are divided into three sub-samples designed to optimise the purity of the following event categories:

1. CC-0- π , defined as events with a true negative muon and with zero pions after FSI;

⁸Specifically, the truncated mean of energy deposited in the TPC.

2. CC-1- π^+ , defined as events with a true negative muon, exactly one positive pion, and exactly zero negative and neutral pions after FSI;
3. CC-other, defined as all other CC events (i.e. with true negative muon and more than one positive pion and/or at least one negative or neutral pion and/or at least one exotic particle (e.g. kaon, eta) after FSI).

It should be noted that no CC inclusive events are cut by the application of these extra cuts (i.e. all CC inclusive events are present in exactly one of the sub-samples). To achieve this, ways of determining the presence of pions in the event are required.

The TPC is used to reconstruct charged pions, electrons, and positrons; the presence of a neutral pion is inferred from the presence of electrons and positrons; FGD1 is used to reconstruct charged pions only. Pions are identified in three ways:

1. **TPC tracks.** The extra tracks must satisfy the same bunching, FGD1 fiducial volume, and TPC track quality cuts as the muon candidate. Particle identification of the track is then performed. If the track is negative with pion probability >0.8 (found using Eq. 3.5), it is tagged as a negative pion. Otherwise, it is tagged as an electron. If the track is positive with momentum $>900 \text{ MeV}/c$, it is tagged as a proton. Otherwise, it is tagged as the most probable particle type, found by choosing i such that

$$P_i = \frac{L_i}{\sum_l L_l} \quad (3.7)$$

is maximised, where L_i is the likelihood as defined in Eq. 3.5, and $i, l = \pi^+, p, e^+$ in the positive case, and $i, l = \pi^-, e^-$ in the negative case.

2. **Michel electron tagging in FGD1.** If there is a time-delayed FGD1 hit cluster, out of time with a beam bunch window, with a total charge deposit

of at least 200 photoelectrons, this is taken as a Michel electron, and is tagged as a positive pion.

3. **FGD-only tracks.** A track is defined as FGD-only if it doesn't have a TPC segment⁹. The charged pion candidate must satisfy the bunching cut. In addition, it should be fully contained in FGD1, and pass the angular cut, with respect to the beam, of $|\cos \theta| > 0.3$. The fully contained cut requires both the start and stop positions lie inside a special fiducial volume ($-887 \text{ mm} < x < 888 \text{ mm}$, $-834 \text{ mm} < y < 942 \text{ mm}$, z not be in the most downstream XY module). The angular cut is applied to be consistent with systematic studies. Charged pion tracks are identified as tracks with $-2.0 < \text{pull}_\pi < 2.5$.

To prevent a single charged pion being reconstructed multiple times (e.g. broken tracks, or an FGD-only track also providing a Michel electron signal), a maximum of one pion can be found in FGD1; only if no Michel electron is found, a maximum of one FGD-only track is searched for.

The sub-samples are then defined as:

1. **CC-0- π .** 0 e^\pm TPC tracks, 0 π^\pm TPC tracks, 0 Michel electrons, 0 π^\pm FGD-only tracks;
2. **CC-1- π^+ .** 0 e^\pm TPC tracks, 0 π^- TPC tracks, a total of exactly 1 π^+ TPC track and Michel electron and π^\pm FGD-only track;
3. **CC-other.** All other events.

The 1-dimensional distributions comparing data and MC are shown in Fig. 3.12 for the reconstructed muon angle. The efficiencies(purities) of the CC-0- π , CC-1- π^+ , and CC-other samples are 47.81%(72.43%), 28.37%(49.24%) and 29.71%(73.60%) respectively.

⁹FGD-only tracks can have ECal and SMRD segments.

Event migration

True $CC-1-\pi^+$ events are classified as $CC-0-\pi$ if the charged pion is missed. Four main reasons for this migration have been found

1. $\approx 30\%$ of missed π^+ undergo a secondary interaction within the FGD. This causes FGD-only reconstruction to become harder (both tracking and PID);
2. $\approx 30\%$ of missed π^+ have a TPC reconstruction failure;
3. $\approx 30\%$ of missed π^+ go directly from the FGD to the ECal. The cuts are not designed to tag this π^+ topology;
4. $\approx 10\%$ of missed π^+ emit a Michel electron that is not detected (either due to it being within a subsequent bunch, or below the 200 photoelectrons threshold).

From the true $CC-1-\pi^+$ category, 57% of π^+ are correctly tagged.

True $CC\text{-other}$ events are classified as $CC-1-\pi^+$ due to the π^+ tagging problems above. An additional reason is that the π^0 tagging is not optimal; approximately half of the true $CC\text{-other}$ events in $CC-1-\pi^+$ have a final state π^0 .

True $CC-0-\pi$ events are classified as $CC-1-\pi^+$ for the following reasons:

1. $\approx 45\%$ of the time due to p in the TPC misidentified as π . This is due to reconstruction failures, and dE/dx separation is poor above $\approx 1 \text{ GeV}/c$;
2. $\approx 45\%$ of the time due to short p or μ tracks being misreconstructed as π ;
3. $\approx 10\%$ of the time due to Michel electrons from other interactions.

3.3.3 Event selection systematics

Systematics due to the ND280 detector arise from many sources. From the FGD, the efficiency of detecting tracks and Michel electrons, track PID, and

the FGD mass contribute. From the TPC, the detection efficiency of clusters and tracks, tracks properties (charge, momentum, PID), and track matching contribute. From external backgrounds, cosmic ray events, beam interactions in the sand and outside of the FGD fiducial volume, and event pile-up contribute. A final systematic is due to uncertainties in the modelling of pion secondary interactions. A detailed discussion of each systematic is given in Appendix A.

The effect of each systematic is summarised in Tab. 3.2. The two systematics which dominate most of the phase space are:

- **Pion secondary interactions.** GEANT4 is used to simulate the propagation of particles outside the nucleus. The pion interaction model used (QGSP_BERT) does not agree well with external data (see for example Ref. [166]), and the datasets contain uncertainties. The most significant secondary interaction modes are absorption and charge exchanges (can cause the event to be misclassified), and QE scattering (can cause the reconstruction to fail).

This systematic dominates the momentum region above $p_\mu = 500$ MeV/ c .

- **Out-of-fiducial-volume events.** Out-of-fiducial-volume (OOFV) events are defined as events in which the true interaction vertex occurred outside of the fiducial volume. The dominant event categories are high energy neutrons from outside the tracker creating a π^- in the FGD which is misidentified as a muon (17.6%), and backwards-going π^+ misreconstructed as forwards going μ (18.0%). Uncertainties on each category are defined using control samples, and extra cross-section uncertainties due to different interaction nuclei.

This systematic dominates the momentum region below $p_\mu = 500$ MeV/ c .

The combined effect of the ND280 detector systematics is shown in Fig. 3.10, for each of the three ν_μ CC samples, in both p_μ and θ_μ binning. The error in each

	<i>CC-0-π</i>	<i>CC-1-π^+</i>	<i>CC-other</i>
Michel electron efficiency	0.5%-0.7%	0.1%-0.3%	0.1%-0.3%
FGD track efficiency	0.2%-1.6%	0.2%-1.2%	0.3%-1.0%
FGD PID	0.1%	0.1%-0.3%	0.0%-0.2%
FGD PID bias	0.0%-0.1%	0.1%-0.4%	0.0%-0.2%
FGD mass	0.2%-0.6%	0.4%-0.6%	0.3%-0.6%
TPC track efficiency	0.1%-0.3%	0.2%-0.4%	0.4%-0.7%
TPC track quality	<0.1%	<0.1%	<0.1%
TPC charge confusion	0.1%-1.2%	0.2%-1.2%	1.0%-2.4%
TPC momentum resolution	0.4%-2.2%	0.3%-5.0%	0.5%-3.0%
TPC momentum scale	0.2%-1.8%	0.1%-2.1%	0.2%-2.1%
B field distortion	0.2%-1.4%	0.0%-1.4%	0.2%-2.0%
TPC electron PID	0.0%-0.6%	0.0%-0.3%	0.0%-6.0%
TPC electron PID bias	0.0%-0.1%	0.0%-0.2%	0.1%-1.0%
TPC muon PID	0.0%-0.5%	0.0%-0.5%	0.0%-0.5%
TPC muon PID bias	0.0%-2.0%	0.1%-3.5%	0.1%-2.5%
TPC proton PID	0.1%-0.9%	0.2%-1.8%	0.7%-1.5%
TPC proton PID bias	0.1%-0.6%	0.2%-1.2%	0.4%-0.9%
TPC track übermerging	<0.1%	<0.1%	<0.1%
Sand muon	0.0%-0.5%	<0.1%	<0.1%
Event pile-up	<0.1%	<0.1%	<0.1%
Out-of-fiducial-volume	1.0%-19%	1.0%-10%	1.0%-12%
Secondary interactions	0.6%-5.0%	1.2%-7.0%	4.0%-10%
Total	2.0%-19%	4.0%-10%	7.0%-13%

Table 3.2: Range of the error on the number of events on p_μ bins in the ND280 ν_μ CC samples for the detector systematic parameters.

bin, above $p_\mu = 500 \text{ MeV}/c$, ranges from 2%-19%, 4%-10%, and 7%-13% for the $\text{CC-0-}\pi$, $\text{CC-1-}\pi^+$, CC-other samples respectively. The total error on the number of expected events in each sample is shown in Tab. 3.4.

3.3.4 Flux and cross-section constraint

The three CC selections ($\text{CC-0-}\pi$, $\text{CC-1-}\pi^+$, CC-other) are fit to constrain flux and cross-section systematics that are common between ND280 and SK. This is referred to as the ND280 fit. Each of the three samples are binned in reconstructed

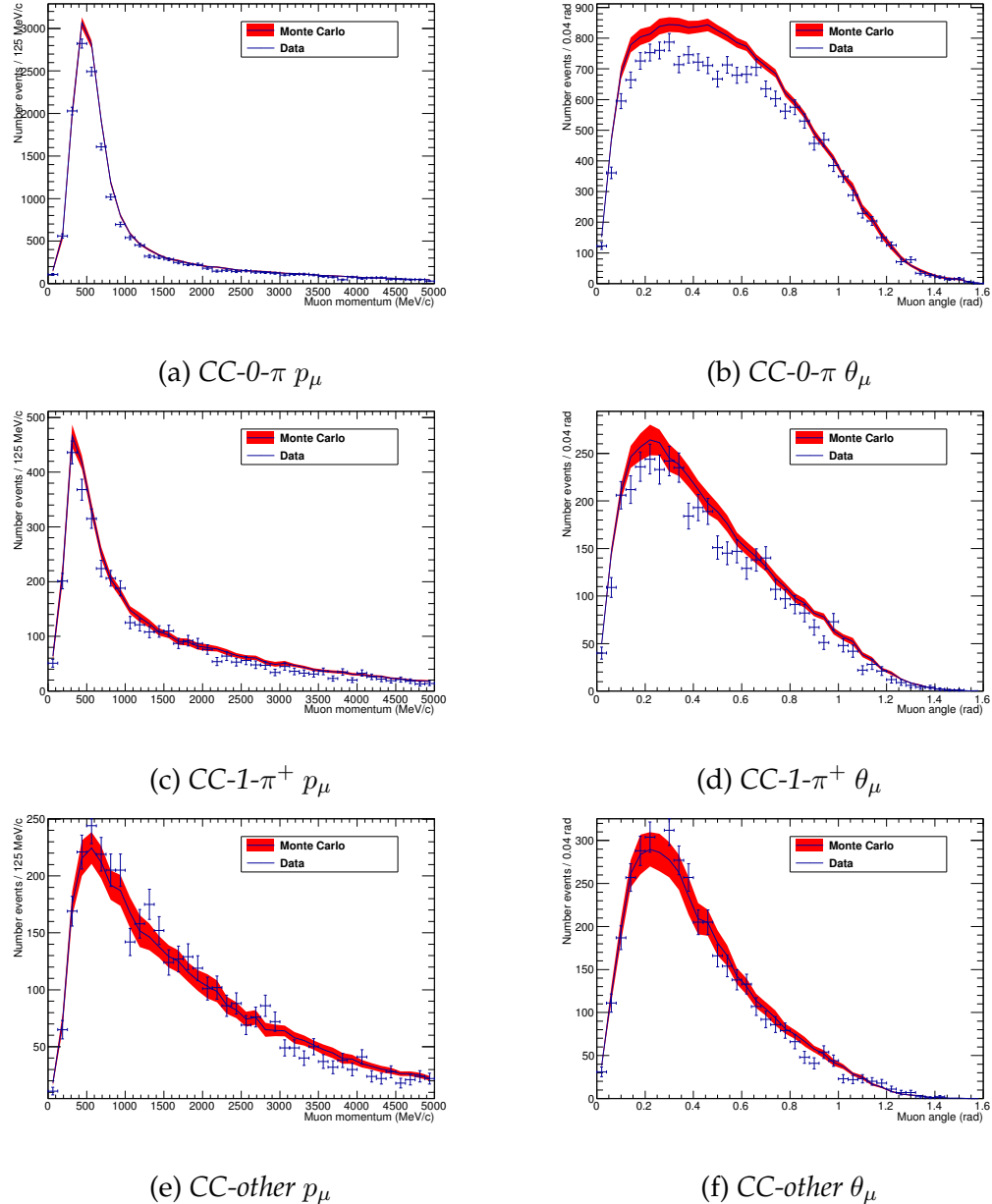


Figure 3.10: Comparison between data and MC for the ND280 ν_μ CC samples. The red band corresponds to the error on the number of events in MC due to the fluctuation of all detector systematics; **the effect of flux and cross-section systematics are not shown.**

muon momentum¹⁰ (p_μ) and reconstructed muon angle¹¹ (θ_μ) so there are a total of 451 bins in the fit. The fit is performed by minimising

$$\chi^2 = 2 \cdot \sum_{i=0}^{N-1} \left(n_i^{\text{obs}} \cdot \ln(n_i^{\text{obs}}/n_i^{\text{exp}}) + (n_i^{\text{exp}} - n_i^{\text{obs}}) \right) + (\mathbf{a} - \mathbf{a}_0)^T \cdot \mathbf{C}^{-1} \cdot (\mathbf{a} - \mathbf{a}_0), \quad (3.8)$$

where \mathbf{a}_0 is an $1 \times N_s$ - dimensional array with the default values of the systematics parameters, \mathbf{a}^T is the transpose of \mathbf{a} , \mathbf{C} is the systematic parameter covariance matrix of dimension $N_s \times N_s$, n_i^{obs} is the observed number of events in the i^{th} bin, and $n_i^{\text{exp}} = n_i^{\text{exp}}(\mathbf{a})$ is the corresponding expected number of events. The fit is performed using the MIGRAD algorithm in MINUIT [167], and errors on parameters are found using the HESSE algorithm. A second fit utilising Markov chain Monte Carlo (MCMC)¹² methods is performed as a cross-check, and gives consistent results.

The fit contains flux parameters using a covariance matrix that correlates the flux of the four neutrino species ($\nu_e, \bar{\nu}_e, \nu_\mu, \bar{\nu}_\mu$) at ND280 and SK. The systematics are binned into energy ranges depending on the neutrino species¹³ with a total of 50 systematic parameters. All systematics from Sec. 3.1.2 are taken into account, and the covariance matrix is shown in Fig. 3.11a.

The cross-section errors described in Sec. 3.2.3 are used in the fit. For shape

¹⁰Fourteen p_μ bins are arranged as follows: 1 0.30-GeV/c bin from 0.0–0.3 GeV/c, 7 0.10-GeV/c bins from 0.3–1.0 GeV/c, 2 0.25-GeV/c bins from 1.0–1.5 GeV/c, 1 0.50-GeV/c bin from 1.5–2.0 GeV/c, 1 1.00-GeV/c bin from 2.0–3.0 GeV/c, 1 2.00-GeV/c bin from 3.0–5.0 GeV/c, and 1 25.00-GeV/c bin from 5.0–30.0 GeV/c. For the CC-1- π^+ sample, the 2.0–3.0 GeV/c and 3.0–5.0 GeV/c bins are combined.

¹¹Eleven $\cos \theta_\mu$ bins are arranged as follows: 1 1.40-width bin from –1.00–0.60, 2 0.10-width bins from 0.60–0.80, 2 0.05-width bins from 0.80–0.90, 4 0.02-width bins from 0.90–0.98, and 2 0.01-width bins from 0.98–1.00.

¹²An introduction to MCMC can be found in Sec. 37.5 of Ref. [31].

¹³Eleven ν_μ energy bins have edges: 0.0, 0.4, 0.5, 0.6, 0.7, 1.0, 1.5, 2.5, 3.5, 5.0, 7.0, 30.0 GeV. Five $\bar{\nu}_\mu$ energy bins have edges: 0.0, 0.7, 1.0, 1.5, 2.5, 30.0 GeV. Seven ν_e energy bins have edges: 0.0, 0.5, 0.7, 0.8, 1.5, 2.5, 4.0, 30.0 GeV. Two $\bar{\nu}_e$ energy bins have edges: 0.0, 2.5, 30.0 GeV.

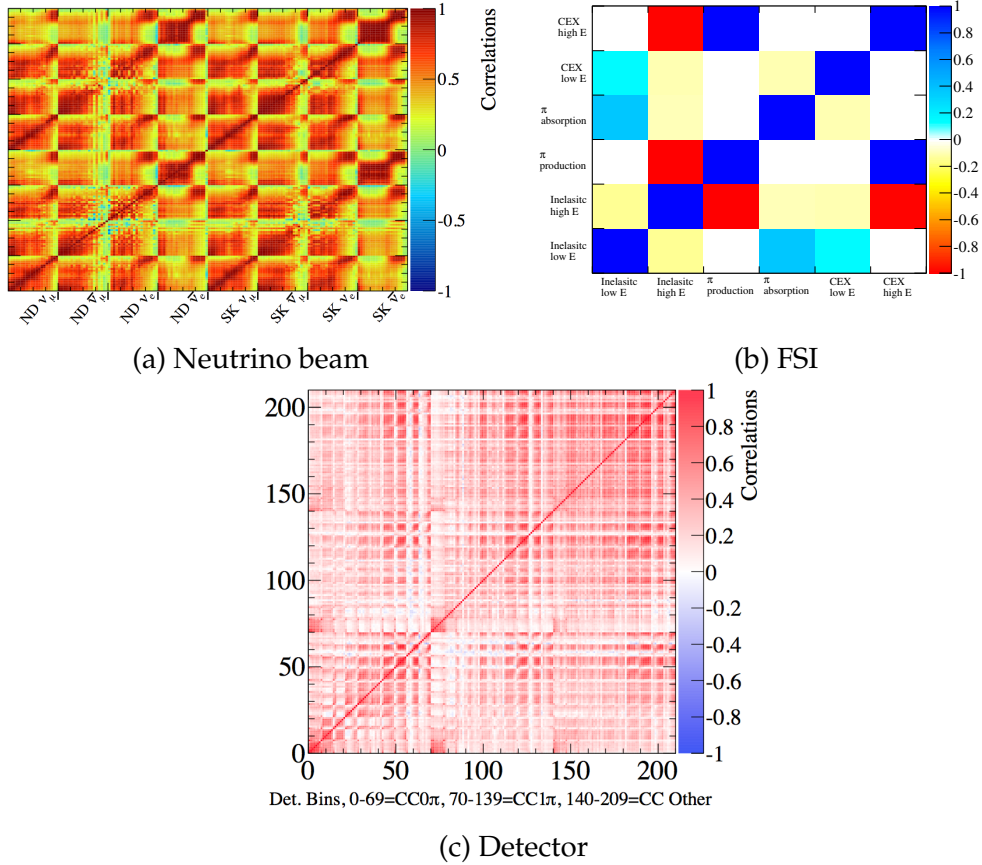


Figure 3.11: Correlations of parameters used in the ND280 fit.

parameters¹⁴, a spline is created for each MC event which describes the non-linear response to that parameter, and the event weight is taken as the spline evaluated at that value of the parameter. For normalisation parameters, the event is simply weighted by the value of the parameter. The errors shown in Tab. 3.1 are used and the covariance of M_A^{RES} , CC1 π $E_\nu < 2.5$ GeV normalisation, and NC1 π^0 normalisation parameters is included.

FSI errors are calculated using the method described in Sec. 3.2.4, and the covariance matrix is shown in Fig. 3.11b.

The fit treats the uncertainties in the ND280 selections as nuisance parameters, handled in a 210-bin covariance matrix (3 samples \times 10 p_μ bins \times 7 $\cos \theta_\mu$ bins).

¹⁴The shape parameters are M_A^{QE} , p_F , E_B , SF, M_A^{RES} , π -less Δ decay, CC other shape.

Coarser binning is used in this covariance matrix compared with the data to reduce the number of parameters in the fit (and therefore computation time), and flux and cross-section errors are usually dominant. All systematics from Sec. 3.3.3 are taken into account, and the covariance matrix is shown in Fig. 3.11c.

The best-fit spectra for each sample are shown in Fig. 3.12 with the data, and the expectation before the ND280 fit, as a function of $\cos \theta_\mu$. The best-fit spectra for each sample are shown in Figs. 3.13 and 3.14 as a function of p_μ , in slices of $\cos \theta_\mu$, broken down by neutrino MC generator interaction mode. The number of events in each sample is shown in Tab. 3.3. The χ^2 per degree of freedom (*dof*) is 564.9/451 and the p-value is 0.66 (see Sec. 4.3.4). The total error from groups of parameters on the number of events at ND280 is shown in Tab. 3.4.

	CC inclusive	CC-0- π	CC-1- π^+	CC-other
Prediction (pre-fit)	29476	19980	5037	4729
Prediction (post-fit)	25581	17352	4110	4119
Data	25589	17369	4047	4173

Table 3.3: Number of events in the ND280 ν_μ CC samples, for data, and prediction both before and after the ND280 fit.

	CC inclusive	CC-0- π	CC-1- π^+	CC-other
Detector	3.3%	2.4%	4.5%	7.3%
Flux	9.7%	9.9%	9.7%	11.6%
Cross section	14.4%	17.7%	16.2%	10.4%
FSI	0.3%	1.0%	3.1%	2.6%
Total	17.7%	20.4%	19.7%	17.4%

Table 3.4: Error on the number of events in the ND280 ν_μ CC samples from groups of systematic parameters.

The ND280-constrained flux and cross-section errors that are used by the ν_μ disappearance oscillation analysis of Chap. 4 are shown in Tab. 3.5. In this table, the nominal values are the best-fit values from the ND280 fit and the error is taken from the square rooting the diagonal of the covariance matrix. The correlation matrix is shown in Fig. 3.15 and is the inverse of the full HESSE error

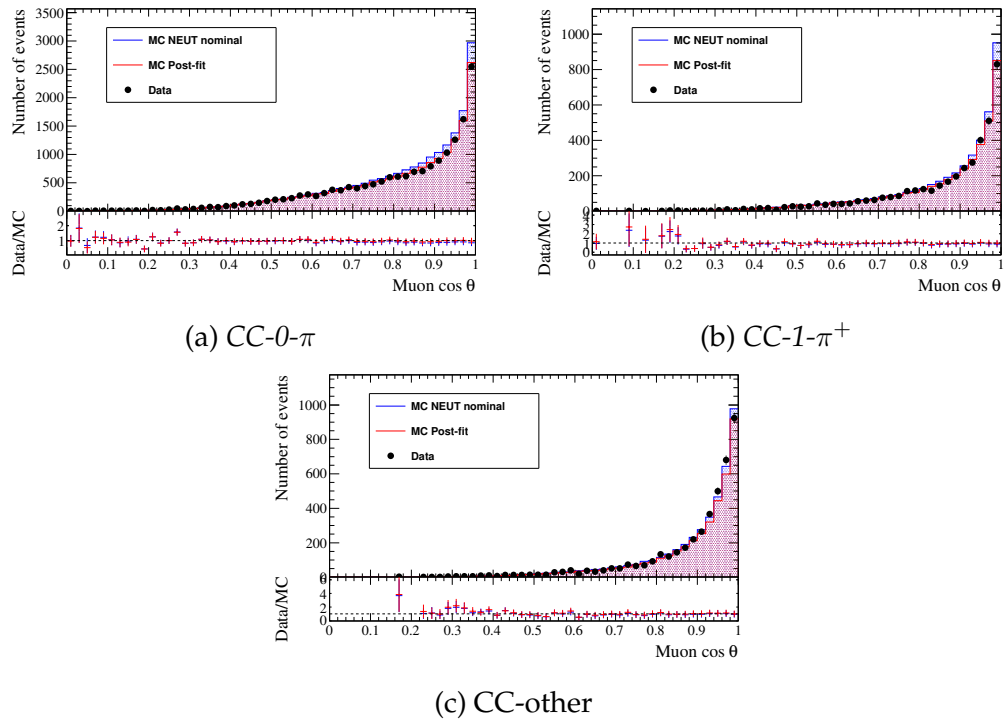


Figure 3.12: The best-fit spectra and data, as a function of $\cos \theta_\mu$. The MC prediction is shown before and after the ND280 fit. Figure taken from [164].

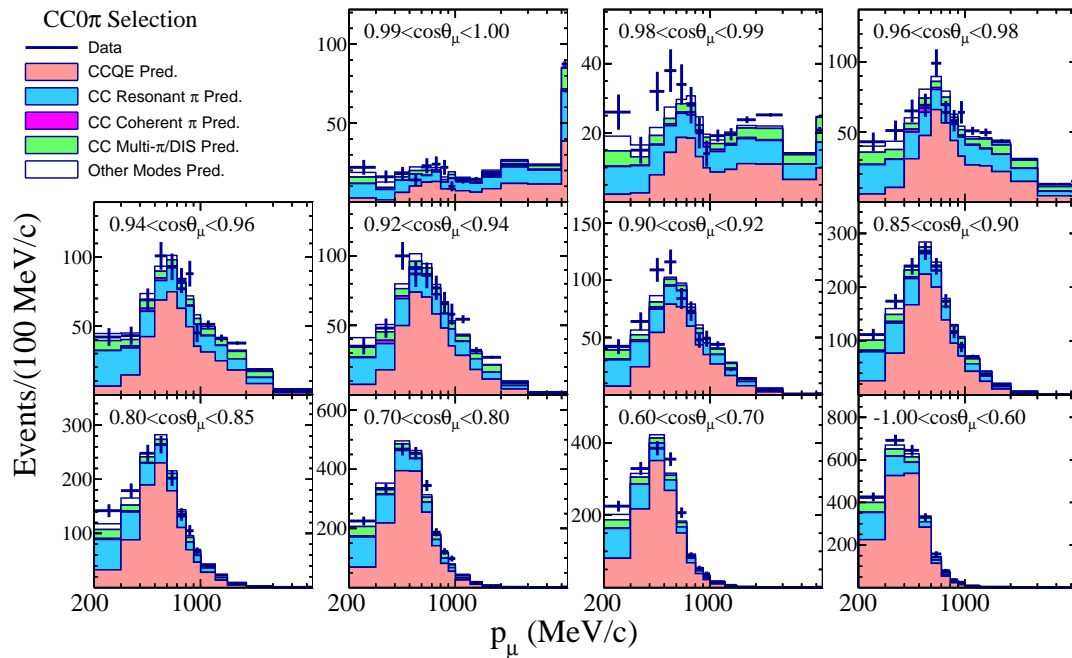


Figure 3.13: The best-fit spectra and data, as a function of p_μ , for the CC-0- π sample. Histograms are in slides of muon angle, and the highest momentum bin includes overflow events and is not normalised by the bin width. Figure taken from [164].

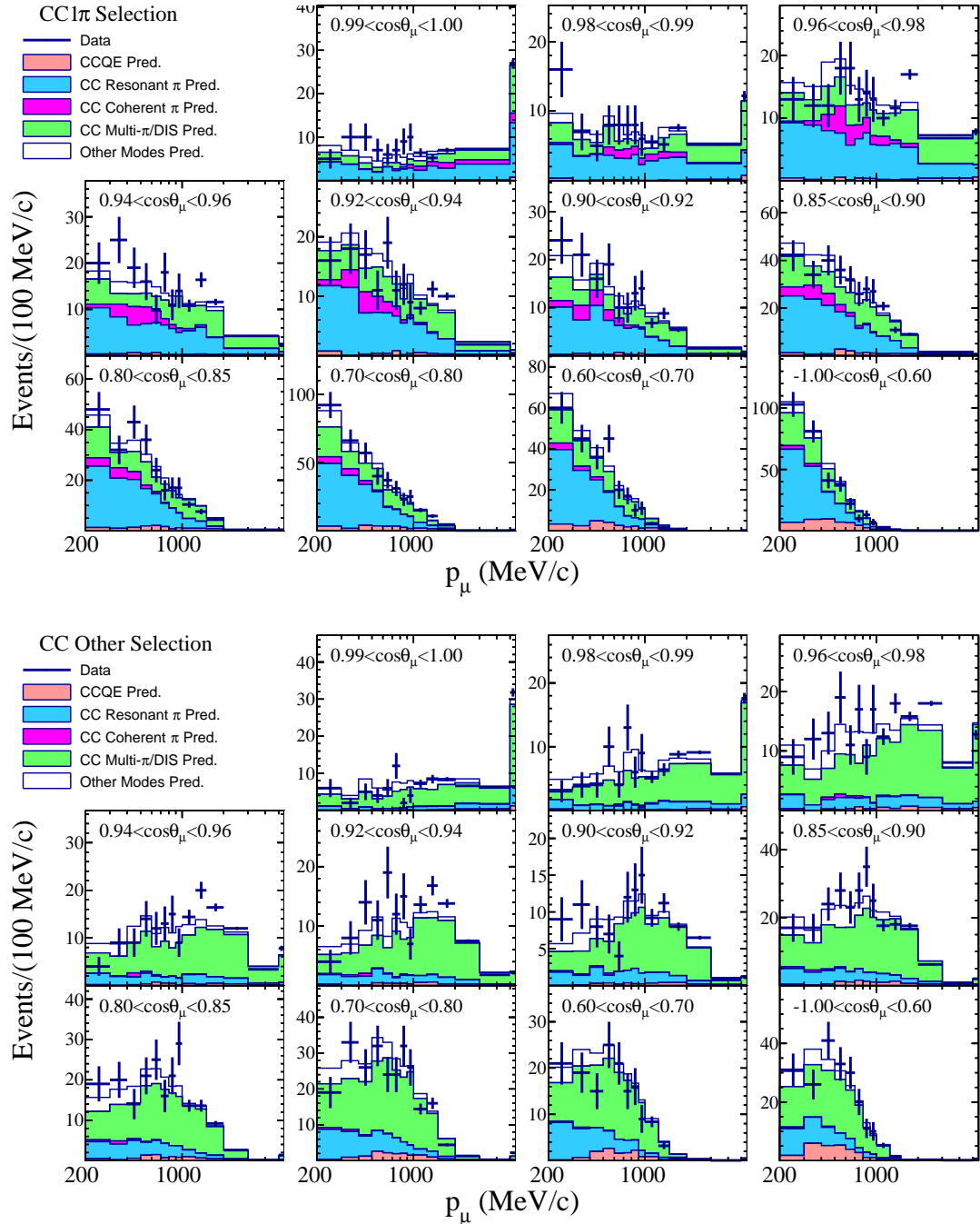


Figure 3.14: The best-fit spectra and data, as a function of p_μ , for the CC-1- π^+ (top) and CC-other (bottom) samples. Histograms are in slides of muon angle, and the highest momentum bin includes overflow events and is not normalised by the bin width. Figures taken from [164].

matrix at the best-fit point, with the rows and columns for parameters that are not constrained by ND280 for SK deleted (e.g. ND280 flux parameters, FSI and nuclear model parameters, etc.).

Name	Description	Best-fit value	Error before / after fit
$f_{0;t}^{ND280}$	ν_μ flux normalisation, $E_\nu = 0.0\text{-}0.4$ GeV	1.029	0.121 / 0.085
$f_{1;t}^{ND280}$	ν_μ flux normalisation, $E_\nu = 0.4\text{-}0.5$ GeV	1.022	0.130 / 0.088
$f_{2;t}^{ND280}$	ν_μ flux normalisation, $E_\nu = 0.5\text{-}0.6$ GeV	0.995	0.122 / 0.080
$f_{3;t}^{ND280}$	ν_μ flux normalisation, $E_\nu = 0.6\text{-}0.7$ GeV	0.966	0.115 / 0.076
$f_{4;t}^{ND280}$	ν_μ flux normalisation, $E_\nu = 0.7\text{-}1.0$ GeV	0.934	0.129 / 0.085
$f_{5;t}^{ND280}$	ν_μ flux normalisation, $E_\nu = 1.0\text{-}1.5$ GeV	0.992	0.116 / 0.077
$f_{6;t}^{ND280}$	ν_μ flux normalisation, $E_\nu = 1.5\text{-}2.5$ GeV	1.037	0.100 / 0.068
$f_{7;t}^{ND280}$	ν_μ flux normalisation, $E_\nu = 2.5\text{-}3.5$ GeV	1.054	0.095 / 0.065
$f_{8;t}^{ND280}$	ν_μ flux normalisation, $E_\nu = 3.5\text{-}5.0$ GeV	1.035	0.112 / 0.072
$f_{9;t}^{ND280}$	ν_μ flux normalisation, $E_\nu = 5.0\text{-}7.0$ GeV	0.975	0.152 / 0.073
$f_{10;t}^{ND280}$	ν_μ flux normalisation, $E_\nu = 7.0\text{-}30.0$ GeV	0.943	0.187 / 0.082
$f_{11;t}^{ND280}$	$\bar{\nu}_\mu$ flux normalisation, $E_\nu = 0.0\text{-}0.7$ GeV	1.030	0.133 / 0.102
$f_{12;t}^{ND280}$	$\bar{\nu}_\mu$ flux normalisation, $E_\nu = 0.7\text{-}1.0$ GeV	1.011	0.117 / 0.090
$f_{13;t}^{ND280}$	$\bar{\nu}_\mu$ flux normalisation, $E_\nu = 1.0\text{-}1.5$ GeV	1.007	0.119 / 0.094
$f_{14;t}^{ND280}$	$\bar{\nu}_\mu$ flux normalisation, $E_\nu = 1.5\text{-}2.5$ GeV	1.026	0.123 / 0.104
$f_{15;t}^{ND280}$	$\bar{\nu}_\mu$ flux normalisation, $E_\nu = 2.5\text{-}30.0$ GeV	1.008	0.122 / 0.107
$f_{16;t,r}^{ND280}$	$x_{\text{MAQE}} = M_A^{\text{QE}} \text{ (tweaked)} / M_A^{\text{QE}} \text{ (nominal)}$	1.025	0.372 / 0.059
$f_{17;t,r}^{ND280}$	$x_{\text{MARES}} = M_A^{\text{RES}} \text{ (tweaked)} / M_A^{\text{RES}} \text{ (nominal)}$	0.797	0.183 / 0.056
$f_{18;t}^{ND280}$	CCQE normalisation, $E_\nu = 0.0\text{-}1.5$ GeV	0.966	0.110 / 0.076
$f_{19;t}^{ND280}$	CCQE normalisation, $E_\nu = 1.5\text{-}3.5$ GeV	0.931	0.300 / 0.103
$f_{20;t}^{ND280}$	CCQE normalisation, $E_\nu = 3.5\text{-}30.0$ GeV	0.852	0.300 / 0.114
$f_{21;t}^{ND280}$	CC1 π normalisation, $E_\nu = 0.0\text{-}2.5$ GeV	1.265	0.317 / 0.163
$f_{22;t}^{ND280}$	CC1 π normalisation, $E_\nu = 2.5\text{-}30.0$ GeV	1.122	0.400 / 0.172

Table 3.5: Summary of the ND280-constrained errors used in the ν_μ disappearance oscillation fit (see Chap. 4). **The name of each parameter corresponds to the convention used in Chap. 4.**

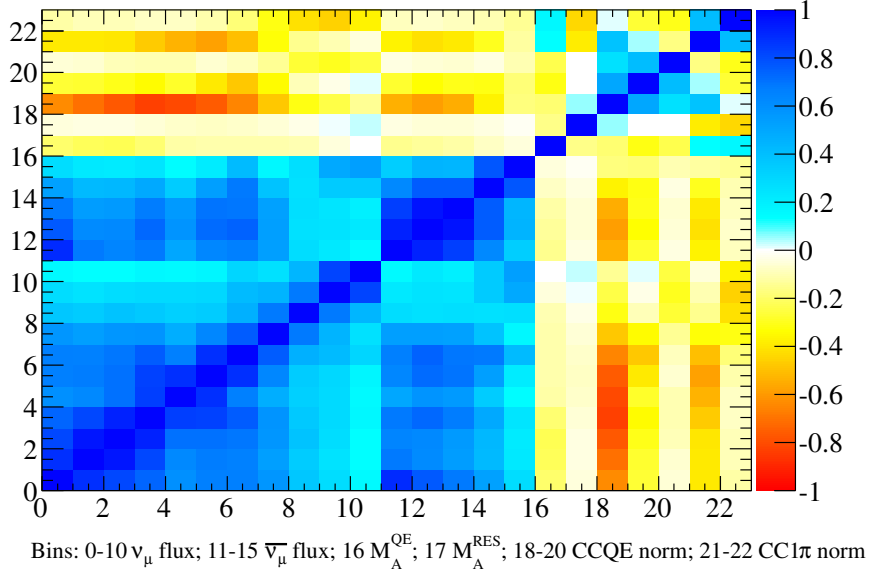


Figure 3.15: Correlations of ND280-constrained flux and cross-section parameters used in the ν_μ disappearance oscillation fit.

3.4 Super-Kamiokande measurements of 1 μ -like ring events

Neutrino energy is determined assuming the event was quasi-elastic, [the target nucleon was at rest](#), and by invoking energy-momentum conservation:

$$E_{\text{reco}} = \frac{m_p^2 c^4 - (m_n c^2 - E_b)^2 - m_\mu^2 c^4 + 2(m_n c^2 - E_b)E_\mu}{2(m_n c^2 - E_b - E_\mu + p_\mu c \cos \theta_\mu)}, \quad (3.9)$$

where p_μ , E_μ , $\cos \theta_\mu$ are the reconstructed muon momentum, energy, and the angle with respect to the beam direction, respectively, m_p , m_n , and m_μ are the masses of the proton, neutron, and muon, respectively, and $E_b = 27$ MeV is the average binding energy of a nucleon in ^{16}O . [Therefore, a high purity sample of \$\nu_\mu + \bar{\nu}_\mu\$ CCQE events is required](#), in order to determine the neutrino energy accurately. In Sec. 3.4.1 a pre-selection of physics events is described. The cuts for this 1 μ -like ring sample are shown in Sec. 3.4.2, and the associated systematics

discussed in Sec. 3.4.3.

3.4.1 Fully-contained and fully-contained fiducial-volume selections

The fully-contained (FC) and FCFV samples are high-statistics selections used in calibration studies. The FC selection is performed using the cuts:

1. **Data quality cuts.** In the whole of the T2K Run 1+2+3+4 dataset, SK records good beam spills with an efficiency of 99.07%. The largest inefficiencies are due to pre-activity (the presence of a trigger in the $100\mu\text{s}$ preceding a beam spill), and SK data acquisition (DAQ) downtime.
2. **Timing cut.** The quantity ΔT_0 is defined as the timing of the event relative to the leading edge of the spill, communicated via GPS, accounting for the travel time of the neutrino from production to detection, including the photon propagation time in the detector. A timing cut of $-2\mu\text{s} < \Delta T_0 < 10\mu\text{s}$ is used to cut backgrounds from other neutrino sources; there are 0.0085 such events expected in the T2K Run 1+2+3+4 dataset.
3. **Flasher cut.** The event should pass cuts designed to reject flasher events.
4. **Containment cut.** The number of PMT hits in the highest-charge OD cluster is less than or equal to 15, in order to reject events in which the particles are not fully-contained within the ID (e.g. events which occur in the rock surrounding SK, pass through the OD, and stop within the ID).

Events which fail the containment cut are classified as OD events. These events are not used in this analysis, but have the potential to increase sensitivity to oscillation parameters due to their high statistics.

The timing distribution of FC events is shown in Fig. 3.16 for T2K Runs 1+2+3 and 4 separately, and clearly shows the eight bunch structure of the beam spill.

The RMS value of the residual time distribution between each FC event and the closest bunch centre is 29 ns.

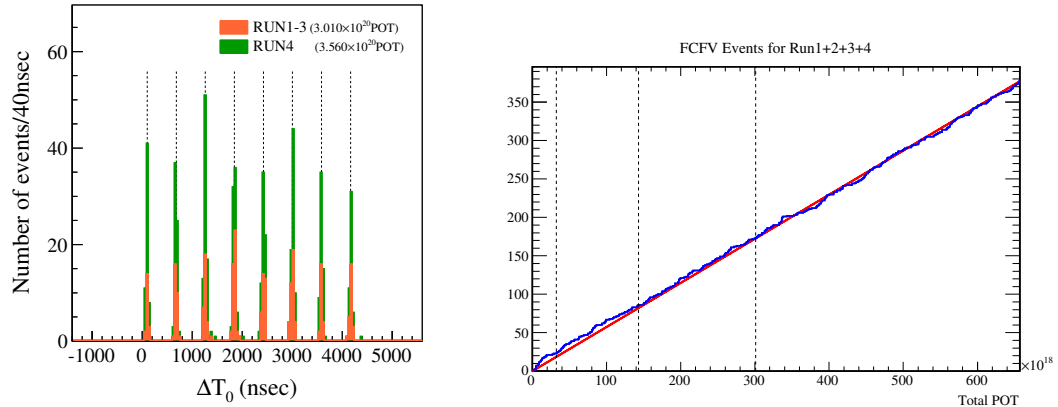


Figure 3.16: ΔT_0 distribution of FC events observed during T2K Runs 1+2+3 and 4. The eight dotted lines represent the 581 ns-interval bunch centre positions fitted to the observed FC event timing. Figure taken from [168].

Figure 3.17: The cumulative number of observed FCFV events in T2K Run 1+2+3+4 as a function of POT. The data (blue) is shown with a hypothesis of constant event rate (red). The dotted lines indicate the boundaries between T2K runs. Figure taken from [168].

The FCFV selection is a subset of the FC selection, using two extra cuts:

5. **Fiducial-volume cut.** The reconstructed vertex should be at least 2 m away from the ID wall.
6. **Visible energy cut.** The visible energy in the event, E_{vis} , defined as the energy of an electron required to produce the observed amount of Cherenkov light, is above 30 MeV.

The cumulative number of FCFV events during T2K Run 1+2+3+4 is shown in Fig. 3.17. The Kolmogorov–Smirnov probability to obtain a larger vertical distance between data the hypothesis of constant event rate (red) due to statistical fluctuations was calculated to be 92.8%.

3.4.2 1 μ -like ring event selection cuts

The 1 μ -like ring event selection is a subset of the FCFV selection, designed to give a pure sample of $\nu_\mu + \bar{\nu}_\mu$ CCQE events. using the extra cuts:

7. **Single ring cut.** There is exactly one reconstructed ring in the event, **in order to reject events with multiple final state mesons and charged leptons** (recall that protons have a Cherenkov threshold of $p_p \geq 1064 \text{ MeV}/c$, and are therefore rarely visible in the T2K neutrino beam). This cut rejects 61.85% of $\nu_\mu + \bar{\nu}_\mu$ CCnonQE events and 71.74% of NC events (Figs. 3.18a and 3.18b). The $\nu_\mu + \bar{\nu}_\mu$ CCQE efficiency is 94.18%.
8. **Muon-like ring cut.** The reconstructed ring is μ -like, **in order to reject events with a final state electron or photon** (e.g. from π^0 decay). This cut rejects 98.93% of $\nu_e + \bar{\nu}_e$ events and 69.73% of NC events (Fig. 3.18c). The $\nu_\mu + \bar{\nu}_\mu$ CCQE efficiency is 98.07%.
9. **Momentum cut.** The reconstructed muon momentum is above $200 \text{ MeV}/c$ (Fig. 3.18d), **where the systematic studies are valid**. The $\nu_\mu + \bar{\nu}_\mu$ CCQE efficiency is 99.78%.
10. **Michel electron cut.** There is at most 1 decay e in the event, **in order to reject events with charged pions below Cherenkov threshold**. This cut rejects 29.41% if $\nu_\mu + \bar{\nu}_\mu$ CCnonQE events (Fig. 3.18e). The $\nu_\mu + \bar{\nu}_\mu$ CCQE efficiency is 98.85%.

The number of events after each cut is shown in Fig. 3.18f for three flavour oscillations with $\sin^2(2\theta_{13}) = 0.10$, $\sin^2(2\theta_{23}) = 1.00$, and $\Delta m_{32}^2 = 2.40 \times 10^{-3} \text{ eV}^2/\text{c}^4$. The purities and efficiencies of the selection under the oscillation hypothesis are shown in Tab. 3.6. Also shown are the purities under the no-oscillation hypothesis. For the T2K Run 1+2+3+4 dataset 120 events pass all cuts.

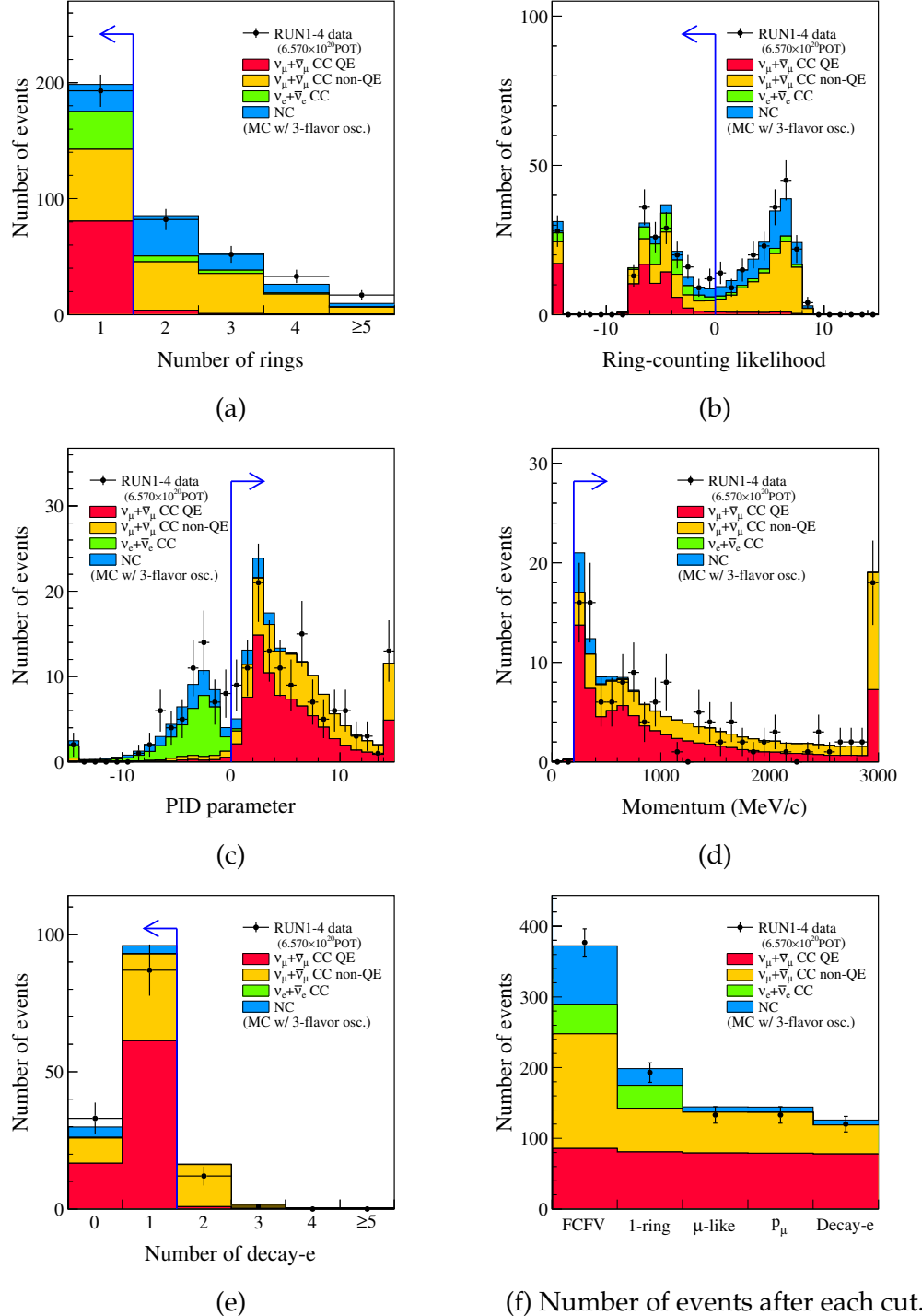


Figure 3.18: Distributions of 1 μ -like ring event selection variables at each selection stage for T2K Run 1+2+3+4 data. Blue arrows indicate the selection criteria. Three flavour oscillation is simulated with $\sin^2(2\theta_{13}) = 0.10$, $\sin^2(2\theta_{23}) = 1.00$, and $\Delta m_{32}^2 = 2.40 \times 10^{-3} \text{ eV}^2/\text{c}^4$. Figures taken from [168].

	Efficiency Oscillations	Purity	Purity No oscillations
MC total	19.2%	-	-
$\nu_\mu + \bar{\nu}_\mu$ CCQE	69.8%	61.9%	81.0%
$\nu_\mu + \bar{\nu}_\mu$ CCnonQE	19.1%	32.4%	17.5%
$\nu_e + \bar{\nu}_e$ CC	0.8%	0.3%	1.5%
NC	2.4%	5.4%	0.02%

Table 3.6: Efficiencies, [relative to the total number of reactions in the SK fiducial volume \(i.e. after cut 5\)](#), and purities of the SK 1μ -like ring event selection for three flavour oscillations with $\sin^2(2\theta_{13}) = 0.10$, $\sin^2(2\theta_{23}) = 1.00$, and $\Delta m_{32}^2 = 2.40 \times 10^{-3} \text{ eV}^2/\text{c}^4$. Also shown are the purities for the no oscillation hypothesis.

3.4.3 Event selection systematics

There are uncertainties in the efficiencies of the containment, flasher, fiducial volume (FV), ring-counting (RC), PID, momentum and Michel-electron cuts described above. An additional uncertainty comes from the SK energy scale. These uncertainties have been evaluated by comparing 1412 days of SK-IV atmospheric data with 500 year equivalent atmospheric neutrino MC, generated with the HONDA flux model 11 solar minimum [169], and are presented in Ref. [170]. Some systematics are broken down into six categories, based on the true reaction mode: $\nu_\mu + \bar{\nu}_\mu$ CCQE in three bins ($E_{\text{reco}} < 0.4 \text{ GeV}$, $0.4 < E_{\text{reco}} < 1.1 \text{ GeV}$, $E_{\text{reco}} > 1.1 \text{ GeV}$) $\nu_\mu + \bar{\nu}_\mu$ CCnonQE, $\nu_e + \bar{\nu}_e$ CC, and NC. The $\nu_e + \bar{\nu}_e$ CC category is assigned a 100% error. Here the methods for calculating the systematics are discussed briefly, and the effect of each systematic is summarised in Tab. 3.7.

Energy scale

Four samples are used to evaluate the energy scale error, to span the momentum range $30 \text{ MeV}/c$ to $6 \text{ GeV}/c$. For low energy, a sample of Michel electrons from stopping cosmic muons is used; the difference in peak positions between data and MC is $-0.7 \pm 0.2\%$. The next sample utilises all 2-ring NC atmospheric events, with a reconstructed π^0 mass between $85 \text{ MeV}/c^2$ and $185 \text{ MeV}/c^2$; the

	ν_μ CCQE	ν_μ CCnonQE	NC
OD activity	$\ll 1.0\%$		
Flasher rejection	1.0%		
FV error	1.0%		
RC efficiency	1.84%, 2.21%, 3.25% with cov. matrix	8.1%	21.8%
PID	0.3%		55%
Momentum uncertainty	$\ll 1.0\%$		
Michel e efficiency	1.0%		
Energy scale	2.4%		

Table 3.7: Summary of the systematic errors for the 1μ -like ring event selection. $\nu_\mu + \bar{\nu}_\mu$ CCQE is split into three E_{reco} bins. The ν_e CC efficiency is 100%.

difference in the mean value of Gaussian fits to data and MC is $0.5 \pm 0.7\%$. The third sample uses cosmic stopping muons in the momentum range $200\text{ MeV}/c$ to $440\text{ MeV}/c$, with momentum reconstructed using the Cherenkov angle, to cross-check the standard photoelectron-based momentum estimate. The ratio of photoelectron-based and Cherenkov-angle-based momentum estimates is taken in bins of momentum, and the data-MC difference ranges from $0.6 \pm 0.3\%$ to $2.4 \pm 0.3\%$. For high energy, a multi-GeV sample of stopping cosmic muons is selected in bins of range, and the ratio of momentum to range is calculated; the difference between data and MC ranges from $0.2 \pm 0.3\%$ to $1.3 \pm 0.3\%$.

The absolute energy scale error is taken as 2.4%, the calculation that deviates most from zero.

Outer detector activity

The OD activity cut error is assigned by comparing data and MC number of OD hit distributions of partially-contained atmospheric neutrino events. There is a 5.9% shift in the peak position, which gives a 1σ error on the cut of 15.00 ± 0.89 hits. This shift corresponds to a $\pm 0.06\%$ shift in the number of T2K FC events, and is negligibly small.

Flasher rejection

Flasher events are rejected by using PMT hit timing and spatial distribution. The average value of the flasher cut variable value is 0.10 higher in data than MC. Applying a 0.10 shift changes the FCFV selection efficiency by 1%, therefore a 1% systematic error is applied.

Fiducial volume error

The FV error for 1-ring events is calculated by comparing the vertex distribution of stopping cosmic muons (split into different momentum and distance from wall bins) between data and MC. The sample is defined as events that enter the ID normal to the wall, 3.1 m from the top/bottom, 5.8 m from the radial wall, only a 1 ring, only 1 decay electron, and the ring is μ -like. Overall agreement is good, and a 1% systematic is assigned.

Ring-counting efficiency

Six atmospheric neutrino control samples are defined to evaluate RC efficiencies, all starting from the FCFV selection:

- ν_μ **CCQE enriched** has exactly 1 Michel electron and the distance between the expected muon stopping point (calculated from the reconstructed momentum of the brightest ring) to the decay electron is less than 80 cm. This sample is split into three bins in E_{vis} , with bin edges at 0.13 GeV and 0.7 GeV.
- ν_μ **CCnonQE enriched** has more than 1 Michel electrons and the distance between the expected muon stopping point to the nearest decay electron is less than 160 cm.

- ν_e CC enriched has exactly 0 Michel electrons, visible energy of at least 100 MeV, the brightest ring is e -like, and the POLFIT invariant mass is less than 105 MeV.
- NC enriched has exactly 0 Michel electrons and is not part of the ν_e CC enriched sample.

All samples can be further subdivided into single- and multi-ring events.

The RC efficiency is calculated using a χ^2 fit in which the efficiency for each of the six control samples and six systematic parameters¹⁵ are varied to achieve the best agreement between data and MC. The systematic parameters are not pulled by more than 1σ away from their default values. Two types of errors are assigned to each mode, the difference between best-fit MC and nominal MC ($\sigma_{\text{best-nom}}$), and the fitting error on the efficiency parameters (σ_{fit}). For the ν_μ CCQE enriched control sample, a covariance between energy bin is assigned assuming 100% correlation for $\sigma_{\text{best-nom}}$ and no correlation for σ_{fit} ¹⁶. No correlations are assigned between ν_μ CCQE, ν_μ CCnonQE, and NC parameters¹⁷. The total systematic is then the sum of the covariance matrices for ν_μ CCQE, or the sum in quadrature for other samples.

For the ν_μ CCQE enriched control sample, a conversion from E_{vis} to E_{reco} is required¹⁸. A conversion matrix, \mathbf{A} , is calculated from MC simulation, and is used to transform the visible energy RC error matrix \mathbf{V} to the reconstructed energy RC error matrix $\mathbf{R} = \mathbf{A}\mathbf{V}\mathbf{A}^T$.

¹⁵Three flux errors (normalisation below and above 1 GeV, ν_e/ν_μ flux ratio), and three cross-section errors (CCQE energy dependent, CCnonQE/CCQE ratio, NC/CCQE ratio).

¹⁶The correlations from the fit are small and are neglected.

¹⁷The choice of 0% or 100% correlation has no effect on the oscillation analysis described in Chap. 4.

¹⁸The ν_μ CCQE sample is split into three bins in E_{reco} , with bin edges at 0.4 GeV and 1.1 GeV.

Particle identification uncertainty

Looking at the difference in the PID probability to be a μ -like ring between data and MC for the stopping cosmic muon sample described above, there is very good agreement, to within 0.3% across all momenta. A second study using atmospheric neutrinos is also performed. Starting with 1-ring events with one decay electron, the followings cuts are applied: the distance between the expected muon stopping point to the decay electron is less than 60 cm, the opening angle between the muon direction and a vector from the muon vertex to decay electron vertex $\cos_{\mu e} > 0.9$, the visible energy is more than 0.1 GeV, and the reconstructed muon momentum is less than $1.2 \text{ GeV}/c$. The sample is 98.6% pure in ν_μ CC interactions. The PID likelihood is then calculated, and the misidentification rate is $0.55 \pm 0.38\%$ (data) and 0.19% (MC), and agree well with data and the cosmic muon study. Therefore a 0.3% fully correlated error is assigned for all $\nu_\mu + \bar{\nu}_\mu$ CC events.

For the PID uncertainty for NC events, an enriched sample of NC1 π^\pm and NC1 p events is selected from atmospheric neutrinos. The sample is created by searching for FCFV events with 1-ring, 0 Michel electrons, $p_\mu > 200 \text{ MeV}/c$, and visible energy $< 100 \text{ MeV}$. The efficiency for selecting NC1 π^\pm and NC1 p is 68.5% and 94.0% respectively, and the sample is 9.0% and 3.8% pure in each. The main backgrounds are low energy ν_μ and ν_e events, ν_μ events with Michel electrons, and multi-pion events. The sample is split into μ -like and e -like events, and a χ^2 fit is performed, to determine the NC1 π^\pm and NC1 p efficiencies. The same six systematic parameters as used for the RC are included in the fit. The result of the fit is a constraint on the NC1 π^\pm efficiency $0.148 \leq \epsilon_{1\pi} \leq 1.000$, and no constraint on the NC1 p efficiency $0.0 \leq \epsilon_{1p} \leq 1.0$. The systematic is calculated by applying the upper and lower efficiency limits to the μ -like NC sample, and observing the change on the total number of NC events in that sample, relative to the nominal

efficiency. Conservatively, the largest change (upper or lower limit) is taken as the systematic for each efficiency, and these are added in quadrature with the nominal efficiency difference between the T2K and NC-enriched samples. The total NC PID error assigned is 55%.

Momentum uncertainty

At the selection threshold of $200\text{ MeV}/c$, the energy scale error of 2.4% induces a $4.8\text{ MeV}/c$ uncertainty in the momentum. This corresponds to a less than 0.1% change in the number of selected events, and is negligible.

Michel electron efficiency

Stopping cosmic muons, with $p_\mu < 1330\text{ MeV}/c$ and distance from reconstructed stopping position to ID wall, are used to evaluate this uncertainty. In MC, the expected μ^+/μ ratio (1.37) and the probability of μ capture on a ^{16}O nucleus are taken into account. The overall tagging efficiencies are $88.4 \pm 0.2\%$ (data) and $89.1 \pm 0.2\%$ (MC), and the difference is taken as the 1% uncertainty.

3.4.4 Combined SK detector and pion interaction modelling systematics

The SK detector efficiency and energy scale errors (Sec. 3.4.3) are combined with the errors due to pion interaction modelling. final state interactions (FSI) errors are calculated using the method described in Sec. 3.2.4. secondary interactions (SI) errors are calculated in an analogous way, using the difference between an older SKDETSIM model¹⁹ and the nominal MC (NEUT cascade combined with the old model).

¹⁹The older model uses custom code [100] for $|\mathbf{p}_\pi| < 0.5\text{ GeV}/c$, and a GCALOR physics package elsewhere, due to its good agreement with data at $|\mathbf{p}_\pi| \sim 1\text{ GeV}/c$ [171].

The combined errors that are used by the ν_μ disappearance oscillation analysis of Chap. 4 are shown in Tab. 3.8. In this table the error is taken from the square rooting the diagonal of the covariance matrix. The correlation matrix is shown in Fig. 3.19. A 2.4% energy scale systematic is also applied.

Name	Description	Error
$f_{0;r}^{SK+FSI}$	$\nu_\mu + \bar{\nu}_\mu$ CCQE, $E_{\text{reco}} < 0.4$ GeV	2.5%
$f_{1;r}^{SK+FSI}$	$\nu_\mu + \bar{\nu}_\mu$ CCQE, $0.4 \text{ GeV} < E_{\text{reco}} < 1.1 \text{ GeV}$	2.8%
$f_{2;r}^{SK+FSI}$	$\nu_\mu + \bar{\nu}_\mu$ CCQE, $E_{\text{reco}} > 1.1$ GeV	3.7%
$f_{3;r}^{SK+FSI}$	$\nu_\mu + \bar{\nu}_\mu$ CCnonQE	11.9%
$f_{4;r}^{SK+FSI}$	ν_e CC	100.0%
$f_{5;r}^{SK+FSI}$	NC	60.0%
$f_{E;r}^{SK}$	Energy scale	2.4%

Table 3.8: Summary of the combined SK detector, FSI and SI errors used in the ν_μ disappearance oscillation fit (see Chap. 4). [The energy scale error is also shown.](#) [The name of each parameter corresponds to the convention used in Chap. 4.](#)

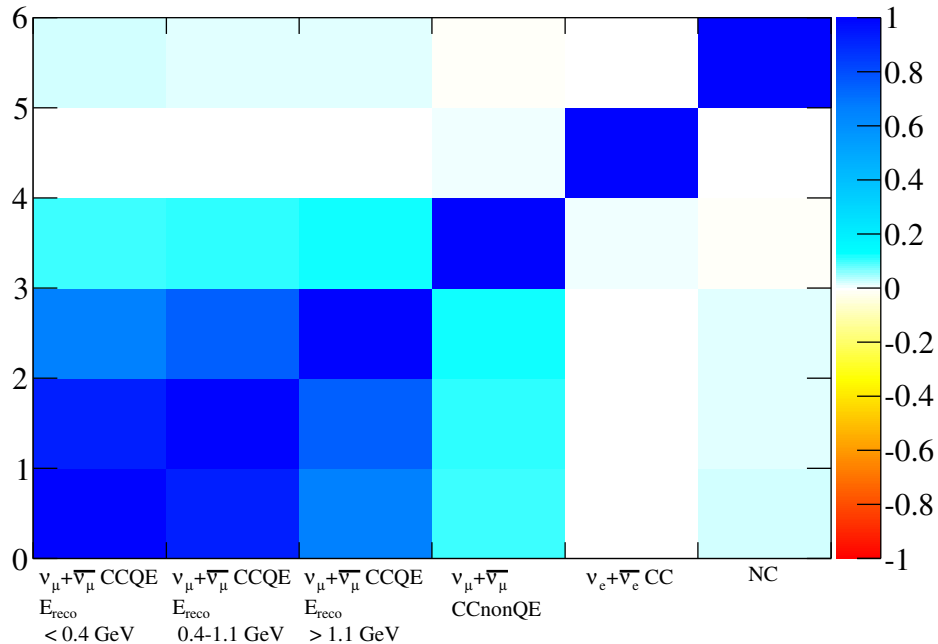


Figure 3.19: Correlations of the combined SK detector, FSI and SI parameters used in the ν_μ disappearance oscillation fit.

Chapter 4

ν_μ disappearance analysis

In this chapter, an analysis is presented to determine the oscillation parameters driving the disappearance of the T2K ν_μ flux over a baseline of around 295 km. This is achieved by measuring θ_{23} and $|\Delta m_{32}^2|$ (in the normal mass hierarchy) or $|\Delta m_{31}^2|$ (in the inverted mass hierarchy) using the rate and reconstructed energy (E_{reco}) spectrum of 1 μ -like ring events at SK. [Fits are performed using the likelihood-ratio method, including 45 systematic parameters, accounting for the known uncertainties in the other oscillation parameters, the cross-section parameters uncorrelated with ND280 \(see Tab. 3.1\), the flux and cross-section parameters correlated with ND280 \(see Tab. 3.5\), and the combined SK detector + FSI + SI uncertainties \(see Tab. 3.8\).](#) The full three-flavour oscillation formulae (e.g. Eq. 1.44), with the addition of matter effects, is used. The results are presented with confidence regions calculated using the Feldman-Cousins method [172] for two-dimensional contours, and a new extension to the Feldman-Cousins method for one-dimensional intervals. The T2K results are compared to other recent experimental results from MINOS (a combination of neutrino beam and atmospheric neutrinos) and SK (atmospheric neutrinos), which have both hinted at a non-maximal value of $\sin^2 \theta_{23}$.

In Sec. 4.1, the 1 μ -like ring E_{reco} spectrum prediction is described. Systematic parameters and their effects are introduced in Sec. 4.2. The fitting procedure and fitter validation is described in Sec. 4.3. The results of the fit on the T2K Run 1+2+3+4 dataset is shown in Sec. 4.4, and the results are discussed in Sec. 4.5.

4.1 SK 1 μ -like ring spectrum prediction

In this section, the calculation of the expected 1 μ -like ring event rate and spectrum, including tunings from both NA61/SHINE and ND280 data, is described. The methodology is discussed in Sec. 4.1.1. The construction of the reconstructed energy spectrum based on the nominal T2K MC is presented in Sec. 4.1.2. The spectrum tuning based on NA61/SHINE hadroproduction data and measurements at ND280 is described in Secs. 4.1.3 and 4.1.4 respectively. The numerical calculation of the effect of three active flavour oscillation in constant-density matter is presented in Sec. 4.1.5. Finally, the Run 1+2+3+4 predictions for various scenarios are presented in Sec. 4.1.6.

4.1.1 Methodology

In this analysis, the oscillation parameters are determined by fitting the reconstructed energy spectrum of 1 μ -like ring events observed at SK with the predicted spectrum. The predicted number of 1 μ -like ring events, $N_{SK;r}$, in the r^{th} reconstructed energy bin is computed as follows:

$$N_{SK;r} = \sum_m \sum_t \sum_{r'} P_{m;t} \cdot T_{r;r';f_{E;r}^{SK}} \cdot S_{m;t;r';f} \cdot N_{SK;m;r;t}^{MC}. \quad (4.1)$$

In Eq. 4.1, $N_{SK;m;r;t}^{MC}$ is the input SK MC template containing the number of events in the 1 μ -like ring MC sample with true reaction mode m in the true

energy bin t and the reconstructed energy bin r . The construction of the nominal MC templates is discussed in Sec. 4.1.2.

In Eq. 4.1, $S_{m;t;r;\vec{f}}$ is an overall, multiplicative, systematic error factor depending on the reaction mode m , the true energy bin t , the reconstructed energy bin r and a vector of nuisance (systematic) parameters \vec{f} . This parameter controls both the tuning of the nominal MC templates, and deviations from the tuned templates of the systematic parameters. Both flux-tuning weights based on NA61/SHINE hadron-production data (see Sec. 4.1.3) and flux and cross-section tuning weights based on ND280 data (see Sec. 4.1.4) are applied to the nominal MC templates. A complete description of the nuisance parameters considered in this analysis is given in Sec. 4.2.

In Eq. 4.1, $T_{r;r';f_{E;r}^{SK}}$ is a transfer function describing the migration of events between the reconstructed energy bins r and r' due to uncertainty in the SK reconstructed energy scale, expressed here in terms of the nuisance parameter $f_{E;r}^{SK}$.

In Eq. 4.1, $P_{m;t}$ is the physics being measured in this analysis. It is the full three-flavour oscillation probability (e.g. Eq. 1.44), with the addition of matter effects, applied to the true energy bin t of the SK MC template which corresponds to mode m . The application of $P_{m;t}$ is discussed in Sec. 4.1.5.

4.1.2 Construction of nominal SK Monte Carlo templates

The nominal SK 1 μ -like ring MC templates $N_{SK;m;r;t}^{MC}$ are constructed by applying the 1 μ -like ring selection cuts to the official SK MC samples. The cuts are listed in Sec. 3.4.2. In this section, the construction of the MC templates is discussed, starting with the MC samples used, then moving on to the normalisation and binning (in true reaction mode, m , binning, true energy, t , binning, and reconstructed energy, r , binning).

Input MC samples

This analysis uses the official SK MC samples generated using the JNUBEAM flux¹. Five MC samples were generated. Four of the samples (ν_μ , $\bar{\nu}_\mu$, ν_e and $\bar{\nu}_e$) were generated using the nominal JNUBEAM flux without oscillations. A fifth sample of ν_e interactions were also generated with the ν_μ flux, without oscillations, corresponding to a $\nu_\mu \rightarrow \nu_e$ oscillation probability of 100%. This fifth sample will be denoted the “oscillated ν_e ” sample. For completeness, an “oscillated ν_μ ” sample is also generated corresponding to $\nu_e \rightarrow \nu_\mu$ ². Since a separate official oscillated $\nu_e \rightarrow \nu_\mu$ SK sample is not available, it is emulated by reweighting the ν_μ SK MC sample with the ν_e flux (the oscillated $\nu_e \rightarrow \nu_\mu$ are not statistically independent of the ν_μ templates). All samples were generated including the neutrino flux estimates up to 30 GeV. The flux histograms used for neutrino event generation had 50 MeV bins.

Normalisation of MC samples

The normalisation (integrated exposure in terms of POT) of each event sample is calculated from the number of events with an MC truth interaction vertex within the 22.5 kt fiducial volume.

$$N = \int dS dIdE \cdot \frac{d^3\Phi_{SK}}{dS dIdE_\nu} \cdot \sigma_{H_2O} \cdot \frac{N_A}{A} \cdot \rho \cdot L, \quad (4.2)$$

where $d^3\Phi_{SK}/dS dIdE$ is the number of flux particles for the given neutrino species per neutrino energy bin dE_ν , per unit area dS and per POT, σ_{H_2O} is the total interaction cross section in water for the given neutrino species, I is the beam intensity in terms of POT, N_A is Avogadro’s number, A is the mass

¹SK MC version 13a, generated with JNUBEAM 11a flux, is used.

² $\bar{\nu}_\mu \rightarrow \bar{\nu}_e$ and $\bar{\nu}_e \rightarrow \bar{\nu}_\mu$ samples are not used because their effects on the 1 μ -like ring spectrum are negligible.

Sample	Number of events /22.5 kt fiducial / 10^{21} POT	Number of events in FV	POT normalisation
ν_μ	1418.68	634998	4.47598×10^{23}
$\bar{\nu}_\mu$	48.6039	319640	6.57643×10^{24}
ν_e	28.312	633715	2.23833×10^{25}
$\bar{\nu}_e$	2.98885	319689	1.06961×10^{26}
Osc. $\nu_\mu \rightarrow \nu_e$	1490.15	320252	2.14913×10^{23}

Table 4.1: Statistics and normalisation of input SK MC samples.

number for water, ρ is the water density and L is the neutrino path length in the water volume. The results of this calculation are shown in Tab. 4.1 for the five SK MC samples along with the numbers of events within the 22.5 kt fiducial volume and the derived POT normalisation of each sample in terms of POT. The derived POT normalisation of each sample is shown in Tab. 4.1. After being generated from an MC sample corresponding to a calculated integrated beam exposure I , each MC template is normalised to the integrated beam exposure of the Run 1+2+3+4 dataset (6.57×10^{20} POT) by scaling the bin contents of the template with $6.57 \times 10^{20} / I$.

List of MC templates

For each SK MC sample, a number of different MC templates is constructed corresponding to different true reaction modes. The template granularity depends on the type of oscillation analysis and the specific systematic parameters considered in the analysis. This analysis uses 32 MC templates.

For each of the ν_μ , $\bar{\nu}_\mu$, ν_e , and $\bar{\nu}_e$ samples there are 6 templates:

- CCQE;
- CC single π resonant production;
- CC coherent π production;
- CC other;
- NC single π^\pm resonant production;

- NC other.

For the oscillated $\nu_\mu \rightarrow \nu_e$ and oscillated $\nu_e \rightarrow \nu_\mu$ samples there are 4 templates each:

- CCQE;
- CC single π resonant production;
- CC coherent π production;
- CC other.

Binning of MC templates

Each of the 32 MC templates has 6132 2-dimensional bins (84 true energy bins \times 73 reconstructed energy bins). The 84 true energy bins are arranged as follows:

- 6 50-MeV bins from 0.0–0.3 GeV;
- 28 25-MeV bins from 0.3–1.0 GeV;
- 40 50-MeV bins from 1–3 GeV;
- 5 100-MeV bin from 3.0–3.5 GeV;
- 1 bin from 3.5–4.0 GeV;
- 1 bin from 4–5 GeV;
- 1 bin from 5–7 GeV;
- 1 bin from 7–10 GeV;
- 1 bin from 10–30 GeV.

The 73 reconstructed energy bins are the following:

- 60 50-MeV bins from 0–3 GeV;
- 4 250-MeV bins from 3–4 GeV;
- 4 500-MeV bins from 4–6 GeV;
- 4 1000-MeV bins from 6–10 GeV;
- 1 bin from 10–30 GeV³.

³The 10–30 GeV bin includes events with reconstructed energy > 30 GeV.

The same reconstructed neutrino energy binning is used for the fit of the 1 μ -like ring reconstructed energy spectrum.

It is too CPU intensive to run the fits required for the Feldman-Cousins method (see Sec. 4.3.7) with an infinite number of bins (or unbinned), therefore the binning was optimised, while retaining accuracy in the important regions. For example, the oscillation probability is quickly varying in the oscillation dip region, therefore many bins are required in this location.

4.1.3 Flux tuning based on NA61/SHINE data

In this analysis, the nominal MC templates are reweighted to a flux tuned on NA61/SHINE hadron production measurements, as described in Sec. 3.1.1. The weights are calculated as a function of E_{true} , in bins of 50 MeV, for each beam neutrino species⁴ separately. The reweighted MC templates are denoted the *NA61-tuned* MC templates in this document. The effect of this NA61 tune on the predicted reconstructed energy spectrum of 1 μ -like ring events is discussed in Sec. 4.1.6 (see Figs. 4.3 and 4.4, and Tabs. 4.3 and 4.4).

4.1.4 Flux and cross-section tuning based on ND280 data

This analysis uses the ND280-fit flux and cross-section parameter tuning described in Sec. 3.3.4 to reweight the NA61-tuned MC templates. The MC templates obtained after this second reweighting will be denoted the *ND280-tuned* MC templates in this document.

A list of ND280-fit parameters and their best-fit values is shown in Tab. 3.5. The tuning is applied to the relevant neutrino mode (see Tab. 4.5) in the relevant E_{true} range, and, in the case of M_A^{QE} and M_A^{RES} , involves E_{true} and E_{reco}

⁴The oscillated $\nu_\mu \rightarrow \nu_e$ sample is tuned using the ν_μ NA61-tuning, and the oscillated $\nu_e \rightarrow \nu_\mu$ sample is tuned using the ν_e NA61-tuning.

dependent splines.

The effect of the ND280-tune on the predicted reconstructed energy spectrum of 1 μ -like ring events is discussed in Sec. 4.1.6 (see Figs. 4.3 and 4.4, and Tabs. 4.3 and 4.4).

4.1.5 Effect of three active neutrino flavour oscillations in constant-density matter

Oscillation probabilities are computed in a 3-flavour framework including matter effects in constant-density matter (assuming an Earth crust density of 2.6 g/cm³ [173]).

Oscillations are applied as a function of true energy to 24 MC templates: the CC templates (CCQE, CC1 π , CC coherent and CC other) for all six MC samples ($\nu_\mu, \bar{\nu}_\mu, \nu_e, \bar{\nu}_e$, oscillated $\nu_\mu \rightarrow \nu_e$, and oscillated $\nu_e \rightarrow \nu_\mu$).

The MC templates constructed from the unoscillated MC samples are weighted with the corresponding survival probability: the ν_μ templates are weighted with $P(\nu_\mu \rightarrow \nu_\mu)$; the $\bar{\nu}_\mu$ templates with $P(\bar{\nu}_\mu \rightarrow \bar{\nu}_\mu)$; the ν_e templates with $P(\nu_e \rightarrow \nu_e)$; and the $\bar{\nu}_e$ templates with $P(\bar{\nu}_e \rightarrow \bar{\nu}_e)$. The MC templates made from the oscillated $\nu_\mu \rightarrow \nu_e$ MC sample are weighted with $P(\nu_\mu \rightarrow \nu_e)$ (the sample was generated assuming 100% of ν_μ transform to ν_e), while the MC templates made from the oscillated $\nu_e \rightarrow \nu_\mu$ MC sample are weighted with $P(\nu_e \rightarrow \nu_\mu)$ (the sample was emulated assuming 100% of ν_e transform to ν_μ).

In the standard 3-flavour oscillation framework, oscillations of ν_e and ν_μ can yield ν_τ , while oscillations of $\bar{\nu}_e$ and $\bar{\nu}_\mu$ can yield $\bar{\nu}_\tau$. In this analysis, contributions from ν_τ -CC and $\bar{\nu}_\tau$ -CC are neglected, as their energy threshold is around 3.5 GeV and their effect is negligible. Accordingly, this analysis uses no ν_τ -CC and $\bar{\nu}_\tau$ -CC MC templates (and, in fact, no official ν_τ and $\bar{\nu}_\tau$ SK MC samples are

Parameter	Best-fit	1σ error
Δm_{21}^2	$7.5 \times 10^{-5} \text{ eV}^2/\text{c}^4$	$\sim 2.7\%$
$\sin^2 \theta_{12}$	0.312	$\sim 5.8\%$
$\sin^2 \theta_{13}$	0.0251	$\sim 13.9\%$

Table 4.2: The best-fit values and 1σ range for the measured *non-23-sector* oscillation parameters [31]. δ_{CP} is allowed to float freely in the range $[-\pi, +\pi]$ without penalty.

available).

It should be emphasised here that the ν_μ NC MC templates for a mode m are proxies for the NC MC templates for the mixture of $\nu_e + \nu_\mu + \nu_\tau$ resulting from 3-flavour ν_μ oscillations for that mode m . The same applies to the $\bar{\nu}_\mu$, ν_e and $\bar{\nu}_e$ NC MC templates. These NC MC templates are unchanged under standard 3-flavour oscillations.

Also it should be noted that there are no explicit NC MC templates made from the oscillated ν_e sample. If they were used, the oscillated ν_e (i.e. ν_e coming from ν_μ oscillations) would be double counted since they are already included in the ν_μ NC MC templates. For the same reason, there are no explicit NC MC templates made from the oscillated ν_μ sample.

The same oscillation parameters are used for neutrinos and antineutrinos.

4.1.6 Predictions of MC 1 μ -like ring spectra

In this section, the expected numbers of events and 1 μ -like ring reconstructed energy spectra in SK for various scenarios is presented. Estimates of the effect of the NA61 and ND280 tunings and of assumptions made in the 3-flavour neutrino oscillation framework used in this analysis are also presented. Unless explicitly stated otherwise, the normal mass hierarchy is assumed, $\delta_{CP} = 0$, and the values shown in Tab. 4.2 are used for $\sin^2 \theta_{13}$, $\sin^2 \theta_{12}$ and Δm_{21}^2 . All plots were generated for an integrated exposure of 6.57×10^{20} POT.

The expected number of 1 μ -like ring events is shown in Fig. 4.1 as a function of the oscillation parameters $\sin^2 \theta_{23}$ and $|\Delta m_{32}^2|$. The expected number of events ranges from a minimum of ~ 122 , to more than ~ 146 for oscillation parameter values still within the T2K Run 1+2+3 90% C.L. region [2]. This illustrates the great sensitivity of the T2K ν_μ -disappearance analysis in measuring $\sin^2 \theta_{23}$ with the Run 1+2+3+4 data.

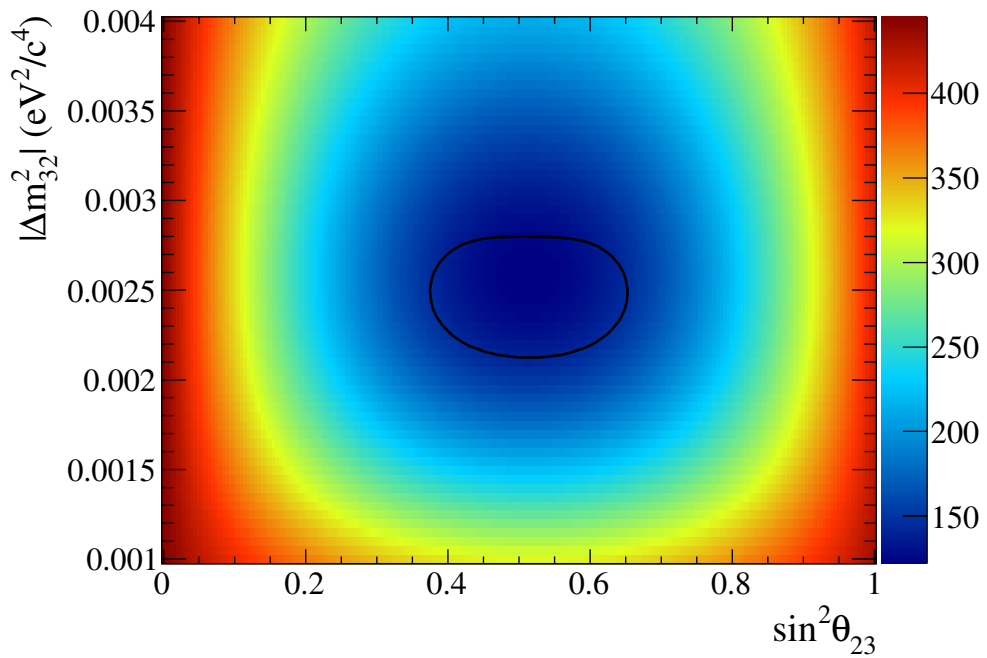


Figure 4.1: Predicted number of 1 μ -like ring events, as a function of $\sin^2 \theta_{23}$ and $|\Delta m_{32}^2|$, for an exposure of 6.57×10^{20} POT. The numbers of events were calculated using the ND280-tuned MC templates. $\sin^2 \theta_{13}$, $\sin^2 \theta_{12}$ and Δm_{21}^2 have the values shown in Tab. 4.2 and $\delta_{CP} = 0$. The numbers shown were generated assuming the normal mass hierarchy. The T2K Run 1+2+3 90% C.L. region [2] is superimposed for reference.

Predicted 1 μ -like ring SK reconstructed energy spectra are shown in Fig. 4.2 for both no oscillations, and oscillations with $\sin^2 \theta_{23} = 0.50$ and $|\Delta m_{32}^2| = 2.40 \times 10^{-3} \text{ eV}^2/\text{c}^4$. The 32 components of the spectrum are calculated separately in the actual analysis, but, for this plot, are grouped into just five categories: $\nu_\mu + \bar{\nu}_\mu$ CCQE; $\nu_\mu + \bar{\nu}_\mu$ CCnonQE; $\nu_\mu + \bar{\nu}_\mu$ CC; $\nu_e + \bar{\nu}_e$ CC; and NC.

An MC tune derived using NA61/SHINE data is applied to the nominal MC templates, and another tune derived using the ND280 data is applied to the NA61-tuned templates, as described in Secs. 4.1.3 and 4.1.4. The fractional difference in the expected number of 1 μ -like ring events when switching from the nominal MC to the NA61-tuned MC templates and when switching from the NA61-tuned MC to the ND280-tuned MC templates is shown in Fig. 4.3 as a function of the oscillation parameters $\sin^2 \theta_{23}$ and $|\Delta m_{32}^2|$. From this figure it can be seen that, for oscillation parameters in the T2K Run 1+2+3 90% confidence region, ~ 12.4 – 13.0% more 1 μ -like ring events are obtained with the NA61-tuned MC than with the nominal MC. In the same part of the parameter space, ~ 7.0 – 8.2% fewer events are expected with the ND280-tuned MC than with the NA61-tuned MC. The effects of the NA61 and ND280 tunes on the total expected number of 1 μ -like ring events and on the numbers in each of the 32 component interaction modes are shown in Tab. 4.3 for no oscillations, and in Tab. 4.4 for oscillations with $\sin^2 \theta_{23} = 0.50$ and $|\Delta m_{32}^2| = 2.40 \times 10^{-3} \text{ eV}^2/\text{c}^4$. Finally, the effects of the NA61 and ND280 tunes on the reconstructed energy spectrum of 1 μ -like ring events are shown in Fig. 4.4. In each case, spectra are shown for both no oscillations and for oscillations with $\sin^2 \theta_{23} = 0.50$ and $|\Delta m_{32}^2| = 2.40 \times 10^{-3} \text{ eV}^2/\text{c}^4$. Also shown in these figures are the ratio of NA61-tuned spectrum to nominal spectrum, and ND280-tuned spectrum to NA61-tuned spectrum. The NA61 tuning has the effect of increasing the predicted number of events at SK by $\sim 10\%$ below 2.5 GeV, increasing to $\sim 35\%$ at 7 GeV. This is mainly due to the default simulation underestimating the number of ν_μ -producing pions at SK by $\sim 8\%$ in the low energy range, and underestimating the number of ν_μ -producing kaons by an increasing factor up to $\sim 35\%$ at 7 GeV, as shown in Fig. 3.3. The tunings for $\bar{\nu}_\mu$ and ν_e show similar distributions with smaller magnitude. For the oscillated case, the ND280 tuning has the effect of reducing the predicted number of events

at SK by $\sim 2\%$ below 2 GeV, with the effect increasing to $\sim 15\%$ at 7 GeV. An extra dip with depth $\sim 5\%$ can also be seen at $E_{\text{reco}} \sim 0.8$ GeV. The major components of the change are:

- $f_{4;t}^{ND280}$ (ν_μ flux normalisation $0.7 \text{ GeV} < E_{\text{true}} < 1.0 \text{ GeV}$). The dip is mainly due to this parameter.
- $f_{6;t}^{ND280} - f_{8;t}^{ND280}$ (ν_μ flux $1.5\text{--}5.0$ GeV). Cause a $\sim 3\%$ increase in events in the range $1.5 \text{ GeV} < E_{\text{true}} < 5.0 \text{ GeV}$.
- $f_{17;t,r}^{ND280}$ (M_A^{RES}). Causes a $\sim 5\%$ decrease in events below 1.5 GeV, with an effect increasing to a $\sim 10\%$ decrease above 3 GeV.
- $f_{19;t}^{ND280} - f_{20;t}^{ND280}$ (CCQE normalisation $E_{\text{true}} > 1.5$ GeV). Cause a $\sim 5\%$ decrease in events above 1.5 GeV.
- $f_{21;t}^{ND280} - f_{22;t}^{ND280}$ (CC1 π normalisation). Cause a $\sim 5\%$ increase in events across all E_{reco} .

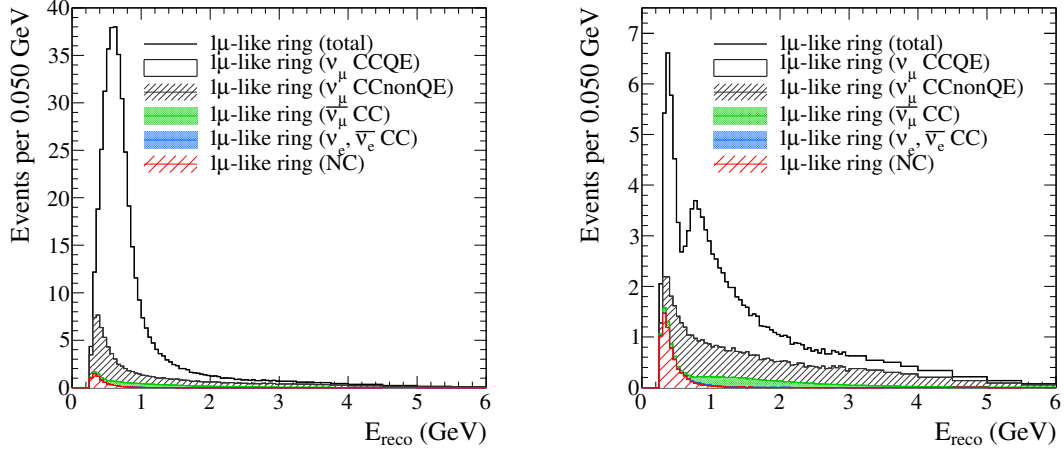


Figure 4.2: Predicted E_{reco} spectrum of 1 μ -like ring events, and contributions from various true neutrino reaction modes, for an exposure of 6.57×10^{20} POT, generated using the ND280-tuned MC templates. Spectra are shown for no oscillations (left) and for oscillations with $\sin^2 \theta_{23} = 0.50$ and $|\Delta m^2_{32}| = 2.40 \times 10^{-3} \text{ eV}^2/\text{c}^4$ (right). For the oscillated spectra $\sin^2 \theta_{13}$, $\sin^2 \theta_{12}$ and Δm^2_{21} have the values shown in Tab. 4.2, $\delta_{CP} = 0$, and the normal mass hierarchy is assumed. Note that the vertical axis of the left is zoomed in by a factor of $5\frac{1}{3}$ relative to the right plot.

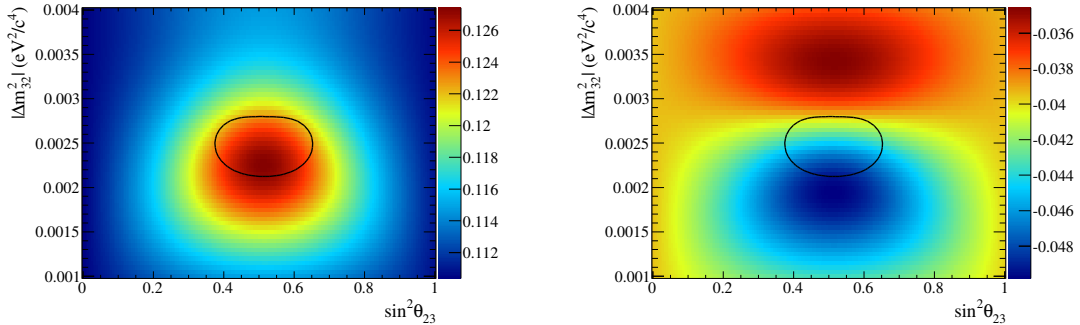


Figure 4.3: Fractional difference in the predicted number of 1 μ -like ring events as a result of applying the NA61 flux tuning to the nominal MC templates (left) and ND280 flux and cross-section tuning to the NA61-tuned MC templates (right). These numbers are shown as a function of $\sin^2 \theta_{23}$ and $|\Delta m^2_{32}|$ for an exposure of 6.57×10^{20} POT. $\sin^2 \theta_{13}$, $\sin^2 \theta_{12}$ and Δm^2_{21} have the values shown in Tab. 4.2 and $\delta_{CP} = 0$. The numbers shown were generated assuming the normal mass hierarchy. The T2K Run 1+2+3 90% C.L. region [2] is superimposed for reference.

	N_{SK} (nominal MC)	N_{SK} (NA61-tuned MC)	N_{SK} (ND280-tuned MC)
Total	418.131220	464.272533	445.980111
ν_μ CCQE	332.238749	367.166655	351.657098
ν_μ CC 1 π	56.190220	63.533041	62.227879
ν_μ CC coherent	1.896444	2.136085	2.108162
ν_μ CC other	7.963009	9.600253	9.615971
ν_μ/ν_τ NC 1 $\pi^{+/-}$	3.403911	3.888131	2.934821
ν_μ/ν_τ NC other	2.912186	3.428374	3.228957
Osc. ν_μ CCQE	0.000000	0.000000	0.000000
Osc. ν_μ CC 1 π	0.000000	0.000000	0.000000
Osc. ν_μ CC coherent	0.000000	0.000000	0.000000
Osc. ν_μ CC other	0.000000	0.000000	0.000000
$\bar{\nu}_\mu$ CCQE	9.008088	9.664244	9.521964
$\bar{\nu}_\mu$ CC 1 π	2.909354	3.114170	3.061538
$\bar{\nu}_\mu$ CC coherent	0.428081	0.458785	0.466122
$\bar{\nu}_\mu$ CC other	0.519092	0.553722	0.548210
$\bar{\nu}_\mu/\bar{\nu}_\tau$ NC 1 $\pi^{+/-}$	0.188316	0.203257	0.143433
$\bar{\nu}_\mu/\bar{\nu}_\tau$ NC other	0.176427	0.188866	0.175090
ν_e CCQE	0.035370	0.038166	0.037333
ν_e CC 1 π	0.021574	0.023840	0.023994
ν_e CC coherent	0.001057	0.001158	0.001158
ν_e CC other	0.005812	0.006914	0.006795
ν_e NC 1 $\pi^{+/-}$	0.091432	0.105093	0.075133
ν_e NC other	0.112184	0.131680	0.121606
Osc. ν_e CCQE	0.000000	0.000000	0.000000
Osc. ν_e CC 1 π	0.000000	0.000000	0.000000
Osc. ν_e CC coherent	0.000000	0.000000	0.000000
Osc. ν_e CC other	0.000000	0.000000	0.000000
$\bar{\nu}_e$ CCQE	0.002174	0.002187	0.002102
$\bar{\nu}_e$ CC 1 π	0.001376	0.001385	0.001345
$\bar{\nu}_e$ CC coherent	0.000135	0.000137	0.000137
$\bar{\nu}_e$ CC other	0.000442	0.000446	0.000432
$\bar{\nu}_e$ NC 1 $\pi^{+/-}$	0.012254	0.012354	0.008390
$\bar{\nu}_e$ NC other	0.013532	0.013592	0.012439

Table 4.3: Calculated numbers of 1 μ -like ring events without oscillations using the nominal MC templates, the NA61-tuned MC templates and the ND280-tuned MC templates. The total numbers of events and the numbers of events from each mode considered in this analysis are shown. These numbers were calculated for an exposure of 6.57×10^{20} POT.

	N_{SK} (nominal MC)	N_{SK} (NA61-tuned MC)	N_{SK} (ND280-tuned MC)
Total	116.283270	131.048525	124.981851
ν_μ CCQE	66.133875	73.447588	70.993870
ν_μ CC 1π	27.733771	31.941870	29.795498
ν_μ CC coherent	0.777452	0.896207	0.908178
ν_μ CC other	7.072249	8.586001	8.597815
ν_μ/ν_τ NC $1\pi^{+/-}$	3.403911	3.888131	2.934821
ν_μ/ν_τ NC other	2.912186	3.428374	3.228957
Osc. ν_μ CCQE	0.117417	0.129898	0.127451
Osc. ν_μ CC 1π	0.027388	0.030497	0.030950
Osc. ν_μ CC coherent	0.000821	0.000913	0.000913
Osc. ν_μ CC other	0.002344	0.002648	0.002609
$\bar{\nu}_\mu$ CCQE	4.428977	4.745506	4.621408
$\bar{\nu}_\mu$ CC 1π	2.080140	2.219962	2.132869
$\bar{\nu}_\mu$ CC coherent	0.228753	0.244521	0.248227
$\bar{\nu}_\mu$ CC other	0.460554	0.490899	0.485509
$\bar{\nu}_\mu/\bar{\nu}_\tau$ NC $1\pi^{+/-}$	0.188316	0.203257	0.143433
$\bar{\nu}_\mu/\bar{\nu}_\tau$ NC other	0.176427	0.188866	0.175090
ν_e CCQE	0.032854	0.035470	0.034683
ν_e CC 1π	0.020475	0.022660	0.022716
ν_e CC coherent	0.000987	0.001084	0.001084
ν_e CC other	0.005716	0.006807	0.006690
ν_e NC $1\pi^{+/-}$	0.091432	0.105093	0.075133
ν_e NC other	0.112184	0.131680	0.121606
Osc. ν_e CCQE	0.179722	0.198093	0.190000
Osc. ν_e CC 1π	0.059387	0.065728	0.070982
Osc. ν_e CC coherent	0.004749	0.005234	0.005093
Osc. ν_e CC other	0.001406	0.001578	0.001558
$\bar{\nu}_e$ CCQE	0.002085	0.002096	0.002014
$\bar{\nu}_e$ CC 1π	0.001337	0.001345	0.001303
$\bar{\nu}_e$ CC coherent	0.000130	0.000132	0.000132
$\bar{\nu}_e$ CC other	0.000438	0.000442	0.000429
$\bar{\nu}_e$ NC $1\pi^{+/-}$	0.012254	0.012354	0.008390
$\bar{\nu}_e$ NC other	0.013532	0.013592	0.012439

Table 4.4: Calculated numbers of 1 μ -like ring events using the nominal MC templates, the NA61-tuned MC templates and the ND280-tuned MC templates. The total numbers of events and the numbers of events from each mode considered in this analysis are shown. These numbers were calculated for an exposure of 6.57×10^{20} POT and oscillations with $\sin^2 \theta_{23} = 0.50$ and $|\Delta m_{32}^2| = 2.40 \times 10^{-3} \text{ eV}^2/\text{c}^4$. Values shown in Tab. 4.2 are used for $\sin^2 \theta_{13}$, $\sin^2 \theta_{12}$ and $|\Delta m_{21}^2|$ and $\delta_{CP} = 0$. The normal mass hierarchy is assumed.

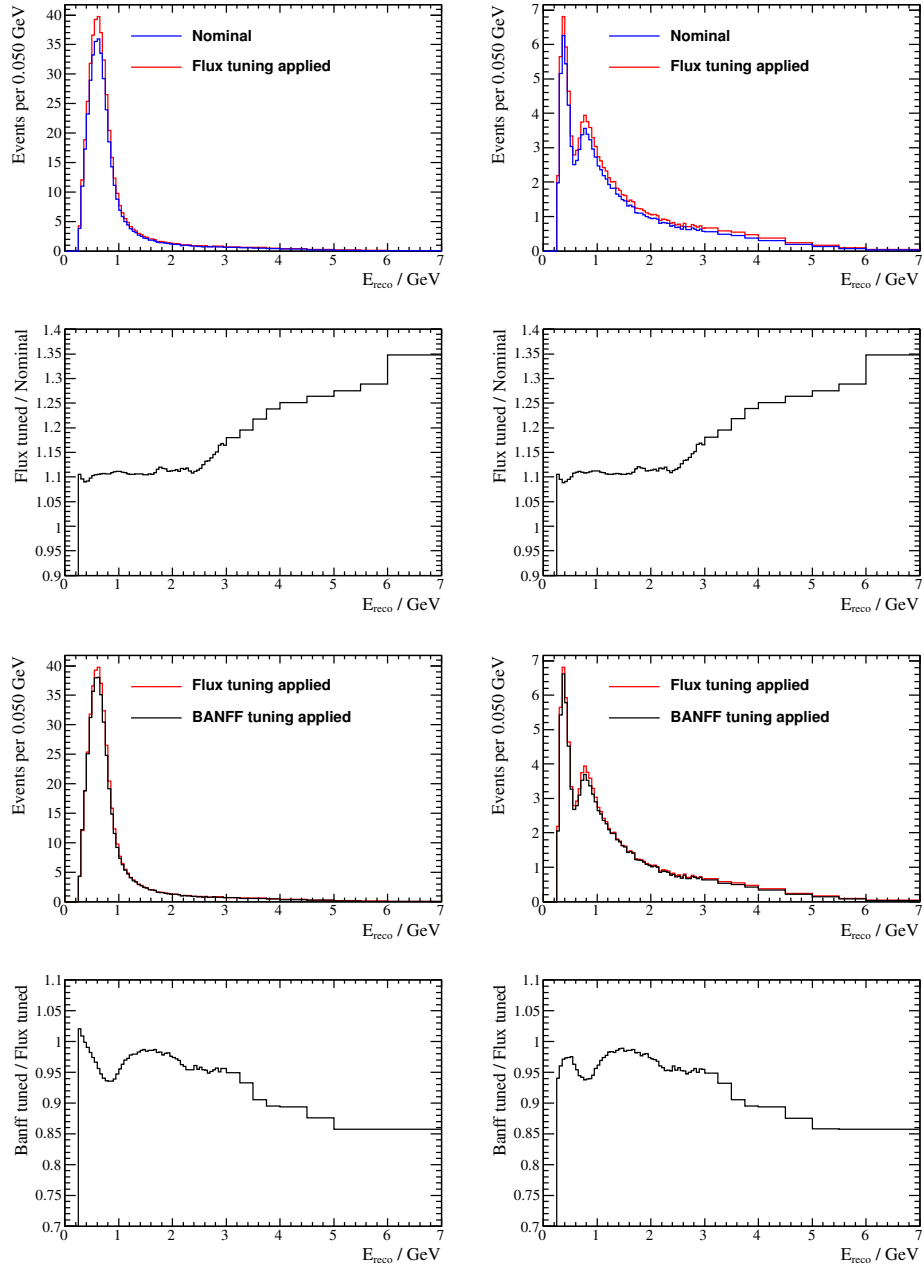


Figure 4.4: Reconstructed-energy spectra of 1 μ -like ring events, for an exposure of 6.57×10^{20} POT, both with and without the effect of the NA61 flux tuning of the nominal MC templates (top) and both with and without the effect of the ND280 tuning of the NA61-tuned MC templates (bottom). The spectra are shown both for no oscillations (left) and for oscillations with $\sin^2 \theta_{23} = 0.50$, $|\Delta m^2_{32}| = 2.40 \times 10^{-3} \text{ eV}^2/\text{c}^4$, the 2012 PDG values for $\sin^2 \theta_{13}$, $\sin^2 \theta_{12}$ and Δm^2_{21} , and $\delta_{CP} = 0$ (right). Results shown for the normal mass hierarchy. The ratio of the NA61-tuned to the nominal MC spectrum, and the ratio of the ND280-tuned to the flux-tuned spectrum are also shown.

4.2 Effect of systematics

4.2.1 Input systematic parameters

This analysis considers 45 systematic parameters which can be grouped into five⁵ categories:

- SK reconstructed energy scale, $f_{E;r}^{SK}$, (1 parameter, described in Sec. 3.4.4). The uncertainty is 2.4%;
- SK detector efficiency and final-state and secondary interactions (hadronic interactions within the nucleus and in the detector volume), $f_{i;r}^{SK+FSI}$, (6 parameters, described in Sec. 3.4.4). The uncertainties are correlated, with 1σ errors are listed in Tab. 3.8, and correlations shown in Fig. 3.19;
- ND280-constrained flux and cross section, $f_{i;t,r}^{ND280}$, (23 parameters, described in Sec. 3.3.4). The uncertainties are correlated, with default values and 1σ errors are listed in Tab. 3.5, and correlations shown in Fig. 3.15;
- ND280-unconstrained cross section (11 parameters, described in Sec. 3.2.3). The uncertainties are uncorrelated, and the default values and 1σ errors are listed in Tab. 3.1;
- *Non-23-sector* oscillation parameters: $\sin^2 \theta_{13}$; $\sin^2 \theta_{12}$; Δm_{21}^2 ; δ_{CP} (4 parameters). The uncertainties are uncorrelated, and the default values and uncertainties are shown in Tab. 4.2).

The MC templates each systematic can effect is shown in Tab. 4.5.

⁵For the studies in Sec. 4.2.2 the SK energy scale is combined with the SK detector efficiency and FSI and SI.

$f_{E;r}^{SK}$	ν_μ CCQE ν_μ CC1 π	ν_μ CC coherent ν_μ CC other ν_μ NC1 π^\pm ν_μ NC other	$\overline{\nu}_\mu$ CCQE $\overline{\nu}_\mu$ CC1 π $\overline{\nu}_\mu$ CC coherent $\overline{\nu}_\mu$ CC other $\overline{\nu}_\mu$ NC1 π^\pm $\overline{\nu}_\mu$ NC other	ν_e CCQE ν_e CC1 π ν_e CC coherent ν_e CC other ν_e NC1 π^\pm ν_e NC other	$\overline{\nu}_e$ CCQE $\overline{\nu}_e$ CC1 π $\overline{\nu}_e$ CC coherent $\overline{\nu}_e$ CC other $\overline{\nu}_e$ NC other	$\text{Osc. } \nu_\mu$ CCQE $\text{Osc. } \nu_\mu$ CC1 π $\text{Osc. } \nu_\mu$ CC coherent $\text{Osc. } \nu_\mu$ CC other $\text{Osc. } \nu_e$ CC, CC coherent $\text{Osc. } \nu_e$ CC, CC other	$\text{Osc. } \nu_\mu$ CCQE $\text{Osc. } \nu_\mu$ CC1 π $\text{Osc. } \nu_\mu$ CC coherent $\text{Osc. } \nu_\mu$ CC other $\text{Osc. } \nu_e$ CC other
$f_{0;r}^{SK+FSI}$	✓						
$f_{1;r}^{SK+FSI}$	✓			✓			
$f_{2;r}^{SK+FSI}$	✓			✓			
$f_{3;r}^{SK+FSI}$	✓✓✓			✓✓✓			
$f_{4;r}^{SK+FSI}$					✓✓✓✓✓		
$f_{5;r}^{SK+FSI}$				✓✓		✓✓✓✓✓	
$f_{0:t}^{ND280}$	✓✓✓✓✓✓						✓✓✓✓✓✓
$f_{1:t}^{ND280}$	✓✓✓✓✓✓						✓✓✓✓✓✓
$f_{2:t}^{ND280}$	✓✓✓✓✓✓						✓✓✓✓✓✓
$f_{3:t}^{ND280}$	✓✓✓✓✓✓						✓✓✓✓✓✓
$f_{4:t}^{ND280}$	✓✓✓✓✓✓						✓✓✓✓✓✓
$f_{5:t}^{ND280}$	✓✓✓✓✓✓						✓✓✓✓✓✓
$f_{6:t}^{ND280}$	✓✓✓✓✓✓						✓✓✓✓✓✓
$f_{7:t}^{ND280}$	✓✓✓✓✓✓						✓✓✓✓✓✓
$f_{8:t}^{ND280}$	✓✓✓✓✓✓						✓✓✓✓✓✓
$f_{9:t}^{ND280}$	✓✓✓✓✓✓						✓✓✓✓✓✓
$f_{10:t}^{ND280}$	✓✓✓✓✓✓						✓✓✓✓✓✓
$f_{11:t}^{ND280}$				✓✓✓✓✓✓			
$f_{12:t}^{ND280}$				✓✓✓✓✓✓			
$f_{13:t}^{ND280}$				✓✓✓✓✓✓			
$f_{14:t}^{ND280}$				✓✓✓✓✓✓			
$f_{15:t}^{ND280}$				✓✓✓✓✓✓			
$f_{16:t,r}^{ND280}$	✓				✓		✓
$f_{17:t,r}^{ND280}$	✓✓✓✓✓			✓✓✓✓✓	✓	✓✓✓✓✓	✓✓✓✓✓
$f_{18:t}^{ND280}$	✓				✓		✓
$f_{19:t}^{ND280}$	✓				✓		✓
$f_{20:t}^{ND280}$	✓				✓		✓
$f_{21:t}^{ND280}$	✓			✓		✓	✓
$f_{22:t}^{ND280}$	✓			✓		✓	✓
$f_{pF;t,r}$	✓			✓		✓	✓
$f_{SF;t,r}$	✓			✓		✓	✓
$f_{\pi-less\Delta;t,r}$	✓	✓✓	✓	✓	✓✓	✓✓	✓✓
$f_{bindE;t,r}$	✓			✓		✓	✓
$f_{CCothShape;t,r}$		✓			✓		✓
$f_{Wshape;t,r}$		✓✓			✓✓		✓✓
$f_{CCcoh;t}$	✓			✓		✓	✓
$f_{NC1\pi^\pm;t}$		✓		✓		✓	
$f_{NCcoth;t}$		✓		✓		✓	
$f_{CC\nu_e;t}$				✓✓✓✓✓		✓✓✓✓✓	✓✓✓✓✓
$f_{CC\overline{\nu};t}$				✓✓✓✓✓		✓✓✓✓✓	
$\sin^2 \theta_{13}$	✓✓✓✓✓			✓✓✓✓✓		✓✓✓✓✓	✓✓✓✓✓
$\sin^2 \theta_{12}$	✓✓✓✓✓			✓✓✓✓✓		✓✓✓✓✓	✓✓✓✓✓
Δm_{21}^2	✓✓✓✓✓			✓✓✓✓✓		✓✓✓✓✓	✓✓✓✓✓
δ_{CP}	✓✓✓✓✓			✓✓✓✓✓		✓✓✓✓✓	✓✓✓✓✓

Table 4.5: Each row of this table represents one of the 45 systematic parameters considered in this analysis (as defined in Tabs. 3.1, 3.5, and 3.8) and each column represents one of the 32 MC templates used to construct the 1μ -like ring reconstructed energy spectrum p.d.f.. A \checkmark symbol denotes that the given MC template is modified when the given systematic parameter is moved away from its nominal value.

Source of uncertainty	$\delta N_{SK}/N_{SK}$ (no oscillations)	$\delta N_{SK}/N_{SK}$ (oscillations with typical parameter values)
SK detector + FSI + SI	3.39%	5.62%
ND280-constrained (pre-ND280-fit)	26.20%	21.92%
ND280-constrained (post-ND280-fit)	2.67%	2.73%
ND280-unconstrained cross section	2.99%	5.00%
<i>Non-23-sector</i> oscillation parameters	0.00%	0.22%
Total (pre-ND280-fit)	26.59%	23.18%
Total (post-ND280-fit)	5.25%	8.01%

Table 4.6: Effect of 1σ systematic parameter variation on the number of 1μ -like ring events, computed for no oscillations and for oscillations with $\sin^2 \theta_{23} = 0.50$, $|\Delta m_{32}^2| = 2.40 \times 10^{-3} \text{ eV}^2/\text{c}^4$, the values shown in Tab. 4.2 for $\sin^2 \theta_{13}$, $\sin^2 \theta_{12}$, and Δm_{21}^2 , and $\delta_{CP} = 0$. The normal mass hierarchy is assumed. The numbers shown were calculated for an exposure of 6.57×10^{20} POT and ND280-tuned MC templates were used.

4.2.2 Evaluation of effects of systematic parameters on the predicted 1μ -like ring reconstructed energy spectrum

In this section, the effects of the systematics described in Sec. 4.2.1 on the predicted number of 1μ -like ring events and the predicted reconstructed energy spectrum in SK are presented. These effects are shown both without oscillations, and with oscillations with $\sin^2 \theta_{23} = 0.50$ and $|\Delta m_{32}^2| = 2.40 \times 10^{-3} \text{ eV}^2/\text{c}^4$. For the oscillated case, the values shown in Tab. 4.2 for $\sin^2 \theta_{13}$, $\sin^2 \theta_{12}$ and Δm_{21}^2 , and $\delta_{CP}=0$ are used, and the normal mass hierarchy is assumed. All results are generated for an integrated exposure of 6.57×10^{20} POT and the ND280-tuned MC templates are used.

The effects of systematic uncertainties on the predicted number of events are summarised in Tab. 4.6, both for no oscillations and for oscillations with the typical parameter values given above. In this table, systematic parameters are grouped into five categories and all parameter correlations are taken into account. Estimated uncertainties are given both before and after the ND280 fit.

The individual effect of each parameter is presented in Tab. 4.7, in which the correlations between parameters are necessarily ignored. The most important systematics from this table are:

- $f_{3;r}^{SK+FSI}$. The SK detector efficiency and FSI+SI parameter for $\nu_\mu/\bar{\nu}_\mu$ CC-nonQE interactions. A $+1\sigma$ change causes an increase across the whole spectrum, with an $\sim 5\%$ effect in the flux peak region, an $\sim 2\%$ effect below the flux peak, and up to $\sim 9\%$ effect above the flux peak.
- $f_{5;r}^{SK+FSI}$. The SK detector efficiency and FSI+SI parameter for NC interactions. A $+1\sigma$ change causes an $\sim 30\%$ increase in the 0.25–0.30 GeV bin, reducing to $\sim 1\%$ at 1 GeV.
- $f_{16;t,r}^{ND280}$. M_A^{QE} . A $+1\sigma$ change causes an $\sim 2\%-4\%$ increase across all E_{reco} , peaking at ~ 1 GeV.
- $f_{18;t}^{ND280}$. CCQE normalisation for $E_{\text{reco}} < 1.5$ GeV. A $+1\sigma$ change causes an $\sim 6\%$ increase for $E_{\text{reco}} < 1.4$ GeV, reducing to a $\sim 1\%$ increase at 2 GeV.
- $f_{\pi-\text{less}\Delta;t,r}$. Systematic due to the uncertainty in the fraction of π -less Δ decays in resonance-production events. A $+1\sigma$ change causes an $\sim 8\%$ increase above 0.6 GeV, reducing to $\sim 2\%$ decrease in at 0.3 GeV.
- δ_{CP} . Has the largest effect in the *non-23-sector* category. A shift by $\pi/2$ results in a $\sim 3\%$ decrease at 0.4 GeV, and a $\sim 5\%$ increase at 0.7 GeV.

It should be noted that while $f_{E;r}^{SK}$ (the SK energy scale) does not change the number of events, it does effect the E_{reco} spectrum by inducing a shift.

The importance of each systematic in the joint determination of ν_μ disappearance oscillation parameters is shown later in Tabs. 4.9 and 4.10.

The effects of the combined systematic uncertainties on the reconstructed energy spectrum of 1 μ -like ring events is shown in Fig. 4.5 for the typical oscillation scenario used. This plot shows the total error envelope for the 1 μ -like

Source of uncertainty	$\delta N_{SK}/N_{SK}$ (no oscillation)		$\delta N_{SK}/N_{SK}$ (oscillations with typical params)	
	pre-ND280-fit	post-ND280-fit	pre-ND280-fit	post-ND280-fit
$f_{E;r}^{SK}$	0.0	0.0	0.0	0.0
$f_{0;r}^{SK+FSI}$	0.090	0.098	0.15	0.18
$f_{1;r}^{SK+FSI}$	1.8	1.9	0.68	0.74
$f_{2;r}^{SK+FSI}$	0.40	0.43	0.92	1.0
$f_{3;r}^{SK+FSI}$	2.4	2.1	4.6	4.0
$f_{4;r}^{SK+FSI}$	0.017	0.016	0.25	0.27
$f_{5;r}^{SK+FSI}$	1.1	0.90	3.8	3.2
$f_{0;t}^{ND280}$	0.36	0.27	0.85	0.66
$f_{1;t}^{ND280}$	1.0	0.74	0.67	0.50
$f_{2;t}^{ND280}$	1.9	1.3	0.12	0.085
$f_{3;t}^{ND280}$	2.3	1.6	0.30	0.22
$f_{4;t}^{ND280}$	3.4	2.4	2.2	1.6
$f_{5;t}^{ND280}$	1.0	0.66	1.8	1.2
$f_{6;t}^{ND280}$	0.63	0.39	1.7	1.1
$f_{7;t}^{ND280}$	0.33	0.20	1.0	0.65
$f_{8;t}^{ND280}$	0.41	0.22	1.3	0.74
$f_{9;t}^{ND280}$	0.19	0.077	0.65	0.27
$f_{10;t}^{ND280}$	0.051	0.019	0.17	0.066
$f_{11;t}^{ND280}$	0.061	0.050	0.035	0.030
$f_{12;t}^{ND280}$	0.061	0.049	0.049	0.040
$f_{13;t}^{ND280}$	0.085	0.067	0.16	0.13
$f_{14;t}^{ND280}$	0.10	0.080	0.27	0.22
$f_{15;t}^{ND280}$	0.078	0.060	0.25	0.20
$f_{16;t,r}^{ND280}$	25.	3.4	18.	2.8
$f_{17;t,r}^{ND280}$	2.8	1.1	6.7	2.4

Source of uncertainty	$\delta N_{SK}/N_{SK}$ (no oscillation)		$\delta N_{SK}/N_{SK}$ (oscillations with typical params)	
	pre-ND280-fit	post-ND280-fit	pre-ND280-fit	post-ND280-fit
$f_{18;t}^{ND280}$	7.9	5.9	4.2	3.3
$f_{19;t}^{ND280}$	1.4	0.55	3.9	1.6
$f_{20;t}^{ND280}$	0.36	0.16	1.2	0.53
$f_{21;t}^{ND280}$	3.7	1.5	4.9	2.0
$f_{22;t}^{ND280}$	1.7	0.47	5.4	1.6
$f_{pF;t,r}$	0.063	0.065	0.13	0.13
$f_{SF;t,r}$	0.82	0.82	0.24	0.26
$f_{Wshape;t,r}$	0.12	0.072	0.40	0.26
$f_{CCCothShape;t,r}$	0.28	0.30	0.78	0.89
$f_{\pi-less\Delta;t,r}$	3.2	2.6	5.6	4.5
$f_{bindE;t,r}$	0.50	0.43	0.24	0.20
$f_{CCcoh;t}$	0.54	0.58	0.81	0.93
$f_{NC1\pi^\pm;t}$	0.31	0.21	1.1	0.75
$f_{NCcoh;t}$	0.25	0.24	0.85	0.85
$f_{CC\nu_e;t}$	0.00051	0.0005	0.0077	0.0081
$f_{CC\bar{\nu};t}$	0.61	0.61	1.2	1.2
$\sin^2 \theta_{13}$	0.0	0.0	0.070	0.078
$\sin^2 \theta_{12}$	0.0	0.0	0.040	0.036
Δm_{21}^2	0.0	0.0	0.027	0.025
δ_{CP}	0.0	0.0	0.21	0.19

Table 4.7: Effects of 1σ systematic parameter variations (as defined in Tabs. 3.1, 3.5, and 3.8) on the number of 1μ -like ring events, computed for no oscillations and for oscillations with $\sin^2 \theta_{23} = 0.50$, $|\Delta m_{32}^2| = 2.40 \times 10^{-3} \text{ eV}^2/\text{c}^4$, the values shown in Tab. 4.2 for $\sin^2 \theta_{13}$, $\sin^2 \theta_{12}$, and Δm_{21}^2 , and $\delta_{CP} = 0$. The normal mass hierarchy is assumed. Numbers are quoted to 2 significant figures. Correlations are ignored for this table. The numbers shown were calculated for an exposure of 6.57×10^{20} POT and ND280-tuned MC templates were used.

ring event reconstructed energy spectrum; this is calculated as the $\pm 1\sigma$ spread of bin contents from 100,000 toy MC experiments generated with randomised systematic parameters. For the uncorrelated systematics, random numbers are drawn from a Gaussian distribution⁶ [174]. For the correlated systematics, Cholesky decomposition [175] of the covariance matrix is performed to give the lower triangular matrix, which is multiplied by a vector of uncorrelated random numbers drawn from a Gaussian distribution, to produce correlated random variables. In Fig. 4.5, all systematic parameters were considered and their correlations were taken into account.

Fig. 4.6 shows the effect of the systematic error, relative to the statistical error at T2K Run 1+2+3+4 exposure, for both the no oscillation and oscillation cases. It can be seen that the statistical error dominates at most energies; the systematic error is comparable below 1 GeV for the no-oscillation scenario. It should be noted that the statistical error is 100% uncorrelated between bins, while the systematic error is correlated between bins, therefore the effect of the systematics is more important than is indicated in Fig. 4.6.

Fig. 4.7 shows the effect of the four categories of systematic error, relative to the total systematic error, for both the no oscillation and oscillation cases. It can be seen that the SK detector, FSI and SI, and ND280-unconstrained cross-section systematics dominate the oscillation dip region.

⁶SF is drawn in the range [0,1] from a Gaussian distribution. δ_{CP} is drawn in the range $[-\pi, \pi]$ from a uniform distribution.

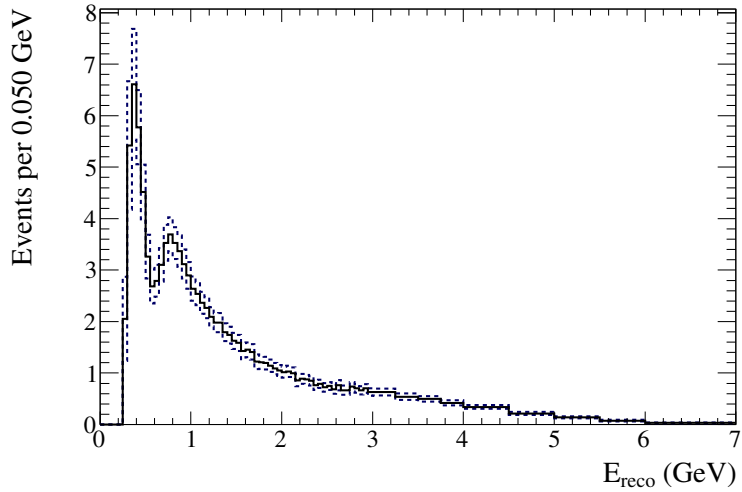


Figure 4.5: Total error envelope of the 1μ -like ring event reconstructed energy spectrum, for oscillations with $\sin^2 \theta_{23} = 0.50$ and $|\Delta m_{32}^2| = 2.40 \times 10^{-3} \text{ eV}^2/\text{c}^4$, the values shown in Tab. 4.2 for $\sin^2 \theta_{13}$, $\sin^2 \theta_{12}$ and Δm_{21}^2 , and $\delta_{CP}=0$. The normal mass hierarchy is assumed. The numbers shown were calculated for an exposure of 6.57×10^{20} POT. ND280-fit-tuned MC templates were used. The error envelope was calculated as the $\pm 1\sigma$ spread of bin contents using an ensemble of 100,000 toy MC experiments generated with randomised systematic parameters. All systematic parameters were considered and their correlations were taken into account.

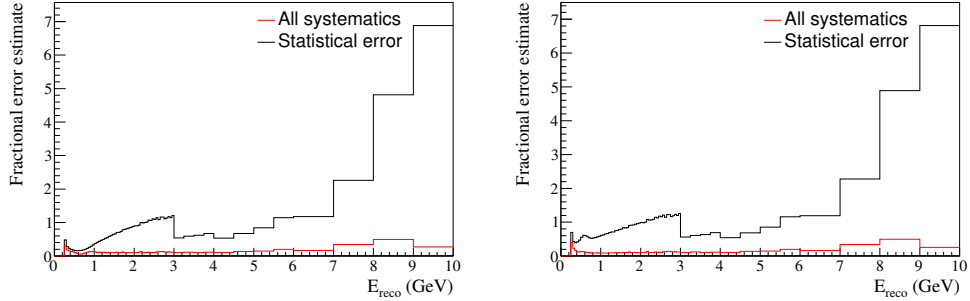


Figure 4.6: Comparative size of systematic and statistical error effects per bin. 100,000 toy MC experiments were generated with randomised systematic parameters and the 1σ spread of bin contents was calculated. The fractional systematic error is estimated as the 1σ spread divided by the expected number of events in each bin. The fractional statistical error is estimated as the inverse square root of the number of events in each bin at 6.57×10^{20} POT. ND280-fit-tuned MC templates were used. All systematic parameters were considered and their correlations were taken into account. Shown with both no oscillations (left) and with oscillations for $\sin^2 \theta_{23} = 0.50$, $|\Delta m_{32}^2| = 2.40 \times 10^{-3} \text{ eV}^2/\text{c}^4$, the values shown in Tab. 4.2 for $\sin^2 \theta_{13}$, $\sin^2 \theta_{12}$ and Δm_{21}^2 , and $\delta_{CP}=0$. The normal mass hierarchy is assumed (right).

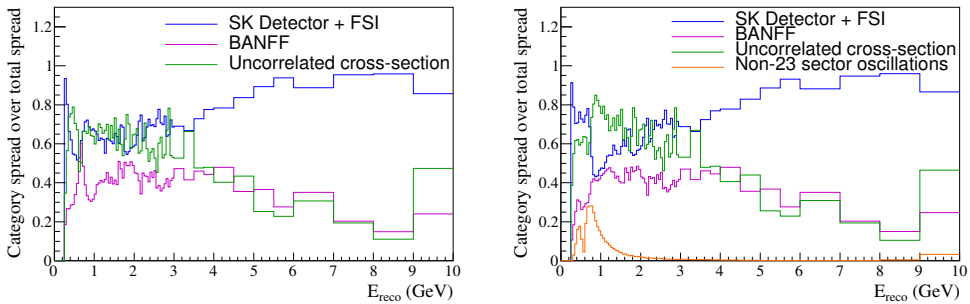


Figure 4.7: Ratio of event-per-bin 1σ spread with individual systematic categories randomised, to the equivalent spread with all systematics randomised. 100,000 toy MC experiments each were generated with different groups of systematics randomised, and with all systematics randomised, and the 1σ spread of bin contents was calculated. ND280-fit-tuned MC templates were used. Shown with both no oscillations (left) and with oscillations for $\sin^2 \theta_{23} = 0.50$, $|\Delta m_{32}^2| = 2.40 \times 10^{-3} \text{ eV}^2/\text{c}^4$, the values shown in Tab. 4.2 for $\sin^2 \theta_{13}$, $\sin^2 \theta_{12}$ and Δm_{21}^2 , and $\delta_{CP}=0$. The normal mass hierarchy is assumed (right).

4.3 Procedure for the joint determination of ν_μ disappearance oscillation parameters

In this section, the method of fitting the SK 1 μ -like ring rate and reconstructed energy spectrum, in order to obtain the values and errors on the 23-sector oscillation parameters ($\sin^2 \theta_{23}$ and $|\Delta m_{32}^2|$ or $|\Delta m_{31}^2|$), is discussed. First, the choice of ν_μ disappearance parameters to determine is described in Sec. 4.3.1. In Sec. 4.3.2 the χ^2 fit statistic is introduced. In Sec. 4.3.3 the fit methodology is described. In Sec. 4.3.4 a method for obtaining the goodness of fit is presented. In Sec. 4.3.5 the fitter is validated. In Sec. 4.3.6 the effect of systematics on the fitted values are presented, in order to determine which systematic parameters have the greatest impact on the fit. In Sec. 4.3.7 the methods for constructing 2-dimensional (in $\sin^2 \theta_{23}$ versus $|\Delta m_{32}^2|$ or $|\Delta m_{31}^2|$) and 1-dimensional (in $\sin^2 \theta_{23}$ and $|\Delta m_{32}^2|$ or $|\Delta m_{31}^2|$) confidence regions are presented. Finally, in Sec. 4.3.8 the sensitivity for the joint determination of ν_μ disappearance oscillation parameters at a number of test points is presented.

4.3.1 Choice of ν_μ disappearance oscillation parameters

Historically, analyses were performed using a two neutrino flavour approximation

$$P(\nu_\mu \rightarrow \nu_\mu) = 1 - \sin^2(2\theta_{23}) \sin^2 \left(\frac{\Delta m_{32}^2 L}{4E_\nu} \right) \quad (4.3)$$

to determine ν_μ disappearance oscillation parameters, fitting for the double angled parameter $\sin^2(2\theta_{23})$ parameter (see, for example, Ref. [176]). However, in the three active neutrino flavour model, there is a dependence on the octant of θ_{23} ($\theta_{23} \leq \pi/4$ or $\theta_{23} \geq \pi/4$) which has a large effect on the determination of $\sin^2(2\theta_{23})$. This is due to the value of $\sin^2 \theta_{23}$ giving maximal disappearance

not being the same as the value giving maximal mixing ($\sin^2 \theta_{23} = 0.50$); this difference is due to the non-zero value of θ_{13} . In the 3-flavour oscillation formula⁷

$$P(\nu_\mu \rightarrow \nu_\mu) \approx 1 - (\cos^4 \theta_{13} \sin^2(2\theta_{23}) + \sin^2 \theta_{23} \sin^2(2\theta_{13})) \sin^2 \left(\frac{\Delta m_{31}^2 L}{4E} \right), \quad (4.4)$$

the maximum amount of disappearance occurs not at $\sin^2 \theta_{23} = 0.50$, but it is offset slightly due to the next-to-leading order term. The extremum occurs at $\sin^2 \theta_{23} = \frac{1}{2(1-\sin^2 \theta_{13})} \approx 0.513$, when using the value of $\sin^2 \theta_{13}$ in Tab. 4.2, instead of at $\sin^2 \theta_{23} = 0.50$ as in the 2-flavour approximation. In addition, the oscillation probability is approximately symmetric about this point, meaning that for every input value $\sin^2 \theta_{23} \neq 0.513$, there exists a “mirror point” with a similar oscillation probability. Therefore, $\sin^2 \theta_{23}$ is fit by default.

There are also different choices for the mass-squared splitting parameter: typically $|\Delta m_{32}^2|$ is used in ν_μ -disappearance analyses, but this is the largest mass-squared splitting for the inverted mass hierarchy and the second largest for the normal mass hierarchy. It is therefore not correct to compare results in $|\Delta m_{32}^2|$ obtained under the different mass hierarchy hypotheses. For the present analysis, it was decided to fit $|\Delta m_{32}^2|$ for the normal mass hierarchy and $|\Delta m_{31}^2|$ for the inverted mass hierarchy (the second largest mass-squared splitting in each hierarchy). The actual inputs to the calculation of the oscillation probabilities are $+|\Delta m_{32}^2|$ for the normal mass hierarchy and $-|\Delta m_{31}^2|$ for the inverted mass hierarchy. Fits of $|\Delta m_{32}^2|$ for the inverted mass hierarchy were also performed for validation.

⁷In the fits, the full 3-flavour oscillation formulae including matter effects is used, and not this approximation.

4.3.2 Construction of likelihood

The ν_μ disappearance analysis uses a binned likelihood-ratio method. Measurements of the oscillation parameters $\sin^2 \theta_{23}$ and $|\Delta m_{32}^2|$ or $|\Delta m_{31}^2|$ are obtained by comparing the observed and predicted SK E_{reco} event rate and spectrum for 1 μ -like ring events using the likelihood-ratio method.

Let N be the number of reconstructed energy bins and n_i^{obs} be the number of events observed in the i th bin. The p.d.f. for the total number of events observed in SK, $n_{\text{tot}}^{\text{obs}} = \sum_{i=0}^{N-1} n_i^{\text{obs}}$, has a Poisson distribution, and the mean of that distribution is equal to the predicted total number of events $n_{\text{tot}}^{\text{exp}} = \sum_{i=0}^{N-1} n_i^{\text{exp}}$, where $n_i^{\text{exp}} = n_i^{\text{exp}}(\sin^2 \theta_{23}, |\Delta m_{32}^2| \text{ or } |\Delta m_{31}^2|; \mathbf{a})$ is the predicted number of events in the i th bin. The p.d.f. for the total number of events is

$$f_{\text{poisson}} = \frac{[n_{\text{tot}}^{\text{exp}}]^{n_{\text{tot}}^{\text{obs}}} e^{-n_{\text{tot}}^{\text{exp}}}}{n_{\text{tot}}^{\text{obs}}!}. \quad (4.5)$$

The reconstructed energies of the observed events are distributed over N bins. Since there are N possible outcomes for the process of placing an event in a bin, the p.d.f. of the distribution of those outcomes is multinomial,

$$f_{\text{multinomial}} = n_{\text{tot}}^{\text{obs}}! \prod_{i=0}^{N-1} \frac{1}{n_i^{\text{obs}}!} \left[\frac{n_i^{\text{exp}}}{n_{\text{tot}}^{\text{exp}}} \right]^{n_i^{\text{obs}}}, \quad (4.6)$$

where $\frac{n_i^{\text{exp}}}{n_{\text{tot}}^{\text{exp}}}$ is the probability of an event being placed in the i th bin.

The joint p.d.f. f_{joint} for the outcome of the reconstructed energy distribution is the product of the Poisson and multinomial distributions shown in Eq. 4.5 and Eq. 4.6 respectively:

$$f_{\text{joint}} = e^{-n_{\text{tot}}^{\text{exp}}} \prod_{i=0}^{N-1} \frac{1}{n_i^{\text{obs}}!} \left[n_i^{\text{exp}} \right]^{n_i^{\text{obs}}}. \quad (4.7)$$

The next step is to divide the p.d.f. in Eq. 4.7 by a factor that does not depend on the oscillation parameters

$$f_0 = e^{-n_{\text{tot}}^{\text{obs}}} \prod_{i=0}^{N-1} \frac{1}{n_i^{\text{obs}}!} [n_i^{\text{obs}}]^{n_i^{\text{obs}}}, \quad (4.8)$$

which leads to the likelihood ratio

$$\lambda = e^{n_{\text{tot}}^{\text{obs}} - n_{\text{tot}}^{\text{exp}}} \prod_{i=0}^{N-1} \left(\frac{n_i^{\text{exp}}}{n_i^{\text{obs}}} \right)^{n_i^{\text{obs}}}. \quad (4.9)$$

Best-fit values are obtained by minimising:

$$\begin{aligned} -2 \ln \lambda (\sin^2 \theta_{23}, |\Delta m_{32}^2| \text{ or } |\Delta m_{31}^2|; \mathbf{a}) = \\ 2 \cdot \sum_{i=0}^{N-1} \left(n_i^{\text{obs}} \cdot \ln(n_i^{\text{obs}} / n_i^{\text{exp}}) + (n_i^{\text{exp}} - n_i^{\text{obs}}) \right) + (\mathbf{a} - \mathbf{a}_0)^T \cdot \mathbf{C}^{-1} \cdot (\mathbf{a} - \mathbf{a}_0), \end{aligned} \quad (4.10)$$

where the second term, *the penalty term*, penalises the fit for moving the N_s systematic (nuisance) parameters that effect the SK reconstructed energy spectrum prediction (e.g. parameters that control the beam, neutrino interaction simulations and the detector response) away from their nominal values. \mathbf{a} is a $1 \times N_s$ -dimensional array of systematic parameters \mathbf{a}_0 is a $1 \times N_s$ -dimensional array with the default values of the systematics parameters, \mathbf{a}^T is the transpose of \mathbf{a} , and \mathbf{C} is the systematic parameter covariance matrix of dimension $N_s \times N_s$.

The likelihood-ratio method is equivalent to the extended maximum-likelihood method up to Eq. 4.7, where the Poisson term (Eq. 4.5) is equivalent to $\mathcal{L}_{\text{norm}}$ and the multinomial term (Eq. 4.6) is equivalent to $\mathcal{L}_{\text{shape}}$. The advantage of the likelihood ratio method is that in the large-sample limit, the quantity $-2 \ln \lambda (\sin^2 \theta_{23}, |\Delta m_{32}^2| \text{ or } |\Delta m_{31}^2|; \mathbf{a})$ in Eq. 4.10 has a χ^2 distribution and it can therefore be used as a goodness-of-fit test. In this thesis, $-2 \ln \lambda (\sin^2 \theta_{23}, |\Delta m_{32}^2| \text{ or } |\Delta m_{31}^2|; \mathbf{a})$ and $\chi^2 (\sin^2 \theta_{23}, |\Delta m_{32}^2| \text{ or } |\Delta m_{31}^2|; \mathbf{a})$ are used interchangeably.

4.3.3 Numerical implementation

Minimisation is performed with MINUIT [167], using the MIGRAD algorithm. MIGRAD proceeds by first calculating the first derivatives and covariance matrix of the free parameters in the problem (the six oscillation parameters and 41 systematic parameters in this case). Using this information, a direction to step is calculated, and a number of calculations of χ^2 along this direction are performed to find the minimum in that direction. The first derivatives and covariance matrix are then recalculated, and the previous step repeated until convergence criteria are satisfied. If MIGRAD does not converge, the starting values of the oscillation parameters are re-initialised: the new initial values are randomly drawn from uniform distributions in the ranges $1.5 \times 10^{-3} \text{ eV}^2/\text{c}^4 \leq |\Delta m_{32}^2|$ or $|\Delta m_{31}^2| \leq 3.5 \times 10^{-3} \text{ eV}^2/\text{c}^4$ and either $0.35 \leq \sin^2 \theta_{23} \leq 0.50$ or $0.53 \leq \sin^2 \theta_{23} \leq 0.68$ (the new initial value of $\sin^2 \theta_{23}$ is in the same octant as the previous initial value, and away from the value of maximal disappearance (a boundary of the model)). All 45 systematic parameters are thrown within their errors to provide new initial values. The fit is retried with the new initial values, and this is repeated up to 10 times. If the fit still fails to converge after 10 attempts, the SIMPLEX algorithm is used. SIMPLEX proceeds by forming a simplex from the starting point and finding local minima along each parameter. The simplex is reformed by replacing the highest point with a new minima along the line between the point and the simplex centroid, until the simplex contracts at a minimum. SIMPLEX does not use derivatives, and so can perform better than MIGRAD in certain circumstances (near a parameter limit or for a fluctuating function). The search for the minimum value of $-2 \ln \lambda$ ($\sin^2 \theta_{23}$, $|\Delta m_{32}^2|$ or $|\Delta m_{31}^2|$; a) (see Eq. 4.10) is performed in the range $0 \leq \sin^2 \theta_{23} \leq 1$ and $1 \times 10^{-3} \text{ eV}^2/\text{c}^4 \leq |\Delta m_{32}^2|$ or $|\Delta m_{31}^2| \leq 6 \times 10^{-3} \text{ eV}^2/\text{c}^4$.

After a successful fit, the HESSE algorithm is called to improve the esti-

mates of the errors on the fitted parameters. HESSE calculates the full second derivative matrix at the best-fit point by taking finite differences. For systematic parameters which do not have a Gaussian effect on the spectrum (e.g. $f_{E;r}^{SK}$), the MINOS algorithm is used. MINOS finds asymmetric errors for each parameter individually by searching for the value of that parameter that gives a $\Delta\chi^2$ of 1, relative to the best-fit point. It achieves this by estimating the position of this point using the covariance matrix, minimising all other free parameters using MIGRAD and repeating until the point is found.

Each fit is repeated twice⁸: in the first fit, the initial values are $|\Delta m_{32}^2|$ or $|\Delta m_{31}^2| = 2.40 \times 10^{-3} \text{ eV}^2/\text{c}^4$ and $\sin^2 \theta_{23} = 0.60$, while the second fit uses as initial values the best fit of $|\Delta m_{32}^2|$ or $|\Delta m_{31}^2|$ and the mirror point in the other octant of the best fit of $\sin^2 \theta_{23}$ from the first fit. Two fits are performed because, for non-maximal mixing, the χ^2 surface contains two local minima in $\sin^2 \theta_{23}$, and the MIGRAD algorithm is unlikely to be able to cross between them. Although Eq. 4.4 suggests that values at either side of maximal disappearance have equal probabilities, Eq. 4.4 is only a leading order approximation and other terms will alter this. There will also be differences in the spectra due to other probabilities changing at either side of the mirror point (e.g. $P(\nu_\mu \rightarrow \nu_e)$). Therefore the value of χ^2 at the local minimum on each side of the mirror point can be different, and so must be calculated. The fit with the lowest χ^2 value is kept.

Parameter ranges

All the systematic parameters are allowed to float in the fit, and are restricted to the range $[-5\sigma_s, +5\sigma_s]$ where σ_s is the one standard deviation error assigned

⁸For reference, when running on a machine with Scientific Linux 6.4 (Carbon) on an Intel®Xeon®CPU X5650 running at a speed of 2.67 GHz, it takes \sim 4 minutes to perform a fit to a single toy MC experiment or data (i.e. to do the fit twice, once in each octant).

to each systematic parameter⁹. Values of systematic parameters that give a negative predicted number of events in any reconstructed energy bin are not allowed. If this scenario arises, the number of events is changed to $+10^{-8}$ in that bin. This is done for the sum of all the interaction modes (rather than for each mode separately) to prevent the \ln term in Eq. 4.10 tending to infinity in the case where n^{obs} is non-zero and n^{exp} is zero.

In a 3-flavour ν_μ -disappearance fit, it is also necessary to make a choice for the treatment of the *non-23-sector* oscillation parameters. In this analysis, each of $\sin^2 \theta_{13}$, $\sin^2 \theta_{12}$, Δm_{21}^2 and δ_{CP} are allowed to float. Penalty terms are used for $\sin^2 \theta_{13}$, $\sin^2 \theta_{12}$, Δm_{21}^2 , and their central values and uncertainties are shown in Tab. 4.2; these are taken from the 2012 PDG [31]. There is no penalty term for δ_{CP} , and it is allowed to float freely in the range $[-\pi, +\pi]$ ¹⁰.

4.3.4 Goodness-of-fit tests

While the χ^2 defined in Eq. 4.10 can be used as a goodness-of-fit test statistic, the 73-bin E_{reco} spectrum cannot be used, as it is too sparsely populated. This is because $-2 \ln \lambda$ only approaches a χ^2 distribution in the large-sample limit of at least five events in every bin [177]. Therefore in this analysis p-values will be calculated using the rate and the reconstructed energy distribution, and that distribution will use a very coarse binning scheme to ensure that there are a sufficient numbers of events in each bin: 5 bins from 0.0–0.4 GeV, 0.4–0.7 GeV, 0.7–1.0 GeV, 1.0–2.0 GeV and 2.0–30.0 GeV gives sufficient statistics in each bin (~ 15 to ~ 35 events).

⁹Such an error is defined for all but one of the systematic parameters considered in this analysis. The exception is the systematic parameters f_{SF} which parameterises the uncertainty on nuclear modelling, switching between the RFG and SF models. The allowed range of the parameter f_{SF} in the oscillation fit is [0,1].

¹⁰The *non-23-sector* oscillation parameters are allowed to float in the fit in the following ranges: $\sin^2 \theta_{13}$ and $\sin^2 \theta_{12}$ in the range [0,1]; Δm_{21}^2 in the range $[6,9] \times 10^{-5} \text{ eV}^2/\text{c}^4$; and δ_{CP} in the range $[-\pi, +\pi]$.

A p-value can be calculated to determine the goodness of fit by using the results of fits to many toy MC experiments. At the best-fit point ($\sin^2 \theta_{23}$ and $|\Delta m_{32}^2|$ or $|\Delta m_{31}^2|$) of the fit to data, 1000 toy MC experiments are generated with statistical fluctuations and all systematics randomised. These toy experiments are fitted and the χ^2 of each compared to χ^2_{data} . The p-value is the proportion of experiments in which a value of $\chi^2 > \chi^2_{\text{data}}$ is recorded.

4.3.5 Fitter validation

The performance of the fitter was evaluated using ensembles of 5000 toy MC experiments, and these were generated with statistical fluctuations and variations of all 45 systematic parameters. Ensembles of experiments were generated for different true input values of $\sin^2 \theta_{23}$ and $|\Delta m_{32}^2|$, and for both 6.57×10^{20} POT (Run 1+2+3+4) and 7.80×10^{21} POT (the ultimate T2K goal). These toy MC experiments were fitted using MIGRAD and the errors were computed using HESSE¹¹.

Distributions of residuals for $\sin^2 \theta_{23}$ and $|\Delta m_{32}^2|$ are shown in Fig. 4.8 for true input values¹² $\sin^2 \theta_{23} = 0.370$ and $|\Delta m_{32}^2| = 2.40 \times 10^{-3} \text{ eV}^2/\text{c}^4$, for both 6.57×10^{20} POT and 7.80×10^{21} POT. A clear three-peak structure is seen at Run 1+2+3+4 POT in the distribution of residuals of $\sin^2 \theta_{23}$, with peaks occurring at the input value, the mirror of the input value in the other octant, and the maximum disappearance value. The peak at the mirror value in the other octant occurs because $P(\nu_\mu \rightarrow \nu_\mu)$ is almost identical for the input and mirror values.

¹¹MINOS errors were computed for the SK energy scale systematic because the number of events in a bin is not a smooth function of $f_{E;r}^{SK}$. Tweaking this systematic involves migrating events to and from neighbouring bins, and, although the number of events itself is a continuous function of $f_{E;r}^{SK}$, there is a discontinuity in the differential when moving from positive to negative values of $f_{E;r}^{SK}$. There is also a discontinuity at large values of $f_{E;r}^{SK}$ since events are also migrated to and from the next-to-neighbouring bins. For these reasons, HESSE has a problem evaluating errors for this systematic parameter.

¹²Chosen as a point away from maximal disappearance.

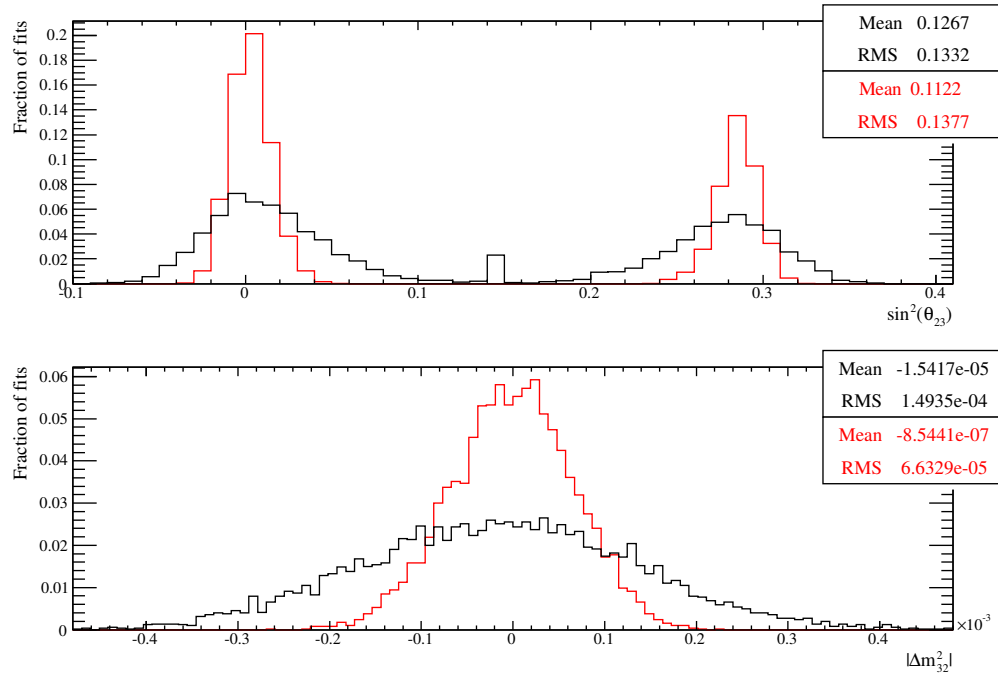


Figure 4.8: Distributions of fitter residuals for $\sin^2 \theta_{23}$ and $|\Delta m_{32}^2|$ for 5000 toy MC experiments, generated at $\sin^2 \theta_{23} = 0.370$ and $|\Delta m_{32}^2| = 2.40 \times 10^{-3} \text{ eV}^2/\text{c}^4$, including statistical fluctuations and with randomised systematic and non-23 oscillation parameters. The distribution is shown for both 6.57×10^{20} POT (Run 1+2+3+4, black histogram) and 7.80×10^{21} POT (the T2K ultimate goal, red histogram).

The peak at maximal disappearance (at $\sin^2 \theta_{23} \approx 0.513$) is due to downward statistical fluctuations in the numbers of events in the bins around the oscillation maximum in some of the toy datasets. When these datasets are fitted, the best fit of $\sin^2 \theta_{23}$ is the value giving the maximum physically-allowed disappearance, i.e. 0.513. This peak is not seen for 7.80×10^{21} POT since downward statistical fluctuations have a smaller effect on the toy datasets at higher statistics.

Distributions of fitter residuals for $\sin^2 \theta_{23}$ and $|\Delta m_{32}^2|$ are shown in Fig. 4.9 for true input values¹³ $\sin^2 \theta_{23} = 0.513$ and $|\Delta m_{32}^2| = 2.40 \times 10^{-3} \text{ eV}^2/\text{c}^4$, for both 6.57×10^{20} POT and 7.80×10^{21} POT. The distribution for $\sin^2 \theta_{23}$ has a large peak at 0.513 as expected, but also two smaller peaks, with one peak in each octant.

¹³Chosen as a point at maximal disappearance.

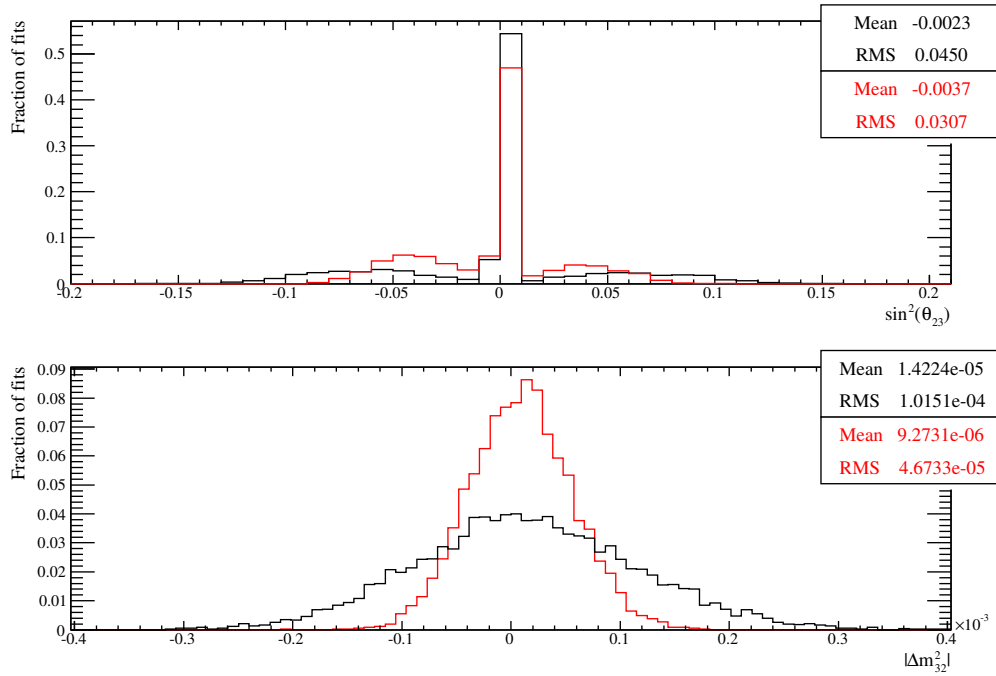


Figure 4.9: Distributions of fitter residuals for $\sin^2 \theta_{23}$ and $|\Delta m_{32}^2|$ for 5000 toy MC experiments, generated at $\sin^2 \theta_{23} = 0.513$ and $|\Delta m_{32}^2| = 2.40 \times 10^{-3} \text{ eV}^2/\text{c}^4$, including statistical fluctuations and with randomised systematic and non-23 oscillation parameters. The distribution is shown for both 6.57×10^{20} POT (Run 1+2+3+4, black histogram) and 7.80×10^{21} POT (the T2K ultimate goal, red histogram).

This can be explained by considering the effects of statistical fluctuations in the bins near the oscillation maximum in the toy datasets. If there are no statistical fluctuations in these bins, the fitted value of $\sin^2 \theta_{23}$ is the same as the input value of 0.513, and downward statistical fluctuations also result in a fitted value of 0.513. However upward statistical fluctuations in these bins in some datasets mean that ν_μ disappearance is less than maximal, and this results in a fitted value of $\sin^2 \theta_{23}$ that is different from the input value of 0.513. The non-maximal values of $\sin^2 \theta_{23}$ returned by the fitter can be quantified by considering the ratio of the number of events in a single bin at the lowest part of the oscillation dip with oscillations to that without oscillations, as shown in Fig. 4.10. Examples of this ratio are shown in Tab. 4.8 for 6.57×10^{20} POT (Run 1+2+3+4) and 7.80×10^{21} POT

(the ultimate T2K goal). As shown in the table, the ratio is $2.672 / 37.93 = 0.070$ at 6.57×10^{20} POT for a dataset without statistical fluctuations. The smallest upward statistical fluctuation that can be made is to 3 events, and this increases the ratio to 0.079; this is the ratio that would be obtained in a dataset made with an input value of $\sin^2 \theta_{23}$ of 0.463 (first octant) or 0.565 (second octant). These input values are close to the values of the non-maximal peaks in the fitted values of $\sin^2 \theta_{23}$ also shown in Tab. 4.8. At 7.80×10^{21} POT, it is necessary to consider upward statistical fluctuations from 31.545 to 32, 33 and 34 events in order to obtain a ratio of number of events with oscillations to that without oscillations corresponding to the values of the non-maximal peaks in the fitted values of $\sin^2 \theta_{23}$. The effect is more complicated than stated here, because it is not a single bin fitter.

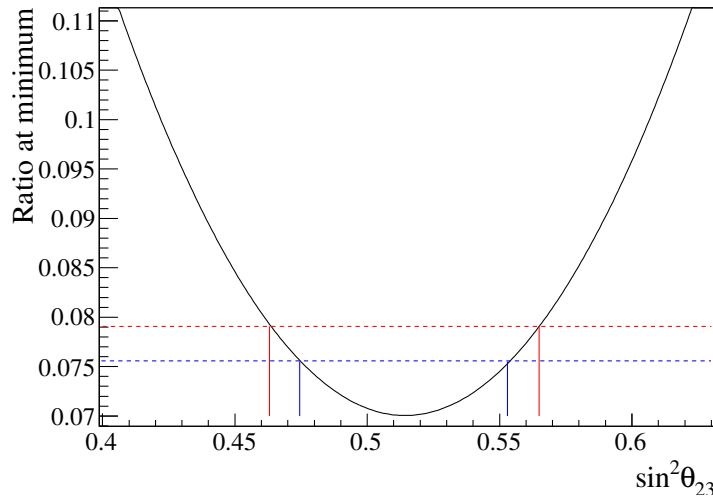


Figure 4.10: Ratio of number of events in a single bin at the lowest part of the oscillation dip for toy datasets created with different input values of $\sin^2 \theta_{23}$ to number without oscillations against the input value of $\sin^2 \theta_{23}$. Red (blue) lines show the value corresponding to the ratio found at 6.57×10^{20} POT (7.80×10^{21} POT, the T2K ultimate POT goal) from Gaussian fits of the $\sin^2 \theta_{23}$ distributions in Fig. 4.9.

Distributions of pulls of the 41 systematic parameters and four non-23 os-

POT	Scenario	Number of events in bin	Ratio: osc / no osc	Input value of $\sin^2 \theta_{23}$ giving this ratio		Peak of non-maximal fitted values of $\sin^2 \theta_{23}$
				Octant 1	Octant 2	
6.57×10^{20}	No oscillations	37.934	1			
	$\sin^2 \theta_{23} = 0.513$ (no fluctuation)	2.672	0.070			
	$\sin^2 \theta_{23} = 0.513$ (fluctuation 1)	3	0.079	0.463	0.565	0.451
7.80×10^{21}	No oscillations	450.352	1			
	$\sin^2 \theta_{23} = 0.513$ (no fluctuation)	31.545	0.070			
	$\sin^2 \theta_{23} = 0.513$ (fluctuation 1)	32	0.071	0.497	0.531	
	$\sin^2 \theta_{23} = 0.513$ (fluctuation 2)	33	0.073	0.484	0.544	0.474
	$\sin^2 \theta_{23} = 0.513$ (fluctuation 3)	34	0.075	0.474	0.553	
	$\sin^2 \theta_{23} = 0.513$ (fluctuation 4)	35	0.078	0.467	0.561	
	$\sin^2 \theta_{23} = 0.513$ (fluctuation 5)	36	0.080	0.461	0.566	

Table 4.8: Numbers of events in a single bin at the lowest part of the oscillation dip with oscillations and ratio to number without oscillations for a true input value $\sin^2 \theta_{23} = 0.513$ at 6.57×10^{20} POT (Run 1+2+3+4) and 7.80×10^{21} POT (the ultimate T2K goal). These numbers are shown without statistical fluctuations and with different upward fluctuations. Also shown are the input values of $\sin^2 \theta_{23}$ to toy datasets from Fig. 4.10 matching the ratio of number of events with oscillations to number without oscillations. These values of $\sin^2 \theta_{23}$ can be compared with the peaks of the non-maximal fitted values of $\sin^2 \theta_{23}$ from Gaussian fits of the $\sin^2 \theta_{23}$ distributions in Fig. 4.9.

illation parameters are shown in Fig. 4.11, for true input values¹⁴ of $\sin^2 \theta_{23} = 0.513$ and $|\Delta m_{32}^2| = 2.40 \times 10^{-3} \text{ eV}^2/\text{c}^4$. In these figures, the pulls are calculated as

$$\frac{f_{\text{bestfit}} - f_{\text{true}}}{\sigma_{\text{bf}}}. \quad (4.11)$$

For most systematics, the distributions are approximately Gaussian with mean 0, width 1, skewness 0, and kurtosis 0. A summary of the pull mean, RMS, skewness, and kurtosis is shown in Fig. 4.12.

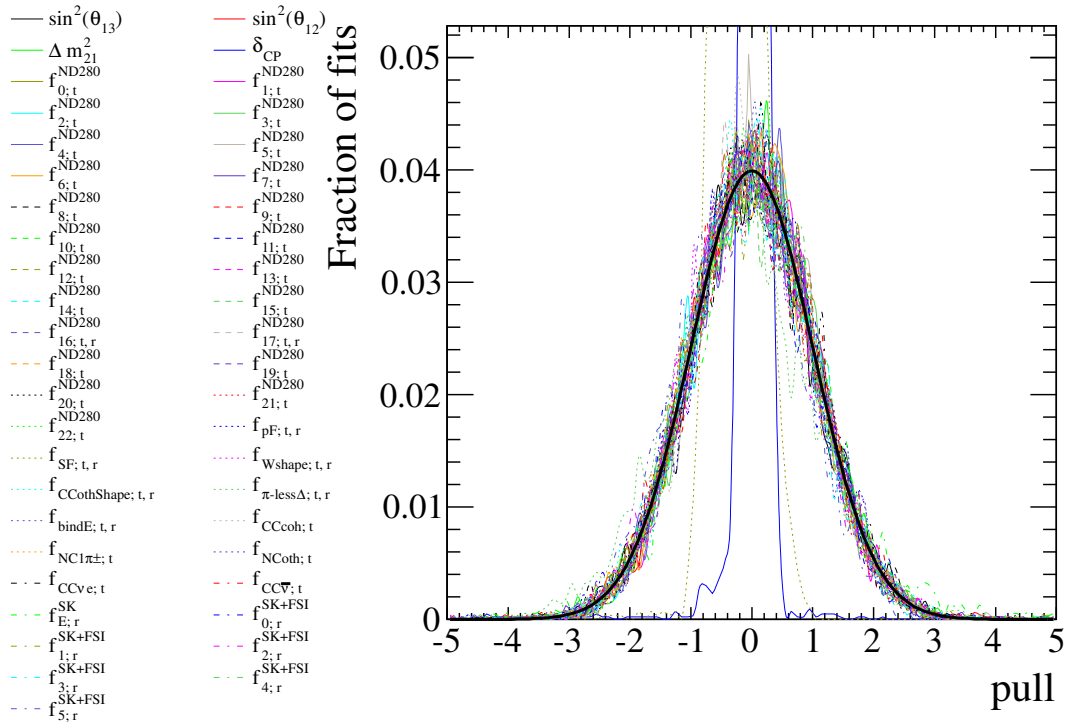


Figure 4.11: Systematic pull distributions for all systematic parameters for 5000 toy MC experiments at 6.57×10^{20} POT generated at $\sin^2 \theta_{23} = 0.513$ and $|\Delta m_{32}^2| = 2.40 \times 10^{-3} \text{ eV}^2/\text{c}^4$, including statistical fluctuations and with randomised systematic parameters. A Gaussian distribution of mean 0, width 1 is shown for reference. The two non-Gaussian parameters are δ_{CP} and $f_{SF;t,r}$.

No problems were identified with the fitter, which performed as expected. There are some small biases in the pull distributions for some systematic param-

¹⁴ $\sin^2 \theta_{23} = 0.370$ and $|\Delta m_{32}^2| = 2.40 \times 10^{-3} \text{ eV}^2/\text{c}^4$ and $\sin^2 \theta_{23} = 0.650$ and $|\Delta m_{32}^2| = 2.40 \times 10^{-3} \text{ eV}^2/\text{c}^4$ have also been studied; there is little dependence on the pull distributions.

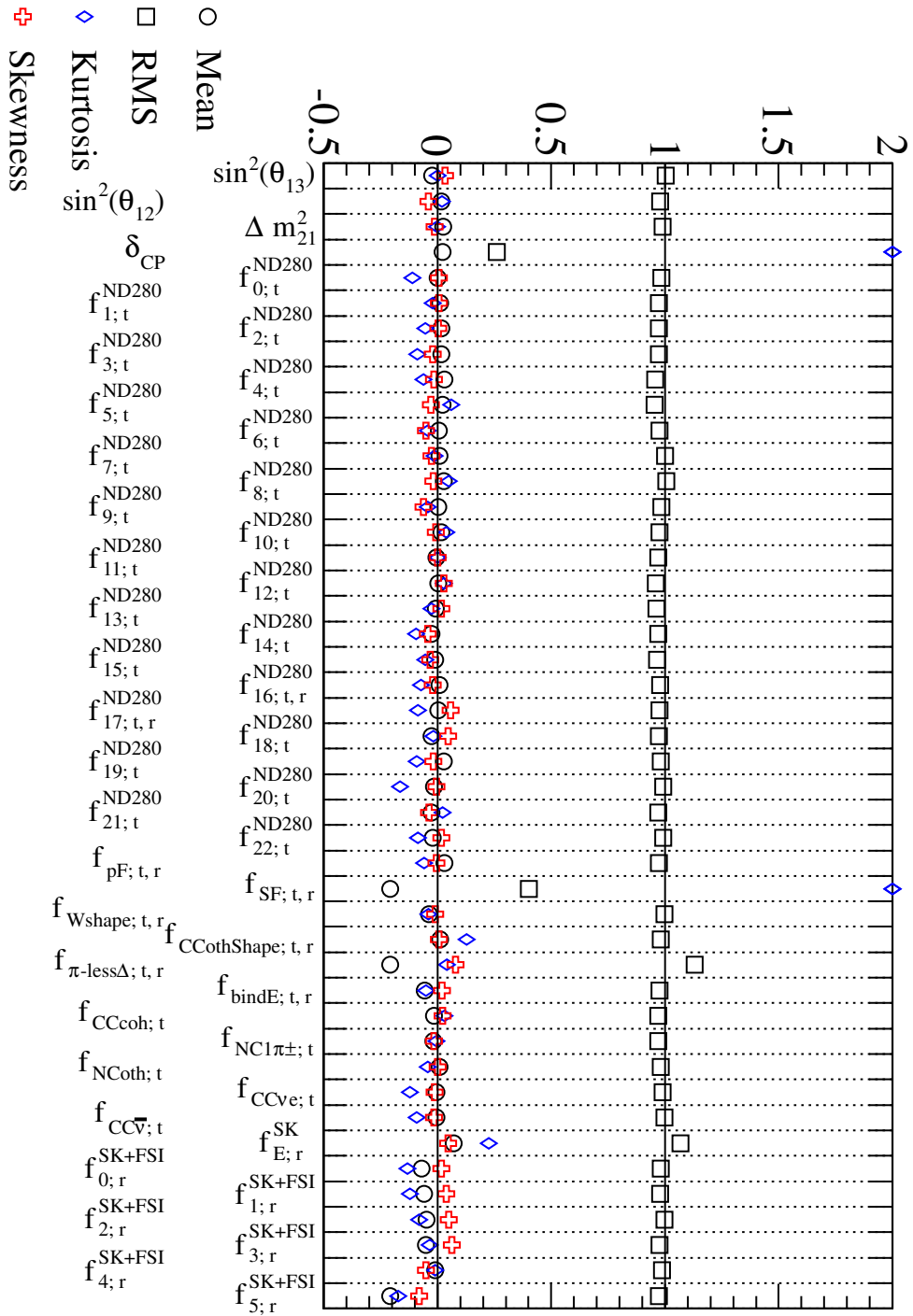


Figure 4.12: Summary of systematic pull distributions for all systematic parameters for 5000 toy MC experiments at 6.57×10^{20} POT generated at $\sin^2 \theta_{23} = 0.513$ and $|\Delta m_{32}^2| = 2.40 \times 10^{-3} \text{ eV}^2/\text{c}^4$, including statistical fluctuations and with randomised systematic parameters. The tests shown are the mean, RMS, skewness and kurtosis.

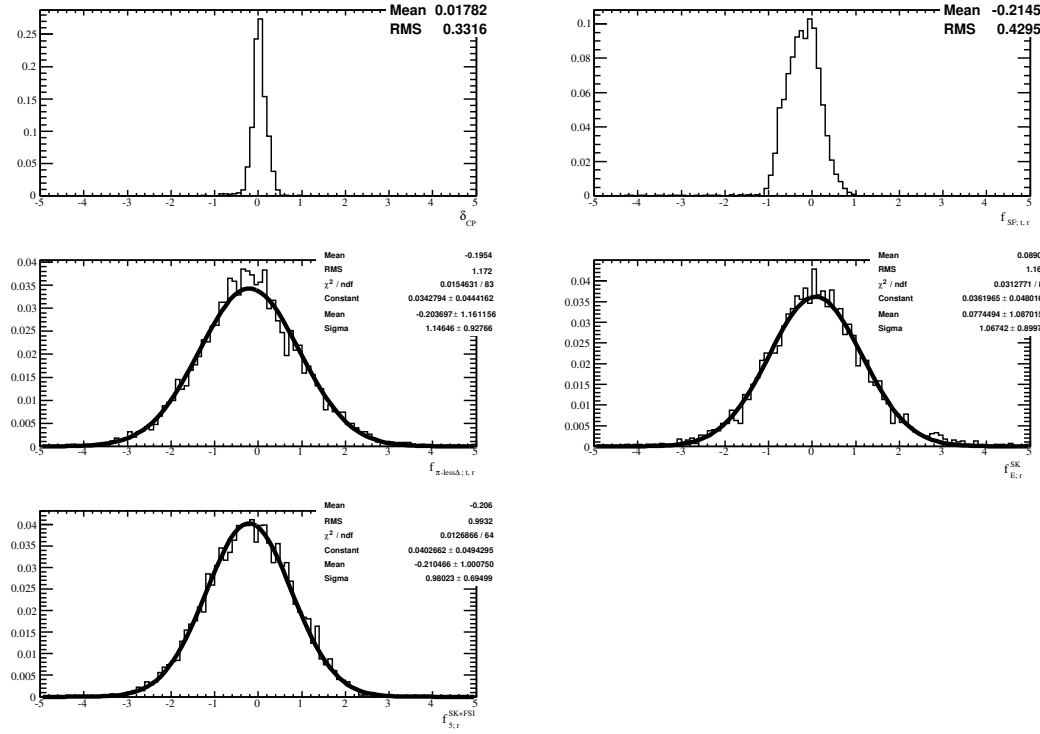


Figure 4.13: Pull distributions for δ_{CP} , $f_{SF; t, r}$, $f_{\pi-less\Delta; t, r}$, $f_{E; r}^{SK}$, and $f_{5; r}^{SK+FSI}$, computed from fits of 5000 toy MC experiments at 6.57×10^{20} POT, generated at $\sin^2 \theta_{23} = 0.513$ and $|\Delta m_{32}^2| = 2.40 \times 10^{-3} \text{ eV}^2/\text{c}^4$, including statistical fluctuations and with randomised systematic parameters.

eters, as shown shown in Fig. 4.13 for input values of $\sin^2 \theta_{23} = 0.513$ and $|\Delta m_{32}^2| = 2.40 \times 10^{-3} \text{ eV}^2/\text{c}^4$, but these biases are understood:

- **δ_{CP} .** This systematic is thrown uniformly between $-\pi$ and $+\pi$ (rather than with a Gaussian distribution), is constrained between $-\pi$ and $+\pi$ in the fit, and has no penalty term. Therefore a Gaussian distribution is not expected.
- **Spectral function: $f_{SF; t, r}$.** This systematic is limited to the range $[0, 1]$, both for toy experiment generation, and in the fit. It is constrained with a Gaussian constraint. Therefore a Gaussian distribution with mean 0, width 1 is not expected.
- **π -less Δ decay: $f_{\pi-less\Delta; t, r}$.** The bias is due to the method of calculation of event weights when this parameter is varied. By default, 20% of Δ reso-

nances decay in this way in NEUT, and the uncertainty is 20%. This means that it is unphysical to change this parameter to be more negative than -1σ . Consequently there is an asymmetry in weights between positive tweaks (which change continuously as the parameter moves away from nominal) and negative tweaks (for which there is no change in the weights below -1σ). This leads to a small negative bias.

- **SK energy scale:** $f_{E;r}^{SK}$. This systematic is different from the others in that it migrates events from bin to bin instead of increasing or decreasing the numbers of events in the bins of reconstructed energy. Its pull is not expected to be a Gaussian with zero mean since the shape of the predicted μ -like ring energy spectrum is not symmetric, and, consequently, a positive modification of this parameter has a different effect on that spectrum from a negative modification, as shown in Fig. 4.14.
- **NC SK detector efficiency + FSI + SI:** $f_{5;r}^{SK+FSI}$. The bias comes from the low statistics at current POT. When Poisson fluctuations are made of the bin contents of the E_{reco} distributions, a downward fluctuation is more likely than an upward fluctuation. For example, a Poisson distribution with mean 3 has $P(1) = 0.149$ and $P(2) = 0.224$, whereas $P(4) = 0.168$ and $P(5) = 0.101$. The NC events are mainly around the oscillation maximum and below (as shown in Figs. 4.2 and 4.15) where there are few events, and downward Poisson fluctuations are more likely than upward ones. Fitting these downward fluctuations involves moving this parameter down from zero, and this explains the negative bias in its pull. When moving away from the point of maximal disappearance as input (and so reducing the depth of the oscillation dip), the NC bin in the SK detector efficiency + FSI + SI matrix bias is reduced.

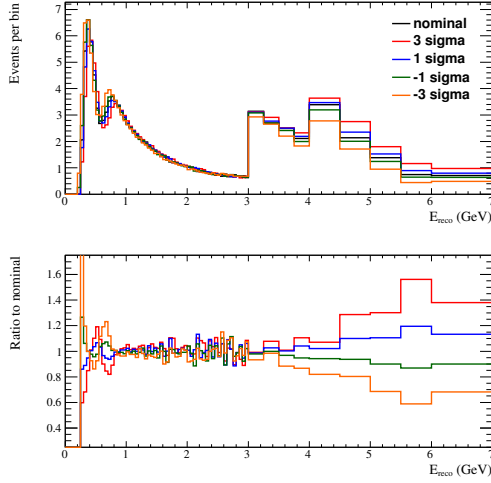


Figure 4.14: Effect of $\pm 3\sigma$ and $\pm 1\sigma$ tweaks of $f_{E;r}^{SK}$ (SK energy scale) on the SK 1 μ -like ring reconstructed energy spectrum, for oscillations with $\sin^2 \theta_{23} = 0.50$ and $|\Delta m_{32}^2| = 2.40 \times 10^{-3} \text{ eV}^2/\text{c}^4$ and for an exposure of 6.57×10^{20} POT. $\sin^2 \theta_{13}$, $\sin^2 \theta_{12}$ and Δm_{21}^2 have the values shown in Tab. 4.2 and $\delta_{CP} = 0$. The normal mass hierarchy is assumed. The effect of the tweaks of $f_{E;r}^{SK}$ are not symmetric.

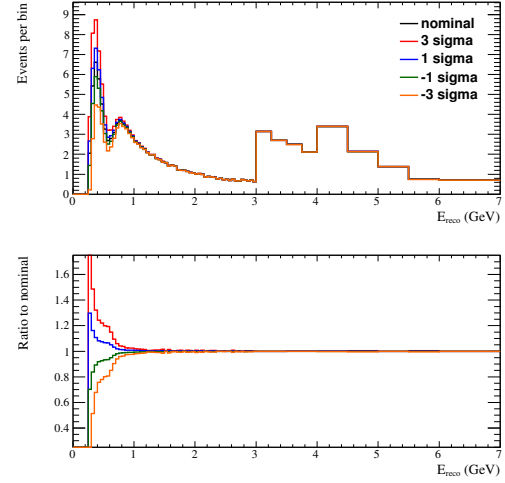


Figure 4.15: Effect of $\pm 3\sigma$ and $\pm 1\sigma$ tweaks of $f_{5;r}^{SK+FSI}$ (NC SK detector efficiency + FSI + SI) on the SK 1 μ -like ring reconstructed energy spectrum, for oscillations with $\sin^2 \theta_{23} = 0.50$ and $|\Delta m_{32}^2| = 2.40 \times 10^{-3} \text{ eV}^2/\text{c}^4$ and for an exposure of 6.57×10^{20} POT. $\sin^2 \theta_{13}$, $\sin^2 \theta_{12}$ and Δm_{21}^2 have the values shown in Tab. 4.2 and $\delta_{CP} = 0$. The normal mass hierarchy is assumed. $f_{5;r}^{SK+FSI}$ has a large effect in the oscillation peak region, and below.

4.3.6 Evaluation of the effects of systematic parameters on the determination of ν_μ disappearance oscillation parameters

The effect of each systematic parameter on the best-fit values of $\sin^2 \theta_{23}$ and $|\Delta m_{32}^2|$ for the normal mass hierarchy was quantified by generating a toy MC experiment with no statistical fluctuations and a $+1\sigma$ tweak of a single systematic parameter. A fit for only $\sin^2 \theta_{23}$ and $|\Delta m_{32}^2|$, with systematics fixed at their nominal values, was performed on that experiment, and the effect of that systematic parameter on the best-fit values of $\sin^2 \theta_{23}$ and $|\Delta m_{32}^2|$ was taken to be the difference between the best-fit values from the experiment with the $+1\sigma$ tweak and the input values of the oscillation parameters. This was repeated

with a toy generated with a -1σ tweak. This procedure was repeated for each systematic parameter in turn. For systematic parameters which are correlated, this procedure was repeated twice, both respecting and ignoring correlations. The study was repeated at multiple input points in the $\sin^2 \theta_{23}$ - $|\Delta m_{32}^2|$ plane.

An estimate of the order of the effect of systematics is given in Tabs. 4.9 and 4.10, ordered by the effect on $\sin^2 \theta_{23}$ and $|\Delta m_{32}^2|$ respectively. To make this estimate, the effect of each systematic is compared with the statistical error for the specific values of $\sin^2 \theta_{23}$ and $|\Delta m_{32}^2|$. The effect of the statistical error was evaluated using 10,000 toy MC datasets with no systematic fluctuations at each input point, with each dataset being fitted for only $\sin^2 \theta_{23}$ and $|\Delta m_{32}^2|$. For each systematic, the largest fractional effect seen in the study is given in the table, whether that is from $+1\sigma$ or -1σ , including or neglecting correlations, and from any true values of $\sin^2 \theta_{23}$ and $|\Delta m_{32}^2|$ in the study.

Parameter	$\frac{\delta_{\text{syst}} \sin^2 \theta_{23}}{\delta_{\text{stat}} \sin^2 \theta_{23}}$	$\frac{\delta_{\text{syst}} \Delta m_{32}^2 (\text{eV}^2/\text{c}^4)}{\delta_{\text{stat}} \Delta m_{32}^2 (\text{eV}^2/\text{c}^4)}$
$f_{5;r}^{SK+FSI}$	1.1773	0.3993
$f_{SF;t,r}$	1.0255	0.3641
$f_{\pi-less\Delta;t,r}$	0.9775	0.2689
$f_{18;t}^{ND280}$	0.9734	0.3171
$f_{3;r}^{SK+FSI}$	0.7611	0.1014
$f_{21;t}^{ND280}$	0.7223	0.1277
$f_{bindE;t,r}$	0.7211	0.4678
$f_{4;t}^{ND280}$	0.6886	0.2540
$f_{16;t,r}^{ND280}$	0.6812	0.2096
$f_{E;r}^{SK}$	0.6529	0.2262
$f_{1;r}^{SK+FSI}$	0.6299	0.0681
$f_{0;r}^{SK+FSI}$	0.6095	0.0573
$f_{NCoth;t}$	0.5898	0.1048
$f_{17;t,r}^{ND280}$	0.5850	0.0810

Parameter	$\frac{\delta_{\text{syst}} \sin^2 \theta_{23}}{\delta_{\text{stat}} \sin^2 \theta_{23}}$	$\frac{\delta_{\text{syst}} \Delta m_{32}^2 (\text{eV}^2 / c^4)}{\delta_{\text{stat}} \Delta m_{32}^2 (\text{eV}^2 / c^4)}$
$f_{NC1\pi^\pm;t}$	0.5830	0.1036
$f_{2;r}^{SK+FSI}$	0.5701	0.0674
$f_{5;t}^{ND280}$	0.5277	0.0987
$f_{1;t}^{ND280}$	0.5266	0.1880
$f_{0;t}^{ND280}$	0.4829	0.1113
$f_{2;t}^{ND280}$	0.4372	0.0991
$f_{Wshape;t,r}$	0.4074	0.0549
$f_{11;t}^{ND280}$	0.3947	0.0722
$f_{3;t}^{ND280}$	0.3907	0.0684
$f_{9;t}^{ND280}$	0.3691	0.0373
$f_{13;t}^{ND280}$	0.3495	0.0333
$f_{7;t}^{ND280}$	0.3484	0.0291
$f_{6;t}^{ND280}$	0.3475	0.0471
$f_{14;t}^{ND280}$	0.3469	0.0238
$f_{8;t}^{ND280}$	0.3450	0.0267
$f_{12;t}^{ND280}$	0.3438	0.0333
$f_{CC\bar{\nu};t}$	0.3421	0.0505
$f_{19;t}^{ND280}$	0.3364	0.0418
$f_{10;t}^{ND280}$	0.3297	0.0312
$f_{CCcothShape;t,r}$	0.3283	0.0281
$f_{CCcoh;t}$	0.3257	0.0460
$f_{4;r}^{SK+FSI}$	0.3046	0.0215
$f_{20;t}^{ND280}$	0.2914	0.0380
$f_{pF;t,r}$	0.2873	0.0732
$f_{15;t}^{ND280}$	0.2683	0.0178
$f_{22;t}^{ND280}$	0.1797	0.0269
$\sin^2 \theta_{13}$	0.1339	0.0084

Parameter	$\frac{\delta_{\text{syst}} \sin^2 \theta_{23}}{\delta_{\text{stat}} \sin^2 \theta_{23}}$	$\frac{\delta_{\text{syst}} \Delta m_{32}^2 (\text{eV}^2/\text{c}^4)}{\delta_{\text{stat}} \Delta m_{32}^2 (\text{eV}^2/\text{c}^4)}$
$\sin^2 \theta_{12}$	0.0568	0.0165
Δm_{21}^2	0.0544	0.0102
δ_{CP}	0.0383	0.1308
$f_{CC\nu_e;t}$	0.0302	0.0006

Table 4.9: Maximum deviations, as a fraction of statistical error at the oscillation parameter grid point, from the input values of fits for only $\sin^2 \theta_{23}$ and $|\Delta m_{32}^2|$ to datasets with $\pm 1\sigma$ individual systematic variations (as defined in Tabs. 3.1, 3.5, and 3.8) at a range of 23-sector oscillation points. $|\Delta m_{32}^2|$ values of $(2.20, 2.50, 2.80) \times 10^{-3} \text{ eV}^2/\text{c}^4$ are used with each of $\sin^2 \theta_{23} = 0.370, 0.500, 0.513, 0.650$. $\sin^2 \theta_{13}$, $\sin^2 \theta_{12}$ and Δm_{21}^2 have the values shown in Tab. 4.2 and $\delta_{CP} = 0$. The parameters are sorted by the size of the deviation in $\sin^2 \theta_{23}$.

Parameter	$\frac{\delta_{\text{syst}} \sin^2 \theta_{23}}{\delta_{\text{stat}} \sin^2 \theta_{23}}$	$\frac{\delta_{\text{syst}} \Delta m_{32}^2 (\text{eV}^2/\text{c}^4)}{\delta_{\text{stat}} \Delta m_{32}^2 (\text{eV}^2/\text{c}^4)}$
$f_{bindE;t,r}$	0.7211	0.4678
$f_{5;r}^{SK+FSI}$	1.1773	0.3993
$f_{SF;t,r}$	1.0255	0.3641
$f_{18;t}^{ND280}$	0.9734	0.3171
$f_{\pi-less\Delta;t,r}$	0.9775	0.2689
$f_{4;t}^{ND280}$	0.6886	0.2540
$f_{E;r}^{SK}$	0.6529	0.2262
$f_{16;t,r}^{ND280}$	0.6812	0.2096
$f_{1;t}^{ND280}$	0.5266	0.1880
δ_{CP}	0.0383	0.1308
$f_{21;t}^{ND280}$	0.7223	0.1277
$f_{0;t}^{ND280}$	0.4829	0.1113
$f_{NCoth;t}$	0.5898	0.1048
$f_{NC1\pi^\pm;t}$	0.5830	0.1036
$f_{3;r}^{SK+FSI}$	0.7611	0.1014
$f_{2;t}^{ND280}$	0.4372	0.0991

Parameter	$\frac{\delta_{\text{syst}} \sin^2 \theta_{23}}{\delta_{\text{stat}} \sin^2 \theta_{23}}$	$\frac{\delta_{\text{syst}} \Delta m_{32}^2 (\text{eV}^2 / c^4)}{\delta_{\text{stat}} \Delta m_{32}^2 (\text{eV}^2 / c^4)}$
$f_{5;t}^{ND280}$	0.5277	0.0987
$f_{17;t,r}^{ND280}$	0.5850	0.0810
$f_{pF;t,r}$	0.2873	0.0732
$f_{11;t}^{ND280}$	0.3947	0.0722
$f_{3;t}^{ND280}$	0.3907	0.0684
$f_{1;r}^{SK+FSI}$	0.6299	0.0681
$f_{2;r}^{SK+FSI}$	0.5701	0.0674
$f_{0;r}^{SK+FSI}$	0.6095	0.0573
$f_{W\text{shape};t,r}$	0.4074	0.0549
$f_{CC\bar{\nu};t}$	0.3421	0.0505
$f_{6;t}^{ND280}$	0.3475	0.0471
$f_{CCcoh;t}$	0.3257	0.0460
$f_{19;t}^{ND280}$	0.3364	0.0418
$f_{20;t}^{ND280}$	0.2914	0.0380
$f_{9;t}^{ND280}$	0.3691	0.0373
$f_{13;t}^{ND280}$	0.3495	0.0333
$f_{12;t}^{ND280}$	0.3438	0.0333
$f_{10;t}^{ND280}$	0.3297	0.0312
$f_{7;t}^{ND280}$	0.3484	0.0291
$f_{CCothShape;t,r}$	0.3283	0.0281
$f_{22;t}^{ND280}$	0.1797	0.0269
$f_{8;t}^{ND280}$	0.3450	0.0267
$f_{14;t}^{ND280}$	0.3469	0.0238
$f_{4;r}^{SK+FSI}$	0.3046	0.0215
$f_{15;t}^{ND280}$	0.2683	0.0178
$\sin^2 \theta_{12}$	0.0568	0.0165
Δm_{21}^2	0.0544	0.0102

Parameter	$\frac{\delta_{\text{syst}} \sin^2 \theta_{23}}{\delta_{\text{stat}} \sin^2 \theta_{23}}$	$\frac{\delta_{\text{syst}} \Delta m_{32}^2 (\text{eV}^2 / c^4)}{\delta_{\text{stat}} \Delta m_{32}^2 (\text{eV}^2 / c^4)}$
$\sin^2 \theta_{13}$	0.1339	0.0084
$f_{CC\nu_e;t}$	0.0302	0.0006

Table 4.10: As in Tab. 4.9, but sorted by the size of the deviation in $|\Delta m_{32}^2|$.

4.3.7 Construction of confidence regions

Construction of 2-dimensional confidence regions

In this analysis, uncertainties in the jointly measured parameters are quoted using both the constant- $\Delta\chi^2$ [31] (Sec. 36) and the Feldman-Cousins [172] methods. The work of Feldman and Cousins uses the freedom which is inherent in the Neyman construction of confidence regions to address cases (in particular, cases with Poisson processes with background and Gaussian errors near a physical boundary) where the classical construction of confidence regions produces over-coverage¹⁵, under-coverage¹⁶, or in extreme cases, an empty region.

The methods differ in the calculation of the critical values of $\Delta\chi^2$, which are used to identify the areas of the parameter space to be included in the allowed region for a given confidence level. The constant- $\Delta\chi^2$ method is a fully frequentist treatment using the Gaussian approximation. One finds the best-fit point and calculates the confidence regions as lines of *constant* $\Delta\chi^2$ from this point¹⁷.

The Feldman-Cousins method finds the critical values of $\Delta\chi^2$ as follows: many toy MC experiment fits are performed for each point of the $(\sin^2 \theta_{23}, |\Delta m_{32}^2| \text{ or } |\Delta m_{31}^2|)$

¹⁵Part of a confidence region in which the stated confidence level is too low; the experimental result stated rejects the false hypothesis less powerfully than the data suggests.

¹⁶Part of a confidence region in which the stated confidence level is too high; the experimental result stated rejects the false hypothesis more powerfully than the data suggests.

¹⁷For 1 fit parameter, the critical values of $\Delta\chi^2$ used are 1.00 (68% C.L.), 2.71 (90% C.L.), 3.84 (95% C.L.), 6.63 (99% C.L.). For 2 parameters fitted simultaneously, the critical values of $\Delta\chi^2$ used are 2.30 (68% C.L.), 4.61 (90% C.L.), 5.99 (95% C.L.), 9.21 (99% C.L.).

2-dimensional grid¹⁸. The value of $\Delta\chi_{\text{MC}}^2$ for each toy MC experiment is calculated as

$$\Delta\chi_{\text{MC}}^2 = \chi^2(\text{MC, true}) - \chi^2(\text{MC, best fit}) \quad (4.12)$$

where “true” means that the χ^2 was computed using the true values of the oscillation parameters at that grid point, and “best-fit” means that the χ^2 was computed using the actual best-fit values for that MC experiment. The χ^2 values are calculated using Eq. 4.10. For each grid point, the critical value of $\Delta\chi^2$ ($\Delta\chi_{\text{critical}}^2$) is found such that a fraction α of the toy MC experiments have $\Delta\chi_{\text{MC}}^2 < \Delta\chi_{\text{critical}}^2$, where α is the desired confidence level.

The principal difference between the Feldman-Cousins and the constant- $\Delta\chi^2$ methods is that the former determines the value of $\Delta\chi_{\text{critical}}^2$ individually for each grid point, whereas the latter uses the same value for all grid points.

The procedure for constructing the $\Delta\chi^2$ ($\sin^2 \theta_{23}$, $|\Delta m_{32}^2|$ or $|\Delta m_{31}^2|$) surface itself from data or a toy MC experiment is common to both methods. Assuming that N nuisance parameters are allowed to float in the oscillation fit, the values of χ^2 ($\sin^2 \theta_{23}$, $|\Delta m_{32}^2|$ or $|\Delta m_{31}^2|$; \mathbf{a}) are calculated via a fit at *each* point of the ($\sin^2 \theta_{23}$, $|\Delta m_{32}^2|$ or $|\Delta m_{31}^2|$) 2-dimensional grid, where only the nuisance parameters are allowed to float and $\sin^2 \theta_{23}$, $|\Delta m_{32}^2|$ or $|\Delta m_{31}^2|$ are fixed to the true values for the given grid point.

The allowed region in the 2-dimensional oscillation parameter space is then given by

$$\begin{aligned} \Delta\chi^2(\sin^2 \theta_{23}, |\Delta m_{32}^2| \text{ or } |\Delta m_{31}^2|) &= \chi^2(\sin^2 \theta_{23}, |\Delta m_{32}^2| \text{ or } |\Delta m_{31}^2|; \mathbf{a}) - \chi_{\text{min}}^2 \\ &< \Delta\chi_{\text{critical}}^2 \end{aligned} \quad (4.13)$$

where χ_{min}^2 is the minimum value of χ^2 ($\sin^2 \theta_{23}$, $|\Delta m_{32}^2|$ or $|\Delta m_{31}^2|$; \mathbf{a}) from the fit of the data or toy MC experiment over the oscillation parameter space considered.

¹⁸For 2-dimensional regions, the following grid spacing is used when finding the Feldman-Cousins $\Delta\chi_{\text{critical}}^2$ MC estimation: $\delta(\sin^2 \theta_{23}) = 0.005$ and $\delta(|\Delta m_{32}^2|)$ or $\delta(|\Delta m_{31}^2|) = 0.05 \times 10^{-3} \text{ eV}^2/\text{c}^4$.

The Feldman-Cousins method does not specify how systematics are to be included in the confidence region construction and different choices exist. This analysis requires the construction of a 2-dimensional ($\sin^2 \theta_{23}$, $|\Delta m_{32}^2|$ or $|\Delta m_{31}^2|$) confidence region, where N_s systematic parameters are included in the p.d.f. and all of these N_s systematics are allowed to float in the fit. The methodology is to calculate the value of $\Delta\chi^2_{\text{critical}}$ at each true ($\sin^2 \theta_{23}$, $|\Delta m_{32}^2|$ or $|\Delta m_{31}^2|$) grid point using an ensemble of 10,000 toy MC experiments, each one of which is generated with the true oscillation parameters of that point and with all N_s systematics randomised. For each toy MC experiment, both $\sin^2 \theta_{23}$, $|\Delta m_{32}^2|$ or $|\Delta m_{31}^2|$ and all N_s nuisance parameters are fitted simultaneously to obtain the value of $\chi^2(\text{MC, best fit})$ used in Eq. 4.12. A separate fit, with $\sin^2 \theta_{23}$, $|\Delta m_{32}^2|$ or $|\Delta m_{31}^2|$ fixed to their true values and with all N_s nuisance parameters allowed to float, is performed to obtain the value of $\chi^2(\text{MC, true})$ (i.e. χ^2 is *independently* minimised, for *each* toy MC experiment, with respect to the nuisance parameters).

In Fig. 4.16, a MC estimation of the 2-dimensional Feldman-Cousins $\Delta\chi^2_{\text{critical}}$ values used for calculation of the 68% and 90% C.L. confidence regions for the normal mass hierarchy is shown¹⁹. One-dimensional slices of these $\Delta\chi^2_{\text{critical}}$ surfaces along $\sin^2 \theta_{23}$ and $|\Delta m_{32}^2|$ are shown in Figs. 4.17 and 4.18 respectively. The Feldman-Cousins values of $\Delta\chi^2_{\text{critical}}$ are lower than the canonical constant- $\Delta\chi^2_{\text{critical}}$ values when the true input value of $\sin^2 \theta_{23}$ is near the value of maximal ν_μ disappearance. Under these circumstances, the best-fit values of $\sin^2 \theta_{23}$ pile-up at the value of maximal disappearance, and this gives lower values of $\Delta\chi^2$ than would be obtained if that boundary did not exist. Consequently, the 68% and 90% critical $\Delta\chi^2$ values are lower than the canonical constant- $\Delta\chi^2$ values. The equivalent plots for $\sin^2 \theta_{23}$ and $|\Delta m_{31}^2|$ in the inverted mass hierarchy show the same features.

¹⁹ $\Delta\chi^2_{\text{critical}}$ is not calculated at all points on the $\sin^2 \theta_{23}$ and $|\Delta m_{32}^2|$ or $|\Delta m_{31}^2|$ grid for the Feldman-Cousins method due to CPU constraints. However it is calculated in all places required to form 68% and 90% C.L. regions.

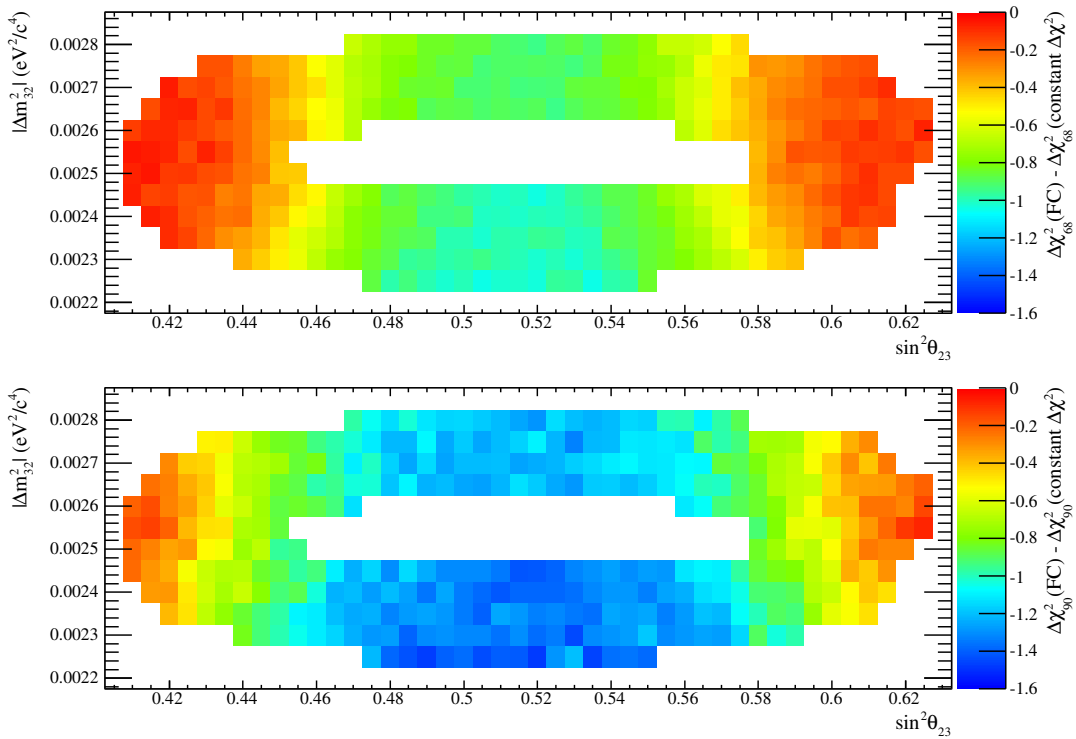


Figure 4.16: Difference between the $\Delta\chi^2_{\text{critical}}$ values obtained from the Feldman-Cousins method [172] and those from the constant- $\Delta\chi^2$ method at confidence levels of 68% (top) and 90% (bottom), as a function of $\sin^2 \theta_{23}$ and $|\Delta m^2_{32}|$. These surfaces were generated from an ensemble of toy MC experiments including both randomised systematic variations and statistical fluctuations. As expected from [172], the Feldman-Cousins $\Delta\chi^2_{\text{critical}}$ values decrease as maximal ν_μ disappearance at $\sin^2 \theta_{23} \approx 0.513$ is approached. The normal mass hierarchy is assumed. $\Delta\chi^2_{\text{critical}}$ is not calculated at all points for the Feldman-Cousins method, due to CPU constraints, but is calculated in all places required to form 68% and 90% C.L. regions.

Construction of 1-dimensional confidence regions

Confidence regions are also constructed separately for each of $\sin^2 \theta_{23}$ and $|\Delta m^2_{32}|$ (NH) or $|\Delta m^2_{31}|$ (IH). These can be found in a straightforward way by calculating the 1-dimensional profile likelihood for each parameter, and finding the values of each parameter corresponding to the constant- $\Delta\chi^2$ for one parameter and the desired confidence level (e.g. $\Delta\chi^2 = 1.0$ for 68% C.L.). Unfortunately, however, there is no standard procedure in the literature for constructing 1-dimensional Feldman-Cousins confidence regions from 2-dimensional confidence regions. To find the 1-dimensional

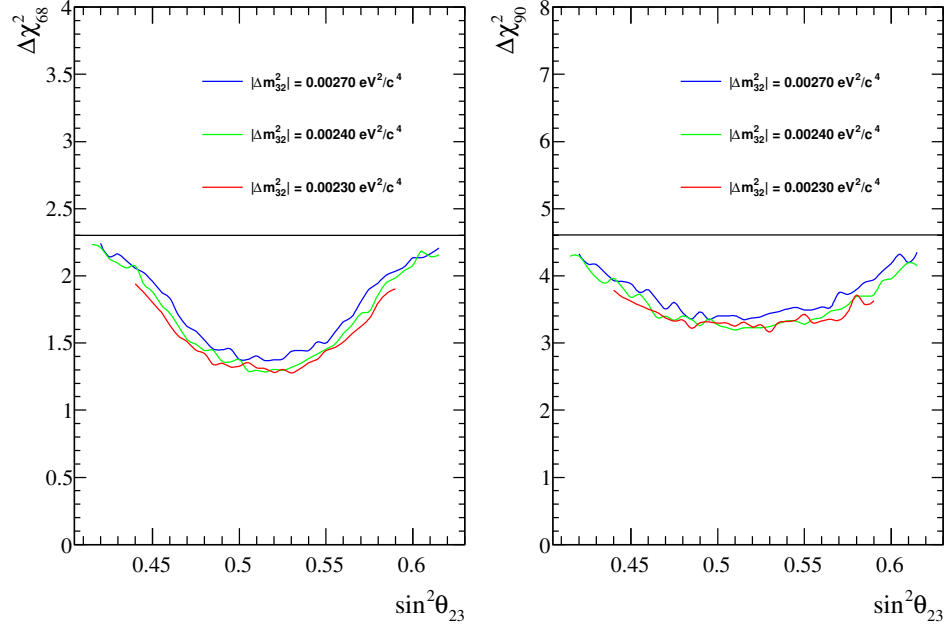


Figure 4.17: One-dimensional slices through the 68% (left) and 90% (right) 2-dimensional surfaces of Feldman-Cousins $\Delta\chi^2_{\text{critical}}$ values as a function of $\sin^2\theta_{23}$ for 3 different values of $|\Delta m^2_{32}|$ ($2.30 \times 10^{-3} \text{ eV}^2/\text{c}^4$, $2.40 \times 10^{-3} \text{ eV}^2/\text{c}^4$ and $2.70 \times 10^{-3} \text{ eV}^2/\text{c}^4$). The $\Delta\chi^2_{\text{critical}}$ values were calculated from an ensemble of toy MC experiments, for an exposure of 6.57×10^{20} POT, including both randomised systematic variations and statistical fluctuations. For comparison, the canonical value used in the constant- $\Delta\chi^2$ method is also shown as a horizontal line. The normal mass hierarchy is assumed. $\Delta\chi^2_{\text{critical}}$ is calculated in all places required to form 68% and 90% C.L. regions.

regions, values of $\Delta\chi^2_{\text{critical}}$ need to be computed, as a function of the corresponding oscillation parameter, using an ensemble of toy MC experiments. One issue concerns the choice of the true input value(s) of the *other* oscillation parameter in those experiments. For example, the true input values of $|\Delta m^2_{32}|$ (NH) or $|\Delta m^2_{31}|$ (IH) must be chosen for the toy MC experiment ensemble used for constructing the confidence region in $\sin^2\theta_{23}$. One option in this case would be to use the data or toy MC experiment best-fit value of $|\Delta m^2_{32}|$ or $|\Delta m^2_{31}|$ as the true input value for all the toy MC experiments, but this fails to account for the uncertainty in $|\Delta m^2_{32}|$ or $|\Delta m^2_{31}|$. Alternatively, a uniform distribution of true input values of $|\Delta m^2_{32}|$ or $|\Delta m^2_{31}|$ could be used in some range, say from $2-3 \times 10^{-3} \text{ eV}^2/\text{c}^4$, but this ignores the fact that some values of $|\Delta m^2_{32}|$ or $|\Delta m^2_{31}|$ are preferred by the T2K data to others.

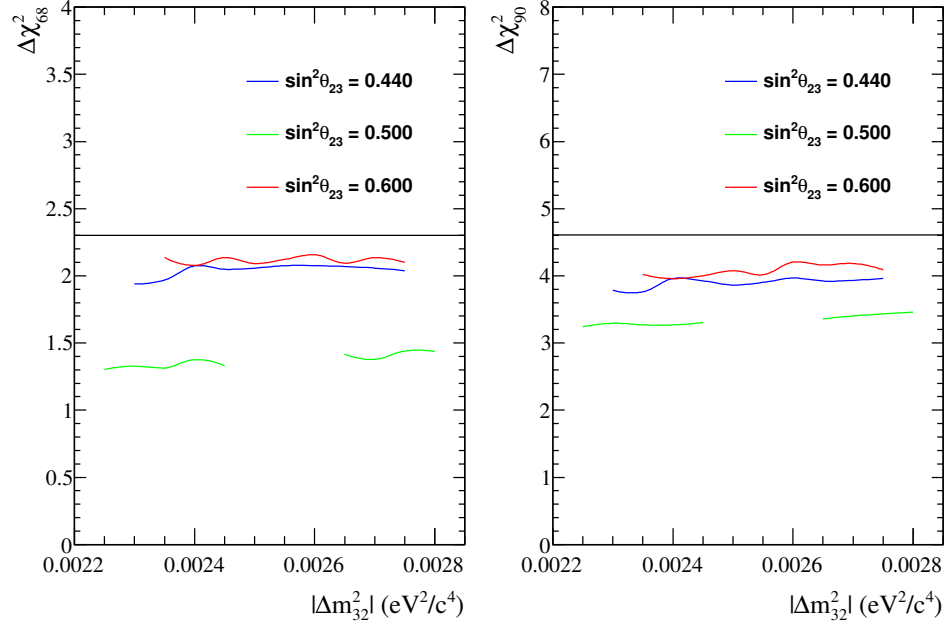


Figure 4.18: One-dimensional slices through the 68% (left) and 90% (right) 2-dimensional surfaces of Feldman-Cousins $\Delta\chi^2_{\text{critical}}$ values as a function of $|\Delta m_{32}^2|$ for 3 different values of $\sin^2 \theta_{23}$ (0.44, 0.50 and 0.60). The $\Delta\chi^2_{\text{critical}}$ values were calculated from an ensemble of toy MC experiments, for an exposure of 6.57×10^{20} POT, including both randomised systematic variations and statistical fluctuations. For comparison, the canonical value used in the constant- $\Delta\chi^2$ method is also shown as a horizontal line. The normal mass hierarchy is assumed. $\Delta\chi^2_{\text{critical}}$ is calculated in all places required to form 68% and 90% C.L. regions.

In this analysis, the true input values of $|\Delta m_{32}^2|$ or $|\Delta m_{31}^2|$ are chosen using the likelihood from the fit from data or a toy MC experiment. At each true value of $\sin^2 \theta_{23}$, the numbers of toy MC experiments with a given true input value of $|\Delta m_{32}^2|$ or $|\Delta m_{31}^2|$ are proportional to $e^{-\frac{\Delta\chi^2}{2}}$, where $\Delta\chi^2$ is the value of the 2-dimensional $\Delta\chi^2$ surface at those values of $\sin^2 \theta_{23}$ and $|\Delta m_{32}^2|$ or $|\Delta m_{31}^2|$ from the fit of the data or toy MC experiment. An example of the distribution of true input values of $|\Delta m_{32}^2|$ is shown in Fig. 4.19 for a fixed input value of $\sin^2 \theta_{23} = 0.55$, using the T2K Run 1+2+3+4 data. Each toy MC experiment is fitted twice; in one fit, $\sin^2 \theta_{23}$, $|\Delta m_{32}^2|$ or $|\Delta m_{31}^2|$ and all the nuisance parameters are allowed to float, and, in the other, $|\Delta m_{32}^2|$ or $|\Delta m_{31}^2|$ and the nuisance parameters are allowed to float while $\sin^2 \theta_{23}$ is fixed to its true value. For each experiment, $\Delta\chi^2_{\text{MC}}$ is calculated as the difference between the minimum values of χ^2

from the two fits. The critical value of $\Delta\chi^2$ at each true value of $\sin^2\theta_{23}$ is found by combining all the toy MC experiments with that input value of $\sin^2\theta_{23}$ and different true input values of $|\Delta m_{32}^2|$ or $|\Delta m_{31}^2|$. It is the value of $\Delta\chi^2$ such that α of the toy experiments have $\Delta\chi_{\text{MC}}^2 < \Delta\chi_{\text{critical}}^2$, where α is the desired confidence level.

The 1-dimensional Feldman-Cousins confidence regions in $|\Delta m_{32}^2|$ or $|\Delta m_{31}^2|$ are constructed in an analogous way. An example of the distribution of true input values of $\sin^2\theta_{23}$ for a fixed input value of $|\Delta m_{32}^2| = 2.9 \times 10^{-3} \text{ eV}^2/\text{c}^4$ is given in Fig. 4.20, using the T2K Run 1+2+3+4 data.

The results of the Feldman-Cousins $\Delta\chi_{\text{critical}}^2$ MC estimation of critical $\Delta\chi^2$ values are shown in Sec. 4.4.3.

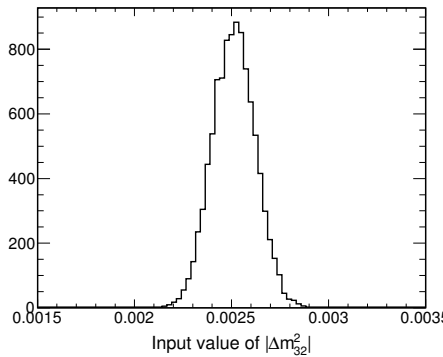


Figure 4.19: True input values of $|\Delta m_{32}^2|$ to the toy MC experiments used to find the 1-dimensional critical value of $\Delta\chi^2$ for $\sin^2\theta_{23} = 0.55$. The normal mass hierarchy is assumed.

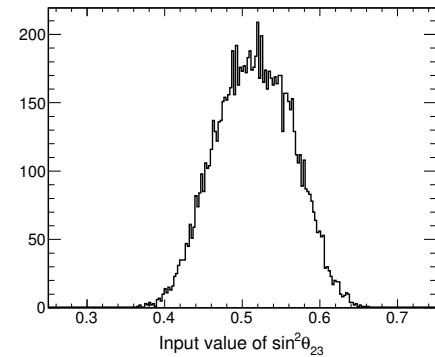


Figure 4.20: True input values of $\sin^2\theta_{23}$ to the toy MC experiments used to find the 1-dimensional critical value of $\Delta\chi^2$ for $|\Delta m_{32}^2| = 2.90 \times 10^{-3} \text{ eV}^2/\text{c}^4$. The normal mass hierarchy is assumed.

4.3.8 Sensitivity for the joint determination of ν_μ disappearance oscillation parameters

Two-dimensional sensitivity regions were computed for 6.57×10^{20} POT (the T2K Run 1+2+3+4 POT) by averaging the regions of 300 toy MC experiments generated with statistical fluctuations and all systematic parameters randomised. The sensitivity has

been calculated at three points:

1. The MINOS best-fit point in the inverted mass hierarchy, $\sin^2 \theta_{23} = 0.41$, $|\Delta m_{31}^2| = 2.33 \times 10^{-3} \text{ eV}^2/\text{c}^4$ [178], as shown in Fig. 4.21;
2. The SK best-fit point in the normal mass hierarchy, $\sin^2 \theta_{23} = 0.60$, $|\Delta m_{32}^2| = 2.82 \times 10^{-3} \text{ eV}^2/\text{c}^4$ [179], as shown in Fig. 4.22;
3. A test point at maximal mixing in the normal mass hierarchy, $\sin^2 \theta_{23} = 0.50$, $|\Delta m_{32}^2| = 2.40 \times 10^{-3} \text{ eV}^2/\text{c}^4$, as shown in Fig. 4.23.

Without knowing the MINOS and SK sensitivities, and thus not knowing whether their results are favourable or unfavourable fluctuations, it is not possible to say which experiment is the most sensitive with their current data. What can be inferred is that, if the T2K best-fit point lies away from maximal mixing or maximal disappearance, the region is expected to cover a similar range in $\sin^2 \theta_{23}$ as MINOS and SK, and be slightly looser and tighter in $|\Delta m_{32}^2|$ than MINOS and SK respectively. If however the T2K best-fit point lies close to maximal mixing, with current statistics, T2K should provide a tighter constraint on $\sin^2 \theta_{23}$ than both MINOS (10.71×10^{20} POT for ν_μ -dominated beam data, 3.36×10^{20} POT for $\bar{\nu}_\mu$ -dominated beam data, and 37.88 kt – years of atmospheric data) and SK (over 11 live-years of atmospheric data).

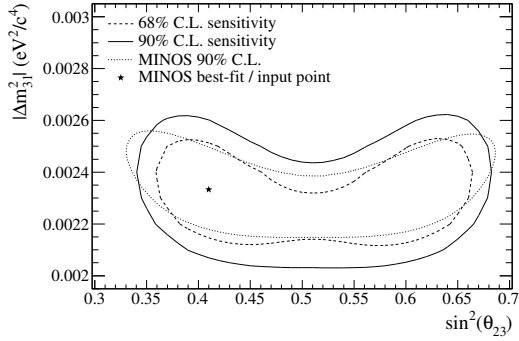


Figure 4.21: Comparison between the MINOS 90% C.L. allowed region [178] and the results of a sensitivity study at the MINOS best-fit point ($\sin^2 \theta_{23} = 0.41$, $|\Delta m^2_{31}| = 2.33 \times 10^{-3} \text{ eV}^2/\text{c}^4$) for statistical+systematic MC toys and 6.57×10^{20} POT. The inverted mass hierarchy is assumed. All regions are constructed using the constant- $\Delta\chi^2$ method.

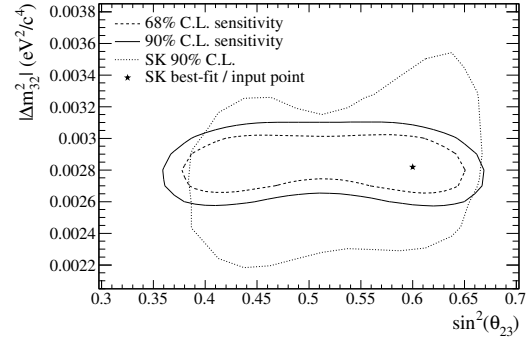


Figure 4.22: Comparison between the SK 90% C.L. allowed region [179] and the results of a sensitivity study at the SK best-fit point ($\sin^2 \theta_{23} = 0.60$, $|\Delta m^2_{32}| = 2.82 \times 10^{-3} \text{ eV}^2/\text{c}^4$) for statistical+systematic MC toys and 6.57×10^{20} POT. The normal mass hierarchy is assumed. All regions are constructed using the constant- $\Delta\chi^2$ method.

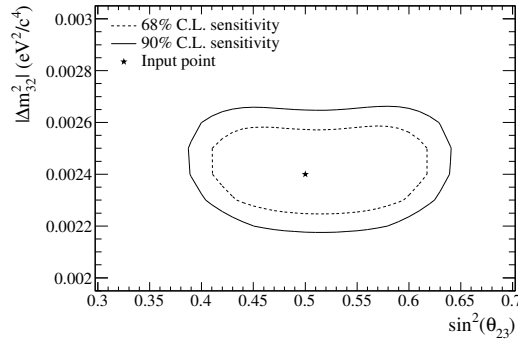


Figure 4.23: Results of a sensitivity study at the point ($\sin^2 \theta_{23} = 0.50$, $|\Delta m^2_{32}| = 2.40 \times 10^{-3} \text{ eV}^2/\text{c}^4$) for statistical+systematic MC toys and 6.57×10^{20} POT. The normal mass hierarchy is assumed. Regions are constructed using the constant- $\Delta\chi^2$ method.

4.4 Results

Two 3-flavour ν_μ -disappearance fits were performed on the 6.57×10^{20} POT T2K Run 1+2+3+4 dataset, using the method described in Sec. 4.3.3. In the first fit, the normal mass hierarchy was assumed, and $\sin^2 \theta_{23}$ and $|\Delta m_{32}^2|$ were allowed to float, while, in the second fit, the inverted mass hierarchy was assumed and $\sin^2 \theta_{23}$ and $|\Delta m_{31}^2|$ were allowed to float. In both fits, all 41 systematic parameters considered in this analysis and the oscillation parameters $\sin^2 \theta_{12}$, $\sin^2 \theta_{13}$, Δm_{21}^2 and δ_{CP} were also allowed to float. The best-fit values were $\sin^2 \theta_{23} = 0.514$ and $|\Delta m_{32}^2| = 2.51 \times 10^{-3} \text{ eV}^2/\text{c}^4$ assuming the normal mass hierarchy, and $|\Delta m_{31}^2| = 2.48 \times 10^{-3} \text{ eV}^2/\text{c}^4$ and $\sin^2 \theta_{23} = 0.511$ assuming the inverted mass hierarchy.

An identical analysis was also carried out separately on both the 3.01×10^{20} POT Run 1+2+3 and 3.56×10^{20} POT Run 4 T2K datasets for the normal mass hierarchy only. Similar best-fit values were obtained from these fits of subsets of the full dataset; the run periods are consistent. The fit to the Run 1+2+3 dataset gave best-fit values of $\sin^2 \theta_{23} = 0.514$ and $|\Delta m_{32}^2| = 2.46 \times 10^{-3} \text{ eV}^2/\text{c}^4$ while a fit to the Run 4 dataset gave $\sin^2 \theta_{23} = 0.514$ and $|\Delta m_{32}^2| = 2.55 \times 10^{-3} \text{ eV}^2/\text{c}^4$.

The results of these fits are summarised in Tab. 4.11. In this table are the best-fit oscillation parameters, the observed and expected numbers of 1 μ -like ring events, and the values of χ^2 per *dof* at the best fit. The stated *dof* (70) corresponds to the number of bins used in the fit (73), minus the number of unconstrained parameters (3: $\sin^2 \theta_{23}$, $|\Delta m_{32}^2|$ or $|\Delta m_{31}^2|$, and δ_{CP}).

The pull for each systematic parameter f included in the fit was calculated as

$$\frac{f_{\text{bestfit}} - f_{\text{nominal}}}{\sigma}, \quad (4.14)$$

where f_{bestfit} is the best-fit value of the systematic parameter, f_{nominal} is the nominal value of the parameter (corresponding to no systematic variation), and σ is either σ_{input} (the prefit error)²⁰ or σ_{bf} (the HESSE error output from MINUIT).

²⁰For δ_{CP} , σ_{input} is taken to be π .

Mass hierarchy	Run period	$\sin^2 \theta_{23}$	$ \Delta m^2 / \text{eV}^2$	n^{obs}	n^{exp}	$\chi^2_{\text{bf}} / \text{dof}$	p-value
Normal	Run 1+2+3+4	0.514	2.51	120	121.46	62.34/70	0.93
	Run 1+2+3+4	0.511	$2.48 \cdot 10^{-3}$	120	121.42	62.34/70	0.93
Inverted	Run 4	0.514	$2.46 \cdot 10^{-3}$	61	57.08	57.93/70	0.80
	Run 1+2+3	0.514	$2.55 \cdot 10^{-3}$	59	64.10	70.79/70	0.72
Normal	Run 1+2+3	0.514	$2.44 \cdot 10^{-3}$	58	57.97	56.04/71	0.83
2012 Normal							

Table 4.11: Summary of best-fit parameters from the fits of the Run 1+2+3, Run 4, and combined Run 1+2+3+4 datasets. In this table, $|\Delta m^2|$ is $|\Delta m^2_{32}|$ for normal mass hierarchy, and $|\Delta m^2_{31}|$ for inverted mass hierarchy. The 2012 result is taken from the analysis presented in [180] (note that the difference in n^{obs} between 2012 and 2013 for the Run 1+2+3 dataset is due to a reanalysis of the data [168]). The quoted best-fit χ^2 values (χ^2_{bf}) were computed from Eq. 4.10 in Sec. 4.3.2. using the 73-bin reconstructed energy binning scheme given in Sec. 4.1.2. The table also shows the p-values obtained from the goodness-of-fit test described in Sec. 4.3.4 for all fits.

The pulls of all 45 nuisance parameters allowed to float in the fit are shown in Fig. 4.24, and the ratio of σ_{bf} to σ_{input} is shown in Fig. 4.25, assuming the normal mass hierarchy. From these figures, it is apparent that most systematic parameters barely move from their nominal values. It should be noted that, although all 45 nuisance parameters are allowed to float in the fit, only 4(5) of them move by more than $\pm 0.1\sigma_{\text{bf}}$ for the normal(inverted) mass hierarchy fit. When a systematic parameter that is free to move stays close to its nominal value, it means that the reduction in χ^2 from moving that parameter is less than the corresponding increase in the penalty term defined in Eq. 4.10 in Sec. 4.3.2. Only certain systematics are able to change the predicted reconstructed energy spectrum to a sufficient extent to offset the penalty term.

Goodness-of-fit tests were performed as described in Sec. 4.3.4, and the p-values from the fits of the Run 1+2+3+4 dataset, Run 1+2+3 and Run 4 datasets are shown in Tab. 4.11. The χ^2 distribution from which these p-values were calculated are shown for the Run 1+2+3+4 data in Figs. 4.26 for the Run 1+2+3+4 fit assuming the normal mass hierarchy. All fits have a high degree of plausibility.

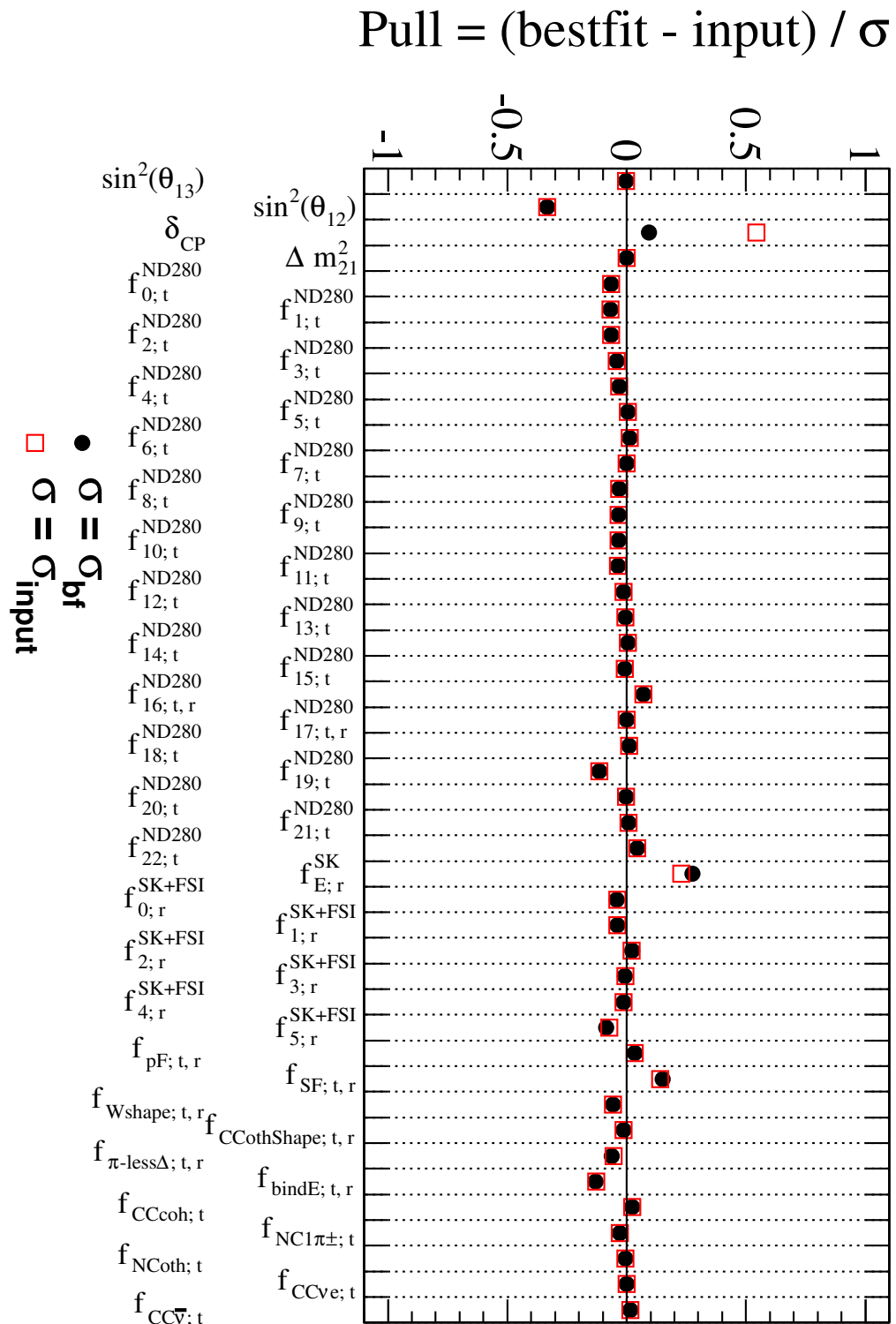


Figure 4.24: Systematic parameter pulls from the fit of the Run 1+2+3+4 dataset. The normal mass hierarchy is assumed.

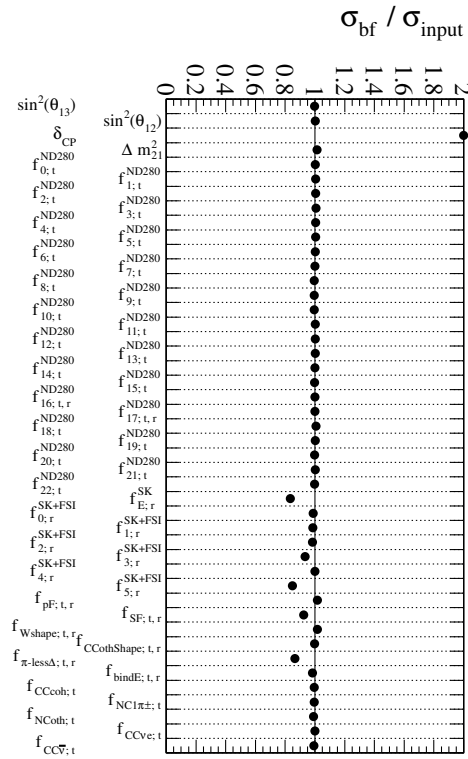


Figure 4.25: Ratio of σ_{bf} to σ_{input} from the fit of the Run 1+2+3+4 dataset. The normal mass hierarchy is assumed.

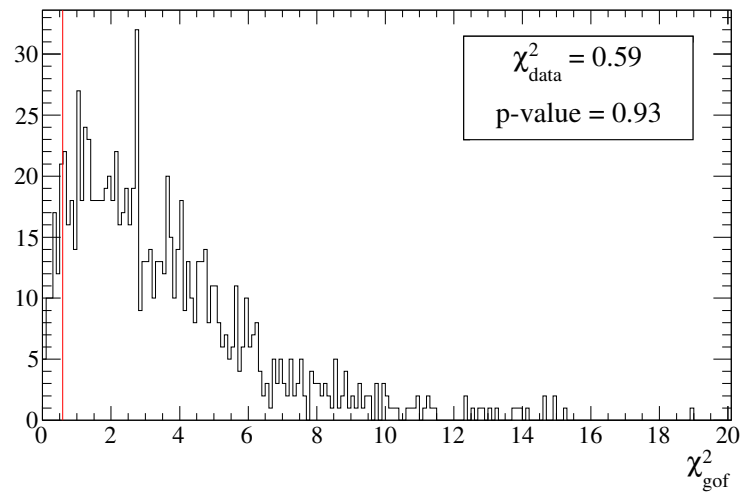


Figure 4.26: Distribution of χ^2_{gof} (the goodness-of-fit (gof) χ^2) from 1k toy MC experiments whose true input values were the Run 1+2+3+4 best-fit oscillation parameters. The χ^2_{gof} value from the fit of the Run 1+2+3+4 data (χ^2_{data}) is highlighted. The normal mass hierarchy is assumed.

4.4.1 Best-fit 1 μ -like ring reconstructed energy spectra

The reconstructed neutrino energy distribution of the 1 μ -like ring events in the Run 1+2+3+4 dataset is shown in Fig. 4.27 along with the best-fit predicted spectrum assuming the normal mass hierarchy and the predicted spectrum under the no-oscillation hypothesis. Also shown is the ratio of the data to the no-oscillation spectrum and the ratio of the best-fit spectrum to the no-oscillation spectrum; in both of these ratios, the characteristic energy-dependent deficit can be clearly seen. Since the reconstructed energy binning used in the fit is relatively fine, some plots use a coarser binning scheme²¹ in, rather than the 73-bin scheme in reconstructed neutrino energy that was used in the fitting procedure (see Sec. 4.1.2), in order to have at least one data event in each bin.

It is interesting to see the components of the best-fit predicted spectrum, and these are shown in Fig. 4.28 for the normal mass hierarchy. In these plots, the 32 components of the predicted spectrum are grouped into five categories: $\nu_\mu/\nu_e \rightarrow \nu_\mu$ CCQE, $\nu_\mu/\nu_e \rightarrow \nu_\mu$ CCnonQE, $\bar{\nu}_\mu$ CC, $\nu_e/\bar{\nu}_e/\nu_\mu \rightarrow \nu_e$ CC, and NC (though each of the 32 components is calculated separately in the actual analysis). It can be seen that $\nu_\mu/\nu_e \rightarrow \nu_\mu$ CCQE, which has the most accurate E_{reco} determination, dominates the region from 0.3–2.0 GeV, with the largest background coming from NC events below the oscillation peak, and $\nu_\mu/\nu_e \rightarrow \nu_\mu$ CCnonQE events in and above the oscillation peak.

The best-fit predicted spectra for the normal and inverted mass hierarchies are compared for the Run 1+2+3+4 dataset in Fig. 4.29, using the coarser binning described above. These two best-fit spectra are nearly identical.

²¹20 reconstructed energy bins arranged as follows: 10 0.1-GeV bins from 0 - 1.0 GeV, 3 0.2-GeV bins from 1.0 - 1.6 GeV, 1 0.4-GeV bin from 1.6 - 2.0 GeV, 2 0.5-GeV bins from 2.0 - 3.0 GeV, 1 1-GeV bin from 3.0 - 4.0 GeV, 1 3-GeV bin from 4.0 - 7.0 GeV, 1 bin above 7.0 GeV.

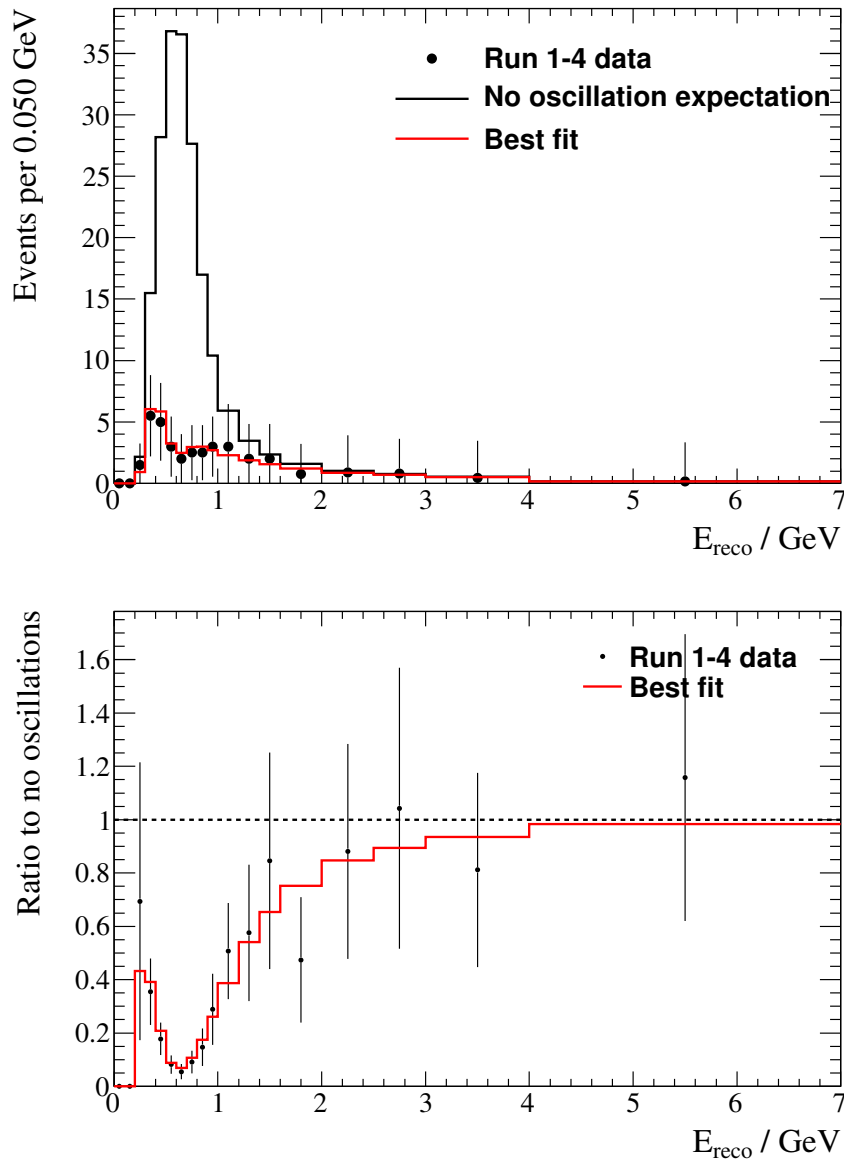


Figure 4.27: Best-fit reconstructed energy spectrum (top) and ratio to the no-oscillation hypothesis (bottom) obtained from the fit of the combined Run 1+2+3+4 dataset. The Run 1+2+3+4 data and the prediction obtained using the no-oscillation hypothesis are also shown. The spectra are shown using the coarse binning scheme. The characteristic energy-dependent deficit can be clearly seen. The normal mass hierarchy is assumed.

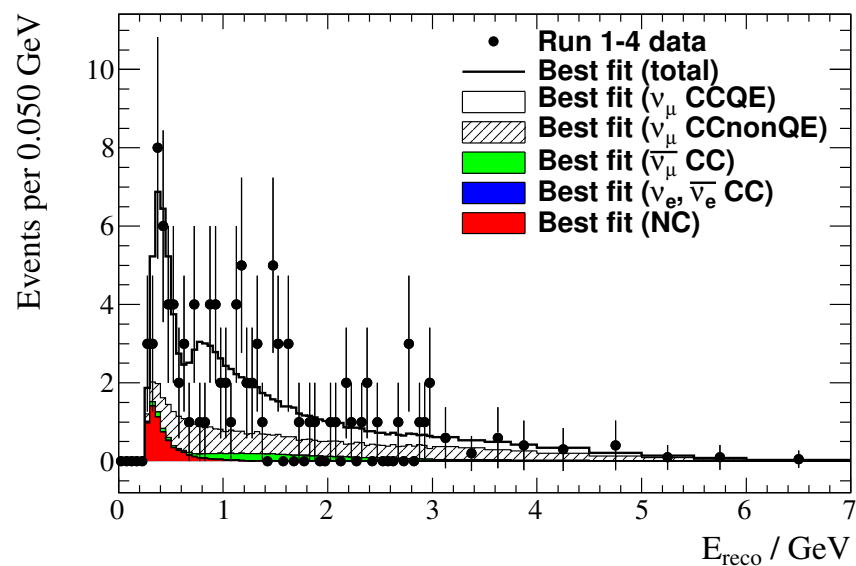


Figure 4.28: Best-fit reconstructed energy spectrum in the coarse binning scheme and its components obtained from the fit of the Run 1+2+3+4 dataset. The 32 components, each of which is calculated separately in the analysis, are grouped into just five categories: ν_μ CCQE, ν_μ CCnonQE, $\bar{\nu}_\mu$ CC, $\nu_e/\bar{\nu}_e$ CC and NC. The normal mass hierarchy is assumed.

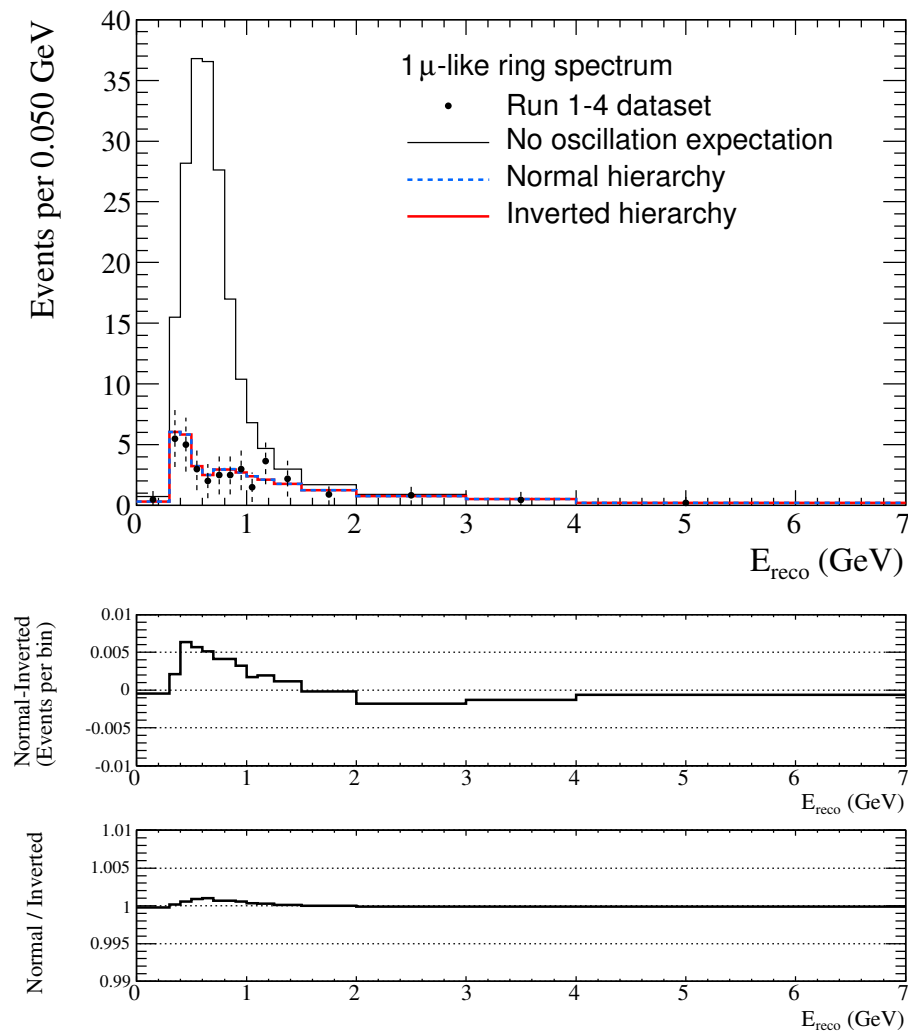


Figure 4.29: Comparison between best-fit reconstructed energy spectra obtained from the normal and inverted mass hierarchy fits of the Run 1+2+3+4 dataset. The spectra are shown using the coarse binning scheme. Also shown are the absolute difference between the normal and inverted mass hierarchy best-fit spectra and the ratio between them. **The two spectra are almost identical.**

4.4.2 Confidence regions for the joint determination of the atmospheric mass squared splitting and 23-mixing angle

The first step in constructing confidence regions in the 2-dimensional $\sin^2 \theta_{23}$ - $|\Delta m_{32}^2|$ or $\sin^2 \theta_{23}$ - $|\Delta m_{31}^2|$ oscillation parameter space is to construct the $\Delta\chi^2$ surface from the fit of the data. The oscillation parameter space is divided into a rectangular grid of width $\sin^2 \theta_{23} = 0.0025$, $|\Delta m_{32}^2|$ or $|\Delta m_{31}^2| = 0.025 \times 10^{-3} \text{ eV}^2/\text{c}^4$, with a grid point at the centre of each rectangle. A fit is performed at each grid point with the values of $\sin^2 \theta_{23}$ and $|\Delta m_{32}^2|$ or $|\Delta m_{31}^2|$ fixed to the true values of the grid point and the 41 systematic and four non-23 oscillation parameters allowed to float. $\Delta\chi^2$ is then calculated as the χ^2 for the fit done at the grid point²² minus χ_{bf}^2 , where χ_{bf}^2 is the fit done with $\sin^2 \theta_{23}$ and $|\Delta m_{32}^2|$ or $|\Delta m_{31}^2|$ free, whose results have been shown previously in Tab. 4.11.

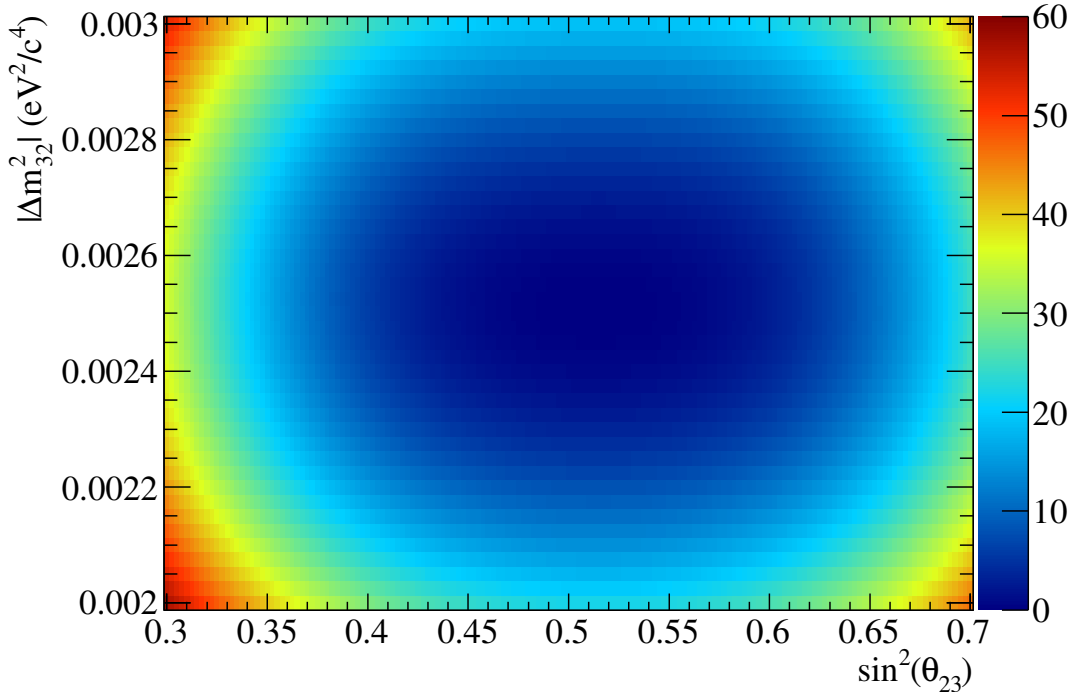


Figure 4.30: $\Delta\chi^2$ surface from the fit of the Run 1+2+3+4 dataset. The normal mass hierarchy is assumed.

This 2-dimensional $\Delta\chi^2$ surface from the fit of the Run 1+2+3+4 dataset is shown

²² χ^2 is defined in Eq. 4.10 in Sec. 4.3.2.

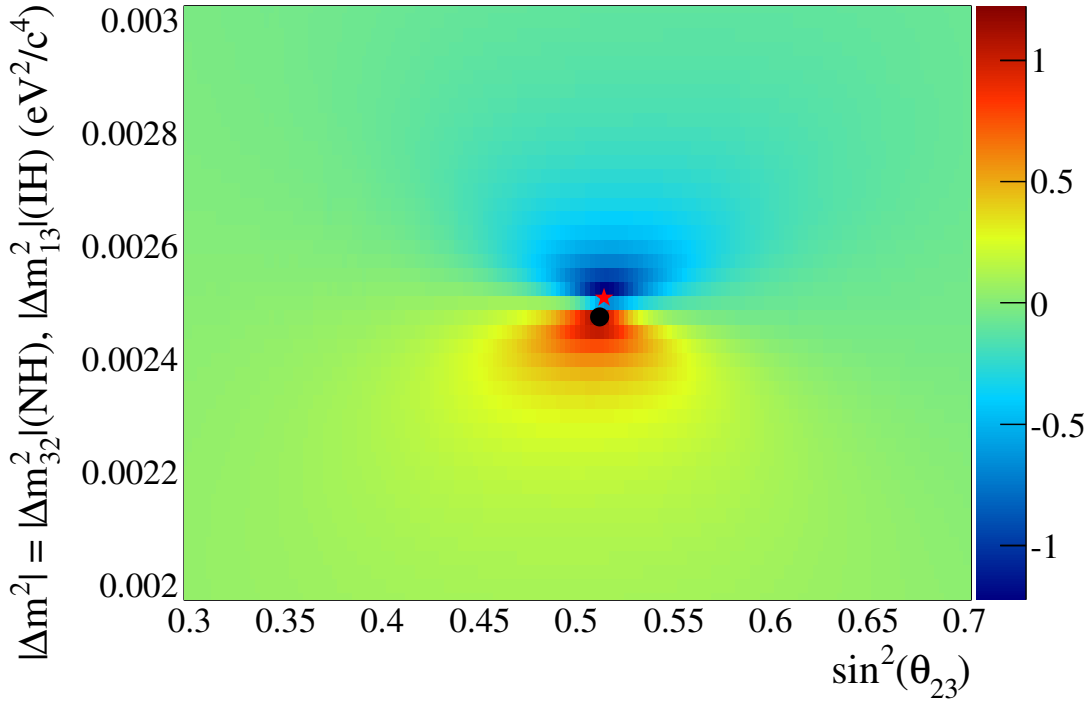


Figure 4.31: Fractional difference between the $\Delta\chi^2$ surfaces obtained from the fits to the Run 1+2+3+4 dataset assuming the normal and inverted mass hierarchies. The fractional difference is calculated as $2 \times (\Delta\chi^2(\text{NH}) - \Delta\chi^2(\text{IH})) / (\Delta\chi^2(\text{NH}) + \Delta\chi^2(\text{IH}))$. The normal and inverted mass hierarchy best-fit points are shown as a red star and a black circle respectively.

in Fig. 4.30 as a function of $\sin^2 \theta_{23}$ and $|\Delta m_{32}^2|$ for the normal mass hierarchy. A comparison between the $\Delta\chi^2$ surfaces from the normal and inverted mass hierarchies is shown in Fig. 4.31. There are large differences, particularly near the best-fit points. However, this is mostly an artefact of comparing $|\Delta m_{32}^2|$ with $|\Delta m_{31}^2|$; when applying an offset such that the best-fit points line up, the fractional difference across the whole range is reduced to less than 10%.

Confidence regions were constructed in the 2-dimensional parameter space $\sin^2 \theta_{23}$ and $|\Delta m_{32}^2|$ or $|\Delta m_{31}^2|$ using both the constant- $\Delta\chi^2$ method, and the Feldman-Cousins method [172] (both described in Sec. 4.3.7) for fits of the Run 1+2+3+4 dataset. Regions constructed using the Feldman-Cousins method are shown in Fig. 4.32 for both the normal and inverted mass hierarchies. Also shown in this figure is a variation on the study presented in Sec. 4.3.6 on the importance of each systematic. The study is run at a

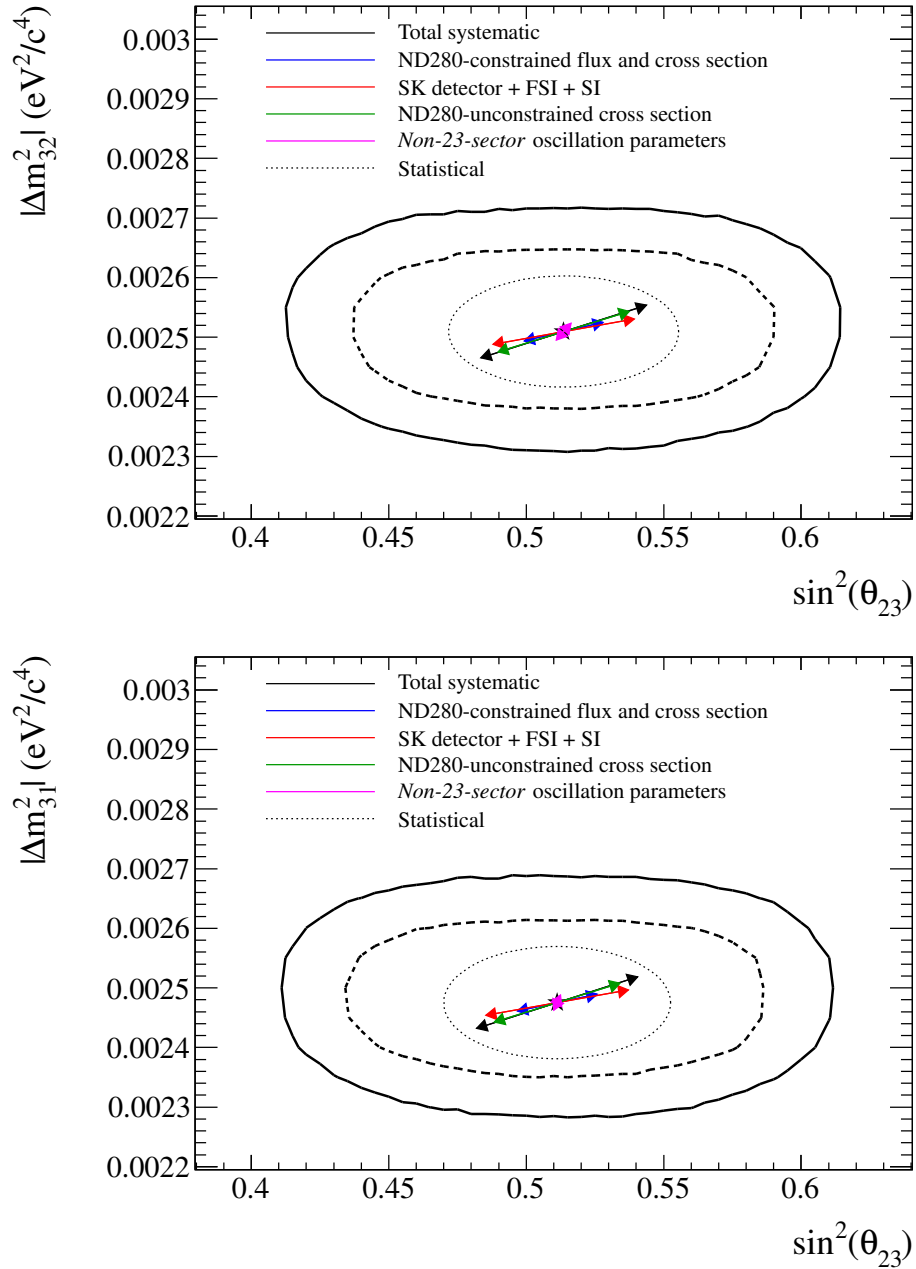


Figure 4.32: 68% C.L. and 90% C.L. allowed regions obtained with the Feldman-Cousins method from the fit of the Run 1+2+3+4 dataset. The normal (top) and inverted (bottom) mass hierarchies are assumed. Also shown are the 1σ effect of each group of systematics (arrows), and the statistical error (dotted ellipse) at the best-fit point.

single ($\sin^2 \theta_{23}$, $|\Delta m_{32}^2|$ or $|\Delta m_{31}^2|$) point (the best-fit point), and groups of systematics are tweaked randomly (respecting correlations) to create 10,000 MC datasets, which are fit for only $\sin^2 \theta_{23}$ and $|\Delta m_{32}^2|$ or $|\Delta m_{31}^2|$. The average effect on the best-fit values of $\sin^2 \theta_{23}$ and $|\Delta m_{32}^2|$ or $|\Delta m_{31}^2|$ is then calculated for each systematic group, which is shown in the figures as arrows extending from the best-fit point. The statistical error is shown as a dotted ellipse for comparison. The total error is dominated by the statistical error. As seen in other estimations of the systematic error effect, the ND280-constrained and ND280-unconstrained cross-section errors dominate the systematic error.

The Run 1+2+3+4 two-dimensional confidence regions obtained using the constant- $\Delta\chi^2$ and Feldman-Cousins methods are compared in Fig. 4.33 for the normal mass hierarchy. The Feldman-Cousins confidence regions are narrower along $|\Delta m_{32}^2|$ or $|\Delta m_{31}^2|$ at maximal disappearance than those made with the constant- $\Delta\chi^2$ method since the Feldman-Cousins $\Delta\chi^2_{\text{critical}}$ values are lower than the canonical constant- $\Delta\chi^2$ values as explained in Sec. 4.4.2. The Feldman-Cousins regions are also very slightly narrower in $\sin^2 \theta_{23}$ for values of $|\Delta m_{32}^2|$ or $|\Delta m_{31}^2|$ near the best fit. This is because the boundary effect spans the whole region (i.e. the Feldman-Cousins $\Delta\chi^2_{\text{critical}}$ values shown in Fig. 4.16 tend towards, but do not reach the constant- $\Delta\chi^2$ values of $\Delta\chi^2_{\text{critical}}$ at the edge of the region).

A comparison is shown in Fig. 4.34 between the Run 1+2+3+4 two-dimensional confidence regions for the normal and inverted mass hierarchies obtained using the Feldman-Cousins method (the vertical axis is $|\Delta m_{32}^2|$ for the normal mass hierarchy and $|\Delta m_{31}^2|$ for the inverted mass hierarchy).

In Fig. 4.35 the T2K Run 1+2+3+4 90% confidence region is compared with those from MINOS (2014 3-flavour beam and atmospheric analysis) [178], SK atmospherics (2013 3-flavour atmospheric zenith-angle analysis) [179], and T2K Run 1+2+3 [2], for both the normal and inverted mass hierarchies. It should be noted that the confidence region construction methods differ; MINOS uses the global minimum from both mass hierarchies (in practice this lies in the inverted mass hierarchy) whereas SK and T2K use the local minimum in each mass hierarchy. This results in the normal mass hierarchy

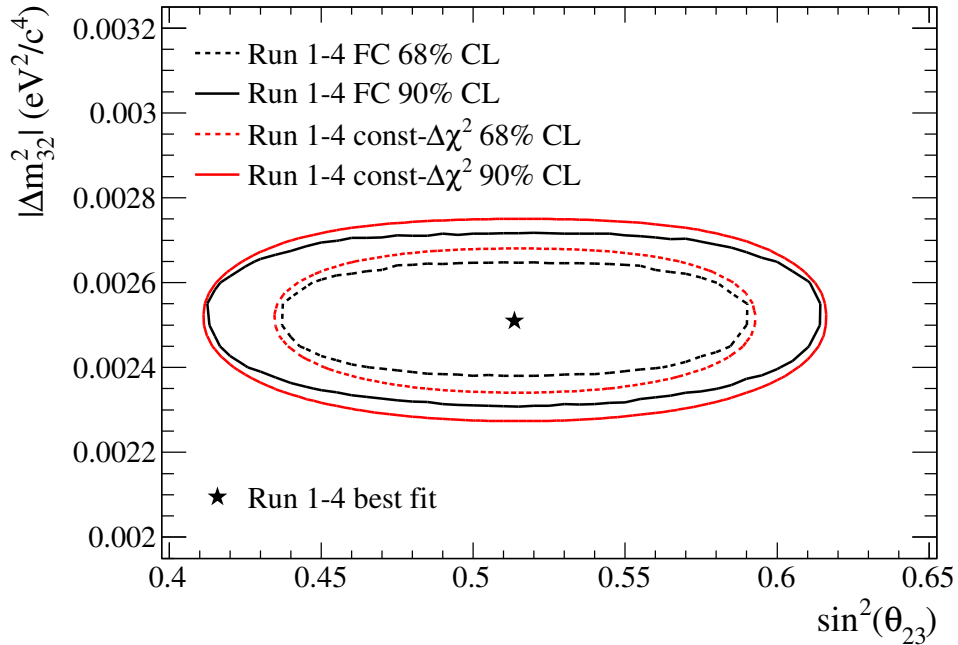


Figure 4.33: Comparison between the 68% C.L. and 90% C.L. allowed regions obtained using the constant- $\Delta\chi^2$ and Feldman-Cousins methods from the fit of the Run 1+2+3+4 dataset. The normal mass hierarchy is assumed.

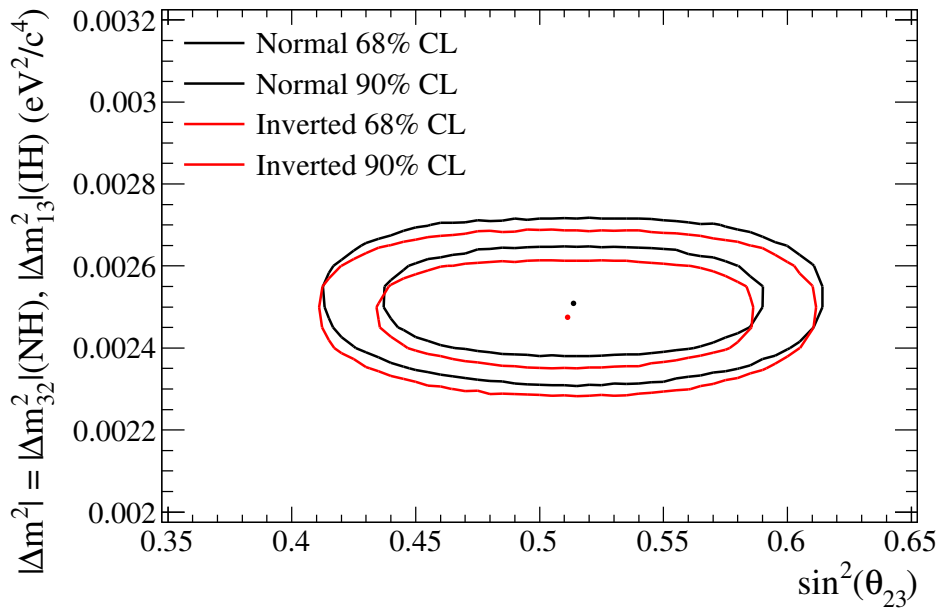


Figure 4.34: Comparison between the 68% C.L. and 90% C.L. allowed regions for the normal and inverted mass hierarchies obtained using the Feldman-Cousins method from the fit of the Run 1+2+3+4 dataset.

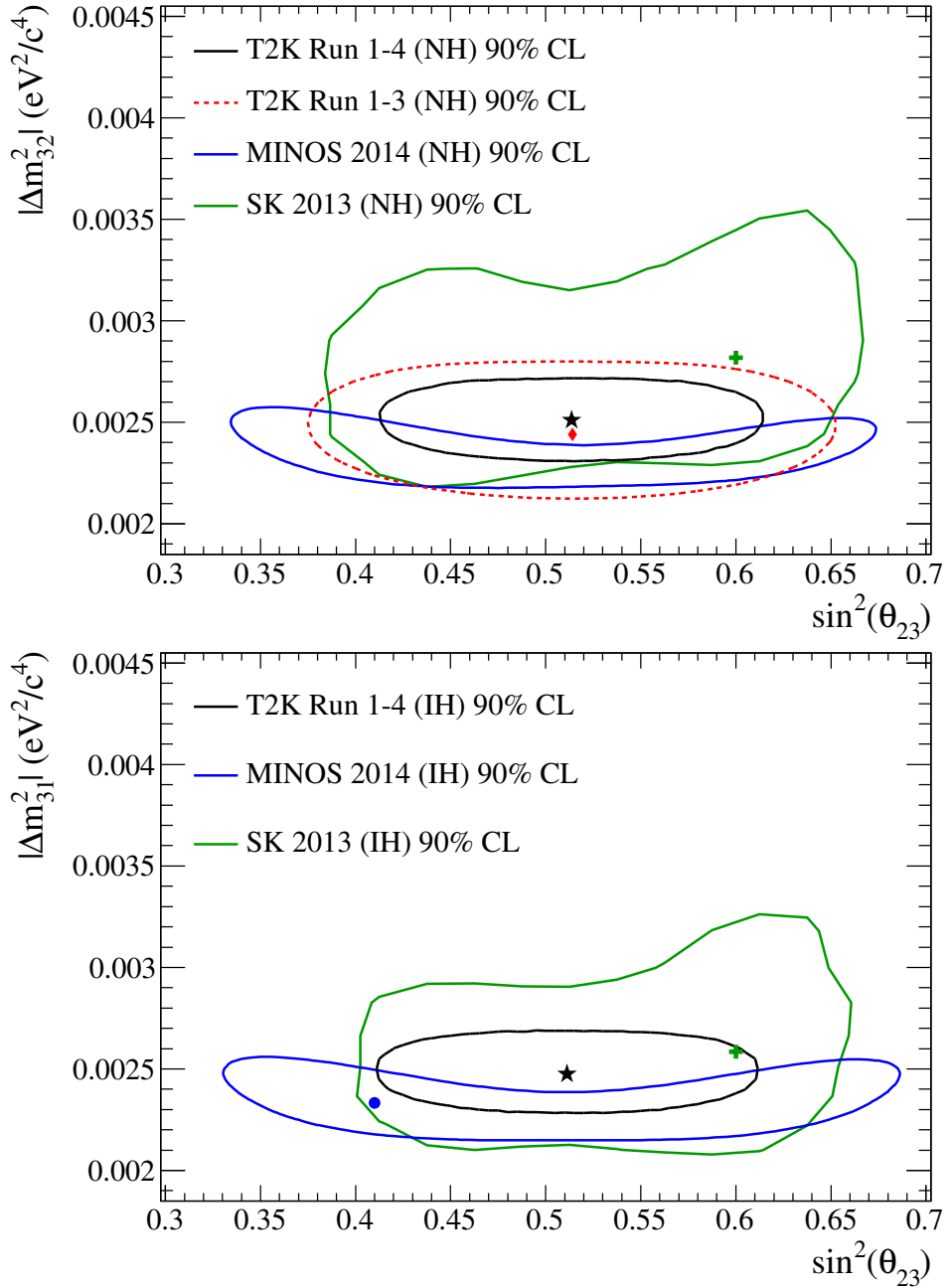


Figure 4.35: Comparison between 90% C.L. allowed regions from MINOS [178], SK atmospherics [179], T2K Run 1+2+3 [2], and the 90% C.L. allowed region obtained from the fit to the T2K Run 1+2+3+4 dataset obtained using the Feldman-Cousins method. Both the normal (top) and inverted (bottom) mass hierarchies are assumed. It should be noted that the MINOS best-fit point lies in the inverted mass hierarchy.

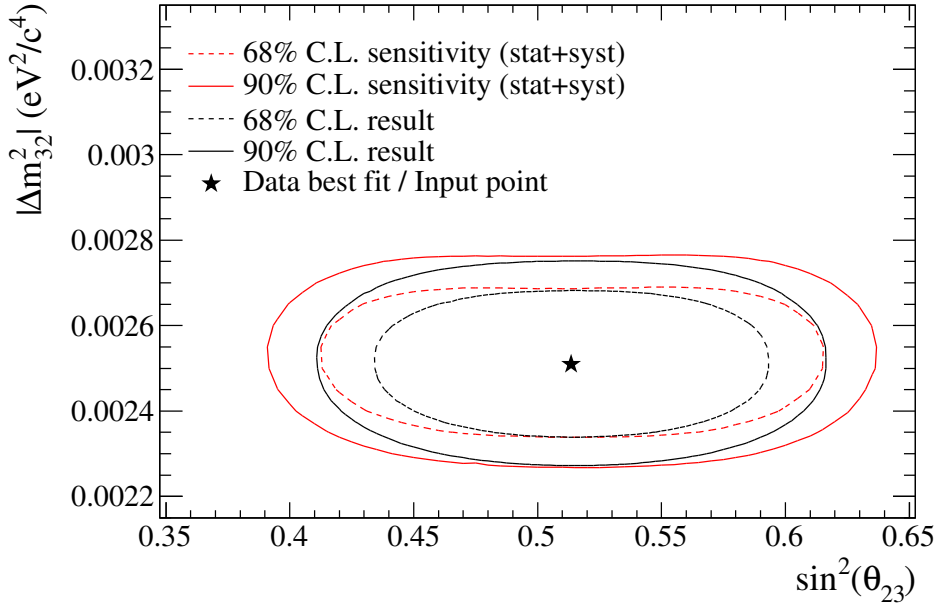


Figure 4.36: Comparison between the 68% C.L. and 90% C.L. allowed regions using the constant- $\Delta\chi^2$ method from the fit of the Run 1+2+3+4 dataset and the results of a sensitivity study at the best-fit point for Run 1+2+3+4 for statistical+systematic MC toys. The normal mass hierarchy is assumed.

MINOS confidence region being smaller than if it were constructed using the local minimum. These plots show that T2K now has the world's best limit in θ_{23} .

In Fig. 4.36 a comparison is shown between the Run 1+2+3+4 allowed region obtained with constant- $\Delta\chi^2$ method and the T2K 6.57×10^{20} POT sensitivity region produced at the best-fit point for the Run 1+2+3+4 dataset. The sensitivity regions were computed by averaging the regions of 300 toy MC experiments generated with statistical fluctuations and all systematic parameters randomised. As can be seen in the the plot, the T2K data results in a smaller region than the sensitivity, particularly for the $\sin^2 \theta_{23}$ region. p-values can be calculated by comparing the data constant- $\Delta\chi^2$ regions with the regions of the sensitivity fits, and represent the fraction of toy experiments that provide a *tighter* allowed region than the data. For $\sin^2 \theta_{23}$ the p-values are 0.21(0.19) for 68% C.L. and 0.19(0.21) for 90% C.L. for the lower(upper) allowed regions respectively. For $|\Delta m_{32}^2|$ the p-values are 0.31(0.20) for 68% C.L. and 0.42(0.27) for 90% C.L. for the lower(upper) allowed region respectively. This shows that the data are not an extreme

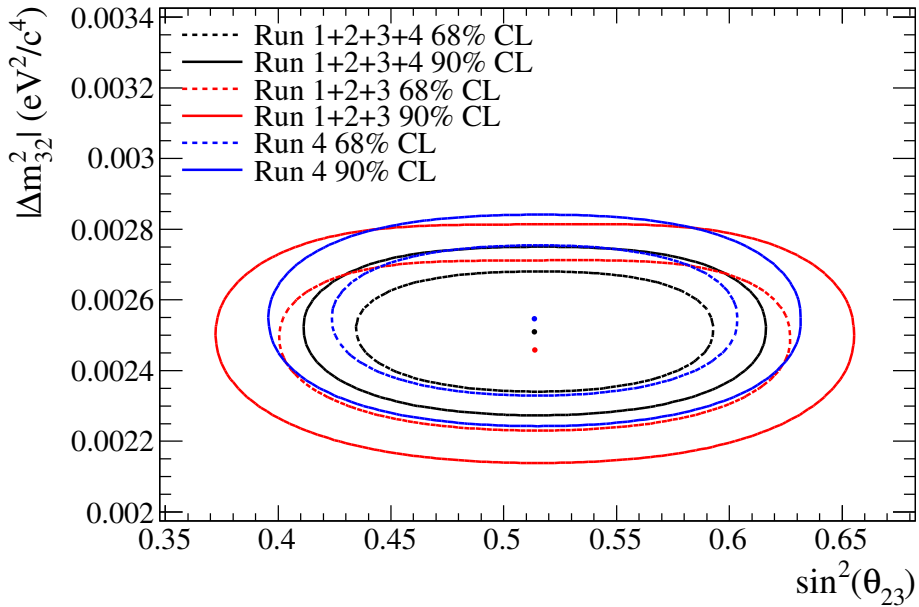


Figure 4.37: Comparison between the 68% C.L. and 90% C.L. allowed regions obtained from separate analyses to the Run 1+2+3+4, Run 1+2+3 and Run 4 datasets. All regions shown were calculated with the constant- $\Delta\chi^2$ method. The normal mass hierarchy is assumed.

fluctuation.

Finally, a comparison between the confidence regions obtained by three separate analyses of the Run 1+2+3+4, Run 1+2+3 and Run 4 datasets is shown in Fig. 4.37. The allowed regions from the different running periods are consistent. [This shows, at a high level, that the different runs of the T2K experiment are compatible; low level analysis of event rates in each detector, and also the results of the ND280 fit \(see Sec. 3.3.4\) also show consistency.](#)

4.4.3 Confidence regions for the individual determination of the atmospheric mass squared splitting and 23-mixing angle

The first step in calculating 1-dimensional parameter allowed regions for $\sin^2 \theta_{23}$, $|\Delta m_{32}^2|$, or $|\Delta m_{31}^2|$ is to construct the $\Delta\chi^2$ profile likelihood from the fit of the data. To construct

the $\sin^2 \theta_{23}$ profile likelihood, $\sin^2 \theta_{23}$ is fit at every point in a 1-dimensional grid with width $\sin^2 \theta_{23} = 0.001$. A fit is performed at each grid point with the value of $\sin^2 \theta_{23}$ fixed to the true values of the grid point and the 41 systematic parameters, four *non-23-sector* oscillation parameters, and $|\Delta m_{32}^2|$ or $|\Delta m_{31}^2|$ allowed to float. $\Delta\chi^2$ is then calculated as the χ^2 for the fit done at the grid point²³ minus χ_{bf}^2 , where χ_{bf}^2 is the fit done with $\sin^2 \theta_{23}$ and $|\Delta m_{32}^2|$ or $|\Delta m_{31}^2|$ free, whose results have been shown previously. The profile likelihood is shown in Fig. 4.38 (left), along with $\Delta\chi^2_{\text{critical}}$ for both the constant- $\Delta\chi^2$ and Felman-Cousins methods.

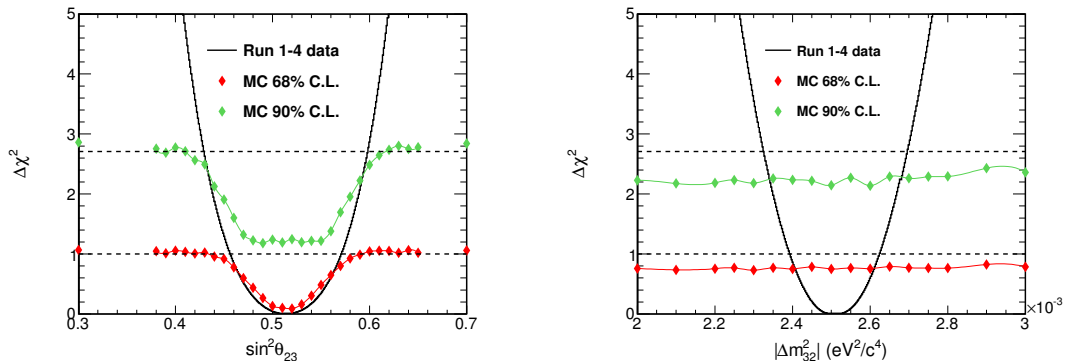


Figure 4.38: Comparison between the 1-dimensional $\Delta\chi^2$ from the fit of the Run 1+2+3+4 data and the MC estimation of the 1-dimensional 68% and 90% critical values of $\Delta\chi^2$ as a function of $\sin^2 \theta_{23}$ (left) and $|\Delta m_{32}^2|$ (right). Each MC critical value is obtained from 10,000 toy experiments with systematic variations and statistical fluctuations; these critical values are fitted with cubic splines. The normal mass hierarchy is assumed. The canonical constant- $\Delta\chi^2$ 68% and 90% critical values for one degree of freedom are shown as dashed lines.

The profile likelihood for $|\Delta m_{32}^2|$ or $|\Delta m_{31}^2|$ is done similarly, using a grid step size of $0.01 \times 10^{-3} \text{ eV}^2/\text{c}^4$, and is shown in Fig. 4.38 (right), along with $\Delta\chi^2_{\text{critical}}$ for both the constant- $\Delta\chi^2$ and Felman-Cousins methods.

It is apparent from Fig. 4.38 that the Feldman-Cousins MC critical $\Delta\chi^2$ values²⁴ are lower than the canonical constant- $\Delta\chi^2$ values when the true input value of $\sin^2 \theta_{23}$ is near the value of maximal ν_μ disappearance. As in the 2-dimensional case, this is due to the best-fit values of $\sin^2 \theta_{23}$ in the toy MC experiments piling up at the value

²³ χ^2 is defined in Eq. 4.10 in Sec. 4.3.2.

²⁴For 1-dimensional regions, the following step size is used when finding the Feldman-Cousins $\Delta\chi^2_{\text{critical}}$ MC estimation: $\delta(\sin^2 \theta_{23}) = 0.01$ and $\delta(|\Delta m_{32}^2|)$ or $\delta(|\Delta m_{31}^2|) = 0.05 \times 10^{-3} \text{ eV}^2/\text{c}^4$.

of maximal disappearance; at input values of $\sin^2 \theta_{23}$ far from the value of maximal ν_μ disappearance, the critical $\Delta\chi^2$ values approach the canonical constant- $\Delta\chi^2$ values as expected. The MC critical $\Delta\chi^2$ values for $|\Delta m_{32}^2|$ are lower than the canonical constant- $\Delta\chi^2$ values for all input values of that parameter. This is due to the input values of $\sin^2 \theta_{23}$ to the toy experiments, many of which are near the value of maximal ν_μ disappearance (see Fig. 4.20 for an example). Again the best-fit values of $\sin^2 \theta_{23}$ pile-up at the value of maximal disappearance, which results in lower values of $\Delta\chi^2$ than would occur if that boundary were not present. The Feldman-Cousins results show that the constant- $\Delta\chi^2$ method overcovers.

Run 1+2+3+4 profile likelihood distributions are compared with those from the fits of the Run 1+2+3 and Run 4 datasets for the normal mass hierarchy in Fig. 4.39. The profile likelihood from the different running periods are consistent.

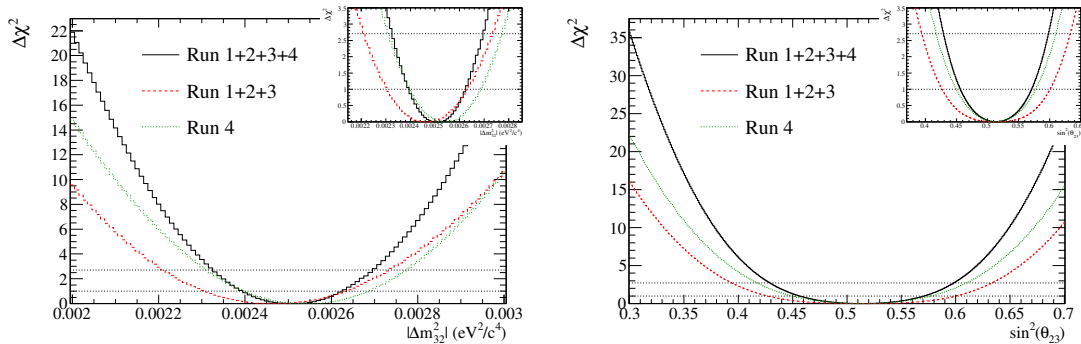


Figure 4.39: Profile likelihood, as a function of $\sin^2 \theta_{23}$ (left) and $|\Delta m_{32}^2|$ (right), from the fits of the Run 1+2+3+4, Run 1+2+3 and Run 4 datasets. The normal mass hierarchy is assumed. An inset shows a zoom of the profile likelihood up to $\Delta\chi^2 = 3.5$.

68% and 90% C.L. regions on $\sin^2 \theta_{23}$ and $|\Delta m_{32}^2|$, or $|\Delta m_{31}^2|$ are shown in Tab. 4.12. These regions are calculated as the first bin which lies above the critical value of $\Delta\chi^2$. For the new procedure, a cubic spline is fit to the calculated values of $\Delta\chi^2_{\text{critical}}$ to be able to extrapolate the points where the $\Delta\chi^2_{\text{critical}}$ calculation was not performed. They clearly show that the confidence regions from the constant- $\Delta\chi^2$ method overcover for both $\sin^2 \theta_{23}$ and the mass-squared difference; this over-coverage is caused by the boundary effects from the value of maximal disappearance in $\sin^2 \theta_{23}$.

Method	Dataset	Mass hierarchy	Confidence level	$\sin^2 \theta_{23}$	$ \Delta m_{32}^2 $ or $ \Delta m_{31}^2 $ (10^{-3} eV 2 /c 4)
Constant $\Delta\chi^2$	Run 1+2+3+4	Normal	68%	0.514 ± 0.058	2.51 ± 0.12
		90%	$0.429 < \sin^2 \theta_{23} < 0.599$	$2.32 < \Delta m_{32}^2 < 2.70$	
	Inverted	68%	$0.511^{+0.058}_{-0.057}$	2.48 ± 0.12	
		90%	$0.427 < \sin^2 \theta_{23} < 0.596$	$2.29 < \Delta m_{31}^2 < 2.67$	
Feldman & Cousins	Run 1+2+3+4	Normal	68%	$0.514^{+0.049}_{-0.050}$	2.51 ± 0.10
		90%	$0.433 < \sin^2 \theta_{23} < 0.593$	$2.34 < \Delta m_{32}^2 < 2.68$	
	Inverted	68%	$0.511^{+0.050}_{-0.049}$	2.48 ± 0.10	
		90%	$0.431 < \sin^2 \theta_{23} < 0.591$	$2.32 < \Delta m_{31}^2 < 2.65$	
Constant $\Delta\chi^2$	Run 1+2+3	Normal	68%	$0.514^{+0.087}_{-0.088}$	$2.46^{+0.18}_{-0.16}$
		90%	$0.394 < \sin^2 \theta_{23} < 0.634$	$2.20 < \Delta m_{32}^2 < 2.74$	
Constant $\Delta\chi^2$	Run 4	Normal	68%	$0.514^{+0.064}_{-0.065}$	$2.55^{+0.14}_{-0.16}$
		90%	$0.417 < \sin^2 \theta_{23} < 0.610$	$2.31 < \Delta m_{32}^2 < 2.78$	
Constant $\Delta\chi^2$	MINOS	Normal	90%/68%	$0.35 < \sin^2 \theta_{23} < 0.65$	2.37 ± 0.09
		Inverted		$0.34 < \sin^2 \theta_{23} < 0.67$	$2.34^{+0.12}_{-0.09}$

Table 4.12: Summary of 1-dimensional limits on $\sin^2 \theta_{23}$ and $|\Delta m_{32}^2|$ or $|\Delta m_{31}^2|$ from the fits of the Run 1+2+3, Run 4, and Run 1+2+3+4 datasets. The limits are shown for both the constant- $\Delta\chi^2$ method and the new procedure described in Sec. 4.3.7. The MINOS 90% $\sin^2 \theta_{23}$ and 68% $|\Delta m_{32}^2|$ or $|\Delta m_{31}^2|$ C.L. limits [178] are shown for comparison.

Also shown in Tab. 4.12 are the MINOS 90% $\sin^2 \theta_{23}$ and 68% $|\Delta m_{32}^2|$ or $|\Delta m_{31}^2|$ C.L. limits [178]²⁵. It can again be seen that T2K now has the world's best limit in θ_{23} . The table also shows that the current limits on $|\Delta m_{32}^2|$ or $|\Delta m_{31}^2|$ are comparable.

4.5 Discussion

The results presented in Secs. 4.4.2 and 4.4.3 have shown that using the latest available results from other experiments, T2K has the world's best limit in θ_{23} , and has a comparable constraint to MINOS for $|\Delta m_{32}^2|$ or $|\Delta m_{31}^2|$. There are two reasons for T2K having such a tight constraint on θ_{23} , when the sensitivity regions shown in Figs. 4.21 and 4.22 suggests that a region of comparable size in $\sin^2 \theta_{23}$ is expected:

- The comparison with the sensitivity at the best-fit point (see Fig. 4.36) shows that a favourable fluctuation has occurred in data. The fluctuation is not extreme; a fluctuation providing these regions or better has a 1 in 5 chance.
- The T2K best-fit point lies close to the point of maximal disappearance, whereas the best-fit points from MINOS and SK lie far away from this point. Being close to maximal disappearance results in a $\Delta\chi^2$ profile that has a single minimum, while being further away results in a naturally wider distribution due to double-peak structure about the point of maximal disappearance.

The allowed regions shown in Fig. 4.35 show some tension between the MINOS and SK results; the MINOS and T2K 90% C.L. regions overlap only in a small area, and the best-fit points are either outside (SK NH and MINOS) or just inside (SK IH) the T2K 90% C.L. region. The level at which the other experiments' best-fit points are excluded by the T2K data can be determined by calculating the probability, assuming Gaussian errors²⁶, using the value of $\Delta\chi^2$ on the 2-dimensional surface (for example, Fig. 4.30) at

²⁵The latest SK atmospherics result in Ref. [179] does not quote 1-dimensional confidence regions.

²⁶The MINOS and SK best-fit points lie in an area of Fig. 4.16, away from maximal disappearance, where the constant- $\Delta\chi^2$ and Feldman-Cousins methods are similar. For example, the SK inverted mass hierarchy exclusion changes from 83.6% when using the constant- $\Delta\chi^2$ method to 86.4% when using the Feldman-Cousins method.

Experiment	Mass hierarchy	T2K $\Delta\chi^2$	T2K exclusion
SK	Normal	10.37	99.4%
SK	Inverted	3.61	83.6%
MINOS	Inverted	6.83	96.7%

Table 4.13: The exclusion of MINOS [178] and SK [179] best-fit points, as calculated using the T2K 2-dimensional $\Delta\chi^2$ surface.

the experiments' best-fit point. The results are shown in Tab. 4.13. It can be seen that the best-fit points are [inconsistent with the T2K result at the \$\sim 1.5\text{--}2.5\sigma\$ level](#).

Chapter 5

Summary and Outlook

A ν_μ -disappearance analysis was performed in a framework of three active neutrino flavour oscillations including matter effects in constant-density matter. The observed reconstructed energy spectrum of 1 μ -like ring events was fitted, and separate fits were made for the normal and the inverted mass hierarchies. In these fits, $\sin^2 \theta_{23}$ and either $|\Delta m_{32}^2|$ (normal mass hierarchy) or $|\Delta m_{31}^2|$ (inverted mass hierarchy) were allowed to float. The oscillation parameters $\sin^2 \theta_{13}$, $\sin^2 \theta_{12}$, Δm_{21}^2 , δ_{CP} , and all 41 systematic parameters considered in this analysis were also allowed to float in the fit.

The 3-flavour ν_μ -disappearance fit of the combined T2K Run 1+2+3+4 dataset corresponding to integrated J-PARC neutrino beam exposure of 6.57×10^{20} POT, gives the 1-dimensional 68% confidence intervals in these parameters as $\sin^2 \theta_{23} = 0.514^{+0.049}_{-0.050}$ $|\Delta m_{32}^2| = 2.51 \pm 0.10 \text{ eV}^2/\text{c}^4$ for the normal mass hierarchy, and $\sin^2 \theta_{23} = 0.511^{+0.050}_{-0.049}$ $|\Delta m_{31}^2| = 2.48 \pm 0.10 \text{ eV}^2/\text{c}^4$ for the inverted mass hierarchy.

The current work has little sensitivity to the octant of θ_{23} , due to $P(\nu_\mu \rightarrow \nu_\mu)$ being symmetric about maximal disappearance, when considering the dominant terms (see Eq. 1.45). Performing a fit including 1 e-like ring events (in addition to 1 μ -like ring events), is required due to $P(\nu_\mu \rightarrow \nu_e)$ being octant dependent (see Eq. 1.46). Since the current work was performed, a joint fit of T2K data has been done [181]. The results from the joint fit are comparable with the ν_μ -disappearance only results presented in the

current work. The joint analysis best-fit point is shifted to larger values of $\sin^2 \theta_{23}$, due to the fit preferring larger values of $\sin^2 \theta_{13}$; maximal disappearance is still preferred. The 2-dimensional confidence regions are also of comparable size.

Looking towards the future, T2K will take more data, aiming to achieve 7.80×10^{21} POT (the current dataset corresponds to 8.4% of the expected total). This will improve the power of the experiment to determine the values of the oscillation parameters as shown in Fig. 5.1. There is also a possibility of determining the octant of θ_{23} , depending on the run plan, as shown in Fig. 5.2. Combinations with NO ν A should provide hints of up to $\sim 90\%$ C.L. on the three major questions in neutrino oscillation physics: the mass hierarchy, θ_{23} octant, and value of δ_{CP} . It will take new experiments to provide conclusive answers to these questions.

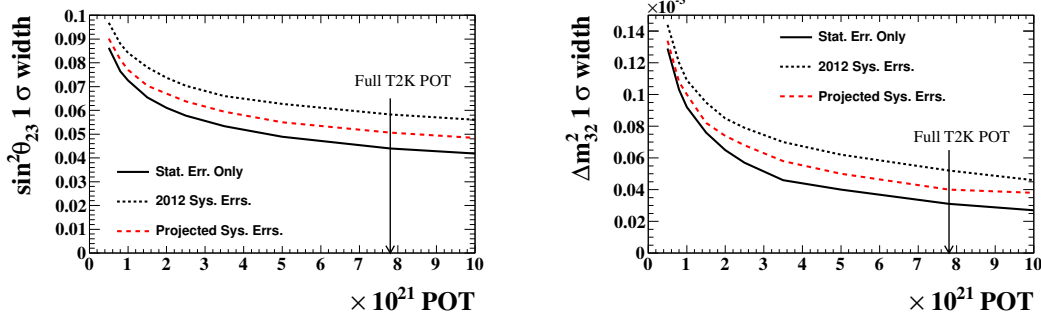


Figure 5.1: The precision of $\sin^2 \theta_{23}$ and $|\Delta m_{32}^2|$ as a function of T2K POT assuming 100% ν -mode running. Plots were generated assuming $\sin^2(2\theta_{13}) = 0.10$, $\delta_{CP} = 0$, $\sin^2 \theta_{23} = 0.50$, and $|\Delta m_{32}^2| = 2.40 \times 10^{-3} \text{ eV}^2/\text{c}^4$. The normal mass hierarchy is assumed. The solid curves include statistical errors only, while the dashed black(red) curves assume the 2012(projected) T2K systematic errors. A constraint based on the ultimate reactor precision is included.

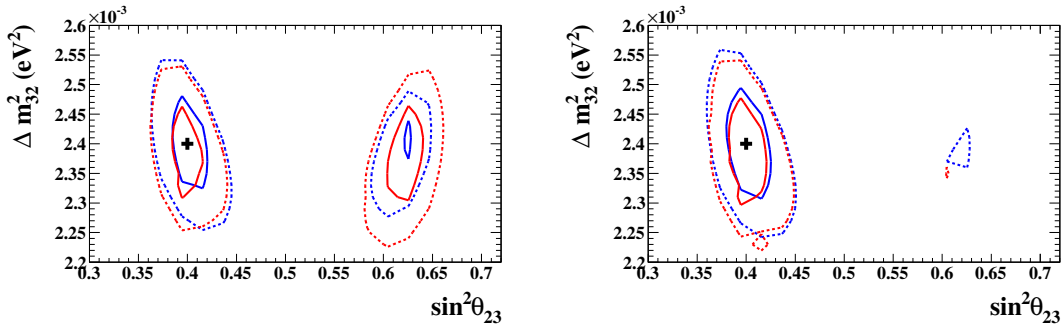


Figure 5.2: 90% allowed regions of $|\Delta m_{32}^2|$ versus $\sin^2 \theta_{23}$ for 7.80×10^{20} POT assuming 100% ν -mode (left) and 50% $\bar{\nu}$ -mode 50% $\bar{\nu}$ -mode (right) running. Plots were generated assuming $\sin^2(2\theta_{13}) = 0.10$, $\delta_{CP} = 0$, $\sin^2 \theta_{23} = 0.40$, and $|\Delta m_{32}^2| = 2.40 \times 10^{-3} \text{ eV}^2/c^4$. The normal mass hierarchy is assumed. The blue curves are fit assuming the correct mass hierarchy, while the red are fit assuming the incorrect mass hierarchy. The solid contours are with statistical error only, while the dashed contours include current systematic errors. A constraint based on the ultimate reactor precision is included.

Appendices

Appendix A

ND280 ν_μ CC selection systematics

This appendix gives a brief summary of each of the detector-related systematics considered in the ND280 ν_μ CC semi-inclusive event selections described in Sec. 3.3. In Sec. A.1, systematics relating to the FGD are discussed. In Sec. A.2, systematics relating to the TPC, and FGD-TPC track matching are discussed. Finally, in Sec. A.2, systematics relating to out-of-FGD backgrounds, event pile-up and pion secondary interactions are discussed.

A.1 FGD detector systematics

FGD1-stopping control samples of both muons and protons are selected by searching for tracks that stop in FGD1 (but not the last layer), with segments in TPC1 but not in TPC2 (or vice versa), and using TPC track quality, charge, momentum and PID information.

- **Michel electron efficiency.** The uncertainty is assigned by looking as the difference between data and MC for FGD1-stopping cosmic muons, whose stopping distance is consistent with the TPC momentum measurement (to reject electrons). The efficiency is $58.1\pm0.8\%$ in Run 4 data and $61.9\pm1.1\%$ in MC.
- **FGD-only track efficiency.** Using a FGD1-stopping proton beam sample, the efficiency is defined as the proportion of tracks that have a FGD-only track (found

using the FGD-only reconstruction) that starts in the first XY module in z , and within 10 cm of where the TPC track would have entered the FGD. The systematic, taken as the ratio of data to MC, ranges from $+12\pm21\%$ in the $|\cos\theta| = 0.3\text{--}0.4$ bin to $-1\pm3\%$ in the $|\cos\theta| = 0.9\text{--}1.0$ bin (no momentum dependence is seen in the ratio).

- **FGD-only hybrid track efficiency.** Hybrid events are generated by adding particle-gun hit information to CC-0- π vertices selected from data and MC, with an extra requirement of exactly zero FGD-only tracks. The purpose is to study the effect on tracking efficiency of FGD-only reconstruction of the presence of long muon tracks and an optional long proton track. 100 p and 100 π^+ particle-gun events are created at each of the selected vertices, isotropically and uniformly in momentum range $0.4 \text{ GeV}/c < p_p < 1.0 \text{ GeV}/c$ or $0.1 \text{ GeV}/c < p_{\pi^+} < 0.3 \text{ GeV}/c$. A hybrid event is generated for each particle gun event that doesn't create a TPC-FGD matched track, in which particle gun hit information is added to the beam MC or data event. The efficiency is defined as the proportion of hybrid events that contain one or more¹ FGD-only tracks; efficiency (compared with the FGD1-stopping proton study) is due to hits being taken by the pre-existing track(s) during reconstruction. The systematic, taken as the ratio of data to MC, is $4.4\pm0.7\%$ for protons and $3.3\pm0.7\%$ for pions.
- **FGD-only track particle identification.** Using FGD1-stopping proton and muon beam samples, that start at $z > 3200 \text{ mm}$ (rejects sand muons), and have reconstructed momentum $0.0 \text{ GeV}/c < p_p < 2.0 \text{ GeV}/c$ or $0.00 \text{ GeV}/c < p_\mu < 0.25 \text{ GeV}/c$. Pion PID systematics are taken to be the same as muon PID systematics because it is difficult to select a sample of non-interacting stopping pions. The peaks of the pull distributions are fitted with a Gaussian function, and MC is corrected to match data; this correction is the systematic.

¹The selection one *or more* is to accept short tracks that are broken in FGD-only reconstruction.

- **FGD mass uncertainty.** The dominant mass uncertainties are the size of the hole in the scintillator bars for the fibres, and the amount of glue used. The 0.67% total uncertainty causes a scaling of the event rate.

A.2 TPC detector systematics

- **TPC cluster efficiency.** The TPC cluster efficiency is the probability to find a reconstructed cluster in a given column where the particle should have produced one and effects the track quality cuts². Cluster efficiency should be dependent on the amount of charge in a given column, therefore columns at the edge of micromegas modules are expected to have different efficiencies (presumably lower) due to edge effects. The CC inclusive sample, without the track quality cut applied, is used to evaluate the systematic as the difference between the efficiencies of data and MC. The systematic for *inner* pads is found by fitting the number of clusters in the muon candidate (in the high statistics, inner-pad dominated $N_{\text{cluster}} \geq 62$ region); the systematic is $0.097 \pm 0.001\%$. The systematic for *outer* pads is found by fitting the TPC2 track start position along z (in the high statistics $z_{\text{start}} < 713$ region), which is normally in the outer column, or the first inner column; the systematic is $2.83 \pm 0.02\%$.
- **TPC track-finding efficiency.** For events with a single track, two control samples are used. For long tracks, a straight through muon control sample is used. The efficiency, for example in TPC2, is found by looking for global tracks with TPC1 and TPC3 segments. For short tracks, a high angle control sample is used. The efficiency, for example in TPC2, is found by looking for global tracks with TPC1 and barrel-ECal segments which should travel through TPC2. The efficiency is the proportion of tracks with a TPC segment when one is expected. The efficiency above 16 TPC clusters is statistically consistent with 100%. The efficiency is taken

²The effects of pattern recognition and micromegas module misalignment are expected to be small.

to be the conservative $99.8_{-0.4}^{+0.2}\%$, due the two samples to not covering the whole angle, momentum, track length phase space with high statistics.

Events in which two tracks that are reconstructed as one track can cause migration of events from e.g. the CC-1- π^+ to the CC-0- π sample. Again two studies are performed. First, events with two TPC2 tracks and an FGD1 fiducial volume vertex using MC truth information are found and the efficiency is the proportion of events that have two reconstructed tracks with TPC2 segments. For Run 1+2+3+4 data, only five events with one reconstructed track instead of two are expected, and the cause is geometrical, therefore the track-finding efficiency for two close tracks is negligible. Second, events with two tracks in TPC2 (two fitted, one fitted and one failed, or two failed tracks), both starting within the FGD fiducial volume in x and y , and within 100 mm of the TPC upstream wall are selected. In addition one track should have at least 18 clusters and the beginning of the second track must overlap with hits from the first track. This overlap can cause the track fit to fail. The fit likelihood efficiency is calculated as the proportion of events with two fitted tracks, and is consistent with 100%.

- **TPC charge misidentification.** A selection of tracks crossing all three TPCs, with >18 vertical clusters in each TPC, is made. The probability of charge misidentification, p_{CM} , is related to the probability that all four charge estimates (three local and one global) are the same, p_{same} , by the relation

$$p_{CM} = \frac{1}{2} \left(1 - \sqrt{\frac{1}{3}(4p_{\text{same}} - 1)} \right), \quad (\text{A.1})$$

which is valid under the assumptions that the charge misidentification rate in each TPC is the same, and the global reconstructed track is from the same particle. An MC-only truth study was also performed, with results similar to the above, meaning the approximations are valid for the event selection used. The charge misidentification rate is $\mathcal{O}(1\%)$ in the region $0.3 \text{ GeV}/c < p_\mu < 1.5 \text{ GeV}/c$. The systematic error is given by the difference between MC and data, and is $0.31 \pm 3.27\%$.

for $0.3 \text{ GeV}/c < p_\mu < 0.6 \text{ GeV}/c$.

- **TPC momentum resolution.** A selection of muon tracks crossing multiple TPCs is made by selecting events with a single negative muon-like track with segments in TPC1, FGD1 and TPC2, with at least 65 hits in each TPC, and a global track start position cut to reject sand muons. One can then study the difference between the TPC1 and the FGD1 energy-loss corrected TPC2 transverse momenta, $\Delta 1/p_t$, which has a Gaussian distribution with mean 0 and standard deviation $\sigma_{\Delta 1/p_t}$, which is dominated by the intrinsic TPC momentum resolutions. Similar distributions can be found by comparing TPC1 momenta with global track momenta (i.e. TPC1-FGD1-TPC2-FGD2-TPC3 and TPC1-FGD1-TPC2). The systematic error is calculated by smearing the MC to match data and is 0.24 ± 0.1 for $0.5 \text{ GeV}/c < p_\mu < 1.4 \text{ GeV}/c$.
- **TPC momentum scale.** An survey of the magnetic field suggests that the TPC momentum scale error is 0.5%. A cross-check, in which FGD1 momentum-by-range is compared to TPC2 momenta for FGD1-stopping cosmic muons for both data and MC. The difference between data and MC is consistent with the field measurements.
- **TPC particle identification.** The muon PID systematic is calculated as the difference between data and MC sand muon track pulls (per TPC and per T2K run); the MC is shifted and smeared to match data. The proton PID systematic is calculated in a similar way, using a high purity (98%) proton sample of high charge and positive tracks in the range $0.3\text{--}1.1 \text{ GeV}/c$.
- **TPC track übermerging.** Track übermerging is a TPC reconstruction bug in which two TPC segments from two different particles are merged causing the track multiplicity, track momentum, and track PID to be incorrect. Übermerging occurs when two TPC segments have identical start and end positions in z , and so it is rare in MC, and doesn't occur in data due to micromegas misalignment. The systematic is calculated by comparing the CC selections using the default

uncorrected reconstruction with the CC selections using a corrected reconstruction, and is $\mathcal{O}(0.1\%)$ or lower, depending on sample and p_μ .

- **TPC-FGD matching.** A selection of through-going muons with long TPC1 and TPC2 segments is chosen. Under the assumption that two TPC tracks imply that the track is long and also passes through FGD1, checking for the presence of a FGD1-TPC2 matched track allows one to compute the matching efficiency for the TPC2 track to be matched to any FGD1 hit. The efficiency is high (99.9% above 200 MeV/c), with good agreement between data and MC (within 0.2% above 200 MeV/c), although the efficiency drops and discrepancies increase below 100 MeV/c.

The same selection is used to compare the position of the upstream-most FGD1 hit in the matched tracks between data and MC. Most FGD1 segments start in the first or second layer (i.e. the first XY module) and data has a 25% higher failure rate than MC in this region. Elsewhere, the discrepancy is higher (40%).

A higher failure rate in data is also seen in a high angle muon selection using cosmic events, without TPC1 or TPC3 segments, but with FGD1, TPC2, and FGD2 segments. This is not understood and a 150% systematic is assigned.

A.3 Other systematics

- **Cosmic ray background.** The cosmic muon MC sample is normalised in two ways [182, 183]. A data sample also exists, in which beam triggers are taken when the neutrino beam was off (“empty spill”). Using the empty spill triggers with a simple selection (no TPC1 tracks, at least 18 nodes in TPC2 or TPC3), a data MC normalisation correction is found. The rate of CC inclusive events from cosmics is then increased from $(0.07\text{--}0.08)\pm0.01$ Hz to 0.09 ± 0.01 Hz and the Run 1+2+3+4 integrated beam spill data period of 6.9 s implies a negligible effect. Using empty spill triggers, the TPC1 veto rate due to cosmics is found to be 0.0055%.

- **Sand muon background.** A separate MC is generated in which beam neutrino induced interactions outside the magnet are simulated, and particles which pass into the magnet reconstructed. The CC event selections are applied, predicting 96 CC inclusive events (0.41% of the total magnet+sand MC prediction).

Data and MC are compared using a selection of events entering the upstream wall of the PØD; the 10% difference is treated as an uncertainty.

- **Event pile-up.** The TPC1 veto is used to reject interactions occurring upstream of the FGD1 fiducial volume and sand muons. Sand muons are not included in the standard MC, and so coincidences between sand and magnet events must be corrected for. The procedure is to calculate the number of TPC1 events in a sand MC sample, and so calculate the average number of events per bunch. The 10% sand MC uncertainty provides a need for a cross-check, therefore a second method is also used, comparing the number of TPC1 events per bunch between data and (sand+magnet) MC. The pile-up is taken as the larger of the two methods.

The effect of TPC1 events being assigned to the wrong bunch is negligible, no events in data or MC are vetoed if the TPC1 veto cut is extended from vetoing a bunch to vetoing a spill.

There are a maximum of 0.0005 CC inclusive selected events per bunch in data, therefore the pile-up is small (0.025%).

The probability of interactions outside the tracker fiducial volume (e.g. in the ECal or sand) producing extra tracks that cause event misclassification (e.g. CC-0- π as CC-1- π^+) is small ($\sim 10^{-5}\%$) due to the FGD fiducial volume cut on all tracks.

- **Out-of-fiducial-volume events.** OOFV events are defined as events in which the true interaction vertex occurred outside of the fiducial volume. There are multiple categories of events that are defined as OOFV; the dominant categories are high energy neutrons from outside the tracker creating a π^- in the FGD which is misidentified as a muon (17.6%), and backwards-going π^+ misreconstructed as

forwards going μ (18.0%).

For categories involving events outside the tracker, a 20% cross-section rate systematic is assigned (the interaction is likely to be on a heavier nuclear target; 20% comes from the uncertainty on PØD, ECal, SMRD event rate data/MC ratio when changing between GENIE and NEUT and the uncertainty on these ratios), while for categories of events occurring in the tracker (e.g. in the tracker dead material) no rate systematic is required. For categories where a relevant control sample exists, additional reconstruction systematics are assigned.

- **Pion secondary interactions.** GEANT4 is used to simulate the propagation of particles outside the nucleus. The pion interaction model used (QGSP_BERT) does not agree well with external data (see for example Ref. [166]), and the datasets contain uncertainties. The most significant secondary interaction modes are absorption (no π s in the final state), charge exchange (π^0 and no other π s in the final state), and QE scattering (inelastic scatter in which there is a single π in the final state, of the same charge as the initial π). Absorption and charge exchange can cause the event to be misclassified (e.g. π^+ is absorbed before it is detected, moving an event from CC-1- π^+ to CC-0- π). QE scattering can cause sudden direction changes complicating reconstruction (an extreme case is redirecting the particle from TPC2 to the ECal, meaning the track could be missed), and also produces pions with lower momenta, with a potentially higher absorption cross section (there is a peak at $p_{\pi^+} \sim 300$ MeV/c [184]). For each pion trajectory in the event, the probability of that trajectory occurring is calculated by checking the momentum and nuclear target dependent cross section at each step in the trajectory. The cross-section model can be altered, changing the trajectory probability, resulting in an event weight. A “correction weight” is calculated to bring data and MC cross sections into agreement; a “variation weight” is calculated based on the data uncertainty, to be used in the ND280 fit (see Sec. 3.3.4). When no π^- data is available, π^+ data is used in its place. When no data is available in the momentum range, the data is extrapolated using tuned GEANT4,

with a conservative assigned systematic. When no data is available on the nuclear target, data from the closest element (by atomic number) is used.

Bibliography

- [1] K. Abe et al. (T2K Collaboration). *"Precise Measurement of the Neutrino Mixing Parameter θ_{23} from Muon Neutrino Disappearance in an Off-axis Beam"*. Phys.Rev.Lett. **112**, 181801, (2014). arXiv:1403.1532 [hep-ex].
- [2] K. Abe et al. (T2K Collaboration). *"Measurement of Neutrino Oscillation Parameters from Muon Neutrino Disappearance with an Off-axis Beam"*. Phys. Rev.Lett. **111**, 211803, (2013). arXiv:1308.0465 [hep-ex].
- [3] K. Abe et al. (T2K Collaboration). *"First Muon-Neutrino Disappearance Study with an Off-Axis Beam"*. Phys.Rev. **D85**, 031103, (2012). arXiv:1201.1386 [hep-ex].
- [4] L. M. Brown. *"The idea of the neutrino"*. Phys.Today **31N9**, 23, (1978).
- [5] C. L. Cowan et al. *"Detection of the Free Neutrino: a Confirmation"*. Science **124**, 103, (1956).
- [6] G. Danby et al. *"Observation of High-Energy Neutrino Reactions and the Existence of Two Kinds of Neutrinos"*. Phys.Rev.Lett. **9**, 36, (1962).
- [7] F. J. Hasert et al. (Gargamelle Neutrino Collaboration). *"Observation of Neutrino Like Interactions Without Muon Or Electron in the Gargamelle Neutrino Experiment"*. Phys.Lett. **B46**, 138, (1973).
- [8] K. Kodama et al. (DONuT Collaboration). *"Observation of tau neutrino interactions"*. Phys.Lett. **B504**, 218, (2001). arXiv:hep-ex/0012035 [hep-ex].

- [9] M. Goldhaber, L. Grodzins, and A. W. Sunyar. *"Helicity of Neutrinos"*. Phys.Rev. **109**, 1015, (1958).
- [10] S. Schael et al. (ALEPH Collaboration, DELPHI Collaboration, L3 Collaboration, OPAL Collaboration, SLD Collaboration, LEP Electroweak Working Group, SLD Electroweak Group, SLD Heavy Flavour Group). *"Precision electroweak measurements on the Z resonance"*. Phys.Rept. **427**, 257, (2006). arXiv:hep-ex/0509008 [hep-ex].
- [11] P. A. R. Ade et al. (Planck Collaboration). *"Planck 2013 results. XVI. Cosmological parameters"*. 2013. arXiv:1303.5076 [astro-ph.CO].
- [12] V. N. Aseev et al. (Troitsk Collaboration). *"An upper limit on electron antineutrino mass from Troitsk experiment"*. Phys.Rev. **D84**, 112003, (2011). arXiv:1108.5034 [hep-ex].
- [13] K. Assamagan et al. *"Upper limit of the muon-neutrino mass and charged pion mass from momentum analysis of a surface muon beam"*. Phys.Rev. **D53**, 6065, (1996).
- [14] R. Barate et al. (ALEPH Collaboration). *"An Upper limit on the tau-neutrino mass from three-prong and five-prong tau decays"*. Eur.Phys.J. **C2**, 395, (1998).
- [15] M. Auger et al. (EXO Collaboration). *"Search for Neutrinoless Double-Beta Decay in ^{136}Xe with EXO-200"*. Phys.Rev.Lett. **109**, 032505, (2012). arXiv: 1205.5608 [hep-ex].
- [16] C. Giunti and C. W. Kim. *"Fundamentals of Neutrino Physics and Astrophysics"*. Oxford, UK: Oxford University Press, 2007.
- [17] G. Barbiellini and G. Cocconi. *"Electric Charge of the Neutrinos from SN1987A"*. Nature **329**, 21, (1987).

- [18] A. Beda et al. "GEMMA experiment: Three years of the search for the neutrino magnetic moment". *Phys.Part.Nucl.Lett.* **7**, 406, (2010). arXiv:0906.1926 [hep-ex].
- [19] M. Deniz et al. (TEXONO Collaboration). "Measurement of $\bar{\nu}_e$ -Electron Scattering Cross-Section with a CsI(Tl) Scintillating Crystal Array at the Kuo-Sheng Nuclear Power Reactor". *Phys.Rev.* **D81**, 072001, (2010). arXiv: 0911.1597 [hep-ex].
- [20] F. Reines, H. Sobel, and H. Gurr. "Stability of the neutrino". *Phys.Rev.Lett.* **32**, 180, (1974).
- [21] J. Beringer et al. (Particle Data Group). "2013 Review of Particle Physics". *Phys.Rev.* **D86**, 010001, (2012 and 2013 partial update for the 2014 edition).
- [22] C. L. Bennett et al. "Nine-year Wilkinson Microwave Anisotropy Probe (WMAP) Observations: Final Maps and Results". *The Astrophysical Journal Supplement Series* **208**, 20, 20, (2013). arXiv:1212.5225 [astro-ph.CO].
- [23] A. Sakharov. "Violation of CP Invariance, C Asymmetry, and Baryon Asymmetry of the Universe". *JETP Lett.* **5**, 24, (1967).
- [24] M. Fukugita and T. Yanagida. "Baryogenesis Without Grand Unification". *Phys.Lett.* **B174**, 45, (1986).
- [25] J. A. Formaggio and G. P. Zeller. "From eV to EeV: Neutrino Cross Sections Across Energy Scales". *Rev.Mod.Phys.* **84**, 1307, (2012). arXiv:1305.7513 [hep-ex].
- [26] D. Casper. "The Nuance neutrino physics simulation, and the future". *Nucl. Phys.Proc.Suppl.* **112**, 161, (2002). arXiv:hep-ph/0208030 [hep-ph].
- [27] B. Pontecorvo. "Mesonium and anti-mesonium". *Sov.Phys.JETP* **6**, 429, (1957).

- [28] B. Pontecorvo. *"Inverse beta processes and nonconservation of lepton charge"*. Sov.Phys.JETP **7**, 172, (1958).
- [29] Z. Maki, M. Nakagawa, and S. Sakata. *"Remarks on the unified model of elementary particles"*. Prog.Theor.Phys. **28**, 870, (1962).
- [30] B. Kayser. *"On the Quantum Mechanics of Neutrino Oscillation"*. Phys.Rev. **D24**, 110, (1981).
- [31] J. Beringer et al. (Particle Data Group). *"2012 Review of Particle Physics"*. Phys.Rev. **D86**, 010001, (2012).
- [32] M. C. Gonzalez-Garcia et al. *"Global fit to three neutrino mixing: critical look at present precision"*. JHEP **1212**, 123, (2012). NuFIT 1.2 (2013) <http://www.nu-fit.org>. arXiv:1209.3023 [hep-ph].
- [33] J. N. Bahcall, M. H. Pinsonneault, and S. Basu. *"Solar models: Current epoch and time dependences, neutrinos, and helioseismological properties"*. Astrophys. J. **555**, 990, (2001). arXiv:astro-ph/0010346 [astro-ph].
- [34] J. N. Bahcall and C. Pena-Garay. *"Solar models and solar neutrino oscillations"*. New J.Phys. **6**, 63, (2004). arXiv:hep-ph/0404061 [hep-ph].
- [35] B. T. Cleveland et al. *"Measurement of the Solar Electron Neutrino Flux with the Homestake Chlorine Detector"*. Astrophys.J. **496**, 505, (1998).
- [36] F. Kaether et al. *"Reanalysis of the GALLEX solar neutrino flux and source experiments"*. Phys.Lett. **B685**, 47, (2010). arXiv:1001.2731 [hep-ex].
- [37] J. N. Abdurashitov et al. (SAGE Collaboration). *"Measurement of the solar neutrino capture rate with gallium metal. III: Results for the 2002–2007 data-taking period"*. Phys.Rev. **C80**, 015807, (2009). arXiv:0901.2200 [nucl-ex].

- [38] B. Aharmim et al. (SNO Collaboration). *"Combined Analysis of all Three Phases of Solar Neutrino Data from the Sudbury Neutrino Observatory"*. Phys. Rev. **C88**, 025501, (2013). arXiv:1109.0763 [nucl-ex].
- [39] J. Hosaka et al. (Super-Kamiokande Collaboration). *"Solar neutrino measurements in Super-Kamiokande-I"*. Phys. Rev. **D73**, 112001, (2006). arXiv: hep-ex/0508053 [hep-ex].
- [40] J. P. Cravens et al. (Super-Kamiokande Collaboration). *"Solar neutrino measurements in Super-Kamiokande-II"*. Phys. Rev. **D78**, 032002, (2008). arXiv: 0803.4312 [hep-ex].
- [41] K. Abe et al. (Super-Kamiokande Collaboration). *"Solar neutrino results in Super-Kamiokande-III"*. Phys. Rev. **D83**, 052010, (2011). arXiv:1010.0118 [hep-ex].
- [42] M. Smy (Super-Kamiokande Collaboration). *"Super-Kamiokande's solar ν results"*. Nucl.Phys.Proc.Suppl. **235–236**, 49, (2013).
- [43] G. Bellini et al. (Borexino Collaboration). *"Measurement of the solar 8B neutrino rate with a liquid scintillator target and 3 MeV energy threshold in the Borexino detector"*. Phys. Rev. **D82**, 033006, (2010). arXiv:0808.2868 [astro-ph].
- [44] G. Bellini et al. (Borexino Collaboration). *"Precision measurement of the 7Be solar neutrino interaction rate in Borexino"*. Phys. Rev. Lett. **107**, 141302, (2011). arXiv:1104.1816 [hep-ex].
- [45] L. K. Pik. *"Study of the neutrino mass hierarchy with the atmospheric neutrino data observed in Super-Kamiokande"*. PhD thesis. University of Tokyo, 2012.
- [46] A. Gando et al. (KamLAND Collaboration). *"Constraints on θ_{13} from A Three-Flavor Oscillation Analysis of Reactor Antineutrinos at KamLAND"*. Phys. Rev. **D83**, 052002, (2011). arXiv:1009.4771 [hep-ex].

- [47] M. Apollonio et al. (CHOOZ Collaboration). *"Limits on neutrino oscillations from the CHOOZ experiment"*. Phys.Lett. **B466**, 415, (1999). arXiv:hep-ex/9907037 [hep-ex].
- [48] F. Boehm et al. *"Final results from the Palo Verde neutrino oscillation experiment"*. Phys.Rev. **D64**, 112001, (2001). arXiv:hep-ex/0107009 [hep-ex].
- [49] Y. Abe et al. (Double Chooz Collaboration). *"Reactor electron antineutrino disappearance in the Double Chooz experiment"*. Phys.Rev. **D86**, 052008, (2012). arXiv:1207.6632 [hep-ex].
- [50] S. Jetter (Daya Bay Collaboration). *"Spectral Measurement of Electron Antineutrino Oscillation Amplitude and Frequency at Daya Bay"*. 2013. NuFact 2013, 15th International Workshop on Neutrino Factories, Super Beams and Beta Beams, 19-24 August 2013, China.
- [51] S.-H. Seo (RENO Collaboration). *"Recent Results from RENO"*. 2013. TAUP 2013, 13th International Conference on Topics in Astroparticle and Underground Physics, 9-13 September 2013, USA.
- [52] P. Adamson et al. (MINOS Collaboration). *"Measurement of Neutrino and Antineutrino Oscillations Using Beam and Atmospheric Data in MINOS"*. Phys.Rev.Lett. **110**, 251801, (2013). arXiv:1304.6335 [hep-ex].
- [53] P. Adamson et al. (MINOS Collaboration). *"Electron neutrino and antineutrino appearance in the full MINOS data sample"*. Phys.Rev.Lett. **110**, 171801, (2013). arXiv:1301.4581 [hep-ex].
- [54] M. Wilking (T2K Collaboration). *"New Results from the T2K Experiment: Observation of ν_e Appearance in a ν_μ Beam"*. 2013. arXiv:1311.4114 [hep-ex].
- [55] F. Capozzi et al. *"Status of three-neutrino oscillation parameters, circa 2013"*. 2013. arXiv:1312.2878 [hep-ph].

- [56] D. V. Forero, M. Tortola, and J. W. F. Valle. "*Global status of neutrino oscillation parameters after Neutrino-2012*". Phys.Rev. **D86**, 073012, (2012). arXiv:1205.4018 [hep-ph].
- [57] P. Huber. "*On the determination of anti-neutrino spectra from nuclear reactors*". Phys.Rev. **C84**, 024617, (2011). arXiv:1106.0687 [hep-ph].
- [58] P. Harrison, D. Perkins, and W. Scott. "*Tri-bimaximal mixing and the neutrino oscillation data*". Phys.Lett. **B530**, 167, (2002). arXiv:hep-ph/0202074 [hep-ph].
- [59] S. F. King and C. Luhn. "*Neutrino Mass and Mixing with Discrete Symmetry*". Rept.Prog.Phys. **76**, 056201, (2013). arXiv:1301.1340 [hep-ph].
- [60] K. N. Abazajian et al. "*Light Sterile Neutrinos: A White Paper*". 2012. arXiv: 1204.5379 [hep-ph].
- [61] A. Aguilar-Arevalo et al. (LSND Collaboration). "*Evidence for neutrino oscillations from the observation of anti-neutrino(electron) appearance in a anti-neutrino(muon) beam*". Phys.Rev. **D64**, 112007, (2001). arXiv:hep-ex/ 0104049 [hep-ex].
- [62] A. A. Aguilar-Arevalo et al. (MiniBooNE Collaboration). "*Improved Search for $\bar{\nu}_\mu \rightarrow \bar{\nu}_e$ Oscillations in the MiniBooNE Experiment*". Phys.Rev.Lett. **110**, 161801, (2013). arXiv:1207.4809 [hep-ex].
- [63] G. Mention et al. "*The Reactor Antineutrino Anomaly*". Phys.Rev. **D83**, 073006, (2011). arXiv:1101.2755 [hep-ex].
- [64] Y.-F. Li et al. "*Unambiguous Determination of the Neutrino Mass Hierarchy Using Reactor Neutrinos*". Phys.Rev. **D88**, 013008, (2013). arXiv:1303.6733 [hep-ex].

- [65] M. G. Aartsen et al. (IceCube Collaboration, PINGU Collaboration). "*PINGU Sensitivity to the Neutrino Mass Hierarchy*". 2013. arXiv:1306.5846 [astro-ph.IM].
- [66] M. S. Athar et al. (INO Collaboration). "*India-based Neutrino Observatory: Project Report. Volume I.*". 2006.
- [67] C. Adams et al. (LBNE Collaboration). "*Scientific Opportunities with the Long-Baseline Neutrino Experiment*". 2013. arXiv:1307.7335 [hep-ex].
- [68] K. Abe et al. "*Letter of Intent: The Hyper-Kamiokande Experiment — Detector Design and Physics Potential —*". 2011. arXiv:1109.3262 [hep-ex].
- [69] K. Abe et al. (T2K Collaboration). "*The T2K Experiment*". Nucl.Instrum. Meth. **A659**, 106, (2011). arXiv:1106.1238 [physics.ins-det].
- [70] Y. Yamazaki et al. "*Accelerator technical design report for J-PARC*". 2003. <http://hadron.kek.jp/accelerator/TDA/tdr2003/index2.html>.
- [71] T. Ogitsu et al. "*Superconducting combined function magnet system for J-PARC neutrino experiment*". IEEE Trans.Appl.Supercond. **15**, 1175, (2005).
- [72] S. van der Meer. "*A directive device for charged particles and its use in an enhanced neutrino beam*". 1961.
- [73] D. Beavis et al. (E889). "*Long Baseline Neutrino Oscillation Experiment at the AGS*". 1995.
- [74] K. Abe et al. (T2K Collaboration). "*The T2K Neutrino Flux Prediction*". Phys.Rev. **D87**, 012001, (2013). arXiv:1211.0469 [hep-ex].
- [75] J. Coulombe et al. (T2K (ND280 Group)). "*T2K ND280 Conceptual Design Report*". <http://www.nd280.org/documents/cdr.pdf/download>, 2005.
- [76] K. Abe et al. "*Measurements of the T2K neutrino beam properties using the INGRID on-axis near detector*". Nucl.Instrum.Meth. **A694**, 211, (2012).

- [77] M. B. Luque et al. (UA1 Collaboration). *"The construction of the central detector for an experiment at the {CERN} p-p collider"*. Nucl.Instrum.Meth. **176**, 175, (1980).
- [78] S. Assylbekov et al. *"The T2K ND280 off-axis pi-zero detector"*. Nucl.Instrum. Meth. **A686**, 48, (2012).
- [79] N. Abgrall et al. *"Time projection chambers for the T2K near detectors"*. Nucl. Instrum.Meth. **A637**, 25, (2011).
- [80] P.-A. Amaudruz et al. *"The T2K fine-grained detectors"*. Nucl.Instrum.Meth. **A696**, 1, (2012).
- [81] D. Allan et al. *"The electromagnetic calorimeter for the T2K near detector ND280"*. Journal of Instrumentation **8**, P10019, (2013).
- [82] S. Aoki et al. *"The T2K Side Muon Range Detector (SMRD)"*. Nucl.Instrum. Meth. **A698**, 135, (2013).
- [83] A. Pla-Dalmau (MINOS Scintillator Group). *"Extruded plastic scintillator for the MINOS calorimeters"*. Frascati Phys.Ser. **21**, 513, (2001).
- [84] M. Yokoyama et al. *"Application of Hamamatsu MPPCs to T2K neutrino detectors"*. Nucl.Instrum.Meth. **A610**, 128, (2009). Proceedings of the Fifth International Conference on New Developments in Photodetection (NDIP08).
- [85] J. B. Birks. *"Theory and practice of scintillation counting"*. Macmillan, New York, 1964.
- [86] L. Bellantoni and P. Rubinov. *"Bench test of first Trip-T prototypes"*. D0 note **4845**, (2005).
- [87] Y. Hayato. *"A neutrino interaction simulation program library NEUT"*. Acta Phys.Polon. **B40**, 2477, (2009).

- [88] C. Andreopoulos et al. "*The GENIE Neutrino Monte Carlo Generator*". Nucl. Instrum.Meth. **A614**, 87, (2010). arXiv:0905.2517 [hep-ph].
- [89] J. A. Nowak. "*Wroclaw neutrino event generator*". Phys.Scr. **2006**, 70, (2006).
- [90] D. Heck et al. "*CORSIKA: a Monte Carlo code to simulate extensive air showers.*". Forschungszentrum Karlsruhe GmbH, Karlsruhe (Germany), TIB Hannover, D-30167 Hannover (Germany), 1998.
- [91] S. Agostinelli et al. "*Geant4 - a simulation toolkit*". Nucl.Instrum.Meth. **A506**, 250, (2003).
- [92] J. Allison et al. "*Geant4 developments and applications*". IEEE Trans.Nucl. Sci. **53**, 270, (2006).
- [93] D. Karlen, P. Poffenberger, and G. Rosenbaum. "*TPC performance in magnetic fields with GEM and pad readout*". Nucl.Instrum.Meth. **A555**, 80, (2005). arXiv:physics/0509051 [physics.ins-det].
- [94] A. Cervera-Villanueva, J. J. Gómez-Cadenas, and J. A. Hernando. "*RecPack a reconstruction toolkit*". Nucl.Instrum.Meth. **A534**, 180, (2004). Proceedings of the IXth International Workshop on Advanced Computing and Analysis Techniques in Physics Research.
- [95] Y. Itow et al. (T2K Collaboration). "*The JHF-Kamioka neutrino project*". 239, 2001. arXiv:hep-ex/0106019 [hep-ex].
- [96] S. Fukuda et al. "*The Super-Kamiokande detector*". Nucl.Instrum.Meth. **A501**, 418, (2003).
- [97] T. Barszczak. "*The Efficient discrimination of electron and pi-zero events in a water Cherenkov detector and the application to neutrino oscillation experiments*". PhD thesis. University of California, Irvine, 2005.
- [98] R. Brun et al. "*GEANT3*". CERN-DD-EE-84-1, 1987.

- [99] C. Zeitnitz and T. A. Gabriel. Proc. of International Conference on Calorimetry in High Energy Physics, 1993.
- [100] M. Nakahata et al. "*Atmospheric Neutrino Background and Pion Nuclear Effect for KAMIOKA Nucleon Decay Experiment*". J.Phys.Soc.Jap. **55**, 3786, (1986).
- [101] E. Davies. "*Machine Vision: Theory, Algorithms, Practicalities*". Burlington, USA: Morgan Kaufmann, 2007.
- [102] R. B. Patterson et al. "*The extended-track event reconstruction for Mini-BooNE*". Nucl.Instrum.Meth. **A608**, 206, (2009).
- [103] S. Mine. "*New POLfit*". T2K-TN-005, 2009.
- [104] K. Abe et al. (T2K Collaboration). "*Observation of Electron Neutrino Appearance in a Muon Neutrino Beam*". Phys.Rev.Lett. **112**, 061802, (2014). arXiv: 1311.4750 [hep-ex].
- [105] Y. Hayato et al. "*Letter of intent: Neutrino oscillation experiment at JHF*". 2003.
- [106] T. Collaboration. "*Physics Potential and Sensitivities of T2K Beyond Observation of ν_e appearance from a ν_μ beam*". Report to J-PARC PAC, 2013.
- [107] M. Friend and M. Ikeda. "*Future Sensitivity Task Force - Three Flavor Log Likelihood Fitter using a Realistic Systematic Error Covariance Matrix*". T2K-TN-151, 2013.
- [108] M. Bass, D. Cherdack, and R. J. Wilson. "*Future Sensitivity to the Neutrino Oscillation Parameters for T2K and NO ν A*". T2K-TN-167, 2013.
- [109] K. Abe et al. (T2K Collaboration). "*Measurement of the Inclusive NuMu Charged Current Cross Section on Carbon in the Near Detector of the T2K Experiment*". Phys.Rev. **D87**, 092003, (2013). arXiv:1302.4908 [hep-ex].

[110] A. V. Waldron. *"Neutrino Oscillation Parameters from ν_e Appearance in the T2K Experiment"*. PhD thesis. University of Oxford, 2012.

[111] A. Ferrari et al. *"FLUKA: A multi-particle transport code"*. CERN-2005-010, SLAC-R-773, INFN-TC-05-11, 2005.

[112] G. Battistoni et al. *"The FLUKA code: Description and benchmarking"*. AIP Conf.Proc. **896**, 31, (2007).

[113] N. Abgrall et al. (NA61/SHINE collaboration). *"NA61/SHINE facility at the CERN SPS: beams and detector system"*. 2014. arXiv:1401.4699 [physics.ins-det].

[114] N. Abgrall et al. (NA61/SHINE Collaboration). *"Measurements of Cross Sections and Charged Pion Spectra in Proton-Carbon Interactions at 31 GeV/c"*. Phys.Rev. **C84**, 034604, (2011). arXiv:1102.0983 [hep-ex].

[115] N. Abgrall et al. (NA61/SHINE Collaboration). *"Measurement of Production Properties of Positively Charged Kaons in Proton-Carbon Interactions at 31 GeV/c"*. Phys.Rev. **C85**, 035210, (2012). arXiv:1112.0150 [hep-ex].

[116] T. Eichten et al. *"Particle production in proton interactions in nuclei at 24 GeV/c"*. Nucl.Phys. **B44**, 333, (1972).

[117] J. Allaby et al. *"High-energy particle spectra from proton interactions at 19.2-GeV/c"*. CERN-70-12, 1970.

[118] I. Chemakin et al. (E910 Collaboration). *"Pion production by protons on a thin beryllium target at 6.4-GeV/c, 12.3-GeV/c, and 17.5-GeV/c incident proton momenta"*. Phys.Rev. **C77**, 015209, (2008). arXiv:0707.2375 [nucl-ex].

[119] N. Abgrall et al. (NA61/SHINE Collaboration). *"Pion emission from the T2K replica target: method, results and application"*. Nucl.Instrum.Meth. **A701**, 99, (2013). arXiv:1207.2114 [hep-ex].

- [120] C. H. Llewellyn Smith. *"Neutrino Reactions at Accelerator Energies"*. Phys. Rept. **3**, 261, (1972).
- [121] R. A. Smith and E. J. Moniz. *"Neutrino Reactions On Nuclear Targets"*. Nucl. Phys. **B43**, 605, (1972).
- [122] A. A. Aguilar-Arevalo et al. (MiniBooNE Collaboration). *"First measurement of the muon neutrino charged current quasielastic double differential cross section"*. Phys.Rev. **D81**, 092005, (2010).
- [123] R. Gran et al. (K2K Collaboration). *"Measurement of the quasielastic axial vector mass in neutrino interactions on oxygen"*. Phys.Rev. **D74**, 052002, (2006).
- [124] X. Espinal and F. Sánchez. *"Measurement of the axial vector mass in neutrino-Carbon interactions at K2K"*. AIP Conf.Proc. **967**, 117, (2007).
- [125] N. S. Mayer. *"Measurement of the M_A^{QE} parameter using multiple quasi-elastic dominated sub-samples in the MINOS near detector"*. PhD thesis. Indiana University, 2011.
- [126] A. Bodek et al. *"Vector and Axial Nucleon Form Factors: A Duality Constrained Parameterization"*. Eur.Phys.J. **C53**, 349, (2008). arXiv:0708.1946 [hep-ex].
- [127] V. Lyubushkin et al. (NOMAD Collaboration). *"A Study of quasi-elastic muon neutrino and antineutrino scattering in the NOMAD experiment"*. Eur. Phys.J. **C63**, 355, (2009). arXiv:0812.4543 [hep-ex].
- [128] K. Abe et al. *"Precise Determination of $\sin^2 \theta_W$ from Measurements of the Differential Cross Sections for $\nu_\mu p \rightarrow \nu_\mu p$ and $\bar{\nu}_\mu p \rightarrow \bar{\nu}_\mu p$ "*. Phys.Rev.Lett. **56**, 1107, (1986).
- [129] D. Rein and L. M. Sehgal. *"Neutrino-excitation of baryon resonances and single pion production"*. Ann.Phys. **133**, 79, (1981).

- [130] D. Rein. *"Angular distribution in neutrino-induced single pion production processes"*. Z.Phys. **C35**, 43, (1987).
- [131] M. Glück, E. Reya, and A. Vogt. *"Dynamical parton distributions revisited"*. Eur.Phys.J. **C5**, 461, (1998).
- [132] A. Bodek and U. K. Yang. *"Modeling neutrino and electron scattering inelastic cross- sections in the few GeV region with effective LO PDFs TV Leading Order"*. Nucl.Phys.Proc.Suppl. 2003. arXiv:hep-ex/0308007 [hep-ex].
- [133] T. Sjostrand, L. Lonnblad, and S. Mrenna. *"PYTHIA 6.2: Physics and manual"*. 2001. arXiv:hep-ph/0108264 [hep-ph].
- [134] Z. Koba, H. B. Nielsen, and P. Olesen. *"Scaling of multiplicity distributions in high-energy hadron collisions"*. Nucl.Phys. **B40**, 317, (1972).
- [135] M. Derrick et al. *"Properties of the hadronic system resulting from $\bar{\nu}_\mu p$ interactions"*. Phys.Rev. **D17**, 1, (1978).
- [136] S. Barlag et al. (Amsterdam-Bologna-Padua-Pisa-Saclay-Turin Collaboration). *"Charged Hadron Multiplicities in High-energy Anti-muon Neutrino n and Anti-muon Neutrino p Interactions"*. Z.Phys. **C11**, 283, (1982).
- [137] V. Ammosov. *"Low multiplicity final states in neutrino interactions at low energies (SKAT BC results)"*. Talk at NuInt01 workshop, Tsukuba, Japan. 2001.
- [138] P. Musset and J.-P. Vialle. *"Neutrino physics with Gargamelle"*. Phys.Rep. **39**, 1, (1978).
- [139] J. E. Kim et al. *"A theoretical and experimental review of the weak neutral current: a determination of its structure and limits on deviations from the minimal $SU(2)_L \times U(1)$ electroweak theory"*. Rev.Mod.Phys. **53**, 211, (1981).

[140] D. Rein and L. M. Sehgal. "Coherent π^0 production in neutrino reactions". Nucl.Phys. **B223**, 29, (1983).

[141] P. Marage et al. "Coherent single pion production by antineutrino charged current interactions and test of PCAC". Z.Phys. **C31**, 191, (1986).

[142] D. Rein and L. M. Sehgal. "PCAC and the deficit of forward muons in production by neutrinos". Phys.Lett. **B657**, 207, (2007).

[143] A. A. Aguilar-Arevalo et al. (MiniBooNE Collaboration). "The MiniBooNE Detector". Nucl.Instrum.Meth. **A599**, 28, (2009). arXiv:0806.4201 [hep-ex].

[144] P. de Perio et al. "Cross section parameters for the 2012a oscillation analysis". T2K-TN-108, 2012.

[145] K. Abe et al. (T2K Collaboration). "Evidence of Electron Neutrino Appearance in a Muon Neutrino Beam". Phys.Rev. **D88**, 032002, (2013). arXiv:1304.0841 [hep-ex].

[146] A. A. Aguilar-Arevalo et al. (MiniBooNE Collaboration). "Measurement of ν_μ -induced charged-current neutral pion production cross sections on mineral oil at $E_\nu \in 0.5 - 2.0 \text{ GeV}$ ". Phys.Rev. **D83**, 052009, (2011). arXiv:1010.3264 [hep-ex].

[147] A. A. Aguilar-Arevalo et al. (MiniBooNE Collaboration). "Measurement of Neutrino-Induced Charged-Current Charged Pion Production Cross Sections on Mineral Oil at $E_\nu \sim 1 \text{ GeV}$ ". Phys.Rev. **D83**, 052007, (2011). arXiv:1011.3572 [hep-ex].

[148] A. A. Aguilar-Arevalo et al. (MiniBooNE Collaboration). "Measurement of ν_μ and $\bar{\nu}_\mu$ induced neutral current single π^0 production cross sections on mineral oil at $E_\nu \sim \mathcal{O}(1 \text{ GeV})$ ". Phys.Rev. **D81**, 013005, (2010). arXiv:0911.2063 [hep-ex].

[149] P. de Perio et al. "Implementation of the NIWG Cross Section Parametrization". T2K-TN-113, 2012.

[150] E. J. Moniz et al. "Nuclear Fermi Momenta from Quasielastic Electron Scattering". Phys.Rev.Lett. **26**, 445, (1971).

[151] A. M. Ankowski and J. T. Sobczyk. "Construction of spectral functions for medium-mass nuclei". Phys.Rev. **C77**, 044311, (2008). arXiv:0711.2031 [nucl-th].

[152] M. Hasegawa et al. (K2K Collaboration). "Search for coherent charged pion production in neutrino-carbon interactions". Phys.Rev.Lett. **95**, 252301, (2005). arXiv:hep-ex/0506008 [hep-ex].

[153] K. Hiraide et al. (SciBooNE Collaboration). "Search for Charged Current Coherent Pion Production on Carbon in a Few-GeV Neutrino Beam". Phys.Rev. **D78**, 112004, (2008). arXiv:0811.0369 [hep-ex].

[154] Y. Kurimoto et al. (SciBooNE Collaboration). "Improved measurement of neutral current coherent π^0 production on carbon in a few-GeV neutrino beam". Phys.Rev. **D81**, 111102, (2010).

[155] P. Adamson et al. (MINOS Collaboration). "Neutrino and Antineutrino Inclusive Charged-current Cross Section Measurements with the MINOS Near Detector". Phys.Rev. **D81**, 072002, (2010). arXiv:0910.2201 [hep-ex].

[156] W. Krenz et al. (Gargamelle Neutrino Propane). "Experimental study of exclusive one-pion production in all neutrino-induced neutral current channels". Nucl.Phys. **B135**, 45, (1978).

[157] M. Derrick et al. "Study of the Reaction $\nu N \rightarrow \nu p \pi^-$ ". Phys.Lett. **B92**, 363, (1980). Erratum-ibid. **B95** 461 (1980).

- [158] M. Day and K. S. McFarland. *"Differences in Quasi-Elastic Cross-Sections of Muon and Electron Neutrinos"*. Phys.Rev. **D86**, 053003, (2012). arXiv: 1206.6745 [hep-ph].
- [159] G. A. Fiorentini et al. (MINER ν A Collaboration). *"Measurement of Muon Neutrino Quasielastic Scattering on a Hydrocarbon Target at $E_\nu \sim 3.5 \text{ GeV}$ "*. Phys.Rev.Lett. **111**, 022502, (2013). arXiv:1305.2243 [hep-ex].
- [160] L. Fields et al. (MINER ν A Collaboration). *"Measurement of Muon Antineutrino Quasielastic Scattering on a Hydrocarbon Target at $E_\nu \sim 3.5 \text{ GeV}$ "*. Phys. Rev.Lett. **111**, 022501, (2013). arXiv:1305.2234 [hep-ex].
- [161] A. A. Aguilar-Arevalo et al. (MiniBooNE Collaboration). *"First measurement of the muon antineutrino double-differential charged-current quasielastic cross section"*. Phys.Rev. **D88**, 032001, (2013). arXiv:1301.7067 [hep-ex].
- [162] P. de Perio et al. *"NEUT Nuclear Effects (FSI)"*. T2K-TN-033, 2012.
- [163] C. Bojeckho et al. *"CC-multiple-pion ν_μ event selections in the ND280 tracker using Run 1+2+3+4 data"*. T2K-TN-152, 2013.
- [164] M. Hartz, A. Kabeth, and K. Mahn. *"Constraining the Flux and Cross Section Models with Data from the ND280 Detector for the 2013 Oscillation Analysis"*. T2K-TN-166, 2013.
- [165] M. Bass et al. *"Data Quality at the near detectors for Run 3"*. T2K-TN-127, 2012.
- [166] D. Ashery et al. *"True absorption and scattering of pions on nuclei"*. Phys.Rev. **C23**, 2173, (1981).
- [167] F. James and M. Roos. *"Minuit: A System for Function Minimization and Analysis of the Parameter Errors and Correlations"*. Comput.Phys.Commun. **10**, 343, (1975).

[168] J. Hignight et al. "Super-Kamiokande events and data quality studies for T2K Run 4". T2K-TN-148, 2013.

[169] M. Honda et al. "Improvement of low energy atmospheric neutrino flux calculation using the JAM nuclear interaction model". Phys.Rev. **D83**, 123001, (2011). arXiv:1102.2688 [astro-ph.HE].

[170] J. Kameda. "Updated study of the systematic error in ν_μ disappearance analysis from Super-Kamiokande". T2K-TN-159, 2013.

[171] C. Zeitnitz and T. A. Gabriel. "The GEANT-CALOR interface and benchmark calculations of ZEUS test calorimeters". Nucl.Instrum.Meth. **A349**, 106, (1994).

[172] G. J. Feldman and R. D. Cousins. "A Unified approach to the classical statistical analysis of small signals". Phys.Rev. **D57**, 3873, (1998). arXiv: physics/9711021 [physics.data-an].

[173] K. Hagiwara, N. Okamura, and K.-i. Senda. "The earth matter effects in neutrino oscillation experiments from Tokai to Kamioka and Korea". JHEP **1109**, 082, (2011). arXiv:1107.5857 [hep-ph].

[174] M. Matsumoto and T. Nishimura. "Mersenne Twister: A 623-dimensionally Equidistributed Uniform Pseudo-random Number Generator". ACM Trans. Model. Comput. Simul. **8**, 3, (1998).

[175] W. H. Press et al. "Numerical Recipes 3rd Edition: The Art of Scientific Computing". 3rd ed. New York, NY, USA: Cambridge University Press, 2007.

[176] Y. Fukuda et al. (Super-Kamiokande Collaboration). "Evidence for oscillation of atmospheric neutrinos". Phys.Rev.Lett. **81**, 1562, (1998). arXiv: hep-ex/9807003 [hep-ex].

[177] G. Cowan. "Statistical Data Analysis". Oxford University Press, Oxford, 1998.

- [178] P. Adamson et al. (MINOS Collaboration). *"Combined analysis of ν_μ disappearance and $\nu_\mu \rightarrow \nu_e$ appearance in MINOS using accelerator and atmospheric neutrinos"*. submitted to Phys.Rev.Lett. 2014. arXiv:1403.0867 [hep-ex].
- [179] A. Himmel (Super-Kamiokande Collaboration). *"Recent Atmospheric Neutrino Results from Super-Kamiokande"*. 7th Intl. Conf. on Interconnection between Particle Physics & Cosmology (PPC 2013), 2013. arXiv:1310.6677 [hep-ex].
- [180] C. Andreopoulos et al. *"T2K 3.01×10^{20} -POT 3-Flavour Muon-Neutrino Disappearance Analysis"*. T2K-TN-141, 2012.
- [181] P. de Perio (T2K Collaboration). *"Oscillation results from T2K"*. Talk at Moriond EW 2014, La Thuile, Italy. 2014.
- [182] O. C. Allkofer et al. *"The absolute cosmic ray flux at sea level"*. J.Phys. **G1**, L51, (1975).
- [183] C. Amsler et al. (Particle Data Group). *"2008 Review of Particle Physics"*. Phys.Lett. **B667**, 1, (2008). Review of Particle Physics.
- [184] J. Myslik. *"Determination of pion secondary interaction systematics for the ND280 tracker ν_μ analysis"*. T2K-TN-125, 2013.